



UNIVERSITY OF
BIRMINGHAM

Proton Transfer Reaction Mass Spectrometric Investigations of
Compounds of Relevance to Homeland Security and Breath
Analysis

by

David Olivenza-León

A thesis submitted to
The University of Birmingham
for the degree of
Doctor of Philosophy

School of Physics and Astronomy
College of Engineering and Physical Sciences
The University of Birmingham
October 2019

Abstract

Acknowledgements

Table of Contents

1	Introduction	1
1.1	Soft Chemical Ionisation Mass Spectrometry	1
1.1.1	Thermodynamics of proton transfer	1
1.1.2	Kinetics of proton transfer	4
1.1.3	Other reagent ions	5
1.1.4	SCI-MS techniques	6
1.1.4.1	Ion Mobility Spectrometry	6
1.1.4.2	Selected Ion Flow Tube Mass Spectrometry	7
1.1.4.3	Proton Transfer Reaction Mass Spectrometry	8
1.2	Thesis outline	10
1.3	Aim of the thesis	10
2	Proton Transfer Reaction Mass Spectrometry	12
2.1	The PTR-ToF-MS	12
2.1.1	Ion source	14
2.1.1.1	The glow discharge: production of reagent ions	14
2.1.2	Drift tube	16
2.1.2.1	Reduced electric field	17
2.1.2.2	Radio frequency ion funnel	21
2.1.2.3	Fast reduced electric field switching	23
2.1.3	Differential pumping region and transfer lenses	24
2.1.4	Mass spectrometer	24
2.1.4.1	Time-of-flight mass spectrometer	25

2.1.4.2	Relectron	26
2.1.4.3	Detector	27
2.1.4.4	Calibration	27
2.2	Data analysis	28
2.2.1	Data acquisition, visualisation and treatment	28
2.2.2	Calculation of ion intensities	29
2.2.3	Fast switching software	32
2.2.4	Density functional theory	35
2.3	PTR-MS Add-ons	35
2.3.1	Thermal Desorption Unit	35
2.3.2	FastGC	36
2.3.3	Liquid Calibration Unit	38
3	Theoretical and experimental investigations of illicit drugs in PTR-MS: Cocaine and related compounds	40
3.1	Introduction	40
3.2	Experimental details	41
3.2.1	Chemicals	41
3.2.2	Sampling methods: thermal desorption unit and headspace analysis	42
3.2.3	Density functional theory	42
3.3	DFT and PTR-MS results	42
3.3.1	Reagent ions	43
3.3.2	Cocaine	44
3.3.3	Methyl ecgonine	49
3.3.4	Benzoate esters	51
3.3.4.1	Methyl benzoate	53
3.3.4.2	Ethyl benzoate	54
3.3.4.3	Isopropyl benzoate	57
3.3.4.4	Benzoic acid	60
3.3.5	Isobutyrates	63
3.3.5.1	Methyl isobutyrate	63

3.3.5.2	Ethyl isobutyrate	66
3.3.6	Cocaethylene	66
3.3.7	Ethyl ecgonine	66
3.3.8	Norcocaine	66
3.3.9	Anhydromethylecgonine	69
3.3.10	<i>o</i> -Hydroxycocaine	69
3.4	Conclusions and further remarks	69
4	Enhancement of Compound Selectivity Using a Radio Frequency Ion Funnel Proton Transfer Reaction Mass Spectrometer: Improved Specificity for Explosive Compounds	72
4.1	Abstract	73
4.2	Introduction	73
4.3	Methodology	75
4.3.1	Experimental details	75
4.3.2	Electronic structure calculations	77
4.4	Results and discussion	77
4.4.1	Reagent ions	77
4.4.2	This is mine – Reagent ion in DC mode and RF mode	79
4.4.3	2,4,6-trinitrotoluene (TNT)	80
4.4.4	Dinitrotoluenes	84
4.4.5	Nitrotoluenes	86
4.5	Conclusions	88
5	Selective Reagent Ion Mass Spectrometric Investigations of the Nitroanilines	89
5.1	Abstract	89
5.2	Introduction	90
5.3	Experimental details	92
5.3.1	Selective Reagent Ion-Mass Spectrometry (SRI-MS)	92
5.3.1.1	Proton Transfer Reaction Mode	92
5.3.1.2	Charge Transfer Reaction Mode	93
5.3.2	Chemicals	93

5.3.3	Operational procedures	94
5.3.4	Density Functional Theory Calculations	95
5.4	Results	95
5.4.1	DFT Results	95
5.4.2	Fragmentation patterns and branching ratios studies in proton transfer mode	96
5.4.2.1	2-nitroaniline	96
5.4.2.2	3-nitroaniline	97
5.4.2.3	4-nitroaniline	98
5.4.3	Fragmentation patterns and branching percentage studies in charge trans- fer mode	100
5.4.3.1	2-nitroaniline	100
5.4.3.2	3-nitroaniline	100
5.4.3.3	4-nitroaniline	101
5.5	Conclusions	103
6	Compendium of the Reactions of H₃O⁺ With Selected Ketones of Relevance to Breath Analysis Using Proton Transfer Reaction Mass Spectrometry	104
6.1	Abstract	105
6.2	Introduction	106
6.3	Materials and Methods	108
6.3.1	Sample preparation	108
6.3.2	FastGC PTR-ToF-MS	109
6.3.3	Chemicals	111
6.3.4	Data analysis	111
6.4	Results and Discussion	112
6.5	Conclusions	123
7	Studies pertaining to the monitoring of isoflurane and sevoflurane by proton transfer reaction mass spectrometry	125
7.1	Introduction	125
7.2	Methodology	125
7.2.1	PTR-MS vs SIFT-MS vs SIFDT-MS	125

7.2.2 Isoflurane and sevoflurane	127
7.2.2.1 Rate constants	127
7.3 Concerns at the moment	127
7.4 Results and discussion	127
7.4.1 PTR-MS	127
7.4.1.1 Isoflurane reaction with H ₃ O ⁺	127
7.4.1.2 Isoflurane reaction with O ₂ ⁺	127
7.4.1.3 Sevoflurane reaction with H ₃ O ⁺	127
7.5 Conclusions and further remarks	127
References	143
Appendices	144
Appendix A Articles in peer-reviewed journals	145

List of Figures

1.1	Schematic diagram of an IMS instrument. Copyright ©Ellis <i>et al.</i> , 2013.	7
1.2	Schematic diagram of a SIFT-MS instrument. Copyright ©Ellis <i>et al.</i> , 2013.	8
2.1	(a) Picture of our PTR-ToF-MS with the TDU attached. (b) Illustration of the same instrument (not to scale) including the naming convention.	13
2.2	Diagram of the hollow cathode of the PTR-MS apparatus manufactured by KORE Technology Ltd.	14
2.3	Picture of the drift tube.	16
2.4	Schematic diagram of the KORE Technology Ltd RFIF Series 1 PTR-ToF-MS drift tube, together with the glow discharge and the source drift.	17
2.5	(a) Half section view of the reactor. (b) Potential energy surface of the cross section of the reactor in DC mode calculated in SIMION® for a random drift voltage.	17
2.6	Plot of the kinetic energy of the collision in the centre-of-mass frame of reference, KE_{CM} , as a function of the E/N for collisions of H_3O^+ with cocaine ($C_{17}H_{21}NO_4$, 303 g/mol) or 2-butanone (C_4H_8O , 71 g/mol) at 300 K with N_2 as buffer gas. The values for K_0 and N_0 are $2.8 \text{ cm}^2\text{V}^{-1}\text{s}^{-1}$ and $2.69 \times 10^{19} \text{ cm}^{-3}$, respectively.	21
2.7	Potential energy view of the cross section of the reactor in RF mode modelled in SIMION® with a random DC field.	22
2.8	Simulation of ion trajectories in (a) DC mode and (b) RF mode in the second half of the drift tube for ions of m/z 19 at a drift voltage of 200 V (ca. 120 Td in DC mode).	23
2.9	Simulation of the ion trajectories in the transfer lens region using SIMION®.	25
2.10	Diagram of a linear time-of-flight mass spectrometer.	26

2.11 Schematic diagram of a flight tube with a reflectron showing the different trajectories of seven ions of the same m/z with different initial velocities simulated in SIMION®	26
2.12 Schematic diagram of a MCP detector.	27
2.13 Screenshot of the GRAMS/AI™ user interface for the PTR-ToF-MS instrument manufactured by KORE Technology Ltd showing (a) an example of mass spectrum, and (b) an example of transient experiment data.	30
2.14 Screenshot of the graphical user interface for the script that analyses fast-switching data	33
2.15 Example plots of data analysed with the fast-switching software	34
2.16 (a) Picture of the TDU near to (top) used and (bottom) new PTFE swabs. (b) Schematic diagram of the TDU [16].	37
2.17 Time profiles of the count rates of two characteristic product ions at m/z 310 and m/z 370 during the thermal desorption of trace amounts of heroin at 120 Td using the TDU in PTR-MS.	38
 3.1 Reagent ion intensities in counts per second as a function of the drift voltage and the reduced electric field in (a) normal and (b) humid conditions.	45
3.2 Product ion signal intensities in counts per second of the product ions resulting from reactions of the $\text{H}_3\text{O}^+ \cdot (\text{H}_2\text{O})_n$ ($n = 0, 1, 2$) with cocaine as a function of the drift voltage and the reduced electric field in (a) normal and (b) humid conditions	50
3.3 Structure of the fragment ion at m/z 182 from the reaction of cocaine with $(\text{H}_2\text{O})_n\text{H}_3\text{O}^+$	51
3.4 Possible structures of the fragment ion at m/z 82 from the reaction of cocaine with $(\text{H}_2\text{O})_n\text{H}_3\text{O}^+$	51
3.5 Product ion signal intensities in counts per second of the product ions resulting from reactions of the $\text{H}_3\text{O}^+ \cdot (\text{H}_2\text{O})_n$ ($n = 0, 1, 2$) with methyl ecgonine as a function of the drift voltage and the reduced electric field in (a) normal and (b) humid conditions.	52
3.6 Rearrangement of the product ion at m/z 182 from protonated methyl ecgonine.	53

3.7 Product ion signal intensities in counts per second of the product ions resulting from reactions of the $\text{H}_3\text{O}^+(\text{H}_2\text{O})_n$ ($n = 0, 1$) with methyl benzoate as a function of the drift voltage and the reduced electric field in (a) normal and (b) humid conditions.	55
3.8 Product ion signal intensities in counts per second of the product ions resulting from reactions of the $\text{H}_3\text{O}^+(\text{H}_2\text{O})_n$ ($n = 0, 1$) with ethyl benzoate as a function of the drift voltage and the reduced electric field in (a) normal and (b) humid conditions.	58
3.9 Structure of the two transition states for the loss of ethene (or ethanol??) from protonated ethyl benzoate.	59
3.10 ΔG for the various reactions of H_3O^+ with EtBz. Note that the neutral water has been omitted from the captions.	59
3.11 Product ion signal intensities in counts per second of the product ions resulting from reactions of the $\text{H}_3\text{O}^+(\text{H}_2\text{O})_n$ ($n = 0, 1$) with isopropyl benzoate as a function of the drift voltage and the reduced electric field in (a) normal and (b) humid conditions.	61
3.12 Structure of the two transition states for the loss of ethene (or ethanol??) from protonated isopropyl benzoate.	62
3.13 ΔG for the various reactions of H_3O^+ with iPrBz. Note that the neutral water has been omitted from the captions.	62
3.14 Product ion signal intensities in counts per second of the product ions resulting from reactions of the $\text{H}_3\text{O}^+(\text{H}_2\text{O})_n$ ($n = 0, 1$) with benzoic acid as a function of the drift voltage and the reduced electric field in (a) normal and (b) humid conditions.	64
3.15 Structure of	65
3.16 Product ion signal intensities in counts per second of the product ions resulting from reactions of the $\text{H}_3\text{O}^+(\text{H}_2\text{O})_n$ ($n = 0, 1$) with methyl isobutyrate as a function of the drift voltage and the reduced electric field.	65
3.17 Product ion signal intensities in counts per second of the product ions resulting from reactions of the $\text{H}_3\text{O}^+(\text{H}_2\text{O})_n$ ($n = 0, 1$) with ethyl isobutyrate as a function of the drift voltage and the reduced electric field.	66

3.18 Product ion signal intensities in counts per second of the product ions resulting from reactions of the $\text{H}_3\text{O}^+ \cdot (\text{H}_2\text{O})_n$ ($n = 0, 1, 2$) with cocaethylene as a function of the drift voltage and the reduced electric field in (a) normal and (b) humid conditions.	67
3.19 Product ion signal intensities in counts per second of the product ions resulting from reactions of the $\text{H}_3\text{O}^+ \cdot (\text{H}_2\text{O})_n$ ($n = 0, 1, 2$) with ethyl ecgonine as a function of the drift voltage and the reduced electric field.	68
3.20 Product ion signal intensities in counts per second of the product ions resulting from reactions of the $\text{H}_3\text{O}^+ \cdot (\text{H}_2\text{O})_n$ ($n = 0, 1, 2$) with norcocaine as a function of the drift voltage and the reduced electric field.	69
3.21 Product ion signal intensities in counts per second of the product ions resulting from reactions of the $\text{H}_3\text{O}^+ \cdot (\text{H}_2\text{O})_n$ ($n = 0, 1, 2$) with anhydromethylecgonine as a function of the drift voltage and the reduced electric field.	70
3.22 Product ion signal intensities in counts per second of the product ions resulting from reactions of the $\text{H}_3\text{O}^+ \cdot (\text{H}_2\text{O})_n$ ($n = 0, 1, 2$) with o-hydroxycocaine as a function of the drift voltage and the reduced electric field in (a) normal and (b) humid conditions.	71
 4.1 Ion intensities in counts per second (cps) of the water reagent ions present in the drift tube as a function of drift tube voltage (a) in DC-only mode and (b) in RF-mode (ion funnel on). For (b) the ion signals at m/z 30 (NO^+) and 32 (O_2^+) are presented because although low intensity they are still significant and are observed as a result of the improved ion transmission in RF-mode. In DC-mode the signal intensities of these ions are negligible and are therefore not presented.	78
4.2 Product ion intensities as a function of drift tube voltage in RF mode. The data have been taken using 100 ng of TNT. The ion signals have been normalized to $10^6 \text{ H}_3\text{O}^+$ reagent ions and drift times. (The lines used in all graphs are just a guide to the eye.)	81
4.3 Intensities in ncps of the product ion [TNT - H_2O] H^+ as a function of drift tube voltage and RF amplitude (volts) with the frequency kept at 760 kHz ($\pm 3\%$). slightly	82

4.4	Two possible configurations resulting from protonation of TNT in the 2 position.	82
4.5	Stable structures of the [TNT - H ₂ O]H ⁺ ion.	83
4.6	Percentage product ion distributions resulting from the reaction of H ₃ O ⁺ with 2,6-DNT in RF-mode including the secondary process resulting in the association of the protonated molecule with water as a function of supplied drift tube voltage.	85
4.7	Percentage product ion distributions resulting from the reaction of H ₃ O ⁺ with 2,6-DNT in DC-only mode including the secondary process resulting in the association of the protonated molecule with water as a function reduced electric field.	85
4.8	Percentage product ion distributions resulting from the reaction of H ₃ O ⁺ with 2-NT in (a) RF-mode and (b) DC-only mode as a function drift tube voltage. Included are the secondary ion-molecule processes resulting in the association of the protonated molecule with water.	87
5.1	Structure of (a) 2-nitroaniline, (b) 3-nitroaniline and (c) 4-nitroaniline.	91
5.2	Ion intensities in counts per second of the water reagent ions (H ₃ O ⁺ .(H ₂ O) _n , n = 0, 1, 2 and 3) recorded at the detector of the KORE SRI-ToF-MS as a function of reduced electric field (approximately 60-250 Td).	92
5.3	Ion intensities in counts per second of O ₂ ⁺ recorded at the detector of the KORE SRI-ToF-MS as a function of reduced electric field (approximately 60-250 Td).	94
5.4	Percentage product ion distribution (PID in %) resulting from the reaction of 2-nitroaniline with H ₃ O ⁺ .(H ₂ O) _n (n = 0 and 1) as a function of the reduced electric field from 60 to 250 Td.	97
5.5	Overlaid mass spectra for 2-nitroaniline at 70 and 230 Td. This figure illustrates the clear difference in ion signal intensities for <i>m/z</i> 121.04, 139.05 and 157.06 upon the reduced electric field applied to the DT of the instrument.	98
5.6	Percentage product ion distribution resulting from the reaction of 3-nitroaniline with H ₃ O ⁺ .(H ₂ O) _n (n = 0 and 1) as a function of the reduced electric field from 60 to 250 Td.	99
5.7	Percentage product ion distribution resulting from the reaction of 4-nitroaniline with H ₃ O ⁺ .(H ₂ O) _n (n = 0, 1, 2) as a function of the reduced electric field from 60 to 250 Td.	100

5.8 Percentage product ion distribution resulting from the reaction of 2-nitroaniline with O ₂ ⁺ as a function of the reduced electric field from 60 to 250 Td.	101
5.9 Percentage product ion distribution resulting from the reaction of 3-nitroaniline with O ₂ ⁺ as a function of the reduced electric field from 60 to 250 Td.	102
5.10 Percentage product ion distribution resulting from the reaction of 4-nitroaniline with O ₂ ⁺ as a function of the reduced electric field from 60 to 250 Td.	102
6.1 Reagent ion intensities in counts per second (cps) as a function of the reduced electric field for (a) normal (dry buffer gas) and (b) humid (5% absolute humidity buffer gas) conditions.	110
6.2 Screenshot of the user interface of the PTR-MS Viewer software used for the data analysis in this study.	112
6.3 Product ion distributions (branching percentages) as a function of <i>E/N</i> resulting from reaction with H ₃ O ⁺ (and potentially H ₃ O ⁺ .H ₂ O as stated above) under (a) normal and (b) high humidity drift tube conditions with several ketones.	121

List of Tables

1.1	Main soft chemical ionisation reactions.	2
1.2	Organic compounds usually found in air sorted by their proton affinity [1].	3
1.3	Predominant reactions of an analyte M with NO^+ and O_2^+	6
2.1	Chemical reactions through which hydronium can be produced starting from products of EI of water vapour and their rate coefficients at 300K [27].	15
3.1	Molecular weight, vapour pressure at 25°C, formula and structure of cocaine, methyl ecgonine, cocaethylene, ethyl ecgonine, norcocaine, anhydromethylecgonine and o-hydroxycocaine.	46
3.2	Molecular weight, vapour pressure at 25°C, formula and structure of benzoic acid, methyl benzoate, ethyl benzoate, isopropyl benzoate, methyl isobutyrate and ethyl isobutyrate.	47
3.3	Proton affinity and Gibbs free energy of the main protonation sites of cocaine. . .	49
3.4	Energetics of the reaction of cocaine with $(\text{H}_2\text{O})_n\text{H}_3\text{O}^+$ ($n = 0, 1$) yielding the respective structure or transition state. ΔH_{298} and ΔG_{298} are relative to cocaine and H_3O^+ and, in brackets, to cocaine and $(\text{H}_2\text{O})\text{H}_3\text{O}^+$	49
3.5	Proton affinity and Gibbs free energy of the main protonation sites of methyl ecgonine.	51
3.6	Energetics relative to methyl ecgonine and H_3O^+ and, in brackets, to methyl ecgonine and $(\text{H}_2\text{O})\text{H}_3\text{O}^+$	53
3.7	Proton affinity and Gibbs free energy of the main protonation sites of methyl benzoate, ethyl benzoate and isopropyl benzoate.	53

3.8	Energetics relative to methyl benzoate and H ₃ O ⁺ and, in brackets, to methyl benzoate and (H ₂ O)H ₃ O ⁺	54
3.9	Energetics relative to ethyl benzoate and H ₃ O ⁺ and, in brackets, to ethyl benzoate and (H ₂ O)H ₃ O ⁺	57
3.10	Energetics relative to isopropyl benzoate and H ₃ O ⁺ and, in brackets, to isopropyl benzoate and (H ₂ O)H ₃ O ⁺	62
3.11	Energetics relative to benzoic acid and H ₃ O ⁺ and, in brackets, to benzoic acid and (H ₂ O)H ₃ O ⁺	63
3.12	Energetics relative to ethyl isobutyrate and H ₃ O ⁺ and, in brackets, to ethyl isobutyrate and (H ₂ O)H ₃ O ⁺	68
4.1	Energetics for the proton transfer from H ₃ O ⁺ to TNT calculated using the B3LYP functional and the 6-31+G(d,p) basis set	81
4.2	Energetics for the elimination of water from TNT following proton transfer from H ₃ O ⁺ for the three stable structures shown in Figure 4.5	83
4.3	Energetics for the elimination of water from (a) 2,4-DNT and (b) 2,6-DNT following proton transfer from H ₃ O ⁺	86
4.4	Energetics for the elimination of water from 2-NT following proton transfer from H ₃ O ⁺	88
5.1	Proton affinities, gas phase basicities and ionisation energies for nitroaniline isomers. The PA and GB values have been calculated using the B3LYP functional and the 6-31+G(d,p) basis set at 298 K. ΔH ₂₉₈ and ΔG ₂₉₈ refer to the enthalpies and free energies for the addition of water to the protonated species. For convenience the ionisation energies of O ₂ and the three nitroanilines are also provided.	96
6.1	Product ions identified and their associated product ion branching ratios (percentages) measured at reduced electric fields of 100, 140, and 180 Td resulting from the reactions of H ₃ O ⁺ with several ketones	113

List of Abbreviations

amu	Atomic Mass Unit ($= 1.66 \times 10^{-27}$ kg).
BR	Branching Ratio.
cps	Counts per second.
DFT	Density Functional Theory.
DSTL	Defence Science and Technology Laboratory.
DT	Drift Tube.
E	Electric field strength.
E/N	Reduced electric field.
EI	Electron Impact.
FWHM	Full Width at Half Maximum.
G	Gibbs free energy.
GB	Gas-phase Basicity.
GC	Gas Chromatography.
GD	Glow Discharge.
H	Enthalpy.
IE	Ionisation Energy.

IMS	Ion Mobility Spectrometry.
k	Reaction rate.
K	Ion's mobility.
K₀	Ion's reduced mobility.
k_B	Boltzmann constant ($= 1.38 \times 10^{-23} \text{ J K}^{-1}$).
KE_{CM}	Kinetic energy in the centre-of-mass frame of reference.
LCU	Liquid Calibration Unit.
LoD	Limit of Detection.
m/z	Mass-to-charge ratio.
MFP	Mean Free Path.
MS	Mass Spectrometer.
N	Gas number density.
N₀	Gas number density at standard pressure and temperature.
N_A	Avogadro's number ($= 6.022 \times 10^{23} \text{ mol}^{-1}$).
ncps	Normalised counts per second.
P₀	Standard pressure ($= 1 \text{ atm} = 1013.25 \text{ mbar}$).
PA	Proton Affinity.
PAH	Polyaromatic hydrocarbon.
PEEK	Polyether ether ketone.
PID	Product Ion Distribution.
ppbv	Parts per billion by volume.

ppmv	Parts per million by volume.
ppqv	Parts per quadrillion by volume.
pptv	Parts per trillion by volume.
PTFE	Polytetrafluoroethylene.
PTR	Proton Transfer Reaction.
PTR-MS	Proton Transfer Reaction Mass Spectrometry.
RFIF	Radio Frequency Ion Funnel.
ROI	Reagion Of Interest.
SCI-MS	Soft Chemical Ionisation Mass Spectrometry.
SD	Source Drift region.
SIFT-MS	Selected Ion Flow-Drift Tube Mass Spectrometry.
SIFT-MS	Selected Ion Flow Tube Mass Spectrometry.
SRI-MS	Selective Reagent Ion Mass Spectrometry.
SVOC	Semi-Volatile Organic Compound.
T₀	Standard temperature (= 0°C = 273.15 K).
t_d	Drift time.
Td	Townsend (= 10 ⁻¹⁷ V cm ²).
TDC	Time-to-Digital Converter.
TDU	Thermal Desorption Unit.
ToF-MS	Time-of-Flight Mass Spectrometer.
TS	Transition state.
v_d	Drift velocity.

V_d Drift voltage.

VOC Volatile Organic Compound.

Chapter 1

Introduction

In this chapter the thesis outline and aim are presented after a brief introduction of soft chemical ionisation mass spectrometry.

1.1 Soft Chemical Ionisation Mass Spectrometry

Soft chemical ionisation mass spectrometry (SCI-MS) comprehends a series of analytical techniques which can be used to detect trace gases by means of the soft ionisation of volatile organic compounds (VOCs). As opposed to other types of ionisation like electron impact (EI) ionisation, where the excessive fragmentation produced by the 70 eV electrons usually generates congested spectra, soft ionisation techniques yield little or no fragmentation, resulting in the readily identification of compounds, which is vital when dealing with complex mixtures like ambient air.

The main reactions occurring in soft chemical ionisation techniques are listed in Table 1.1, where X^+ or XH^+ represents the reagent gas, M or MH is the targeted analyte and in the last reaction Z is a third body required to stabilise the MX^+ adduct through collisions. Proton transfer reactions from protonated water (hydronium, H_3O^+) and its water clusters are the main object of study in the present thesis, although also charge transfer reactions occurring between O_2^+ and nitroanilines are presented in chapter 6.

1.1.1 Thermodynamics of proton transfer

The protonation reaction of an analyte M from hydronium is shown in Equation 1.1. This reaction occurs at near the collisional rate if the proton affinity (PA) of the analyte is higher

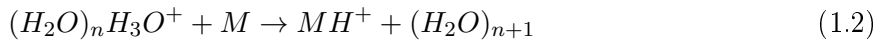
Table 1.1: Main soft chemical ionisation reactions.

Charge transfer	$X^+ + M \rightarrow M^+ + X$
Proton transfer	$XH^+ + M \rightarrow MH^+ + X$
Hydride (H^-) transfer	$X^+ + MH \rightarrow M^+ + XH$
Adduct formation	$X^+ + M + Z \rightarrow MX^+ + Z$

than that of water following.



Furthermore, protonation is also possible from the water clusters, if the proton affinity of the analyte is higher than that of the n^{th} water cluster, following Equation 1.2:



where $(H_2O)_n H_3O^+$ denotes the n^{th} water cluster ion.

The proton affinity of some compounds of interest are shown in Table 1.2. One of the main advantages of PTR-MS is that ambient air can be directly sampled as its main constituents have smaller proton affinity than water, and hence they will not undergo proton transfer and the reagent ion signal will not get depleted. Moreover, the proton affinity of the water clusters is higher than that of the monomer, because of the added stability by sharing the proton with additional water molecules. This translates into a softer protonation process when an analyte reacts with these. Also, some analytes have a proton affinity close to that of the reagent ions. This is the case, for instance, of isoflurane (670 kJ/mol) and formaldehyde (712.9 kJ/mol). For these molecules, once they have been protonated, the back reaction, or deprotonation reaction, (Equation 1.3, for $n = 0, 1, \dots$) can also occur.



The tendency of a compound M to act as proton acceptor is called gas-phase basicity (GB) and it is equal to the negative Gibbs energy, G, change of the reaction in Equation 1.4: $GB(M) = -\Delta G^0$, where the superscript 0 denotes the standard conditions of pressure and temperature. Similarly, the proton affinity of a molecule is the negative of the enthalpy, H, change in

Table 1.2: Organic compounds usually found in air sorted by their proton affinity [1].

Compound	Formula	PA (kJ/mol)
Oxygen	O ₂	421
Hydrogen	H ₂	422.3
Nitrogen	N ₂	465
Nitrogen oxide	NO	531.8
Carbon dioxide	CO ₂	540.5
Nitrogen dioxide	NO ₂	591
Water	H₂O	684*
Formaldehyde	CH ₂ O	712.9
Benzene	C ₆ H ₆	750.4
Methanol	CH ₃ O	754.3
Acetic acid	C ₂ H ₄ O ₂	783.7
Acetone	C ₃ H ₆ O	812
Water dimer	(H₂O)₂	842*
Ammonia	NH ₃	853.6
Water trimer	(H₂O)₃	937*
Water tetramer	(H₂O)₄	1013*

*The proton affinity values for the water oligomers were calculated using the B3LYP functional and the 6-31+G(d,p) basis set by Dr Peter Watts.

Equation 1.4: PA(M) = -ΔH⁰.



The Gibbs free energy and the enthalpy fulfil Equation 1.5, and, likewise, the proton affinity and gas-phase basicity are related through Equation 1.6.

$$\Delta G^0 = \Delta H^0 - T\Delta S^0 \quad (1.5)$$

$$PA = GB - T\Delta S^0 \quad (1.6)$$

where T is the absolute temperature and ΔS^0 is the entropy difference between reactants and products in the protonation reaction at standard conditions of pressure and temperature. This term is usually negligible for proton transfer reactions, and hence $\Delta H^0 \sim \Delta G^0$ and $PA \sim GB$. It is therefore possible to use the proton affinity as a measure of the spontaneity of a protonation reaction.

For Equation 1.1, $\Delta H^0 = PA(H_2O) - PA(M)$ and $\Delta G^0 = GB(H_2O) - GB(M)$. Proton transfer following Equation 1.1 is thermodynamically allowed and will occur spontaneously when $\Delta G < 0$

(exergonic reaction) and, following the assumption made above, $\Delta H < 0$ (exothermic reaction). Thus, protonation of the analyte M will occur when $GB(M) > GB(H_2O)$ and $PA(M) > PA(H_2O)$.

1.1.2 Kinetics of proton transfer

The fact that a proton transfer reaction is allowed does not say at what speed it will occur. However, Schiff *et al.* experiments in the 70s found that these reactions are occurring at or close to the collisional rate, which means that a protonation will occur in every collision [2]. The rate constant, k, at which the reaction in Equation 1.1 occurs is related to the concentration of the reactants and products as shown in Equation 1.7. This rate equation shows that the decrease of H_3O^+ with time is equal to the increase of MH^+ and that the reaction is governed by the concentration of the reactants and the rate constant.

$$-\frac{d[H_3O^+]}{dt} = \frac{d[MH^+]}{dt} = k[H_3O^+][M] \quad (1.7)$$

where square brackets denotes concentration, usually given in cm^{-3} .

Assuming that the concentration of the analyte, $[M]$, is much smaller than that of the hydronium (which is the case when studying trace concentrations) and that only a proportion of the analyte is protonated, Equation 1.7 can be integrated to get Equation 1.8.

$$[MH^+] = [H_3O^+] \left(1 - e^{-k[M]t} \right) \quad (1.8)$$

where t is the reaction time (i.e. the time it takes the analyte molecules to cross the drift tube). Following the same trace concentration approximation, Equation 1.8 can be approximated to Equation 1.9, which allows to quantify the concentration of the analyte if the rate constant, the reaction time and the concentration of the protonated analyte and reagent ions are known accurately, assuming that the protonated analyte molecule is the only product ion.

$$\frac{[MH^+]}{[H_3O^+]} = -k[M]t \quad (1.9)$$

1.1.3 Other reagent ions

Besides hydronium, other ions can be used as reagent in SCI-MS. These are generated by introducing different gases into the ion source, whose working principle is explained in the following chapter. The most common reagent ions used in SCI-MS besides H_3O^+ are NO^+ and O_2^+ . However, these are also unwanted impurities that are found when the gas containing the analyte is back-streamed from the drift tube into the ion source, but if the ratio of intensities of NO^+ and O_2^+ with H_3O^+ is less than 3% their influence in the measurements can be ignored as they won't contribute much to the total product ion signal. This can be easily achieved by running the experiments using N_2 as buffer gas instead of lab air.

Strictly speaking, with NO^+ and O_2^+ we must refer to the ionisation process as charge exchange or charge transfer rather than proton transfer. NO^+ has a first ionisation energy of 9.26 eV, which is 12.1 eV for O_2^+ . This means that they can undergo charge transfer reactions with molecules with ionisation energies below 9.26 eV and 12.1 eV, respectively, and NO^+ can also undergo association if charge transfer is not energetically allowed (see Table 1.3). Note that collisions with a third body Z are required to remove some energy from the adduct formation to be stable. Adduct formation does not occur frequently in the case of O_2^+ as organic molecules' ionisation energies are generally in the range of 8 to 11 eV, which results in a considerable amount of energy (e.g. up to 3 eV) deposited into the molecule, which usually originates excessive fragmentation. In fact, for some molecules the mass spectrum resulting from charge transfer with O_2^+ as reagent ion is quite similar to the EI spectrum, for which energies of 70 eV are commonly used.

Furthermore, in some of my experiments I had a small pressure difference between the hollow cathode and the drift tube to achieve the driest conditions possible. A consequence of this is that some N_2 is introduced into the cathode and ammonium cations can be generated. The proton affinity of ammonia is 853.6 kJ/mol [1], so proton transfer from ammonium is softer than that from hydronium, being actually energetically comparable to that from $(\text{H}_2\text{O})\text{H}_3\text{O}^+$. However, the main problem in this case would be if the proton affinity of the analyte lies between that of water and ammonia, as collision of the protonated analyte with ammonia would result in protonated ammonia molecules.

Table 1.3: Predominant reactions of an analyte M with NO^+ and O_2^+ .

Charge transfer from NO^+	$\text{NO}^+ + \text{M} \rightarrow \text{M}^+ + \text{NO}$
Charge transfer from O_2^+	$\text{O}_2^+ + \text{M} \rightarrow \text{M}^+ + \text{O}_2$
Adduct formation with NO^+	$\text{NO}^+ + \text{M} + \text{Z} \rightarrow \text{M}.\text{NO}^+ + \text{Z}$

1.1.4 SCI-MS techniques

A brief description of three of the most widely used SCI-MS techniques is shown below.

1.1.4.1 Ion Mobility Spectrometry

In ion mobility spectrometry (IMS) ions are separated according to their mobilities through a gas. The typical experimental setup is shown in Figure 1.1. An IMS device consists of three main parts: a cathode, where the reagent ions are generated; a drift tube, where an electric field drags the ions downstream as they are being separated; and a Faraday plate that collects the ions.

Although radioactive ion sources are the most common ones [3], other systems like corona discharge are becoming more popular [4]. The reagent ions used in IMS are usually hydronium and its water clusters, which enter the drift tube when the gate that separates the ion source and the drift tube is pulsed. This is typically done at tens of Hz. The most common design of drift tube consists of a series of stacked metallic rings, each one at a different electric potential in order to create a uniform electric field, E , along the revolution axis. This dragging electric field, together with the collisions with the background gas, make the ions reach the so-called drift velocity, v_d , as they move along the reactor until they are collected by the Faraday plate. This yields an ion current as a function of the drift time.

The results are plotted in a histogram-like spectrum that shows the ion signal, typically in counts per second (cps), versus drift time. It is also common to plot the data as ion signal versus the reduced ion mobility, K_0 , which can be calculated from the Equation 1.11 once the ion mobility, K , has been calculated using Equation 1.10. Note that P_0 and T_0 denote the standard pressure and temperature, P and T refer to the pressure and temperature in the drift tube, L is the length of the drift tube, t_d is the drift time and V_d is the drift voltage. Peaks in this spectrum can be assigned to targeted compounds if their mobilities are known. As a general

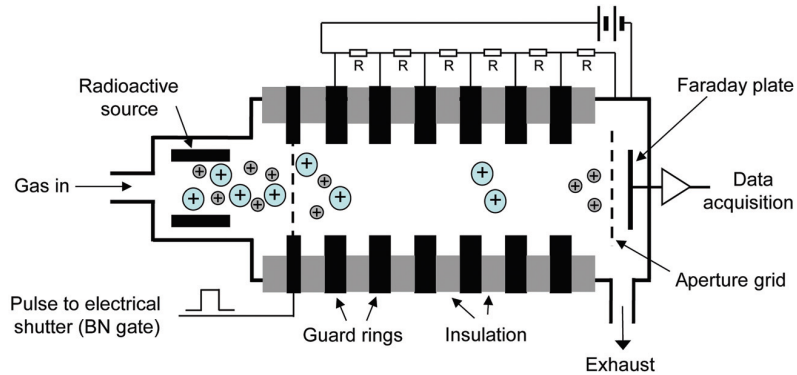


Figure 1.1: Schematic diagram of an IMS instrument. Copyright ©Ellis *et al.*, 2013.

rule, the lighter the ion, the higher its mobility is, although other characteristics, like the ion's structure, can affect the mobility as it influences how the ion interacts with the buffer gas.

$$K = \frac{L^2}{t_d V_d} \quad (1.10)$$

$$K_0 = K \frac{P}{P_0} \frac{T_0}{T} \quad (1.11)$$

Some of the advantages of IMS are that it is quite cheap, small and does not need big pumps as it works at a pressure similar to the atmospheric one. Due to this, this technique is nowadays widely used in security and military applications [5]. For instance, it can be often found in the security checks in airports. Moreover, its sensitivity allows it to detect trace concentrations as low as parts per billion by volume (ppbv), allowing this technique to be used for real time measurements without pre-concentration. On the other hand, IMS lacks good selectivity, being many compounds difficult to be completely separated and identified.

1.1.4.2 Selected Ion Flow Tube Mass Spectrometry

Unlike IMS, selected ion flow tube mass spectrometry (SIFT-MS) does not use a drift tube, but a flow tube, to drag the ions downstream. As shown in Figure 1.2, a SIFT-MS instrument consists of an ion source, a quadrupole mass filter, a flow tube and a mass analyser.

The reagent ions (e.g. H_3O^+ , NO^+ and O_2^+) are created in the ion source, which is typically a microwave resonator [7]. Then, the quadrupole mass filter selects the reagent ion by its mass. This piece of equipment also allows fast switching (tens of milliseconds) between the reagent

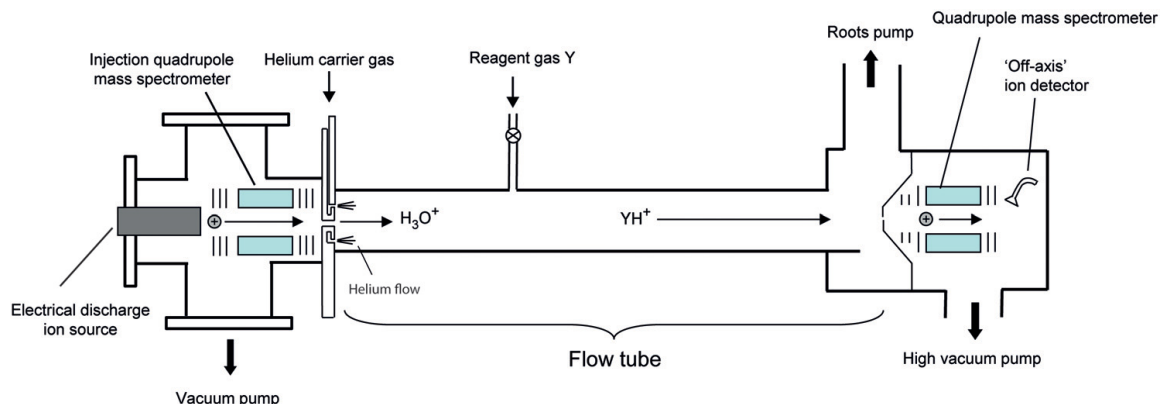


Figure 1.2: Schematic diagram of a SIFT-MS instrument. Copyright ©Ellis *et al.*, 2013.

ions, which can be used to extract more information of the analyte during transient experiments. From the quadrupole mass filter, the ions enter the flow tube. Here helium is used as a carrier gas and it is also in the flow tube where the analyte gas is injected. Finally, the ions are detected in a mass analyser, typically a quadrupole mass spectrometer, and the detection system builds the mass spectra obtained from the reaction of the reagent ions with the analyte.

The presence of helium in the flow tube makes it possible to explore ion-molecule reactions at thermal energies. One of the main applications of SIFT-MS is the ability to measure reaction coefficients. This has allowed SIFT-MS to become a valuable tool in areas like atmospheric and interstellar chemistry, and it has also been used as an analytical tool in other fields, being breath analysis the most remarkable one [8].

1.1.4.3 Proton Transfer Reaction Mass Spectrometry

Proton transfer reaction mass spectrometry (PTR-MS) is the main instrument used in the experimental work presented in this thesis. It has both similarities and differences with both IMS and SIFT-MS techniques. This method was developed by Werner Lindinger at the University of Innsbruck (Austria) in the 1990 as the successor of the flowing afterglow and the selected ion flow drift tube techniques [9]. The main components of a PTR-MS instrument are the ion source, the drift tube and the mass spectrometer. Hydronium (and its water clusters) is generated in the ion source, typically a hollow cathode, from the water injected from the water reservoir. The reagent ions are then introduced into the drift tube (DT). It is at this stage where they meet the analyte and proton transfer (and possible fragmentation) takes place, before the ions are transferred then into the mass analyser, typically a time-of-flight or quadrupole mass spectrometer,

for their detection. Further details of the working procedure of a PTR-MS instrument are given in the following chapter.

PTR-MS has many advantages, most of them also shared with other SCI-MS techniques. To begin with, it can detect a significant number of VOCs such as aldehydes, ketones, aromatic compounds, alcohols, nitriles and esters. Because of its high sensitivity, PTR-MS can reach limits of detection of parts per quadrillion by volume (ppqv) [10]. Furthermore, reactions occurring close to the collisional rate and the possibility of directly sampling air allows for online, real-time operating conditions. Besides this, the only resources needed to run a PTR-MS instrument are distilled water and electric power. Additionally, little or no fragmentation of the parent ions is observed, as compared to other ionisation mechanisms like EI. This can however be manipulated to some extent by changing the conditions in the reactor. Also, selectivity can be enhanced by applying the recent instrumental developments which include, for instance, the development and implementation of an RF ion funnel [11, 12] and the use of a fast switching reduced electric field [13].

On the other hand, PTR-MS also shows some disadvantages, being one of the most important ones the inability to directly distinguish between isomeric compounds, although this can be mitigated by using tandem MS^n or fastGC techniques. Also, water cluster formation and detection can interfere with the detection of other molecules. For example, the ^{18}O isotope of the first water cluster, $(\text{H}_2\text{O})\text{H}_3\text{O}^+$, and the ion $(\text{C}_3\text{H}_3)\text{H}^+$ will be both found at m/z 39. However, this issue can be solved with a high-resolution mass spectrometer and proper data analysis (e.g. using multi-peak fitting techniques or taking into account the isotopic distribution of the ions). Likewise, for compounds like benzene and toluene, which react with H_3O^+ but not with $(\text{H}_2\text{O})\text{H}_3\text{O}^+$, the sensitivity depends on the humidity of the air, because higher humidity means higher concentration of $(\text{H}_2\text{O})\text{H}_3\text{O}^+$ and lower of H_3O^+ . Finally, not all VOCs can be detected in PTR-MS. There exist some VOCs that don't react with H_3O^+ , like some alkanes, which have proton affinities below that of H_2O .

The ability of PTR-MS to detect and monitor trace concentrations of VOCs is advantageous in many fields. The main areas of application and some examples to illustrate them are: atmospheric chemistry, where it has been used to study the emission of biogenic VOCs and their effect in the environment [14], and to monitor pollution and urban plumes [15]; homeland security, where it has been applied to the detection of explosives [13, 16, 17], rape drugs [18], and narcotics [19]; in

medical sciences, for the detection and monitoring of diseases through breath analysis [20–22]; and in food sciences, to study food aroma, flavour and quality control [23–25].

1.2 Thesis outline

In the first chapter I present an introduction to soft chemical ionisation mass spectrometry together the outline and the aim of the present thesis.

In the second chapter, the PTR-MS technique and relevant experimental aspects are explained in detail.

The first chapter including experimental work is the third one, where cocaine and related compounds of interest are investigated, including results from both PTR-MS and density functional theory calculations.

The fourth chapter carries on with the same topic, with PTR-MS results from the measurements of other illicit drugs of common societal abuse.

The fifth chapter is an adapted version of my paper regarding the enhancement of selectivity in the detection of explosives through the implementation of an RF ion funnel in the reactor of a PTR-ToF-MS.

The sixth chapter is a reformatted version of my paper about the use selective reagent ion mass spectrometry for the study of nitroanilines isomers.

The seventh chapter is an adapted version of my paper regarding the investigations of phthalates in PTR-MS using direct headspace sampling.

The eighth chapter is a rewritten version of my paper of relevance to breath analysis about the study of ketones using a fastGC-PTR-ToF-MS instrument in dry and humid conditions.

In the ninth chapter the final conclusions and closing remarks are stated.

1.3 Aim of the thesis

My research project was focused on the study of ion-molecule interactions in the reaction region of proton transfer reaction mass spectrometry, mainly in the area of homeland security, but other applications have also been investigated, including a study of ketones of relevance to breath analysis.

Compounds of specific interest for my research are illicit drugs, explosives and phthalates. The available studies, if any, had been done at only one reduced electric field (typically between 120 – 140 Td). The experimental work in this thesis is supplemented by quantum chemical calculations, which are used to help interpret the results. These were conducted using Gaussian09W and GaussView05 for Windows by Dr Peter Watts. All calculations used the B3LYP hybrid functional and the 6-31+G(d,p) basis set.

The main outcome of my research has strengthened knowledge of ion-molecule interactions in soft chemical ionisation mass spectrometry techniques, in collaboration with other groups within the Marie Skłodowska-Curie Actions Innovative Training Network IMPACT.

Chapter 2

Proton Transfer Reaction Mass Spectrometry

In this chapter, proton transfer reaction mass spectrometry, its underlying chemistry and relevant experimental aspects are explained.

2.1 The PTR-ToF-MS

As stated in the introduction, PTR-MS is a sensitive technique for real-time monitoring of VOCs in air with a minimal sample preparation. PTR-MS uses hydronium as reagent ion to donate protons to the VOCs present in the analyte gas and detect trace concentrations of targeted compounds. The newest PTR-MS instrument in our laboratory is shown in Figure 2.1. It is a KORE Technology Ltd. RFIF Mk I PTR-ToF-MS. Briefly, the main parts of a PTR instrument and their functions can be simplified to:

1. Ion source: production of reagent ions.
2. Drift tube: protonation and possible fragmentation of the analyte.
3. Mass spectrometer: detection and identification of product ions.

These are explained in detail in the following sections.

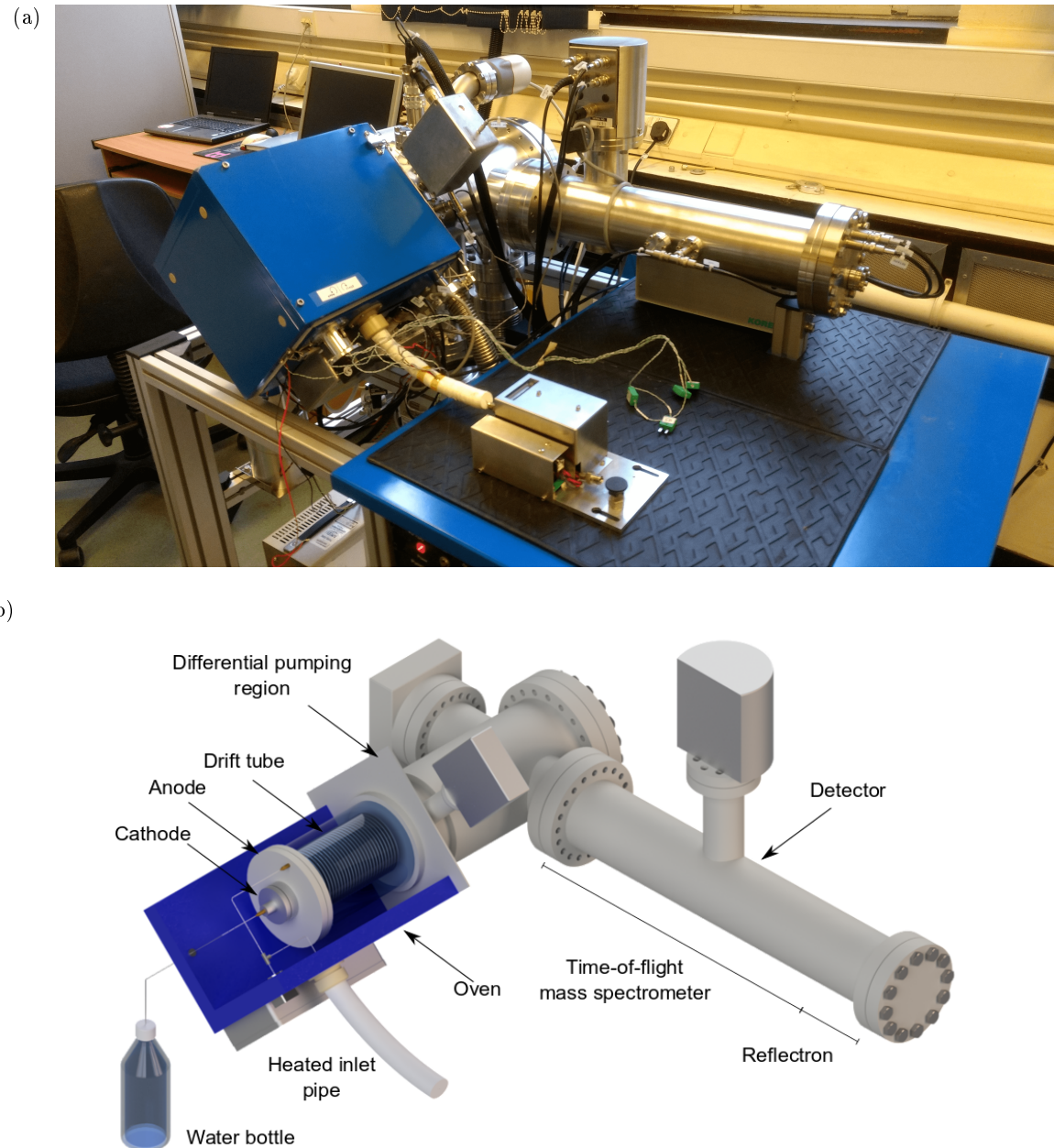


Figure 2.1: (a) Picture of our PTR-ToF-MS with the TDU attached. (b) Illustration of the same instrument (not to scale) including the naming convention.

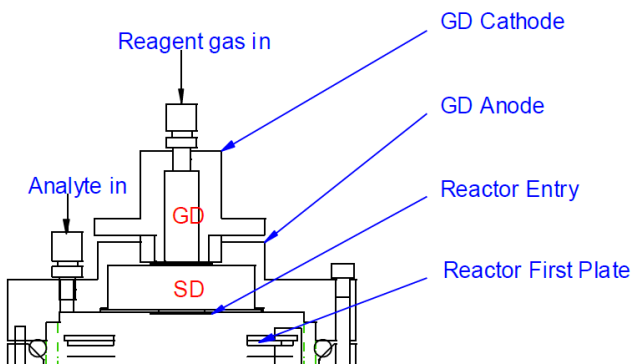


Figure 2.2: Diagram of the hollow cathode of the PTR-MS apparatus manufactured by KORE Technology Ltd.

2.1.1 Ion source

The reagent ions that will ionise the sample are generated in the glow discharge (GD) in the ion source. Most PTR-MS instruments carry a hollow cathode discharge ion source, to which a voltage is supplied to ionise the gas that flows through it and create the plasma in which the reagent ions are being produced. There are different configurations in the market, like the recently developed one from Ionicon Analytik GmbH, which allows to quickly switch from different reagent ions by simultaneously using multiple off-axis cathodes [26]. The one in our PTR-MS instrument is shown in Figure 2.2. Note that from now on I will indistinctly refer to plasma, discharge and glow discharge.

2.1.1.1 The glow discharge: production of reagent ions

Glow discharge is a type of electrical discharge that occurs at low pressures (mbar range) and is characterised by a maintained current, ranging from 1uA to 1A, between the cathode and the anode. It receives this name because the ionised gas produces a shining glow whose characteristics depends on the nature of the gas, its pressure and the voltage applied.

During the standard use of the instrument, water vapour is supplied from the water reservoir through a needle valve to the cathode, where H_3O^+ ions are generated. The main reaction occurring in the ion source leading to the production of H_3O^+ from the electrical discharge of water vapour is the first one shown in Table 2.1. It starts when H_2O^+ has been produced through the electron impact ionisation of water. However, other water fragment ions can also undergo reactions that generate hydronium, following the other reactions shown in Table 2.1. The rate

Table 2.1: Chemical reactions through which hydronium can be produced starting from products of EI of water vapour and their rate coefficients at 300K [27].

H_2O^+ + H_2O	\rightarrow	$\text{H}_3\text{O}^+ + \text{OH}$	$k = 1.8 \times 10^{-9} \text{ cm}^3\text{s}^{-1}$
$\text{OH}^+ + \text{H}_2\text{O}$	\rightarrow	$\text{H}_3\text{O}^+ + \text{O}$	$k = 1.3 \times 10^{-9} \text{ cm}^3\text{s}^{-1}$
	\rightarrow	$\text{H}_3\text{O}^+ + \text{OH}$	$k = 1.8 \times 10^{-9} \text{ cm}^3\text{s}^{-1}$
$\text{O}^+ + \text{H}_2\text{O}$	\rightarrow	$\text{H}_2\text{O}^+ + \text{O}$	$k = 2.6 \times 10^{-9} \text{ cm}^3\text{s}^{-1}$
$\text{H}_2^+ + \text{H}_2\text{O}$	\rightarrow	$\text{H}_3\text{O}^+ + \text{H}$	$k = 3.4 \times 10^{-9} \text{ cm}^3\text{s}^{-1}$
	\rightarrow	$\text{H}_2\text{O}^+ + \text{H}_2$	$k = 3.7 \times 10^{-9} \text{ cm}^3\text{s}^{-1}$
$\text{H}^+ + \text{H}_2\text{O}$	\rightarrow	$\text{H}_2\text{O}^+ + \text{H}$	$k = 8.2 \times 10^{-9} \text{ cm}^3\text{s}^{-1}$

at which these reactions happen is very close to the collisional rate. Furthermore, hydronium ions can cluster to water molecules via hydrogen bonds to form the so-called water clusters, i.e. $(\text{H}_2\text{O})_n\text{H}_3\text{O}^+$ with $n = 1, 2, 3, \dots$. Ideally, we want pure hydronium being injected into the drift tube. Otherwise, if the water cluster ions come into play, there are proton transfer reactions simultaneously occurring in the drift tube with different energies, which makes it more difficult to understand the energetics associated with the different protonation and fragmentation pathways.

The breakdown voltage, which is the voltage difference needed between cathode and anode to start the plasma, is approximately 750 volts in our instrument, but after the plasma has started, the cathode voltage decreases, as the potential difference required to maintain the discharge is smaller than the breakdown voltage and it is usually between 350 and 400 volts. The anode voltage floats with the voltage of the first plate of the drift tube, which can be adjusted by the user to set the drift voltage, which will be discussed in the next section. After the glow discharge switch is turned on, it can take the plasma up to a couple of minutes to start. In our instrument, the typical ion source pressure values are between 1 and 1.4 mbar. The plasma struggling to get started or maintained indicates that the hollow cathode must be cleaned, as an aluminium oxide layer can form inside and needs to be removed after some months of use. Another factor that affects the stability of the glow is the temperature of the oven that contains the ion source and the drift tube. We have experienced that the higher the temperature of the oven is, the higher the cathode pressure must be for the glow to be maintained.

Downstream from the ion source, the ions reach the so-called source drift (SD) region (shown in Figure 2.2), whose goal is to break the clusters apart before they enter the drift tube. If

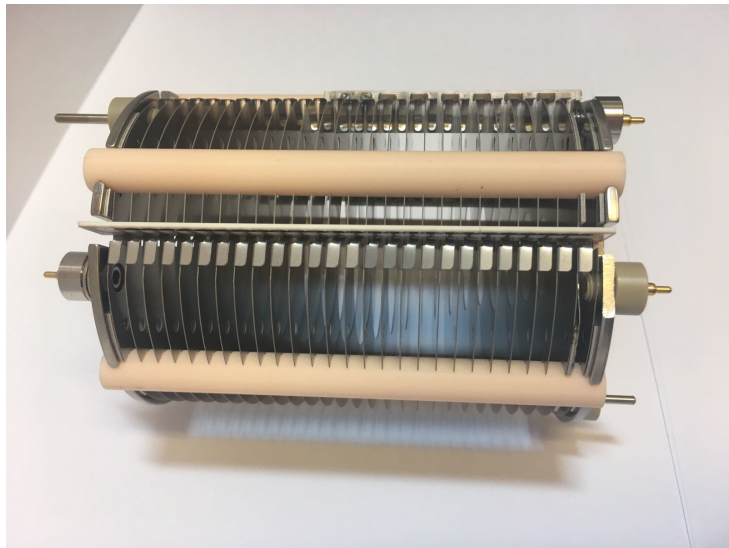


Figure 2.3: Picture of the drift tube. Note that in this model the diameter of the electrodes steadily decreases in the second half of the stack.

said clusters are not broken before entering the drift tube, they can also split up there through collisions with the buffer gas.

2.1.2 Drift tube

The drift tube is the region of a PTR-MS instrument where the protonation and possible fragmentation of the analyte occurs. It is also often referred to as the reactor. A picture of the DT is shown in Figure 2.3.

As mentioned before, our instrument is a KORE Technology Ltd RFIF Series 1 PTR-ToF-MS. Its drift tube, whose schematic layout is shown in Figure 2.4, consists of 29 stainless-steel ring electrodes of 0.2 mm of thickness with a spacing of 3.2 mm per plate inside a cylinder of resistive glass. The inner diameter of these electrodes is 40 mm in the first half of the stack and it gradually decreases in the second half to 6 mm. A $1 \text{ M}\Omega$ resistor chain connected to the electrodes allows to supply a linearly decreasing potential to each of them when a voltage is applied between the first and the last plates, generating an electric field in the reactor known as DC field. When the instrument is operating in these conditions (i.e. without the RF field explained later in subsubsection 2.1.2.2), we refer to it as working in DC mode or DC-only mode.

The DC electric field (see Figure 2.5) drags the ions across the reactor and towards the

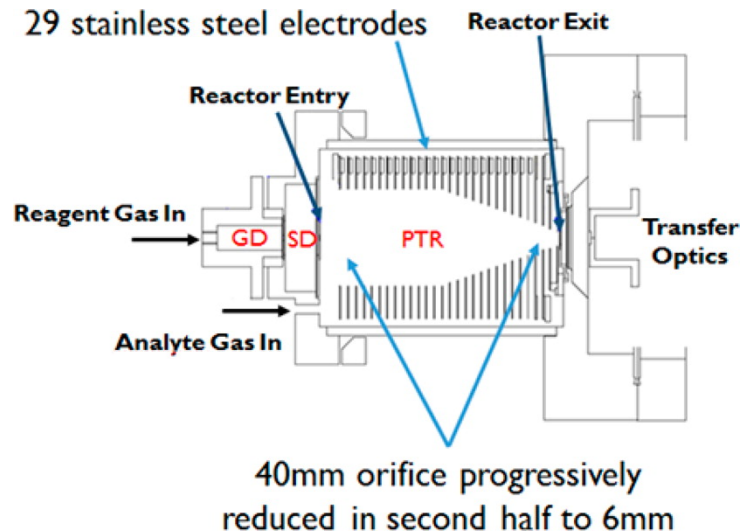


Figure 2.4: Schematic diagram of the KORE Technology Ltd RFIF Series 1 PTR-ToF-MS drift tube, together with the glow discharge and the source drift.

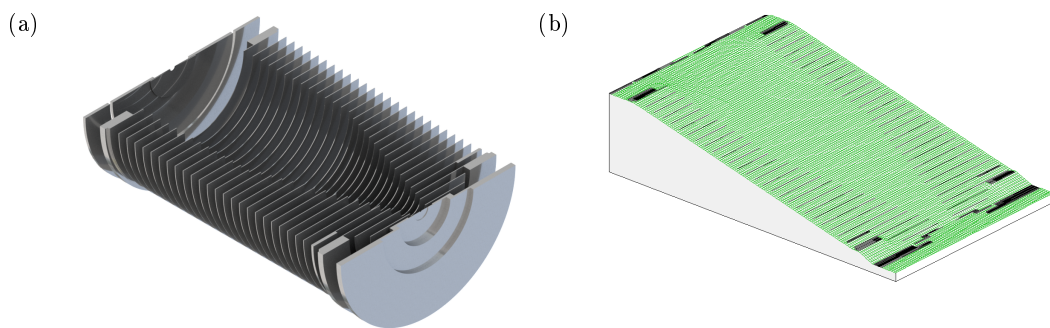


Figure 2.5: (a) Half section view of the reactor. (b) Potential energy surface of the cross section of the reactor in DC mode calculated in SIMION® for a random drift voltage.

transfer lenses, where they will get transmitted into the mass spectrometer. As they are drawn through the reactor, ions collide with the neutrals molecules of the background and analyte gases, which can result in protonation and fragmentation of the analyte. The collisional energy can be manipulated by tuning the DC field as well as the reactor's pressure and temperature, whose standard operating values are around 1 mbar and between 100 and 150°C, respectively, although our oven can reach up to 200°C.

2.1.2.1 Reduced electric field

As the collisional energy depends not only on the electric field, E , but also on the buffer gas in the reactor, it is convenient to use the reduced electric field, E/N , as a measure of the collisional

energy delivered to the ions. First, the electric field strength is defined by the potential difference between the first and the last plate in the reactor divided by its length (Equation 2.1):

$$E = \frac{V_d}{L} \quad (2.1)$$

where V_d is the so-called drift voltage and it is equal to the voltage difference between the first and the last plate of the reactor, known as PTR Entry and PTR Exit, that can be adjusted by the user, and L is the length of the drift tube, which is 9.36 cm in our newest instrument. For instance, a voltage difference between first and last plates of 250 V corresponds to an electric field of 26.71 V/cm.

Similarly, the gas number density, N , is defined as the number of gas particles per unit volume and can be calculated from the ideal gas equation to be (Equation 2.2):

$$N = \frac{N_A}{V_{mol}} \frac{P_d}{P_0} \frac{T_0}{T_d} \quad (2.2)$$

where N_A is the Avogadro's number ($6.022 \times 10^{23} \text{ mol}^{-1}$), V_{mol} ($22414 \text{ cm}^3 \text{ mol}^{-1}$) is the molar volume of an ideal gas at standard temperature and pressure conditions P_0 and T_0 , T_d is the temperature of the drift tube in Kelvin and P_d is the gas pressure in the drift tube in mbar. For the standard operations conditions of 1 mbar and 100°C, N is $1.94 \times 10^{16} \text{ cm}^{-3}$. The ratio E/N in this case would be $26.71 \text{ V cm}^{-1}/1.94 \times 10^{16} \text{ cm}^{-3} \simeq 1.38 \times 10^{-15} \text{ V cm}^2$. However, it is usual to express the reduced electric field in a different unit called Townsend (Td), which corresponds to 10^{-17} V cm^2 . Thus, $1.38 \times 10^{-15} \text{ V cm}^2$ corresponds to a value of 138 Td. Typically, a PTR-MS instrument is operated between 120 and 140 Td but going as low as 80 Td or as high as 240 Td is sometimes crucial to get a good picture of the dependence of the fragmentation with the collisional energy.

The ions inside the reactor reach a steady velocity, the so-called drift velocity, v_d , which is proportional to the electric field (Equation 2.3):

$$v_d = K \cdot E \quad (2.3)$$

where K is the ion mobility, which depends on the ion's mass and structure, and the temperature and pressure in the reactor, and E the electric field in the drift tube. Note that the product of the

ion mobility and the electric field must not be mistaken with the kinetic energy, often referred to as KE. Also note that the drift velocity does not represent the velocity of an individual ion but an average over the ion cloud, and it can be also expressed in terms of the reduced mobility, K_0 , and the gas number density at standard pressure and temperature, N_0 :

$$v_d = K_0 N_0 \frac{E}{N} \quad (2.4)$$

Moreover, the expression for the total mean kinetic energy of an ion, including both the thermal energy and the energy coming from the electric field, was formulated by Wannier [28, 29] (Equation 2.5):

$$KE_{ion} = \frac{3}{2} k_B T + \frac{1}{2} m_{ion} v_d^2 + \frac{1}{2} m_b v_d^2 \quad (2.5)$$

The first term represents the contribution of the thermal energy to the ion's kinetic energy, with k_B the Boltzmann constant and T the drift tube temperature. The second term relates to the kinetic energy of the ion from being dragged by the electric field at a drift velocity v_d , with m_{ion} the mass of the ion. Finally, Wannier added the last term as the contribution to the ion's kinetic energy from the randomly-oriented velocity of the ions coming from collisions between the ions and the buffer gas molecules of mass m_b , which would be 28.0 or 28.8 g/mol, depending on if N_2 or lab air is used as buffer gas.

However, to properly characterise the energy involved in an ion-molecule collision, the relative energy of the participating bodies must be used instead of the total kinetic energy. This is given by the the kinetic energy of the collision in the centre-of-mass frame of reference, KE_{CM} (Equation 2.6) [30]:

$$KE_{CM} = \frac{1}{2} \mu (v_{ion}^2 + v_n^2) \quad (2.6)$$

where μ is the reduced mass of the 2-body system (Equation 2.7)

$$\frac{1}{\mu} = \frac{1}{m_{ion}} + \frac{1}{m_n} \quad (2.7)$$

and the kinetic energy of the ion and the neutral are defined by Equation 2.8 and Equation 2.9, respectively.

$$KE_{ion} = \frac{1}{2} m_{ion} v_{ion}^2 \quad (2.8)$$

$$\frac{3}{2}k_B T = \frac{1}{2}m_n v_n^2 \quad (2.9)$$

Combining the expressions above, KE_{CM} can be expressed as well as shown in Equation 2.10.

$$KE_{CM} = \frac{m_n}{m_n + m_{ion}} \left(\frac{m_{ion}v_d^2}{2} + \frac{m_b v_d^2}{2} \right) + \frac{3}{2}k_B T \quad (2.10)$$

where the sub-index n refers to the neutral molecule in both an ion-buffer gas collision or an ion-analyte collision, where only proton or charge transfer will occur in the latter case. The difference between m_n and m_b for an ion-buffer gas collision is that m_b is an average of the masses of the different species in the buffer gas, while m_n is the mass of the species the ion is colliding with in each case (e.g. N₂ or O₂ for lab air). It is also important to bear in mind that v_d and v_{ion} are not necessarily the same, as v_{ion} refers not only to the field-aligned velocity. Note that, as v_d is proportional to the E/N , the KE_{CM} is quadratic with the E/N , as shown in Figure 2.6 for cocaine and 2-butanone, which are two analyte molecules with a considerable mass difference and both are mentioned in this thesis. Their mass difference results in more energetic collisions (10-15%) for cocaine than for 2-butanone.

Contrary to the reduced electric field, the centre-of-mass kinetic energy is mass-dependent. The centre-of-mass is used rather than the lab reference frame as the proton transfer reactions are inelastic collisions because there is a transference of mass but still in the centre-of-mass reference frame the sum of the linear momentum of each of the molecules is equal to zero both before and after the collision. However, the main challenge when using Equation 2.10 is to measure the drift velocity accurately enough. This can be done, for instance, using the Hadamard transformation [31], or it can be calculated from the ion mobility from Equation 2.4.

The ions will predominantly collide with the buffer gas molecules. Equation 2.11 gives the expression for the kinetic mean free path, MFP, defined as the average distance travelled between collisions, if the colliding particles are considered hard-spheres [32].

$$\lambda = \frac{1}{\sqrt{2}N\pi d^2} \quad (2.11)$$

$N = 2.41 \times 10^{22} \text{ m}^{-3}$ at 1 mbar and 300 K and with d , the so-called kinetic diameter, which is $3.64 \times 10^{-10} \text{ m}$ for N₂ [33], gives a mean free path of around 70 μm in the reactor, corresponding

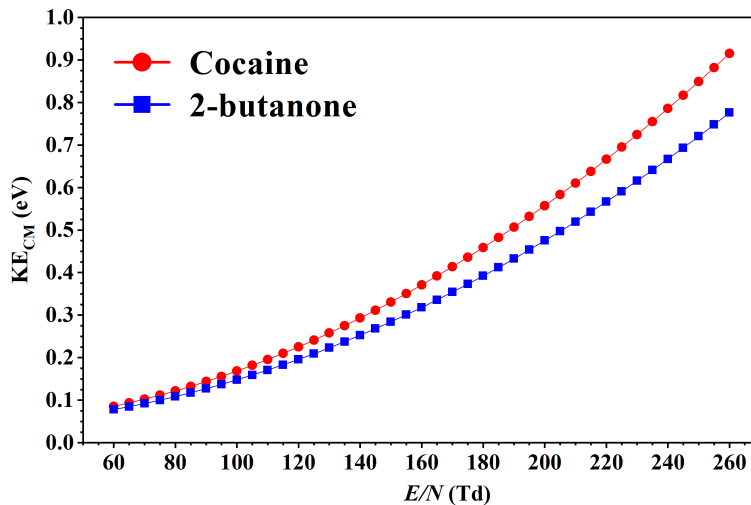


Figure 2.6: Plot of the kinetic energy of the collision in the centre-of-mass frame of reference, KE_{CM} , as a function of the E/N for collisions of H_3O^+ with cocaine ($C_{17}H_{21}NO_4$, 303 g/mol) or 2-butanone (C_4H_8O , 71 g/mol) at 300 K with N_2 as buffer gas. The values for K_0 and N_0 are $2.8 \text{ cm}^2\text{V}^{-1}\text{s}^{-1}$ and $2.69 \times 10^{19} \text{ cm}^{-3}$, respectively.

to a viscous flow. If we compare this with the mass spectrometer, where pressure is around 10^{-8} mbar and N is around 10^{15} m^{-3} , the mean free path grows up to the km order of magnitude, becoming much bigger than the dimensions of the chamber. In this case the flow is molecular and the predominant collisions are no longer with other particles but with the walls of the chamber. The transition from the viscous to the molecular regime occurs in the differential pumping region.

2.1.2.2 Radio frequency ion funnel

The Radio Frequency Ion Funnel (RFIF) in the reactor of our instrument is a novel piece of equipment developed by KORE Technology Ltd that both delivers extra collisional energy and focuses the ions towards the exit aperture of the drift tube, enhancing both sensitivity and selectivity of the PTR-MS instrument.

As mentioned earlier, in the second half of the drift tube stack the electrode's diameter gradually decreases from 40 mm to 6 mm in a funnel-like configuration. The suitable electronics to provide these funnel electrodes with an RF field are mounted in the instrument. These electronics provide the second half of the drift tube's electrodes with a signal of approximately

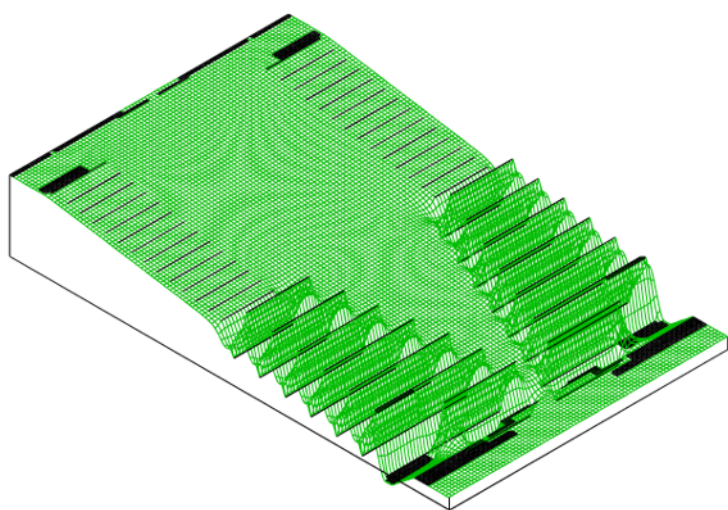


Figure 2.7: Potential energy view of the cross section of the reactor in RF mode modelled in SIMION® with a random DC field. Contrary to Figure 2.5, this is a snapshot as the RF field is time-dependent.

760 kHz and 200 V peak-to-peak in resonance that we will refer to as RF field (see Figure 2.7). At any given time, adjacent funnel plates are supplied with an RF field of opposite polarity. Also, this RF field can be turned on and off in the front panel of the instrument and when it is superimposed to the DC field, which is always on, we say the instrument is operating in RF mode. Furthermore, in RF mode we do not use the reduced electric field, E/N , to refer to the collisional energy as in this mode the electric field is not uniform in the drift tube. A comparison of the ion trajectory in the second half of the drift tube in DC and RF modes is shown in Figure 2.8 for ions of m/z 19 at a drift voltage of 200 V which corresponds to around 120 Td in DC mode. The funnel effect can be observed on Figure 2.8(b) achieving a higher ion density near the exit of the reactor than in DC mode, even though a lower number of ions were flown in RF mode to reduce simulation times because this mode is computationally more demanding than DC mode.

Besides this design from KORE Technology Ltd, there are other configurations available in the market. For instance, the reactor of IONICON Analytik GmbH instruments can include the so-called *ION BOOSTER*, which is a short, funnel-like stack of electrodes at the end of the drift tube [34]. On the other hand, the approach from TOFWERK consists of a resistive glass drift tube that generates a more uniform electric field than the traditional electrode stack, to which an RF field is superimposed from a quadrupole enveloping said drift tube [35].

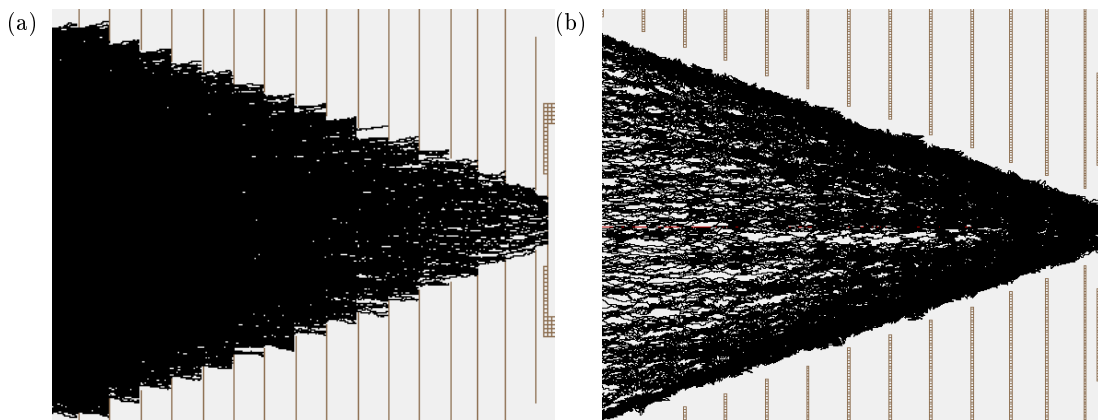


Figure 2.8: Simulation of ion trajectories in (a) DC mode and (b) RF mode in the second half of the drift tube for ions of m/z 19 at a drift voltage of 200 V (ca. 120 Td in DC mode).

2.1.2.3 Fast reduced electric field switching

Besides the RFIF, another of the recent hardware developments from KORE Technology Ltd, this time in conjunction with the Defence Science and Technology Laboratory (DSTL), is the fast reduced electric field switching, or just fast switching. It consists of a programmable 500 V power supply unit that can quickly switch at a chosen frequency between two preselected PTR Entry voltages in the range from 50 V to 450 V, which corresponds to roughly the interval from 10 Td to 250 Td. This unit can be retrofitted into any other PTR-ToF-MS instrument from the same manufacturer. This technology has been applied to the detection of explosives [13].

A previous E/N study of the molecule is needed to identify the characteristic product ions beforehand. Then the two relevant PTR Entry voltage (E/N) values and the switching frequency are selected. The lower limit of the switching frequency, while achieving optimal analytical results, is around 1 Hz. This limit is a consequence of the time the reactor takes to clear out from product ions at a different reduced electric field, the so-called “capacitance”, which is typically of around 150-200 ms. The rise and fall times of the voltages given by the power supply unit are not symmetrical, but as these are tens of milliseconds, these get masked out by the capacitance. A temporal spacing of 25 ms has been found to give the best temporal resolution and also proper data analysis is needed in order to discard the data acquired during the voltage changes. This is done by means of a script I wrote in Matlab[®], which is described in detail in section 2.2.3.

2.1.3 Differential pumping region and transfer lenses

When the ions leave the drift tube through the exit plate's orifice, which has a diameter of 400 μm , they enter the differential pumping region, where the transfer lenses are. There is a pressure drop from the 1 mbar range in the drift tube to the 10^{-4} mbar range in the differential pumping stage. This translates into a change in the type of flow, from viscous flow in the drift tube to a molecular flow in the transfer lenses region and further downstream in the mass analyser. This means that the mean free path of the ions gets bigger than the dimensions of the chamber, and thus ion-wall collisions are predominant over ion-neutral or ion-ion collisions.

The aim of the transfer lenses is to focus the ion beam and transport it to the mass spectrometer. For this purpose, the ion beam is driven through a set of ring electrodes at different voltages. These ion optics focus the ions in the centre of a pinhole in the same way optical lenses do with light. The pinhole helps to clean the beam from chromatic aberrations, which translates into narrower peaks in the mass spectra because the ion beam that reaches the mass analyser is less spatially spread out. This is qualitatively illustrated in Figure 2.9. Also, two pairs of deflectors (not included in Figure 2.9) can be tuned to steer the beam to maximise the transmission into the mass spectrometer.

It is important to note that a high potential gradient between exit plate and the first transfer optics electrode can help to increase the transmission but can create a hard extraction of ions. In the case of a hard extraction, ions are uncontrollably being fragmented beyond the exit plate in the early stages of the transfer optics, where the density of ions is still high. This undesired fragmentation can be avoided by setting the electric field between the exit plate and the first electrode in the transfer optics to no more than a few V/cm. In a series of experiments not included in this thesis, Renaud R. Dassonville and I made sure that in the standard operating conditions of our PTR-MS instruments hard extraction was not occurring. This was checked by monitoring the product ions from n-butylbenzene at different extraction and transfer lenses voltages.

2.1.4 Mass spectrometer

The ion beam is transferred from the drift tube to the mass spectrometer (MS) via the transfer optics. The MS detects the ions according to their mass-to-charge ratio and allocate them in a

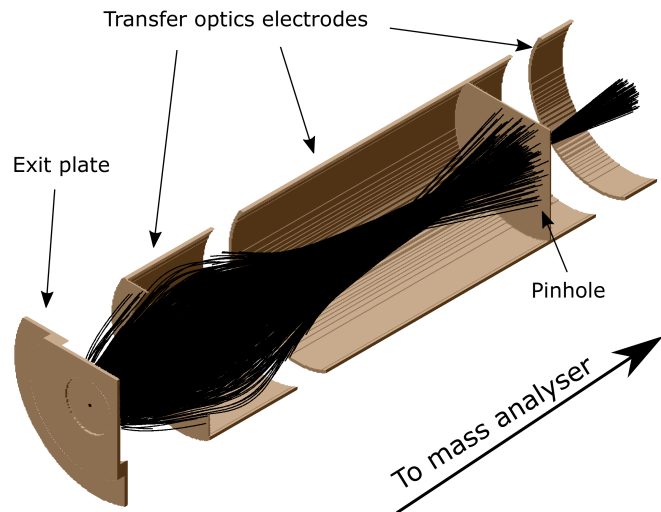


Figure 2.9: Simulation of the ion trajectories in the transfer lens region using SIMION®. 1000 ions of m/z 100 with kinetic energies uniformly distributed between 0 and 1 eV were flown.

histogram-like plot called spectrum. This requires a vacuum pressure in the flight tube of less than 10^{-7} mbar. I will indistinctly refer to mass spectrometer and mass analyser.

The mass-to-charge ratio is abbreviated to m/z and it refers to the ratio of the ions' mass divided by their charge. SI units are not used for the m/z . For simplicity, atomic mass units (amu) are used for the mass ($1 \text{ amu} = 1.66 \times 10^{-27} \text{ kg}$) and the number of fundamental electric charges are used for the charge ($1 \text{ e} = 1.60 \times 10^{-19} \text{ C}$). Depending on the mass resolution of the MS, m/z can be given as an integer (nominal mass) or as a real number (monoisotopic mass).

2.1.4.1 Time-of-flight mass spectrometer

The time-of-flight mass spectrometers (ToF-MS, Figure 2.10) are the most widely mass spectrometers used in PTR-MS.

A ToF-MS works as follows: when ions reach the entrance of the MS (pulser region), a pulsed (tens of kHz) high voltage V of some kilovolts orthogonally repels them towards the other end of the flight tube. Lighter ions will gain more speed than heavier ions, which means that they will reach the detector faster. The time it takes an ion to reach the detector and its m/z are related by Equation 2.13, which comes from the energy balance in Equation 2.12.

$$qV = \frac{1}{2}m \left(\frac{l}{t} \right)^2 \quad (2.12)$$

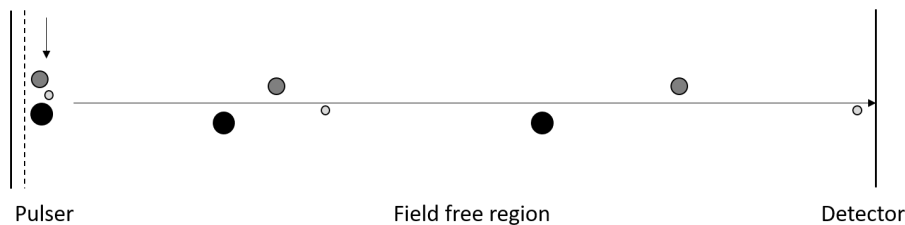


Figure 2.10: Diagram of a linear time-of-flight mass spectrometer. Circles represent ions, being their diameter proportional to their mass-to-charge ratio.

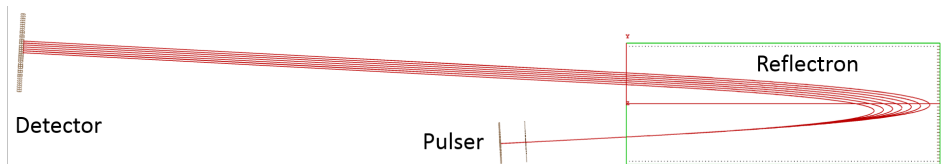


Figure 2.11: Schematic diagram of a flight tube with a reflectron showing the different trajectories of seven ions of the same m/z with different initial velocities simulated in SIMION®.

$$t = \sqrt{\frac{m}{z} \frac{l^2}{2eV}} \quad (2.13)$$

where m/z is the mass-to-charge ratio of the ion, l is the length of the flight tube, t is the flight time and $q = ez$ is the ion's charge. This allows to calculate the m/z of the ions as they are being collected at the detector and build the mass spectrum by measuring the ions' time of flight.

2.1.4.2 Reflectron

A spatially spread distribution of ions of the same m/z in the pulser region can result in different ion velocities, and hence being detected at different times. This translates into broaden peaks in the mass spectrum. To amend this a reflectron can be implemented in the flight tube of a ToF-MS.

A diagram showing how a reflectron works is shown in Figure 2.11. It basically consists of a series of electrodes with increasing voltage that will reverse the trajectory of the ions. When a cloud of ions reaches the reflectron, ions of the same m/z but going faster go deeper in it, having a longer flight distance than slower ions. This way, slow and fast ions of the same m/z will reach the detector at the same time, having travelled different distances, yielding narrower peaks and improved mass resolution when the mass spectrum is built.

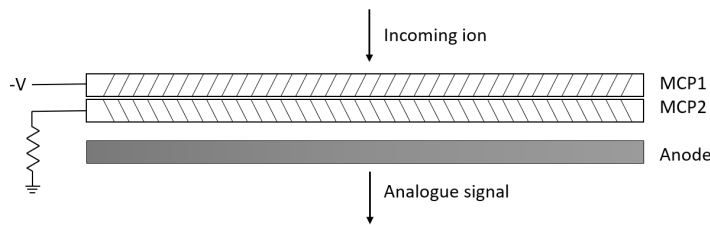


Figure 2.12: Schematic diagram of a MCP detector.

2.1.4.3 Detector

Prior to detection, the individual ion signal needs to be amplified to a detectable level. A common pre-amplification setup consists of two microchannel plates (MCPs), which are circular plates of a few millimetre of thickness with an array of tubes that go from one face to the other. These tubes form an angle with the ion trajectory and the second MCP is rotated 180° from the first one as shown in Figure 2.12 so ions cannot go through without hitting the plates.

Incoming ions are accelerated to ~ 2 kV before they hit the MCPs' walls. Said MCPs are made of a high resistive material with a secondary electron emission factor greater than one, so that when the incoming ion hits it, one or more electrons are emitted per collision, generating an avalanche that can amplify a single event by up to a factor of 10^8 . The cascade electron signal will then reach the anode, where the time-to-digital converter (TDC) will process the analogue signal and convert it into digital.

2.1.4.4 Calibration

As any other scientific instrument, the PTR-ToF-MS must be calibrated before performing any experiment. Note that in this section we refer to calibration as the method to calculate the mass conversions parameters, not the calibration to calculate a concentration from a signal in counts per second. The mass conversions parameters can be calculated by selecting some reference peaks and assigning them their exact m/z . Some peaks that can be used to calibrate the instruments are the ^{18}O isotope of hydronium ($\text{H}_3^{18}\text{O}^+$, m/z 21.023), NO^+ (m/z 29.998) and NO_2^+ (m/z 45.993). It is also useful to use the analyte ion that will be measured as a calibration peak and other peaks resulting from compounds present in air, like protonated acetone ($(\text{C}_3\text{H}_6\text{O})\text{H}^+$, m/z 59.050). The TDC uses Equation 2.14 for this task doing a least squares fitting.

$$m/z = \left(\frac{t - t_0}{C_b} \right)^2 \quad (2.14)$$

where m/z is the mass-to-charge ratio, t is the ion's time-of-flight, and t_0 and C_b are parameters that depend in the mass range the instrument will measure and in some experimental quantities like the length of the flight tube. Note that this equation is the same as Equation 2.13 for $t_0 = 0$ and $C_b = l/\sqrt{2eV}$.

2.2 Data analysis

2.2.1 Data acquisition, visualisation and treatment

The analogue data acquired by the PTR-ToF-MS is translated into digital files by the time-to-digital converter (TDC) to be visualised and analysed with the proper software. An experiment can consist in either a static measurement, yielding a stable signal throughout the experiment, or a transient measurement, where the ion counts are time-dependent. These different types of experiments are usually acquired as a mass spectrum in the form of a Galactic .spc file from Thermo Fisher Scientific®, or as a temporal evolution of the mass spectrum, in the form of a .lst file, respectively.

As mentioned earlier, a mass spectrum is the histogram-like plot of the counts of detected ions as a function of their m/z which, in our case, is stored in .spc files. Figure 2.13(a) shows an example of a mass spectrum visualised with the Thermo Fisher Scientific® GRAMS/AI™ Spectroscopy Software, which is adapted by KORE Technology Ltd to be used with their equipment. The software does the time to m/z conversion following Equation 2.14.

On the other hand, the transient experiments are stored in .lst files. These files record the timestamp (in microseconds) of each event in three consecutive bytes in hexadecimal notation, with the most significant byte first, and they are accompanied by a text file containing information about the experiment (.ini file). An event can be either the start of a cycle in the detector, always indicated by 0x000000 (i.e. $t = 0$ µs), or a detected ion (for instance, an ion detected at $t = 12500$ µs would be recorded as 0x0030D4). This means that an .lst file holds all the information about the experiment and can be plotted as both a cumulative mass spectrum as a function of the m/z or as a transient experiment as a function of the experiment time. The software

GRAMS/AITM allows to open the .lst files as a mass spectrum, like that in Figure 2.13(a), or as the time-evolution of some particular m/z , as shown in Figure 2.13(b). For the latter plot, the so-called regions of interest (ROI) must be selected before starting the experiment, by selecting the left and right ends of intervals of interest whose ion count will be integrated, displayed and updated as the data is acquired.

With a PTR-MS instrument, a lot of data can be acquired quite quickly so basic programming knowledge comes in handy when dealing with these big datasets. One of the best options is to use the Matlab[®] command `tgspcread()`, which reads Galactic .spc files from Thermo Fisher Scientific[®]. This imports all the fields in the datafile into an object-oriented data type called *struct*, which allows quick and easy extraction and manipulation of large amounts of data. In the case of the .lst files, the extraction of the data has to be done without help from any library. It is a bit more tedious, as it requires reading the hexadecimal file, building the mass spectra using the parameters stored in the .ini file, do the time-mass conversion and extract the m/z of interest for transient experiments. Using this as starting point, I wrote my own code to do the data analysis. It extracts all the data from a whole study or experiment to analyse it in Matlab[®], measuring peak positions using the FWHM of the peaks, calculating peak intensities, extracting transient data, subtracting background signals and assigning possible chemical compositions.

2.2.2 Calculation of ion intensities

Once the data is acquired and stored in the files explained in the previous section, it can be analysed and plotted for interpretation, although there are some concerns to take into account when doing this.

The counting electronics in the PTR-ToF-MS assumes that each pulse measured at the MCP corresponds to one ion. This can be not true if two or more ions arrive at the detector very close together and their analogue signals overlap so that the TDC translates it as a single event. This phenomenon is known as saturation and happens more often when a high concentration of a compound is being measured. At a given m/z , the maximum number of counts per second the instrument can measure corresponds to the number of cycles per second of the mass spectrometer, which is the number of times the ions are pulsed each second. In other words, at a certain m/z only one ion per cycle can be measured. Therefore, a compromise must be found when the experiment is being designed to avoid situations of saturation while getting a suitable signal.

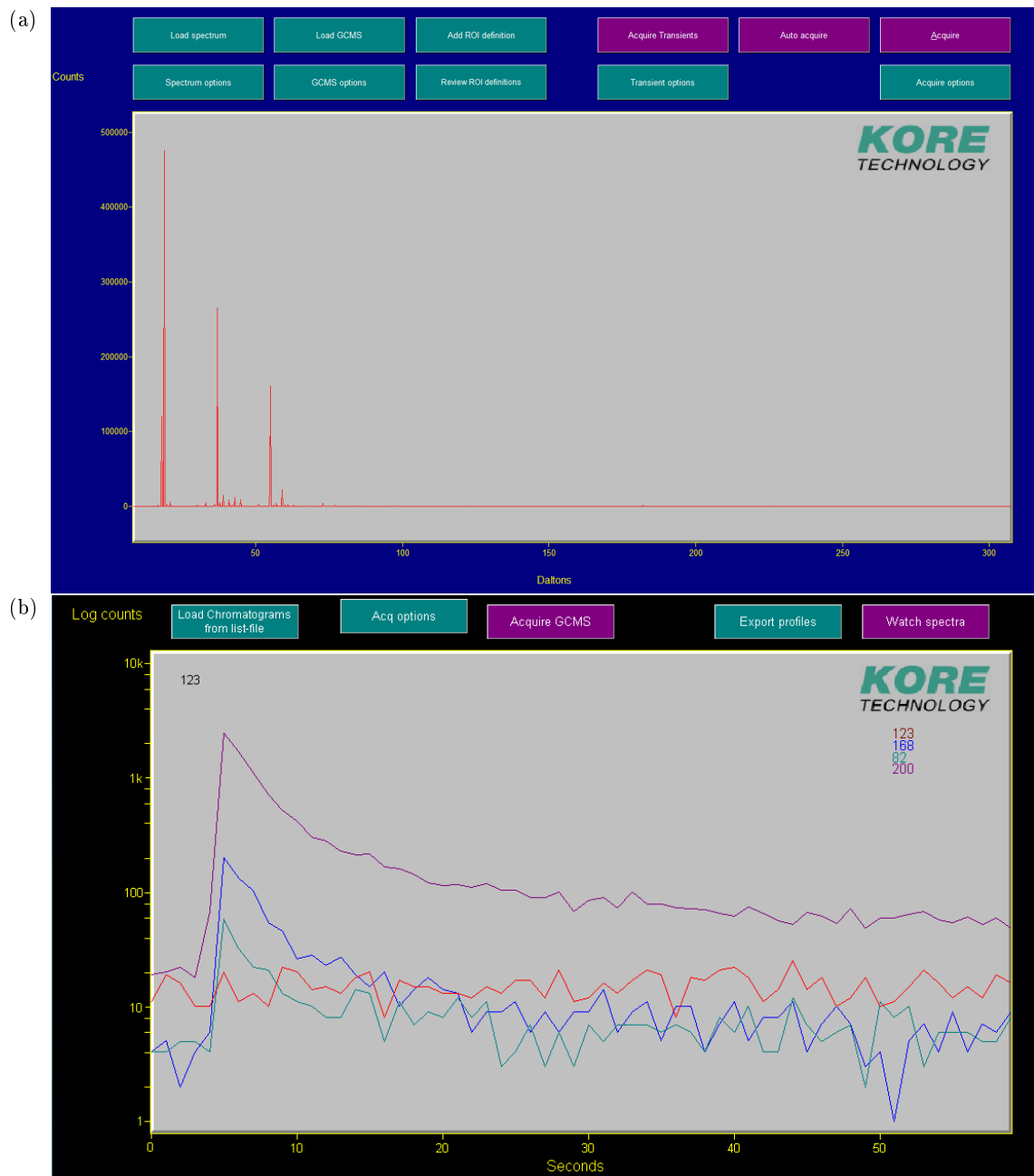


Figure 2.13: Screenshot of the GRAMS/AI™ user interface for the PTR-ToF-MS instrument manufactured by KORE Technology Ltd showing (a) an example of mass spectrum, and (b) an example of transient experiment data.

This is given by the rule of thumb that says that saturation occurs when the ion signal at a certain m/z is more than 60% of the cycles per second in the time of flight. This means that a peak can present saturation effects even before showing a distorted shape. For instance, for a cycle length of 36 μ s, the mass spectrometer will be pulsing at a rate of ~ 27777 cycles per second. In this case, the 60% saturation limit would be at an ion signal of ~ 16666 cps.

Peak saturation situations should be avoided when it occurs at product ion peaks, as it can carry other effects like reagent ion depletion. However, in some scenarios they can be worked around by calculating the ion intensities using the suitable isotopes in each case. The ^{18}O isotope peak is used to calculate the reagent ion intensities of H_3O^+ or O_2^+ as their more abundant ^{16}O peak is often saturated. The natural composition of oxygen is ^{16}O (99.76%), ^{17}O (0.03%) and ^{18}O (0.21%) [36]. The ^{18}O isotope is found at m/z 21.023 for H_3O^+ and at m/z 33.994 for O_2^+ . However, for NO^+ it is better to use the $^{15}\text{NO}^+$ at m/z 30.995 rather than the N^{16}O^+ at m/z 32.002 for two reasons: the $^{15}\text{NO}^+$ isotope is more abundant and also it does not interfere with the signal of the isobaric compound O_2^+ at m/z 32.

The ^{13}C isotope is often used to calculate product ion intensities in saturated peaks and to verify composition assignments if the mass resolution is not enough to distinguish between isobaric compounds. It is the second most abundant isotope (1.07%) after ^{12}C (98.93%), with ^{14}C is only present at 1 ppt [37]. ^{13}C is obviously more useful with bigger molecules because normally the bigger the molecule, the more carbons it will have, yielding an intensity of more than 10% at $(m+1)/z$ of that at m/z for molecules with ten or more carbon atoms. Of special interest are as well the halogenated compounds containing Cl or Br, which produce very characteristic isotopic peaks. ^{35}Cl and ^{37}Cl are naturally present at abundances of 75.76% and 24.24%, while for ^{79}Br and ^{81}Br these are 50.69% and 49.31%, respectively [38, 39]. Thus, Cl-containing compounds shows a pattern of ratios ca. 3:1 at m/z and $(m+2)/z$, while for Cl_2 this is 9:6:1 at m/z , $(m+2)/z$ and $(m+4)/z$. For Br this is approximately 1:1 at m/z and $(m+2)/z$ and for Br_2 it is 1:2:1 at m/z , $(m+2)/z$ and $(m+4)/z$.

With these considerations in mind, for the rest of this thesis when an ion's m/z is given with a chemical composition, it will refer to the most abundant isotopologue. It is also quite common to show the ion signal in normalised counts per second, ncps, by normalising the ion signals to 10^6 counts of reagent ion signal. For this, the proton affinity of the analyte must be known because proton transfer from the water clusters can also occur and their ion signal must

be considered when calculating the ncps. However, in most of this thesis the data is shown in raw cps to ease the comparison with other instruments, after being usually repeated two times and subtracted the background signal.

2.2.3 Fast switching software

Analysing data from fast switching experiments can be tedious if needed to be done working manually with each file. For this, and knowing already how to work with the experiment files, it was useful to write a script in Matlab® together with a graphical user interface to analyse the data in a quicker way. This interface is shown in Figure 2.14. It basically imports the suitable files, opens the cumulative mass spectrum to select the regions of interest, calculates and plots the ion intensities splitting the data in frames, and exports to an excel file in both counts per second and percentage together with the experiment time and the E/N . Note that different colours are used in the raw and averaged data to ease the visualisation.

The files that this script imports are the .lst ones and its accompanying .ini files, which contain the information of the fast switching experiment that is necessary to work with the data. This comprehends, among other parameters, the number of phases, the number of cycles per phase, the total number of cycles, the cycle period, the number of frames and the dead time of the switching. The number of phases refers to the number of different values that the E/N takes during a single experiment. This value is two for the fast switching experiments, which we will refer to as E/N low and E/N high. The fast switching frequency is not explicitly recorded but it is given by the inverse of multiplying the cycle period by the number of cycles per phase. For instance, for a cycle period of 40 μs and 25000 cycles per phase, the switching frequency is 1 Hz. The total length of the experiment is not recorded either but, similarly to the switching frequency, it can be calculated by multiplying the cycle period by the total number of cycles. For example, a cycle period of 40 μs and 1.5×10^6 total cycles corresponds to a 1 minute experiment. Each of the time intervals in which the drift tube is kept at the same E/N is called a frame. In a measurement lasting 60 seconds at a fast switching frequency of 1 Hz there are 60 total frames and 30 frames per phase. The dead time recorded in the .ini file in this case refers to that given by the delay in the electronics to supply the right voltage to the drift tube, i.e. the rise and fall times, and it is around 70 ms. The software automatically ignores the interval three times bigger than this dead time to account for the capacitance of the reactor, which was explained in section

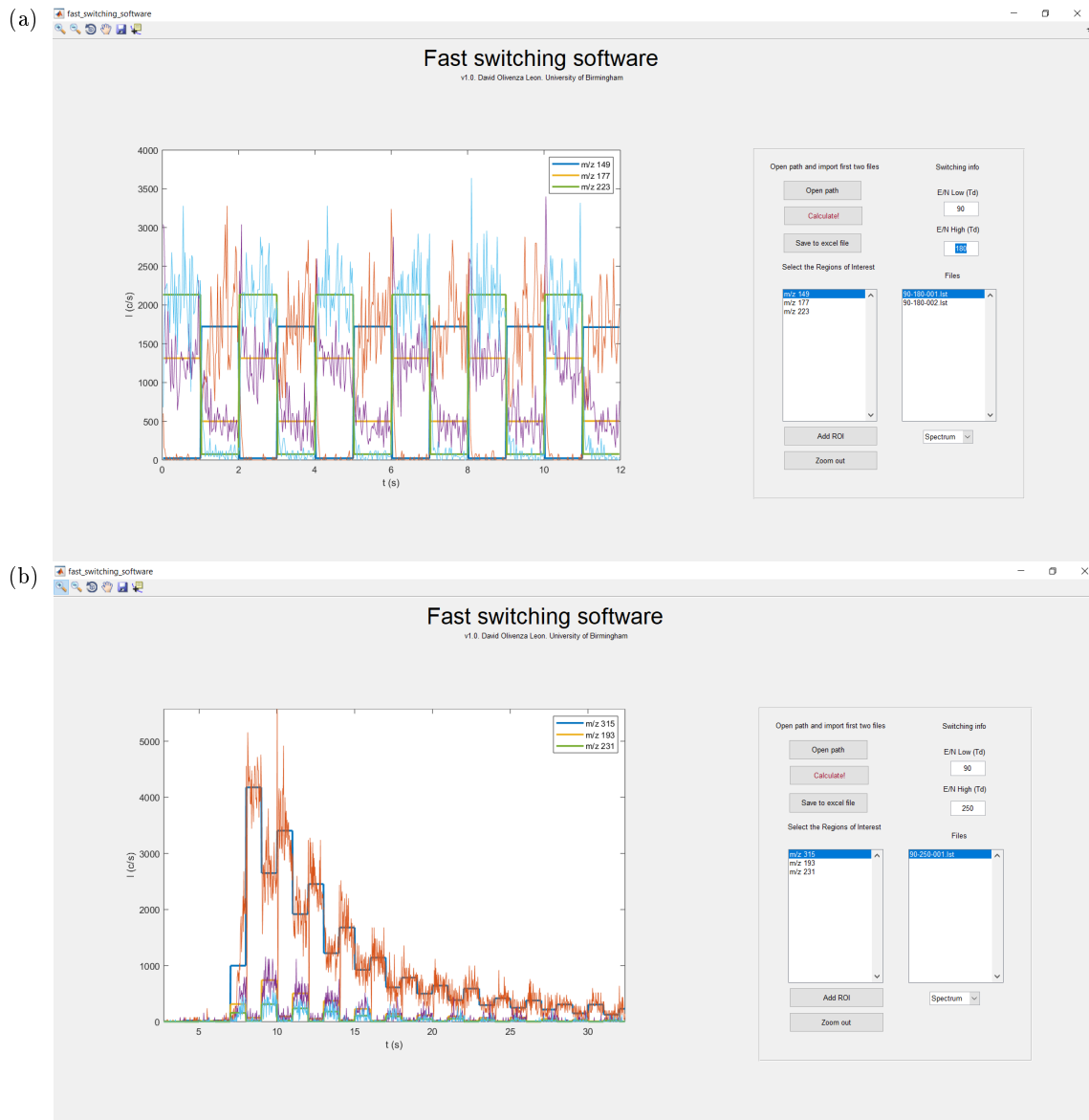


Figure 2.14: Screenshot of the graphical user interface for the script that analyses fast-switching data for: (a) a steady signal, and (b) a transient experiment.

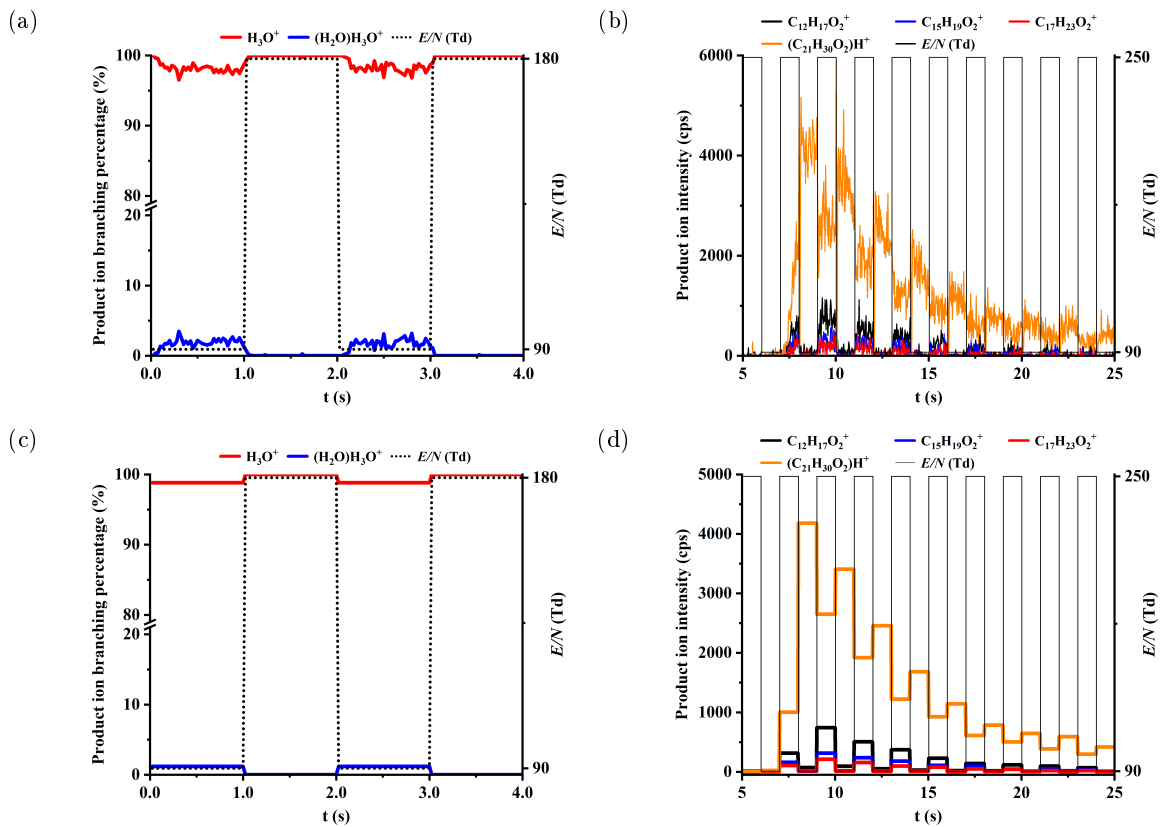


Figure 2.15: Example plots of data analysed with the fast-switching software. Left: (a) raw and (c) averaged plots of H_3O^+ and $(\text{H}_2\text{O})\text{H}_3\text{O}^+$ for the fast switching between 90 and 180 Td. Right: (b) raw and (d) averaged plots of the signal obtained from the desorption of trace amounts of cannabidiol while fast switching the reduced electric field between 90 and 250 Td.

2.1.2.2.

If the name of the files when doing the experiment is recorded is set to [*low E/N*]-[*high E/N*]-[*file number*], the script automatically reads and writes in the output file the values of the low and high E/N . If not, they must be manually added. The data inside each frame can be exported in raw format or averaged. For steady experiments like the one shown in Figure 2.14(a), the data from all the frames from a phase (i.e. high or low E/N) can also be averaged like it is shown in this figure. Obviously, this does not make sense for transient measurements like that in Figure 2.14(b). Once the data analysis is finished, the results can be exported. The format these files are saved at allows easy double-y axis plot of the ion intensities and E/N as a function of the experiment time, as it is shown in Figure 2.15, for a (a,c) steady-state and (b,d) transient measurement.

2.2.4 Density functional theory

Experimental data in this thesis is often provided including theoretical values of the proton affinity, gas-phase basicity and energetics of the protonation and/or fragmentation reactions. These theoretical values were computed using density functional theory (DFT) by Dr Peter Watts (unless otherwise stated). Gaussian09W and GaussView05 for Windows were used for this purpose [40] and the B3LYP functional with the 6-31+G(d,p) basis set were used.

2.3 PTR-MS Add-ons

Besides the essential components described earlier in this chapter, there are some accessories that can be coupled to a PTR-MS instrument for different purposes. There are many interesting devices available in the market, like the CHARON real-time aerosol inlet [41] or the PREFICS pre concentrator with chromatographic separation [42]. The ones explained in this section are the ones used for the experimental work included in this thesis.

2.3.1 Thermal Desorption Unit

For many applications, PTR-MS has been demonstrated to be a sensitive tool, yet the primary method in homeland security is IMS. Most substances of concern in this sector, including drugs and explosives, as well as in other fields have a small vapour pressure at room temperature, which challenges their identification. These are often referred to as semi-volatile organic compounds (SVOCs). The sampling method is then critical in the detection of these traces.

This issue has been addressed in many interesting ways. For instance, patents for hand-held suction systems capable of identifying small quantities of explosives were granted to Conrad and Carroll *et al.* [43, 44]. Jjunju *et al.* also created a portable tool to detect nitroaromatic explosives on-site via atmospheric pressure chemical ionisation that can operate for 12 h in one charge [45]. Additionally, the development of a biomimetic electronic dog's nose by Staymates *et al.* is a exciting new approach [46].

Swab desorptions are commonly used in IMS and the same approach can be brought into PTR-MS. KORE Technology Ltd has created a thermal desorption unit (TDU, Figure 2.16) which can be used to study SVOCs together with a PTR-MS device. This was used to study the detection of explosives reaching limits of detection (LoD) of nanograms [16] and to analyse

polyaromatic hydrocarbons [47]. The TDU works with polytetrafluoroethylene (PTFE) swabs (ThermoFisher Scientific, Cheshire, UK) mounted in a cardboard frame (shown in Figure 2.16(a)) onto which the targeted compounds are deposited. Then, the swab is inserted in the TDU, whose plates come together clamping the swab and creating a high-quality circular seal. The metal plates are kept at high temperature (150°C) and a carrier gas is flown through their holes, pulling the analyte towards the inlet pipe, whose surfaces are passivated (treated with SilcoNert® 2000) to minimise adsorption. This creates a desorption profile like the one in Figure 2.17, where the two main fragment ions from trace amounts of the desorption of heroin are shown. The duration of the desorption depends on many factors, being some of them the volatility of the analyte, the temperature of the inlet and TDU and the carrier gas flow. It usually takes between 60 and 120 seconds for a sample to be completely desorbed into the instrument after the swab has been inserted in the TDU and its jaws have clamped together. After the measurement is finished, the TDU can be opened to extract the swab, which can be reused.

2.3.2 FastGC

The fastGC (IONICON Analytik GmbH, Austria) is an add-on that can be used to aid in the product ion identification process separating the analyte molecule from possible contaminants and impurities.

The working principle of the fastGC is the same as that of gas chromatography (GC) systems, where the components of a gas mixture (mobile phase) present different retention times when flowing through a liquid or solid (stationary phase) packed inside a capillary column, which temporarily separates them. This separated mixture can be then injected into an analytical instrument for compound identification, where ions peaks occurring at the same retention time as the parent ion correspond to product ions. The main differences between GC and fastGC are that GC columns are tens of meters long, while fastGC ones are 10 meters long or less, and also that the heating ramp in fastGC is up to forty times faster than in conventional GC systems. These make possible to perform spectral analysis in less than one minute with a fastGC add-on.

We have used the fastGC in conjunction with a PTR-ToF 8000 (IONICON Analytik GmbH, Austria) to study the reactions of several ketones with H₃O⁺ [48], where this add-on was used to ease the ion identification as the purity of the ketones was in the range 97-99% and also decomposition of the sample could have occurred during storage. This fastGC is a modification

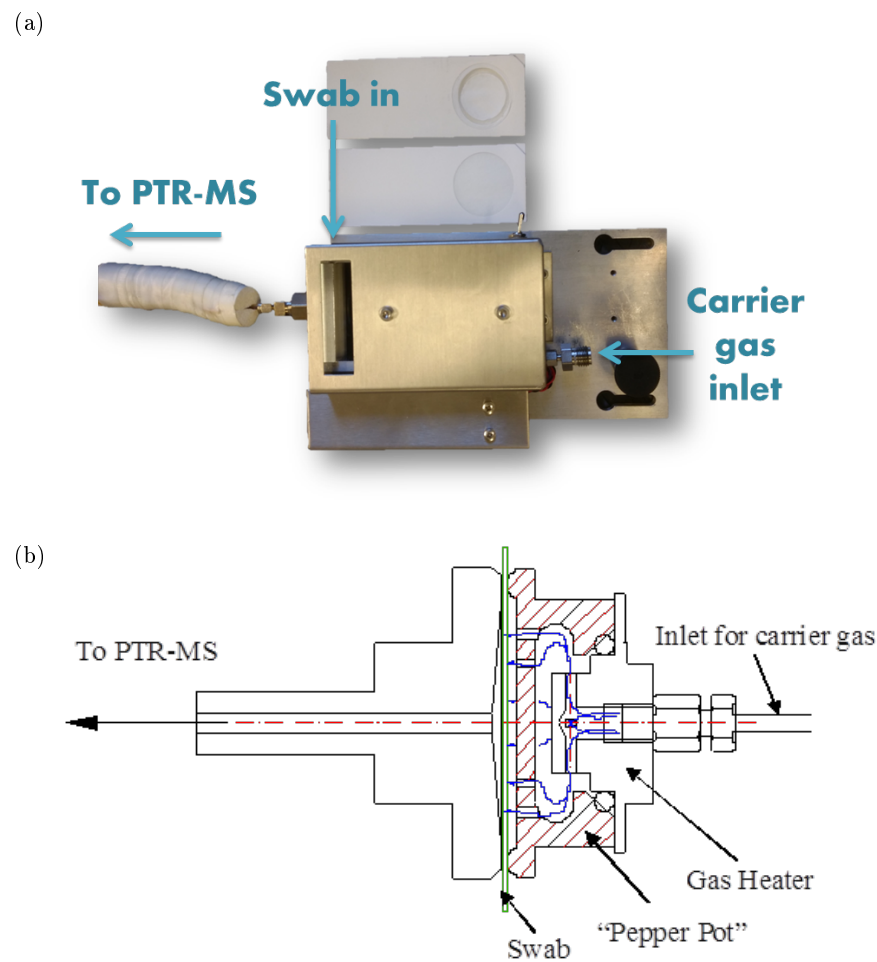


Figure 2.16: (a) Picture of the TDU near to (top) used and (bottom) new PTFE swabs. (b) Schematic diagram of the TDU [16].

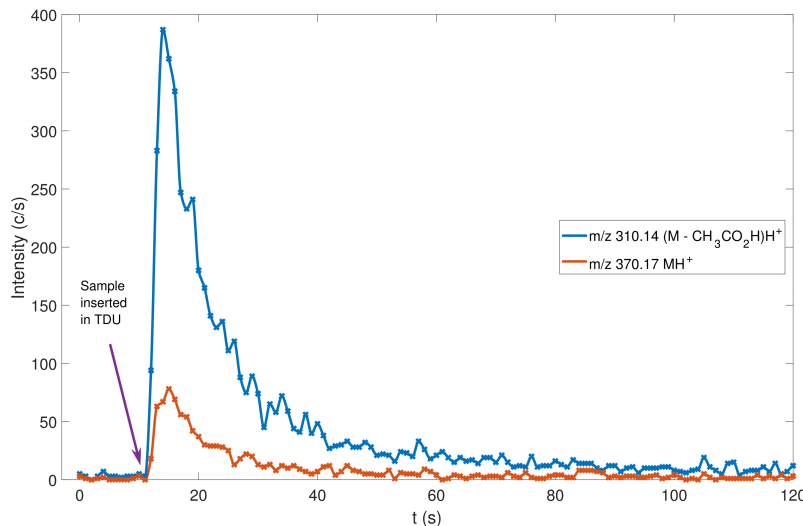


Figure 2.17: Time profiles of the count rates of two characteristic product ions at m/z 310 and m/z 370 during the thermal desorption of trace amounts of heroin at 120 Td using the TDU in PTR-MS.

of that used by Ruzsanyi *et al.* and Romano *et al.* [49, 50], so only the differences with these will be briefly mentioned here. The stationary phase in our system was a MXT-1 column ($10\text{ m} \times 0.53\text{ mm}$, film thickness $0.25\text{ }\mu\text{m}$, dimethyl polysiloxane phase, Restek, USA), which was heated from room temperature up to 240°C in 2 minutes and 40 seconds. Also, a 10-port passivated valve (VICI AG, Switzerland) and a three-way gas valve made from polyether ether ketone (PEEK) replaced the four three-way valves and needle valve in the previous design. In the oven which houses the drift tube, all sections of the inlet system are mounted to avoid cold spots. This updated configuration allowed the sample loop to be constantly filled and the capillary column to be constantly back-flushing with the carrier gas. The carrier gas and make-up gas flows used were 8 ml/min and 20 ml/min of 6.0 N_2 .

2.3.3 Liquid Calibration Unit

The liquid calibration unit (LCU, IONICON Analytik GmbH, Austria) is a standalone device that can be coupled to trace gas analysers for calibration purposes where liquid standards are evaporated into a gas stream to yield known trace concentrations.

The working principle of the LCU has been explained in detail by Fischer *et al.* [51]. The liquid sample is pumped from its container by a liquid flow controller into the nebuliser (X175,

Burgener Research[®]), where it mixes with the carrier gas (N_2 or zero air). The nebulisation process creates a stream of micro-droplets that is then injected into the evaporation chamber. This chamber is held at 100°C to continue the process of evaporation, leading in a continuous flow of a known trace gas dilution that is then injected through a heated sampling line into the analytical instrument.

We used the LCU to study the reactions of several ketones with H_3O^+ in humid conditions [48], where this add-on was not used to calibrate the instrument but to create a steady signal of ketones samples in humid conditions. The sampling vials, kept at 30°C, contained trace quantities of ketones diluted in 100 ml of purified water and were connected to the liquid inlet of the LCU. The liquid sample flow was of 35 $\mu l/min$, which with the carrier gas (N_2) flow of 950 ml/min gave an absolute humidity of 5%.

Chapter 3

Theoretical and experimental investigations of illicit drugs in PTR-MS: Cocaine and related compounds

In this chapter a PTR-MS study of cocaine and associated compounds (e.g. cocaethylene, methyl ecgonine, ethyl ecgonine and benzoate esters) is presented, together with the proton affinity, gas-phase basicity and energetics corresponding to the structures and transition states arising from reaction of these compounds with $(\text{H}_2\text{O})_n\text{H}_3\text{O}^+$ ($n = 0, 1, \dots$), which were computed using density functional theory by Dr Peter Watts.

3.1 Introduction

PTR-MS has already proved to be a useful tool for the detection of drugs. It has successfully been used to detect rape drugs even when mixed in drinks [18] and ion-molecule processes can be manipulated to differentiate between isomeric substances [52]. Cocaine is one of the most consumed illicit drugs. A recent study has shown that only the use of cannabis is higher than that of cocaine [53]. Often, cocaine users are heavy drinkers of alcohol. When both cocaine and ethanol are present in the bloodstream, the metabolite cocaethylene is produced in the body

[54], which in itself is a recreational drug.

Law enforcement agencies need to detect cocaine or similar compounds rapidly and with a high level of confidence. One real time analytical technique that can provide this is PTR-MS. To be able to use this instrument in the field, we first need to determine and understand the protonation and fragmentation processes that cocaine and related compounds undergo as a function of the key operational parameter, namely the reduced electric field, which is the ratio of the electric field strength to the gas number density in the drift (reaction) tube.

Cocaine is a white solid with a vapour pressure of 2.5×10^{-7} mbar at 25°C [55], which makes challenging to detect it without any pre-separation system. González-Méndez *et al.* implemented a thermal desorption unit to tackle this low vapour pressure issue for explosives and Blenkhorn used it for polyaromatic hydrocarbons [16, 47]. The same thermal desorption unit was used for this study.

3.2 Experimental details

The KORE Technology Ltd PTR-ToF-MS instrument described in chapter 2 was used for this experiment. The reactor was kept at a pressure of 1 mbar and at 150°C throughout all the experiments, while the pressure in the hollow cathode was set at 1.1 mbar for normal measurements and 1.4 mbar for humid ones. More details of this are given in subsection 3.3.1.

3.2.1 Chemicals

All the substances used in this study were acquired from Sigma Aldrich. Some of the samples were sourced as solids diluted in organic solvents: cocaine (1 mg/mL in acetonitrile, certified reference material), methyl ecgonine (1 mg/mL in acetonitrile, certified reference material), cocaethylene (1 mg/mL in acetonitrile, certified reference material), ethyl ecgonine (1 mg/mL in acetonitrile, certified reference material), norcocaine hydrochloride (1 mg/mL in acetonitrile (as free base), certified reference material), o-hydroxycocaine (1 mg/mL in acetonitrile, certified reference material) and anhydroecgonine methyl ester (1 mg/mL in acetonitrile, certified reference material). These were further diluted using HPLC grade solvents to give a concentration of 100 µg/mL. Although cocaine is a schedule 2 drug, no license is required for research purposes given that (i) it is acquired dissolved in a solvent from which it cannot be recovered from, (ii) it is not for

human or animal use, and (iii) minimal quantities (i.e. mg level or less) are used. The benzoates (i.e. methyl, ethyl and isopropyl benzoate) and the isobutyrates (i.e. methyl and ethyl isobutyrate) are colourless liquids. Benzoic acid is a white crystalline powder. These liquid substances and benzoic acid were acquired with a purity of at least of 99% and were used without further purification.

3.2.2 Sampling methods: thermal desorption unit and headspace analysis

A thermal desorption unit was used to desorb the diluted samples into the PTR-MS instrument. Details of this TDU have been given elsewhere [16]. In brief, a volume of 1-5 μL of the diluted samples was spotted onto the PTFE swab and it was inserted into the TDU after waiting 1 minute for the solvent to evaporate. The carrier gas, in this case oxygen-free nitrogen (99.998% purity, BOC Gases, Manchester, UK), drags the analyte through the heated inlet pipe and into the drift tube, creating a desorption “pulse” of 10-20 seconds depending on the analyte.

The liquid samples and benzoic acid are more volatile and were studied by means of headspace analysis. Oxygen-free nitrogen was used as carrier gas to drag the headspace of 22 mL vials containing trace amounts (<1 mL) of the samples, which were also connected to the inlet line of the instrument.

3.2.3 Density functional theory

DFT calculations have been undertaken to determine proton affinities, gas-phase basicities and to study the energetics of the formation of the main product ions of interest. All calculations use the B3LYP functional and the 6-31+G(d,p) basis set at a temperature of 298 K.

3.3 DFT and PTR-MS results

The PTR-MS and DFT calculations are presented in this section. The PTR-MS results are provided over the broadest achievable E/N range: approximately 20 - 255 Td, which corresponds to a drift voltage interval from 35 to 410 V (i.e. the whole voltage that the instrument can supply). It is important to note that the main reason for the ion counts to be low at low E/N is the low abundance of reagent ions (see Figure 3.1). At the same time, the residence time, which is proportional to $1/(E/N)$, is much higher at low E/N and the ions spend longer in the drift tube

than at high E/N . As it can be seen in Figure 3.1 the availability of reagent ions is around five times higher in humid conditions, but so is the presence of water clusters from which the proton transfer is softer because their PA is higher than that of the water monomer (see Table 1.2).

3.3.1 Reagent ions

For many of the compounds discussed in this chapter, a "normal" and humid E/N study was done. The reagent ion signal for hydronium and the corresponding water cluster for these two sets of data are shown in Figure 3.1. The abundance of the different water cluster species (i.e. $(\text{H}_2\text{O})_n\text{H}_3\text{O}^+$) as a function of the reduced electric field that is observed in these figures are in agreement with those reported by Price *et al.* as a function of the reactor pressure, temperature and E/P [56].

A higher humidity in the drift tube can be achieved by increasing the humidity in the buffer gas, like Malásková *et al.* did [48]. However, the measurements at higher humidity were unintended in my case, as the standard parameters setting (i.e. drift tube at 1 mbar and hollow cathode at 1.3 - 1.4 mbar) yield such proportions of water cluster ions that H_3O^+ is only more abundant than $(\text{H}_2\text{O})\text{H}_3\text{O}^+$ at >150 Td (Figure 3.1b), which is occurring because the $(\text{H}_2\text{O})_n\text{H}_3\text{O}^+$ ions do not break up prior their injection to the drift tube. This was found after doing a whole set of experiments in these humid conditions. Nevertheless, with the proton transfer from $(\text{H}_2\text{O})\text{H}_3\text{O}^+$ being softer than that from H_3O^+ , it is also necessary to acquire data in the driest conditions that the instrument could achieve to compare that data with the humid one. The main consequence of the presence of the higher abundance of water cluster ions at low E/N and hydronium at high E/N is that it gets more complicated to ascertain whether the formation of a product ion at high E/N is due to the higher collisional energy supplied by the electric field or is a consequence of the remaining energy after a harder proton transfer. However, there are two limitations when reducing the hollow cathode pressure: (i) at lower pressure difference between cathode and drift tube the buffer gas can back-stream into the hollow cathode generating unwanted ions, and also (ii) at lower pressures the instrument power boxes struggle to maintain the glow (i.e. the glow discharge indicator is flickering). This drier configuration shown in Figure 3.1a is referred to as "normal" conditions in this chapter.

The combination of the signal of all the reagent ion in the plots from Figure 3.1 show a maximum intensity at different collisional energy. This is correlated by the product ion plots

provided in this chapter, as they are given in raw counts per second to avoid the possible misleading effects created by normalising by the reagent ion signal or by calculating the branching percentages.

3.3.2 Cocaine

The structure of cocaine ($C_{17}H_{21}NO_4$) is shown in Table 3.1

Table 3.1 contains a summary of the compounds investigated in this study, excluding the benzoates and isobutyrates, which are shown in table Table 3.2. In the tables included in this chapter the given m/z refers to the detected ion, i.e. where the charge remains, and the neutrals (H_2O or $(H_2O)_2$) have been omitted in all the cases.

Figure 3.2 shows the product ion intensities in cps for the reaction of $(H_2O)_nH_3O^+$ ($n = 0, 1, \dots$) with cocaine.

The PA and GB for the main protonation sites of cocaine are given in Table 3.3.

Whilst the most basic site is the pyrrolidine nitrogen, DFT calculations show that the most stable structure is with the proton on N1 hydrogen bonded to O3 and this will be designated Cocaine1H $^+$. Similarly, when protonated, atom O2 becomes 2H $^+$ and atom O3 becomes 3H $^+$. However, inspection of the various structures shows that the proton is mobile between all basic sites. As a result of this mobility and the relative basicity of the various sites, the proton in MH $^+$ will reside mainly on N1. Migration to the other sites results in primary fragmentation although direct protonation of the ester sites is possible.

Thus proton transfer can occur from $(H_2O)_nH_3O^+$ up to $n = 3$.

The plots shows the variation of product ions as E/N is varied. The cps do not give a quantitative measure on the ions present in the PTR and cannot be used to determine branching ratios as the efficiency of ion transport from the PTR to the mass spec is dependent upon both the E/N and the m/z . The dominant ion is M.H $^+$ which is designated Cocaine1H $^+$. There are two significant fragment ions. They are m/z 182 (M.H $^+$ - benzoic acid, a carbocation), and m/z 272 (M.H $^+$ - MeOH, a substituted acyl $^+$). A further fragment ion with m/z 82 is observed at high values of E/N. Normally loss of MeOH from a methyl ester is relatively straightforward. The transition state is the migration of the proton from the more basic carbonyl oxygen (O3) to the less basic ester oxygen (O5) with the concomitant breaking of the C – O5 bond and barrierless dissociation of MeOH. This transition state will be designated TS2. However, a

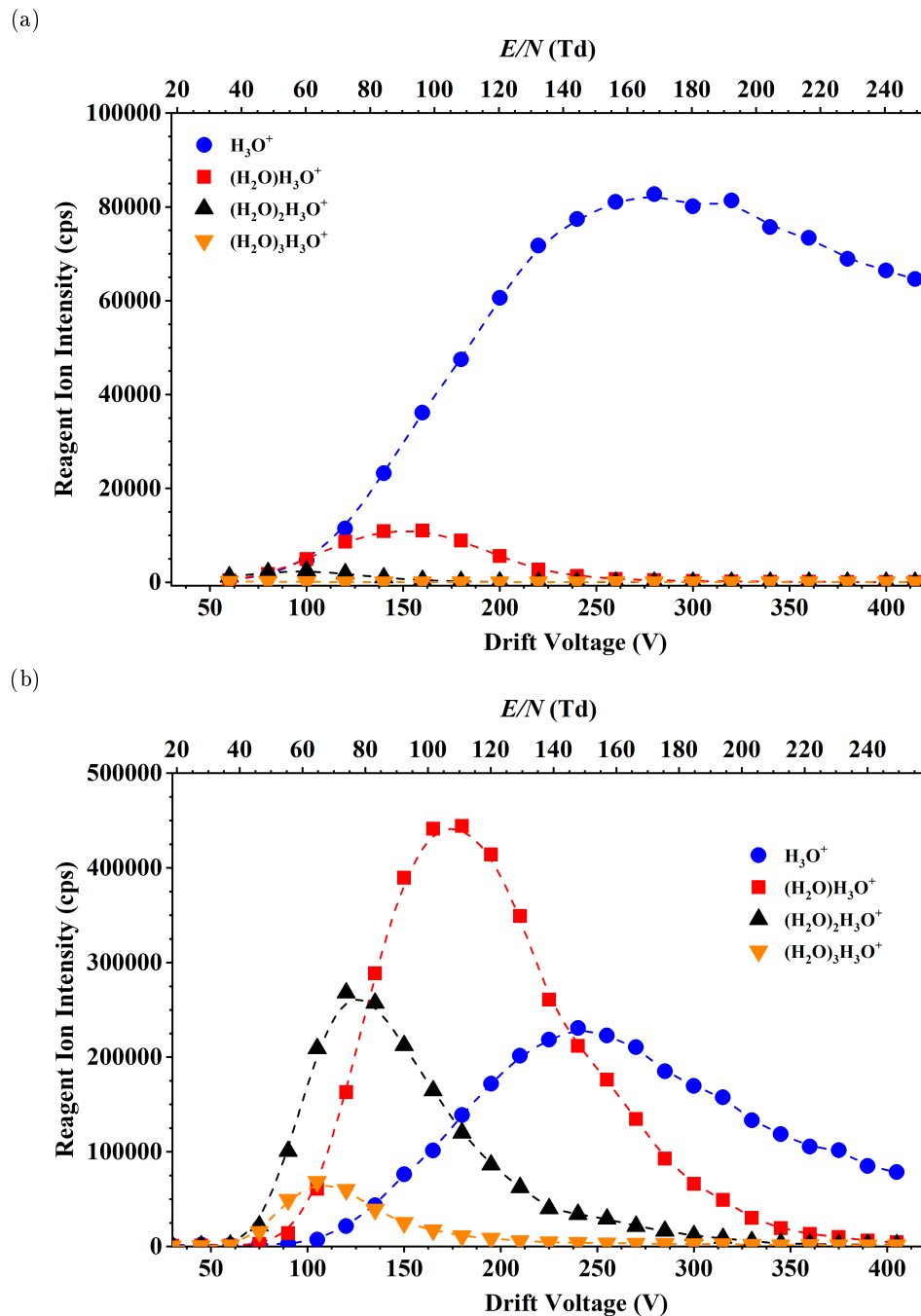


Figure 3.1: Reagent ion intensities in counts per second as a function of the drift voltage and the reduced electric field in (a) normal and (b) humid conditions.

Table 3.1: Molecular weight, vapour pressure at 25°C, formula and structure of cocaine, methyl ecgonine, cocaethylene, ethyl ecgonine, norcocaine, anhydromethylecgonine and o-hydroxycocaine.

Compound	Nominal MW	VP (mbar)	Formula	Structure
Cocaine	303	2.5×10^{-7}	C ₁₇ H ₂₁ NO ₄	
Methyl ecgonine	199	4.9×10^{-5}	C ₁₀ H ₁₇ NO ₃	
Cocaethylene	317	1.0×10^{-6}	C ₁₈ H ₂₃ NO ₄	
Ethyl ecgonine	213	-	C ₁₁ H ₁₉ NO ₃	
Norcocaine	289	-	C ₁₆ H ₁₉ NO ₄	
Anhydromethylecgonine	181	-	C ₁₀ H ₁₅ NO ₂	
o-Hydroxycocaine	319	-	C ₁₇ H ₂₁ NO ₅	

Table 3.2: Molecular weight, vapour pressure at 25°C, formula and structure of benzoic acid, methyl benzoate, ethyl benzoate, isopropyl benzoate, methyl isobutyrate and ethyl isobutyrate.

Compound	Nominal MW	VP (mbar)	Formula	Structure
Benzoic acid	122	9.3×10^{-4}	C ₇ H ₆ O ₂	
Methyl benzoate	136	0.51	C ₈ H ₈ O ₂	
Ethyl benzoate	150	0.36	C ₉ H ₁₀ O ₂	
Isopropyl benzoate	164	4.6×10^{-4}	C ₁₀ H ₁₂ O ₂	
Methyl isobutyrate	102	65.7	C ₅ H ₁₀ O ₂	
Ethyl isobutyrate	116	33.9	C ₆ H ₁₂ O ₂	

similar transition state involving the migration of a proton from the benzoyl oxygen O₂ to O₅ has been found and is designated TS2A. This is considerably lower in energy than TS2. Whilst TS2 is slightly exergonic and is thus an accessible pathway the similarity in yield to the other fragmentation pathways suggests that the fragmentation involving TS2A is operative. In order to eliminate Benzoic acid a proton will have to be present on either O₂ or O₄ during the transition state. Unfortunately, attempts to find a transition state were unsuccessful with the proton migrating to O₃. Irrespective of whether the proton is on O₂ or O₄ when the benzoic acid departs the resulting carbocation will have the structure shown in figure Figure 3.3, which is a protonated methylecgonidine.

Table 3.4 gives the overall energetics of the fragmentations together with the transition state energies for loss of MeOH.

Because of the unsuccessful search for a TS for the loss of benzoic acid to give m/z 182 and the observation of two other ions arising from the benzoate moiety viz. m/z 123 and m/z 105 under wet conditions it was thought useful to examine a series of benzoate esters and related compounds. Before that is was considered interesting to investigate another abbreviated homologue of cocaine, methyl ecgonine (MeEcg). The fragment ion with m/z 82 was initially thought to have the first structure in Figure 3.4 but experiments using D₂O in a Triple Quad by Wang *et al.* showed no inclusion of deuterium in the ion which must therefore have one of the other two structures, the final structure being marginally more stable by 16 kJ mol⁻¹ [57]. They also observed it in larger quantities than in the present work as did Clauwaert *et al.* [58]. It is also observed with BzEcg, MeEcg and other analogues of Cocaine but in such small amounts and high E/N its formation will not be pursued further at present. It is interesting that whilst all fragmentation routes are energetically favourable (see later discussion for loss of Benzoic acid from protonated Benzoate esters) little fragmentation is observed. This could be ascribed to very little H₃O⁺ being present and the dominance of MH⁺ being due to reaction of Cocaine with m/z 37 and m/z 55. But since similar patterns of behaviour are observed under both wet and dry conditions whilst the mass spec of the reagent ions are very different for the two conditions (see figures at the end of the document) David – you need to put the reagent ion mass specs somewhere and refer to their placement) this is most unlikely. A more plausible explanation is that the proton is sequestered on N1 and its migration to the fragmentation sites whilst thermodynamically feasible is very slow. At present we have no explanation as to why

m/z 105 and *m/z* 123 are only seen under wet conditions.

Table 3.3: Proton affinity and Gibbs free energy of the main protonation sites of cocaine.

Structure	PA (kJ/mol)	GB (kJ/mol)
Cocaine1	1013	980
Cocaine2	933	895

Table 3.4: Energetics of the reaction of cocaine with $(H_2O)_nH_3O^+$ ($n = 0, 1$) yielding the respective structure or transition state. ΔH_{298} and ΔG_{298} are relative to cocaine and H_3O^+ and, in brackets, to cocaine and $(H_2O)H_3O^+$.

Reaction or transition state	<i>m/z</i>	ΔH_{298} (kJ/mol)	ΔG_{298} (kJ/mol)
Cocaine1H ⁺	304	-328 (-170)	-326 (-202)
(CocaineH ⁺ - MeOH) + MeOH	272	-138 (+20)	-186 (-62)
(CocaineH - benzoic acid) ⁺ + benzoic acid	182	-272 (-114)	-336 (-212)
(CocaineH - benzoyl) + benzoyl ⁺	105	-54 (+104)	-104 (+20)
(Cocaine - benzoic acid) + benzoic acidH ⁺	123	-88 (+70)	-144 (-20)
MeOH loss: TS2 for H migration O3 to O5		-8 (+150)	-9 (+115)
MeOH loss: TS2A for H migration O2 to O5		-119 (+39)	-111 (+13)

3.3.3 Methyl ecgonine

Methyl ecgonine (MeEcg, C₁₀H₁₇NO₃) is the

It is used as biomarker for crack (smoked cocaine) consumption.

Figure 3.5 shows the product ion intensities in cps for the reaction of methyl ecgonine with $(H_2O)_nH_3O^+$ ($n = 0, 1, \dots$).

As with cocaine, inspection of the various protonated structures shows that the proton is mobile and has no difficulty in moving between the various basic sites although as with Cocaine it will be primarily sequestered on N1. The energetics for the two most stable structures are given in Table 3.5.

Unlike the case of Cocaine the only differences between the dry and wet conditions are those expected from the preponderance of H_3O^+ in dry conditions compared to wet conditions. The overall energetics for the fragmentations are given in Table 3.6.

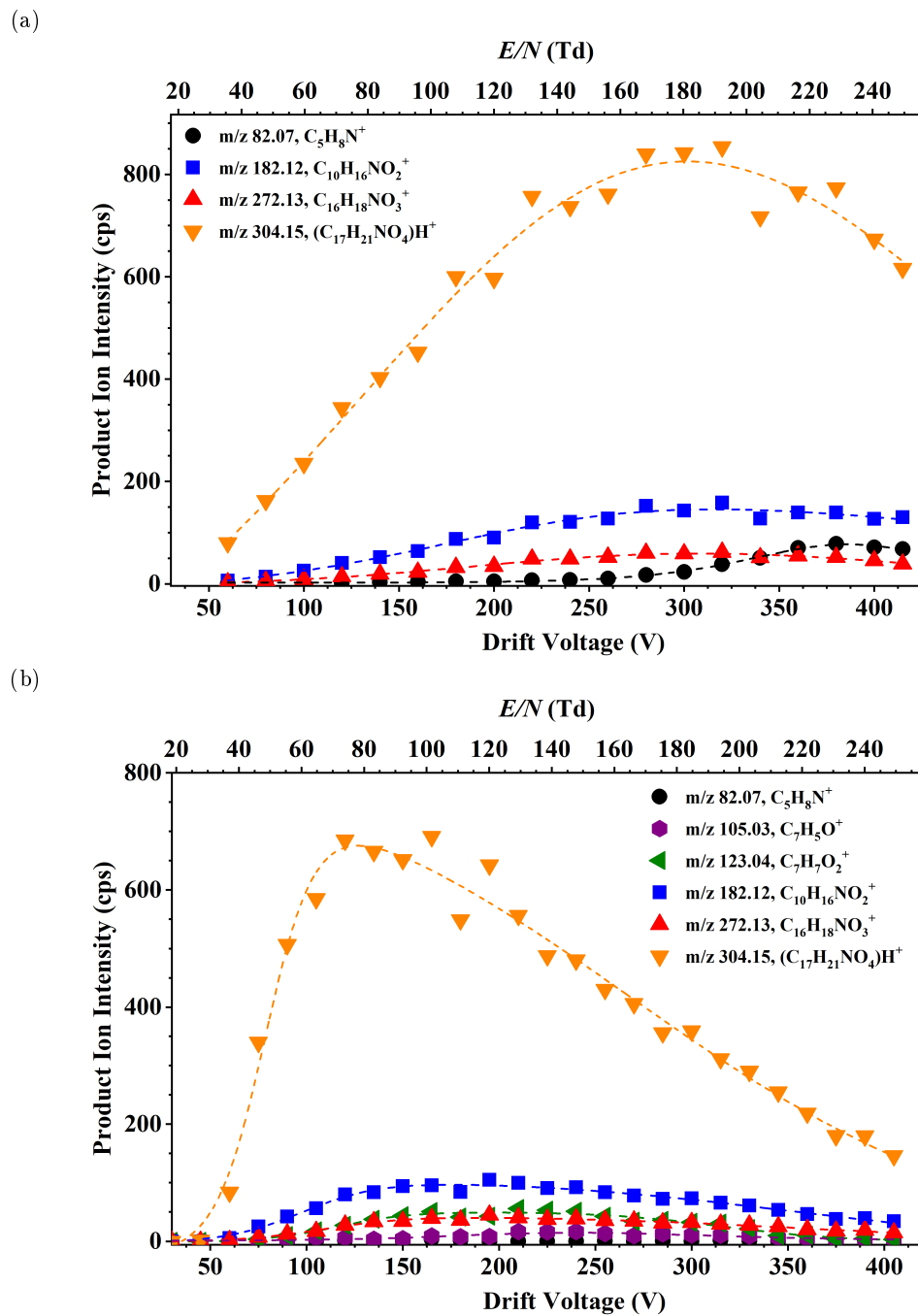


Figure 3.2: Product ion signal intensities in counts per second of the product ions resulting from reactions of the $H_3O^+.(H_2O)_n$ ($n = 0, 1, 2$) with cocaine as a function of the drift voltage and the reduced electric field in (a) normal and (b) humid conditions

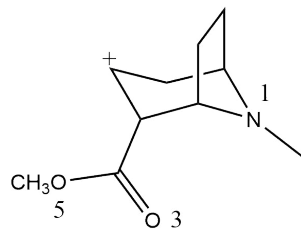


Figure 3.3: Structure of the fragment ion at m/z 182 from the reaction of cocaine with $(H_2O)_nH_3O^+$.

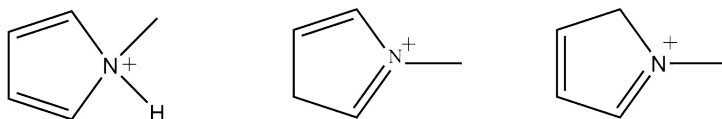


Figure 3.4: Possible structures of the fragment ion at m/z 82 from the reaction of cocaine with $(H_2O)_nH_3O^+$.

As with cocaine when the proton is on the pyrrolidine nitrogen N1 it is hydrogen bonded to O3. In MeEcg $3H^+$ the proton is hydrogen bonded between O4 and O3. The transition state for the loss of MeOH is migration of the proton from O3 to O5 followed by the barrierless dissociation of MeOH. The energetics are similar to those found for TS2 in cocaine. However direct protonation of O5 may occur. Loss of water from MeEcg H^+ m/z 182 requires the proton to migrate to O4. The subsequent loss of water is a barrierless process as shown by a relaxed scan. Further ring breaking and major rearrangement occurs – see Figure 3.6.

Table 3.5: Proton affinity and Gibbs free energy of the main protonation sites of methyl ecgonine.

Structure	PA (kJ/mol)	GB (kJ/mol)
MeEcg1	996	965
MeEcg3	906	873

3.3.4 Benzoate esters

Protonated cocaine eliminates benzoic acid to yield protonated methylecgonidine (m/z 182). This requires the proton to be on either O2 or O4 during the transition state. Unfortunately, attempts to find a transition state were unsuccessful with the proton migrating to O3. Owing to the lack of finding a transition state for the loss of benzoic acid, we have also examined a series

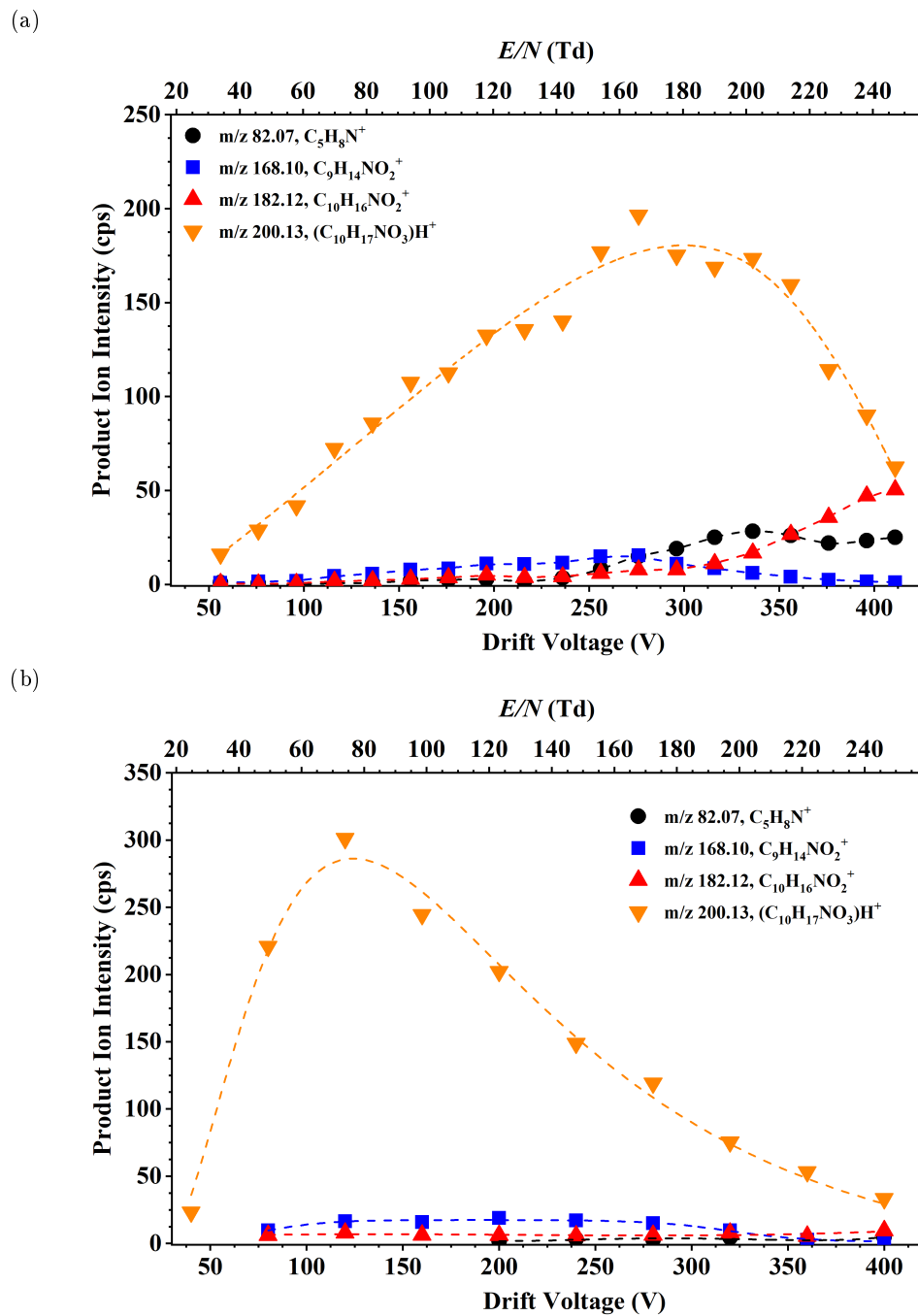


Figure 3.5: Product ion signal intensities in counts per second of the product ions resulting from reactions of the $H_3O^+.(H_2O)_n$ ($n = 0, 1, 2$) with methyl ecgonine as a function of the drift voltage and the reduced electric field in (a) normal and (b) humid conditions.

Table 3.6: Energetics relative to methyl ecgonine and H_3O^+ and, in brackets, to methyl ecgonine and $(\text{H}_2\text{O})\text{H}_3\text{O}^+$.

Reaction or transition state	m/z	ΔH_{298} (kJ/mol)	ΔG_{298} (kJ/mol)
MeEcg1H ⁺	200	-312 (-154)	-312 (-188)
$(\text{MeEcgH} - \text{MeOH})^+ + \text{MeOH}$	168	-118 (+40)	-171 (-47)
TS for loss of MeOH		+4 (+162)	0 (+124)
$(\text{MeEcgH} - \text{H}_2\text{O})^+ + \text{H}_2\text{O}$	182	-62 (+96)	-120 (+4)

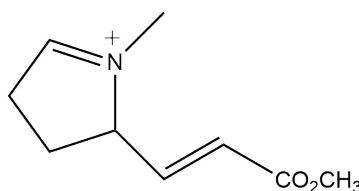


Figure 3.6: Rearrangement of the product ion at m/z 182 from protonated methyl ecgonine.

of benzoate esters (ethyl benzoate, methyl benzoate and isopropyl benzoate).

Table 3.7 shows the proton affinity and Gibbs free energy of the two studied protonation sites of methyl, ethyl and isopropyl benzoate. These protonation sites are indicated in Table 3.2.

Table 3.7: Proton affinity and Gibbs free energy of the main protonation sites of methyl benzoate, ethyl benzoate and isopropyl benzoate.

Structure	PA (kJ/mol)	GB (kJ/mol)
MeBz1	839	808
MeBz2	764	741
EtBz1	859	831
EtBz2	779	750
iPrBz1	861	831
iPrBz2	786	760

3.3.4.1 Methyl benzoate

Methyl benzoate (MeBz, C₈H₈O₂)

The PA and GB for the most stable conformation of the proton on the carbonyl oxygen (MeBz1H⁺) are 839 and 808 kJ mol⁻¹ and thus methyl benzoate will be protonated by H₃O⁺ and (H₂O)H₃O⁺ but not by higher clusters.

Table 3.8 shows the energetics and Figure 3.7 the PTR-MS data.

As mentioned previously the normal pathway for fragmentation to MeOH is by migration of the proton from the carbonyl oxygen to the alkoxy oxygen i.e. 1H^+ to 2H^+ . A second mechanism is however feasible; this is direct protonation of the alkoxy oxygen i.e. O_2 to give MeBz2H^+ . Both cases result in the breaking of the ester oxygen-carbonyl C bond leading to a concerted loss of MeOH and formation of benzoyl $^+$. However, whilst the second mechanism is barrierless (the overall fragmentation being exergonic) the first mechanism has an endergonic transition state and will only occur when field activated CID occurs. Whilst it is not possible to be certain which of the two mechanisms is operating in the present case, the conclusion that direct protonation of O_2 in EtBz occurs leads to the suggestion that it also occurs with MeBz (see below). Other fragment ions are m/z 93, m/z 91 and m/z 77. The ion m/z 93 can only be C_7H_9^+ (exact mass confirms) formed by loss of CO_2 from MeBz1H^+ and is likely to have the structure Toluene4 H^+ . Its formation is overall energetically favourable although a high TS is expected and this view is supported by m/z 93 only being seen at high values of E/N. This fragmentation will not be considered further at this time. Similarly the fragmentations leading to m/z 91 and m/z 77 (loss of H_2 and CH_4 from m/z 93 respectively) will not be considered further at this time.

Table 3.8: Energetics relative to methyl benzoate and H_3O^+ and, in brackets, to methyl benzoate and $(\text{H}_2\text{O})\text{H}_3\text{O}^+$.

Reaction or transition state	m/z	ΔH_{298} (kJ/mol)	ΔG_{298} (kJ/mol)
MeBz1 H^+	137	-155 (+3)	-155 (-31)
Benzoyl $^+$ + MeOH	105	-29 (+134)	-82 (+42)
TS to above		+15 (+173)	+14 (+138)
MeBz2 H^+	137	-80 (+78)	-88 (+36)
$\text{C}_7\text{H}_9^+ + \text{CO}_2$	93	-188 (-20)	-228 (-104)

3.3.4.2 Ethyl benzoate

Ethyl benzoate (EtBz, $\text{C}_9\text{H}_{10}\text{O}_2$)

Table 3.9 shows the energetics and Figure 3.8 the PTR-MS data.

The PA and GB for the most stable conformation of the proton on the carboxyl oxygen, O1, (EtBz1H^+ are 859 and 831 kJ mol $^{-1}$ and thus EtBz will be protonated by H_3O^+ and

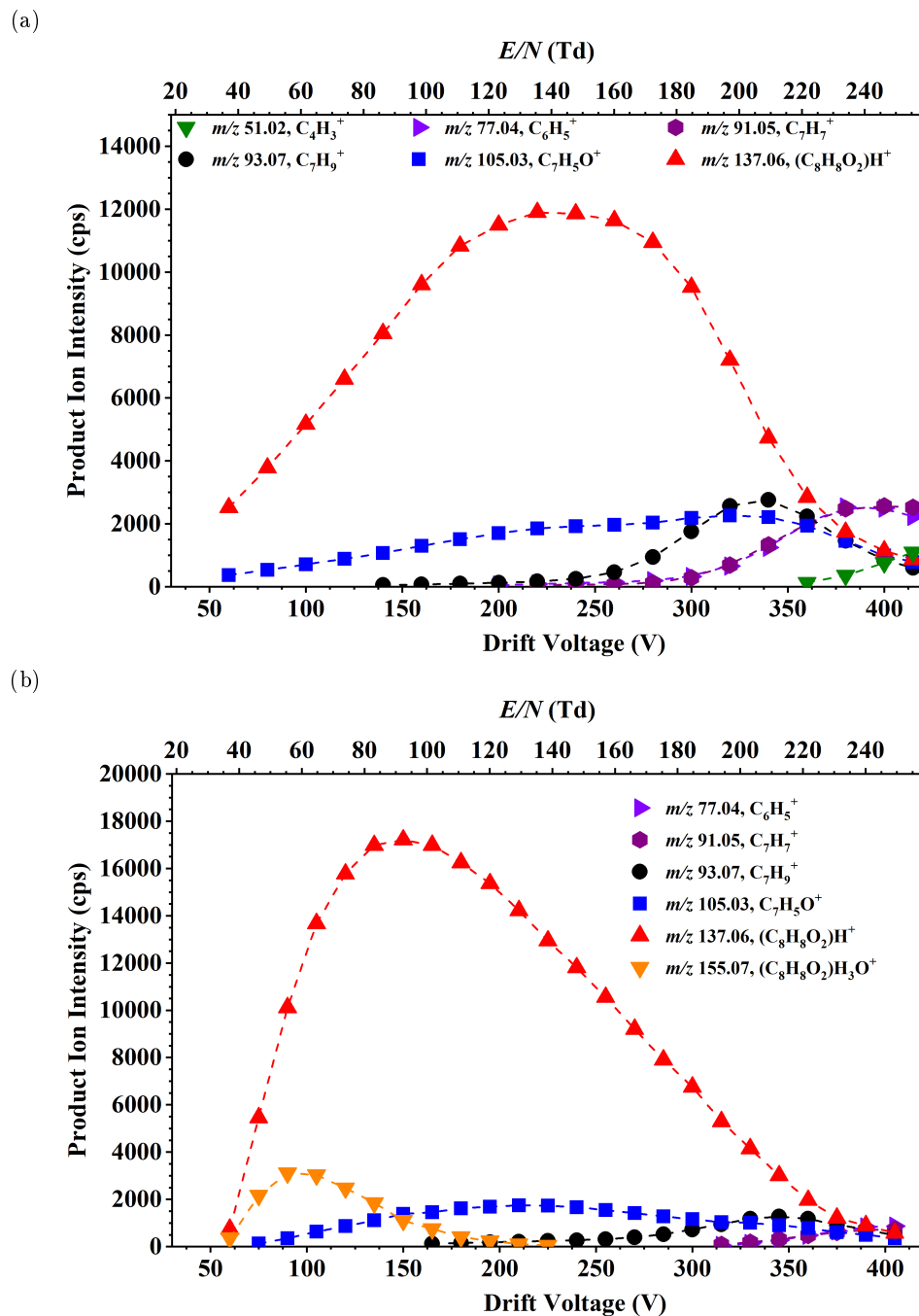


Figure 3.7: Product ion signal intensities in counts per second of the product ions resulting from reactions of the $\text{H}_3\text{O}^+\cdot(\text{H}_2\text{O})_n$ ($n = 0, 1$) with methyl benzoate as a function of the drift voltage and the reduced electric field in (a) normal and (b) humid conditions..

$(H_2O)H_3O^+$ but not by higher clusters. The expected primary fragmentation was loss of ethene to give protonated benzoic acid. But as with cocaine the ion with m/z 105, the benzoyl cation was observed. This can result either from loss of ethanol from $EtBzH^+$ or from loss of water from protonated benzoic acid. It will be seen however that loss of water from protonated Benzoic acid proceeds via an endergonic TS. Since m/z 105 is seen at low values of E/N and m/z 123 is only seen at high values of E/N it is concluded that the m/z 105 observed is formed directly from $EtBzH^+$ and not from Benzoic acid H^+ . The ion with m/z 79 is postulated to be protonated benzene resulting from loss of CO₂ from protonated benzoic acid. It is likely that the fragmentation will have a similar TS to that for the loss of CO₂ from MeBzH $^+$. The energetics of the system are given in the tables below.

That large amounts of $EtBzH^+$ are observed at low values of E/N demonstrates that a major reagent ion is $(H_2O)H_3O^+$ as protonation by H_3O^+ would lead to direct fragmentation to ethene and benzoic acid H^+ . This conclusion may however be simplistic. Loss of EtOH occurs at all values of E/N. But the expected loss of C₂H₄ only occurs as E/N is increased. It is not possible to determine what proportion of this is due to H_3O^+ being formed at higher E/N and what to collisional activation of $EtBzH^+$ by the field. An additional factor is that as E/N increases so does the internal energy of H_3O^+ . Two transition states for the fragmentation to ethene are shown below.

Loss of ethene via TS1 is the most likely pathway. Whilst TS2 is exergonic it requires $EtBz2H^+$ to be formed directly as the TS for the shift 1H $^+$ to 2H $^+$ is much higher than the elimination of ethene via TS1. Moreover $EtBz2H^+$ will fragment by a barrierless process to benzoyl $^+$ + EtOH rather than fragment to ethene via TS2. Similarly, whilst benzoyl $^+$ + EtOH could be formed via 1H $^+$ to 2H $^+$ the energetics will favour loss of ethene via TS1. Thus it is concluded that direct protonation to $EtBz2H^+$ occurs. But as both loss of ethanol and ethene are exergonic why is loss of ethanol more favoured at the lower E/Ns? This is perhaps best explained by reference to the figure below.

Whilst both $EtBz1H^+$ and $EtBz2H^+$ are both formed readily, loss of ethanol from $EtBz2H^+$ will occur immediately, loss of ethene from $EtBz1H^+$ has to go via TS1 and, whilst there is sufficient energy for this to occur, it is expected to be slower than the initial proton transfer. Thus at low E/Ns ethanol formation is kinetically more favourable than ethene elimination. This may be reflected in the cps versus E/N plot where m/z 105 appears before m/z 123 but, as has

been stated earlier, the cps do not give a good indication of relative ion concentrations in the drift tube. At higher E/Ns ethene elimination becomes the dominant fragmentation as we are now fragmenting the initially stable EtBz1H⁺ formed from (H₂O)H₃O⁺. benzoyl⁺ can also be formed indirectly via loss of water from benzoic acid .H⁺ but this is energetically unfavourable and is only likely to occur at high E/N whereas the cps versus E/N plot shows benzoyl⁺ being formed at low E/N. The relationship between benzoic acid.H⁺ and benzoyl⁺ will be explored more fully later

Table 3.9: Energetics relative to ethyl benzoate and H₃O⁺ and, in brackets, to ethyl benzoate and (H₂O)H₃O⁺.

Reaction or transition state	<i>m/z</i>	ΔH ₂₉₈ (kJ/mol)	ΔG ₂₉₈ (kJ/mol)
EtBz1H ⁺	151	-180 (-22)	-178 (-54)
EtBz2H ⁺	151	-95 (+63)	-97 (+27)
Benzoyl ⁺ + EtOH	105	-36 (+122)	-83 (+41)
TS to above, i.e. to 2H ⁺		-3 (+155)	+2 (+126)
Benzoic acid.H ⁺ + C ₂ H ₄	123	-74 (+84)	-120 (+4)
TS1 for loss of ethene from 1H ⁺		-36 (+122)	-41 (+83)
TS2 for loss of ethene from 2H ⁺		-15 (+143)	-14 (+110)
Benzoyl ⁺ + C ₂ H ₄ + H ₂ O	105	+15 (+173)	-77 (+47)
TS3 for loss of H ₂ O from benzoic acid.H ⁺		+98 (+256)	+52 (+176)
Benzene.H ⁺ + C ₂ H ₄ + H ₂ O	79	+34 (+192)	-132 (-8)

3.3.4.3 Isopropyl benzoate

Isopropyl benzoate (iPrBz, C₁₀H₁₂O₂)

This was next investigated as the benzoate moiety in cocaine and BzEcg is attached to a secondary carbon.

The fragmentation of iPrBz is remarkably different from that of EtBz. Whilst benzoic acid.H⁺ is still the major fragment ion it is now the dominant ion and occurs at much lower E/N. The benzoyl⁺ fragment ion occurs over a similar range of E/N as was observed with EtBz and a new fragment ion with *m/z* 43, the iPr⁺ cation is observed over a similar range of E/N and with a similar intensity. The PA and GB are 861 and 831 kJ mol⁻¹ respectively and as with EtBz

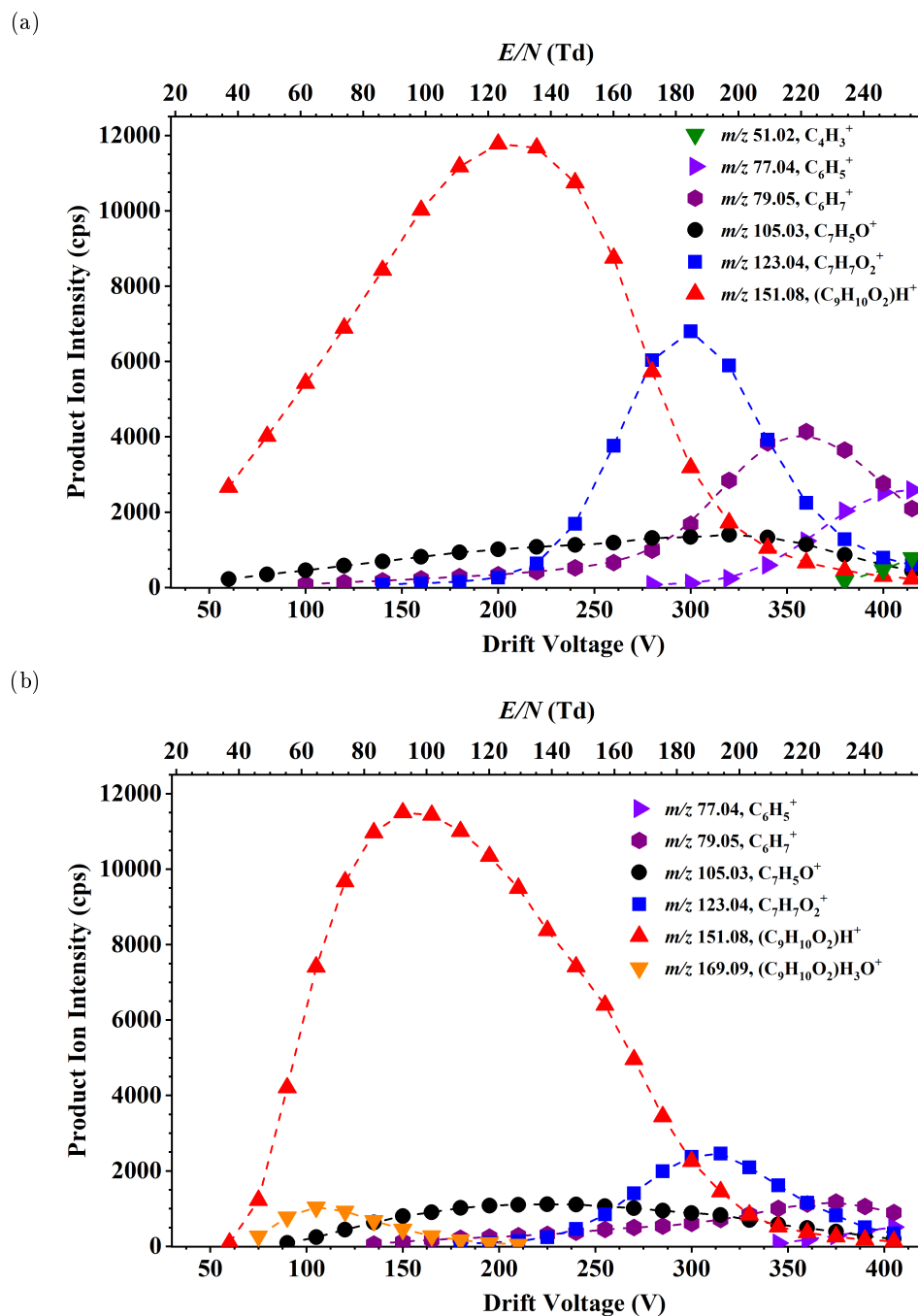


Figure 3.8: Product ion signal intensities in counts per second of the product ions resulting from reactions of the $\text{H}_3\text{O}^+ \cdot (\text{H}_2\text{O})_n$ ($n = 0, 1$) with ethyl benzoate as a function of the drift voltage and the reduced electric field in (a) normal and (b) humid conditions.

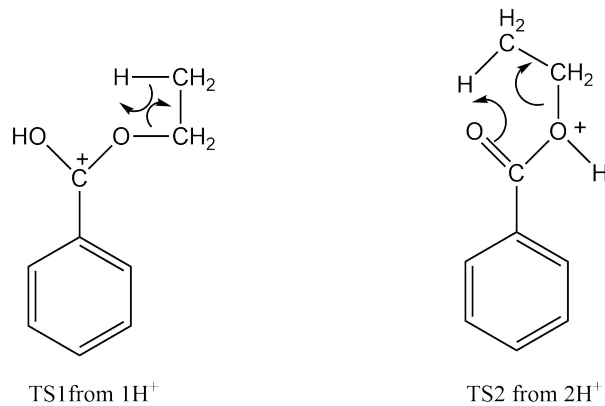


Figure 3.9: Structure of the two transition states for the loss of ethene (or ethanol??) from protonated ethyl benzoate.

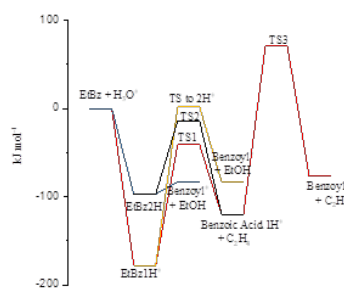


Figure 3.10: ΔG for the various reactions of H_3O^+ with EtBz . Note that the neutral water has been omitted from the captions.

protonation will occur by H_3O^+ and $(\text{H}_2\text{O})\text{H}_3\text{O}^+$ but not by higher clusters, but as will be seen the iPrBzH^+ must be formed from $(\text{H}_2\text{O})\text{H}_3\text{O}^+$.

iPrBz2H^+ is the precursor to both the loss of iPrOH and iPr^+ . To see why both pathways occur it is instructive to compare the structures of EtBz2H^+ and iPrBz2H^+ .

In EtBz2H^+ the C-O bond of the potential alcohol compares well with the 1.43\AA in EtOH or 1.45 in EtBz) with a concomitant lengthening of the carbonyl oxygen bond. In iPrBz2H^+ the C-O of the potential alcohol is less well developed in comparison with the C-O bond in iPrOH 1.44\AA leading to a shortening of the carbonyl oxygen bond. A consequence of the long C-O bond of the potential iPrOH is the potential formation of the iPr^+ cation. As the energies for both of the dissociation channels of iPrBz2H^+ are virtually identical, and both dissociation processes are barrierless as confirmed by relaxed scans, it is not surprising that both are followed to a similar degree. "You will appreciate I now have a problem to explain why 43 has such a low intensity particularly as the formation of 182 in cocaine (the dominant fragment ion) has similar energetics. Moreover the similarity to the benzoate moiety of cocaine was the reason we investigated iPrBz – see earlier in this section".

Inspection of the reaction coordinate above shows that protonation by H_3O^+ will result in immediate fragmentation to all primary products thus any iPrBz.H^+ observed results from protonation by $(\text{H}_2\text{O})\text{H}_3\text{O}^+$. The only significant dependence of a product ion upon E/N is that of $m/z 141$ Benzoic acid. $\text{H}^+\text{.H}_2\text{O}$. That the dominant product is benzoic acid. H^+ indicates that whilst direct protonation of O2 can occur, protonation of the more basic O1 is more likely, probably influenced by dipolar attraction.

3.3.4.4 Benzoic acid

Benzoic acid ($\text{C}_7\text{H}_6\text{O}_2$)

Because of the possible formation of benzoic acid H^+ from benzoyl $^+$ and H_2O and vice versa, it was interesting to study benzoic acid in the PTRMS. (A brief investigation of benzoic anhydride was attempted but the relative vapour pressures of benzoic acid and benzoic acid are such that the former dominated the spectrum and the attempt was discontinued.)

The plot shows that whilst benzoyl $^+$ is formed over the same range of E/N as observed with EtBz, its precursor, protonated benzoic acid, is present in a high concentration. With EtBz protonated benzoic acid was present in much lower concentrations, indeed at the low E/N where

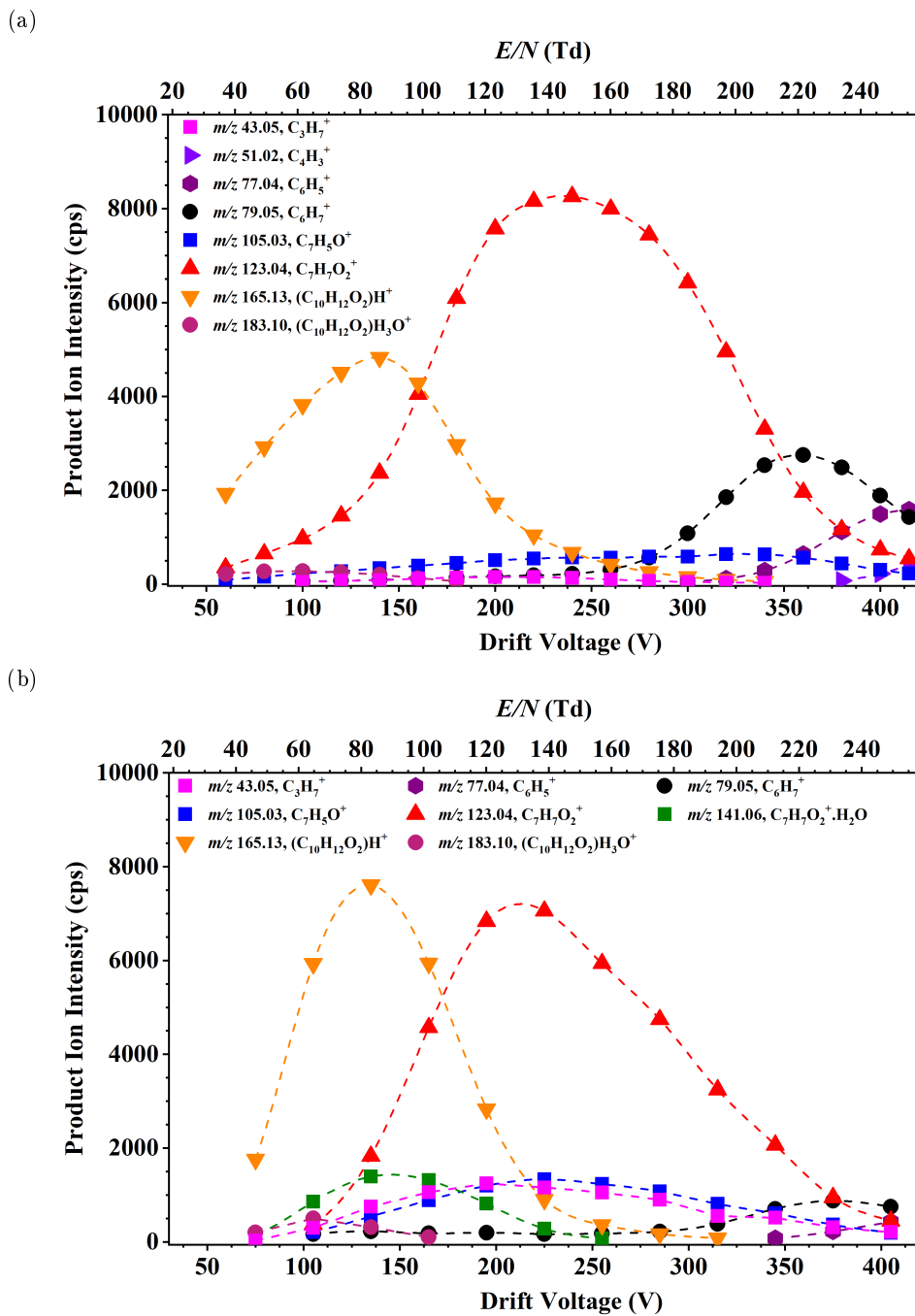


Figure 3.11: Product ion signal intensities in counts per second of the product ions resulting from reactions of the $\text{H}_3\text{O}^+\cdot(\text{H}_2\text{O})_n$ ($n = 0, 1$) with isopropyl benzoate as a function of the drift voltage and the reduced electric field in (a) normal and (b) humid conditions.

Table 3.10: Energetics relative to isopropyl benzoate and H_3O^+ and, in brackets, to isopropyl benzoate and $(\text{H}_2\text{O})\text{H}_3\text{O}^+$.

Reaction or transition state	<i>m/z</i>	ΔH_{298} (kJ/mol)	ΔG_{298} (kJ/mol)
iPrBz1H ⁺	165	-176 (-18)	-177 (-53)
iPrBz2H ⁺	165	-102 (+56)	-107 (+17)
TS 1H ⁺ to 2H ⁺		-24 (+134)	-25 (+99)
Benzoyl ⁺ + iPrOH	105	-45 (+113)	-99 (+25)
Benzoic acid + iPr ⁺	43	-35 (+123)	-91 (+33)
TS1 for loss of propene from 1H ⁺		-105 (+53)	-115 (+9)
Benzoic acidH ⁺ + C ₃ H ₆	123	-84 (+74)	-137 (-13)
BenzeneH ⁺ + C ₃ H ₆ + CO ₂	79	-52 (+106)	-151 (-27)

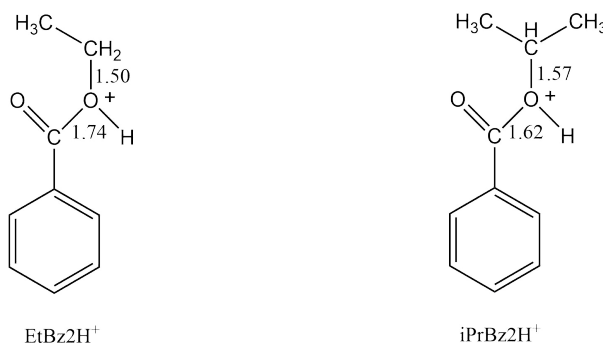


Figure 3.12: Structure of the two transition states for the loss of ethene (or ethanol??) from protonated isopropyl benzoate.

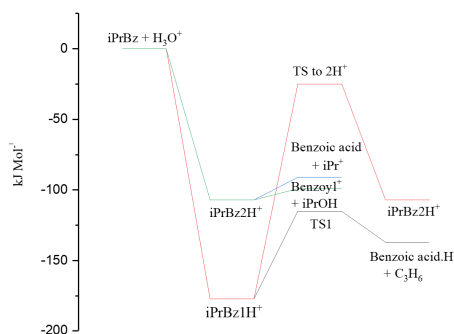


Figure 3.13: ΔG for the various reactions of H_3O^+ with iPrBz. Note that the neutral water has been omitted from the captions.

benzoyl⁺ was the second most dominant ion, protonated benzoic acid was barely discernible. This supports the conclusion that benzoyl⁺ is formed directly from EtBz by direct protonation of the alkoxy oxygen. These results also confirm that *m/z*79 is formed from protonated benzoic acid at high *E/N* via field activated CID. Also note *m/z*77 in large amounts produced by loss of H₂ from BenzeneH⁺. This has been demonstrated by introducing benzene directly into a PTRMS.

Table 3.11: Energetics relative to benzoic acid and H₃O⁺ and, in brackets, to benzoic acid and (H₂O)H₃O⁺.

Reaction or transition state	<i>m/z</i>	ΔH₂₉₈ (kJ/mol)	ΔG₂₉₈ (kJ/mol)
Benzoic acid1H ⁺	123	-128 (+30)	-130 (-6)
Benzoic acid2H ⁺	123	-40 (+118)	-88 (+36)
TS 1H ⁺ to 2H ⁺		+44 (+202)	+45 (+169)
Benzoyl ⁺ + H ₂ O	105	-83 (+75)	-100 (+24)
BenzeneH ⁺ + CO ₂	79	-97 (-61)	-143 (-19)

3.3.5 Isobutyrates

Compare with the structure of the cocaine: Some isobutyrate were studied because of the similarities with the carboxylate moiety in cocaine and its analogues.

3.3.5.1 Methyl isobutyrate



Significant fragmentation only occurs at high values of *E/N* and is mainly concerned with the isobutyrate moiety. Only a trace of MeOH loss is observed. Whilst initially surprising, inspection of the associated TS shows it to be explicable – see below.

It was suggested earlier that because of the endergonic TS for loss of MeOH following protonation of the carboxy oxygen that the facile loss of MeOH from MeBz was due to direct protonation of the alkoxy oxygen. If this were so a similar facile loss of MeOH would be expected from MeIso. But this is not observed. It is therefore concluded that the energy imparted from the field is sufficient to overcome the endergonic TS for MeBz but the higher TS for MeIsoBut. Need to return to MeBz and EtBz discussion.

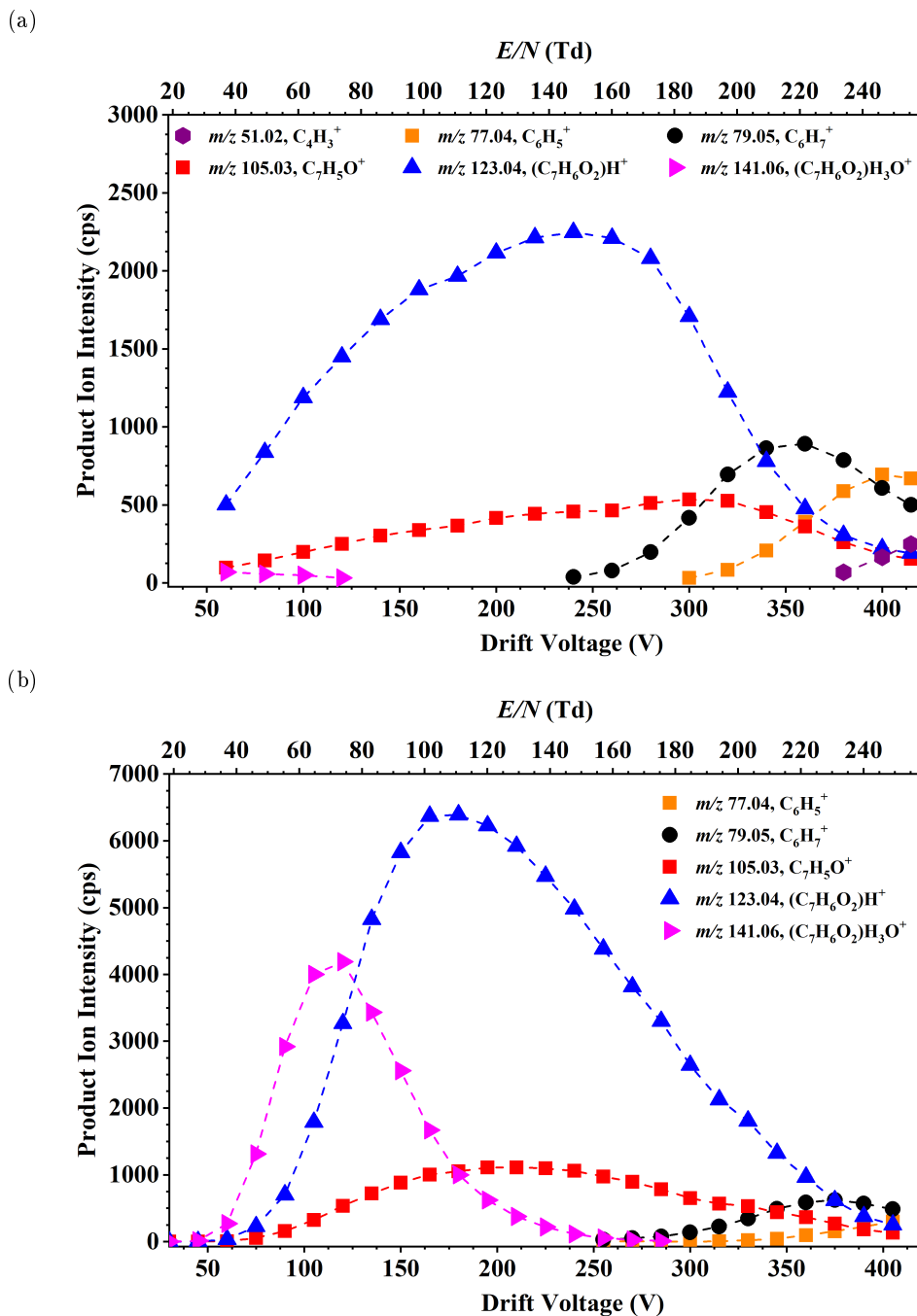


Figure 3.14: Product ion signal intensities in counts per second of the product ions resulting from reactions of the H₃O⁺·(H₂O)_n (n = 0, 1) with benzoic acid as a function of the drift voltage and the reduced electric field in (a) normal and (b) humid conditions.

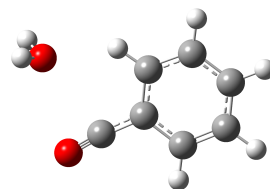


Figure 3.15: Structure of

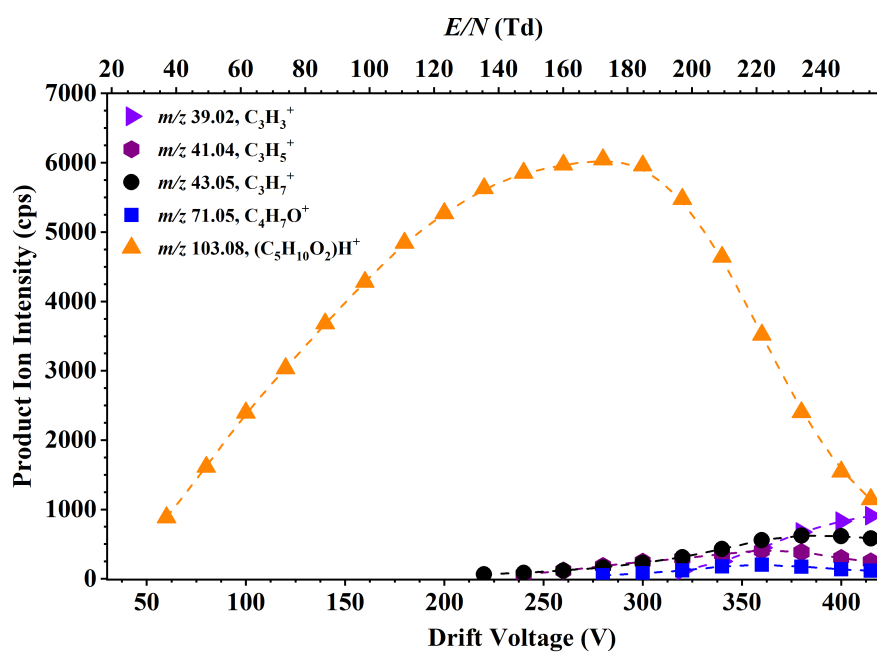


Figure 3.16: Product ion signal intensities in counts per second of the product ions resulting from reactions of the $H_3O^+.(H_2O)_n$ ($n = 0, 1$) with methyl isobutyrate as a function of the drift voltage and the reduced electric field.

3.3.5.2 Ethyl isobutyrate

(EtIsob, C₆H₁₂O₂)

The dominant fragmentation is loss of ethene; the remaining fragmentations are similar to those observed with MeIsoBut i.e. only occur at high values of E/N with most being concerned with the isobutyrate moiety and a trace of loss of EtOH.

It can be seen that protonation by H₃O⁺ should lead to ethene loss. That it does not occur below 100Td suggests that observed MH⁺ is formed from (H₂O)H₃O⁺. Above 100Td production of ethene may occur by direct protonation by H₃O⁺ or field activation of MH⁺ or probably both.

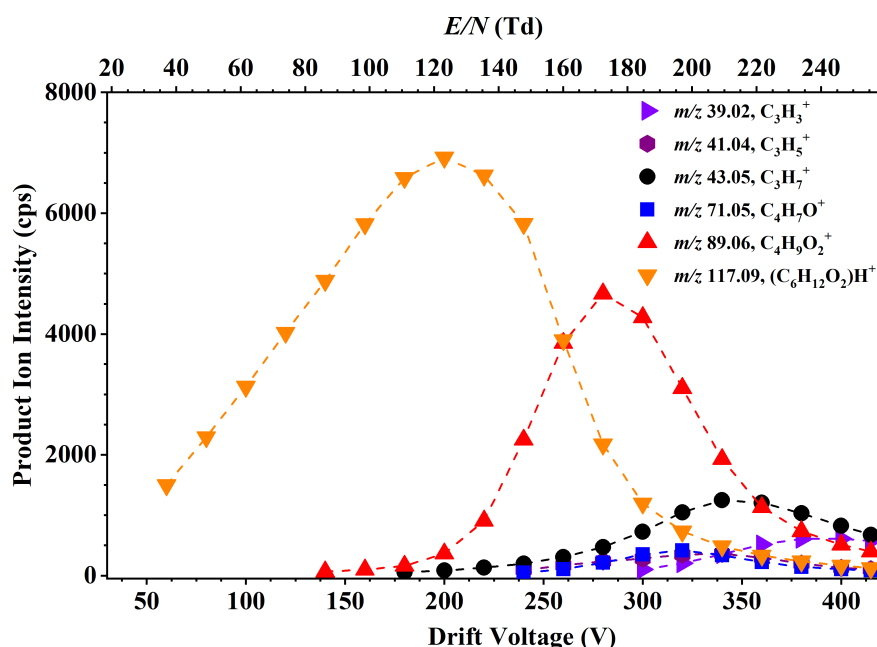


Figure 3.17: Product ion signal intensities in counts per second of the product ions resulting from reactions of the H₃O⁺.(H₂O)_n (n = 0, 1) with ethyl isobutyrate as a function of the drift voltage and the reduced electric field.

3.3.6 Cocaethylene

3.3.7 Ethyl ecgonine

3.3.8 Norcocaine

Norcocaine (

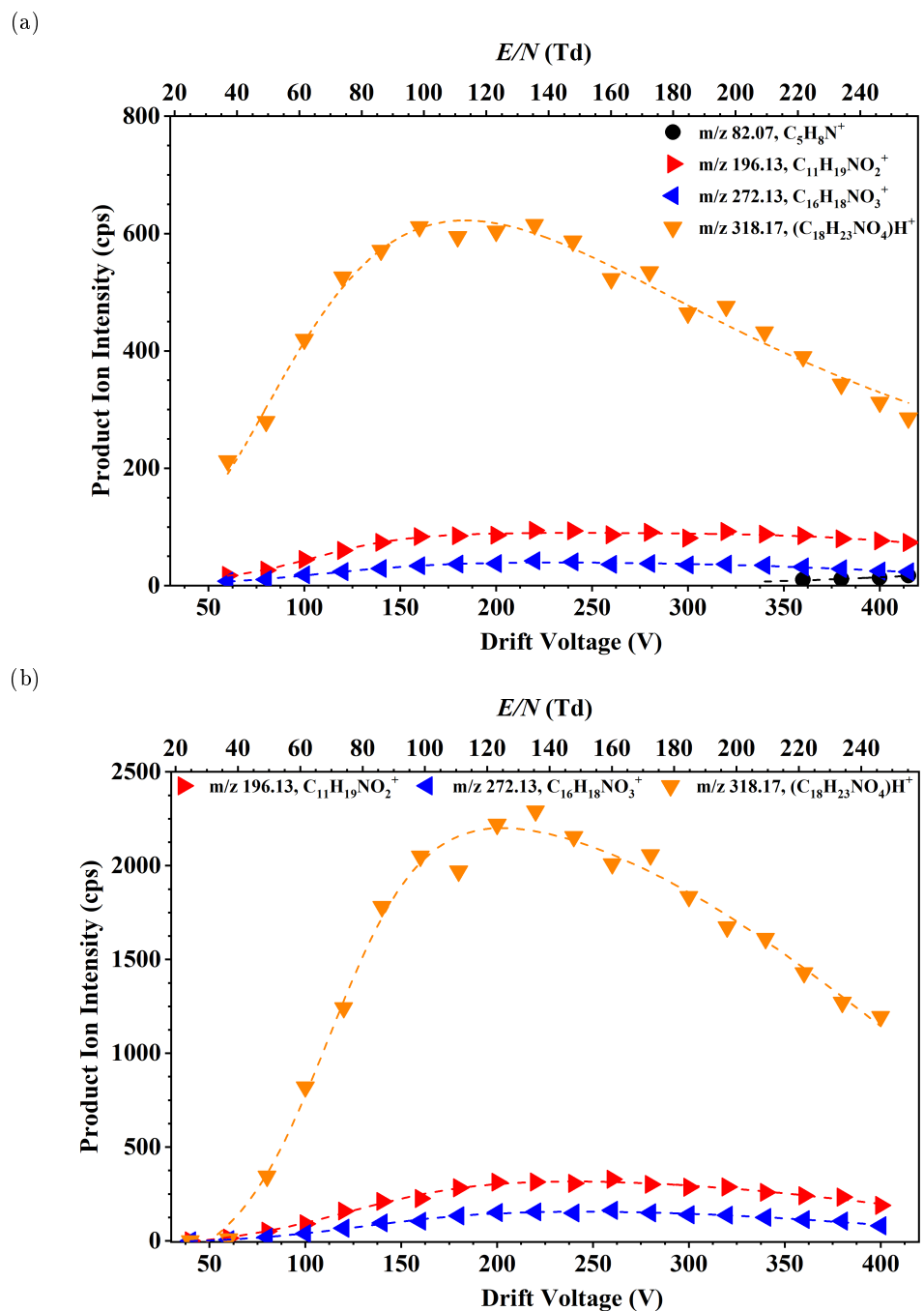


Figure 3.18: Product ion signal intensities in counts per second of the product ions resulting from reactions of the $H_3O^+.(H_2O)_n$ ($n = 0, 1, 2$) with cocaethylene as a function of the drift voltage and the reduced electric field in (a) normal and (b) humid conditions.

Table 3.12: Energetics relative to ethyl isobutyrate and H_3O^+ and, in brackets, to ethyl isobutyrate and $(\text{H}_2\text{O})\text{H}_3\text{O}^+$.

Reaction or transition state	m/z	ΔH_{298} (kJ/mol)	ΔG_{298} (kJ/mol)
EtIsoBut1H ⁺	117	-145 (+13)	-146 (-22)
EtIsoBut2H ⁺	117	-81 (+77)	-86 (+38)
IsoButyryl ⁺ + EtOH	71	-9 (+149)	-59 (+65)
TS 1H ⁺ to 2H ⁺		+18 (+176)	+17 (+141)
IsoButyric acidH ⁺ + C ₂ H ₄	89	-38 (+120)	-85 (+39)
TS1 to above		-28 (+130)	-34 (+90)
TS2 to above		-6 (+152)	-11 (+113)

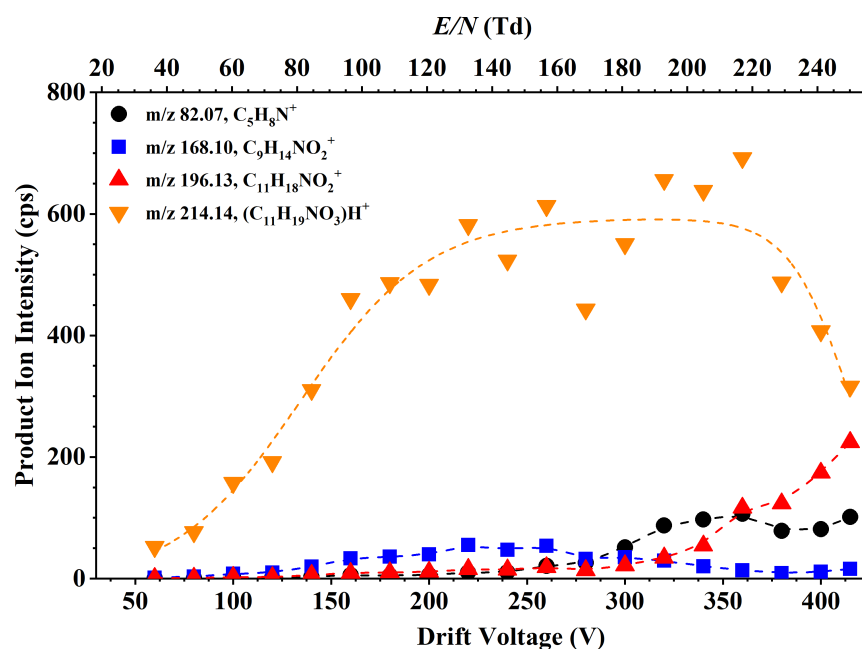


Figure 3.19: Product ion signal intensities in counts per second of the product ions resulting from reactions of the $\text{H}_3\text{O}^+\cdot(\text{H}_2\text{O})_n$ ($n = 0, 1, 2$) with ethyl ecgonine as a function of the drift voltage and the reduced electric field.

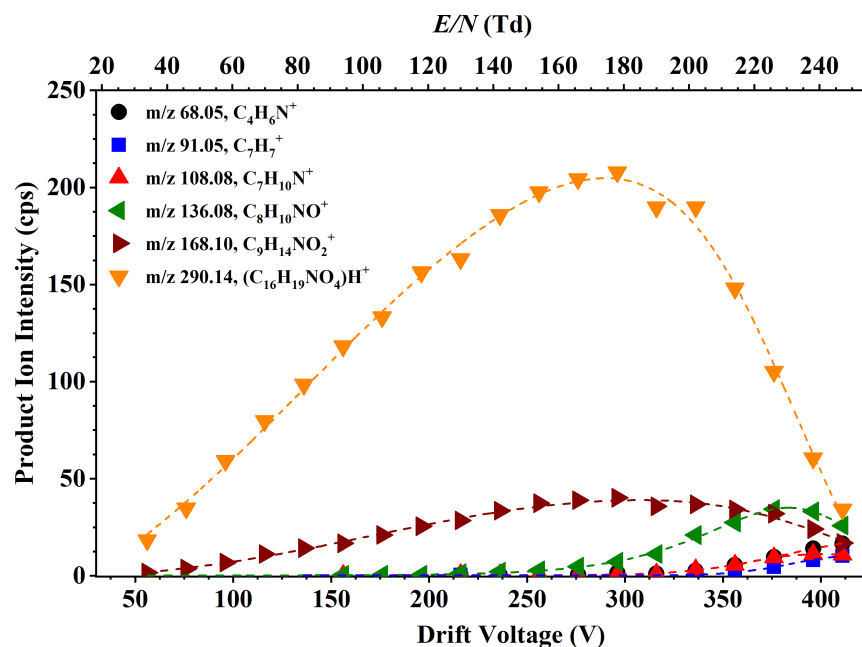


Figure 3.20: Product ion signal intensities in counts per second of the product ions resulting from reactions of the $H_3O^+.(H_2O)_n$ ($n = 0, 1, 2$) with norcocaine as a function of the drift voltage and the reduced electric field.

3.3.9 Anhydromethyllecgonine

3.3.10 o-Hydroxycocaine

3.4 Conclusions and further remarks

In this chapter I have shown....

The experiments were done in two different ways....

The use of the TDU explains the dispersion of the data points for some compounds and raises concerns about the repeatability and reproducibility, although they have been checked already by González-Méndez *et al.* [16].

- For cocaine and methyl ecgonine (and) it is surprising that, although the proton is mobile between the various studied sites, the protonated parent molecule is the main reaction channel. This suggests that.... the proton stays (sequestered) in the nitrogen atom.

For many compounds (benzoates, anything else?), the MH^+ product ion is formed through

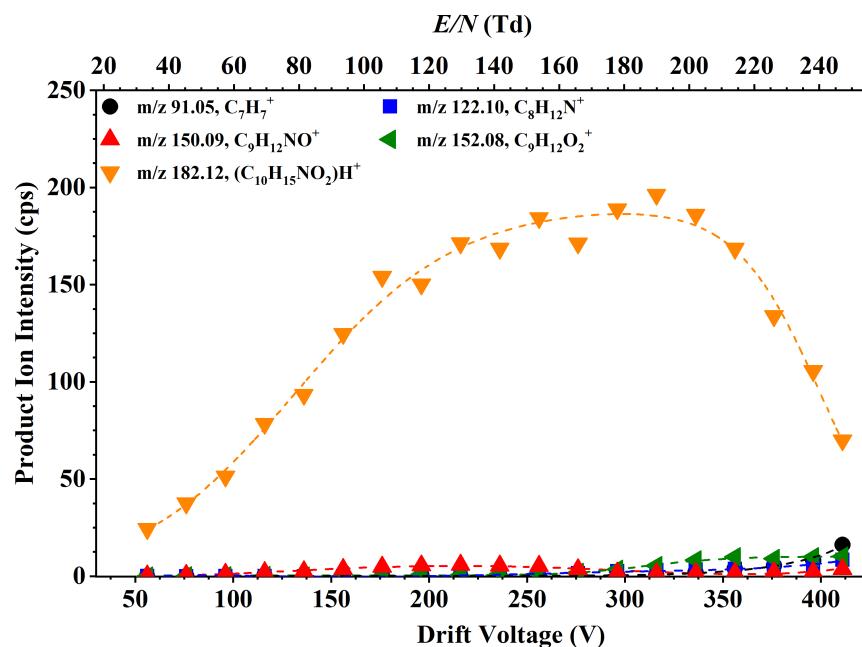


Figure 3.21: Product ion signal intensities in counts per second of the product ions resulting from reactions of the $H_3O^+.(H_2O)_n$ ($n = 0, 1, 2$) with anhydromethylecgonine as a function of the drift voltage and the reduced electric field.

the reactions with $(H_2O)H_3O^+$ rather than with H_3O^+ , as proton transfer from the latter are dissociative. This explains in part the fact that, for the same E/N , fragmentation is higher in the normal (dry) case.

The loss of an alcohol (i.e. MeOH or EtOH) is a common fragmentation channel found in this chapter. This is methanol for cocaine, while it is ethanol for cocaethylene.

DFT reveal that some fragments are not thermodynamically allowed, which hints that they are a consequence of field-activated collision induced dissociation

It is also important to note that other compounds (benzoylecgonine, ecgonine and ecgonidine) that are related to cocaine presented difficulties to be measured in the same way (i.e. with the TDU). Discussions about this are still undergoing and further experiments are planned using different instrumentation. These three compounds have a carboxylic acid group instead of the methyl or ethyl ester from the other compounds.

Benzoylecgonine is the main metabolite of cocaine. It is often measured derivatised (add ref)

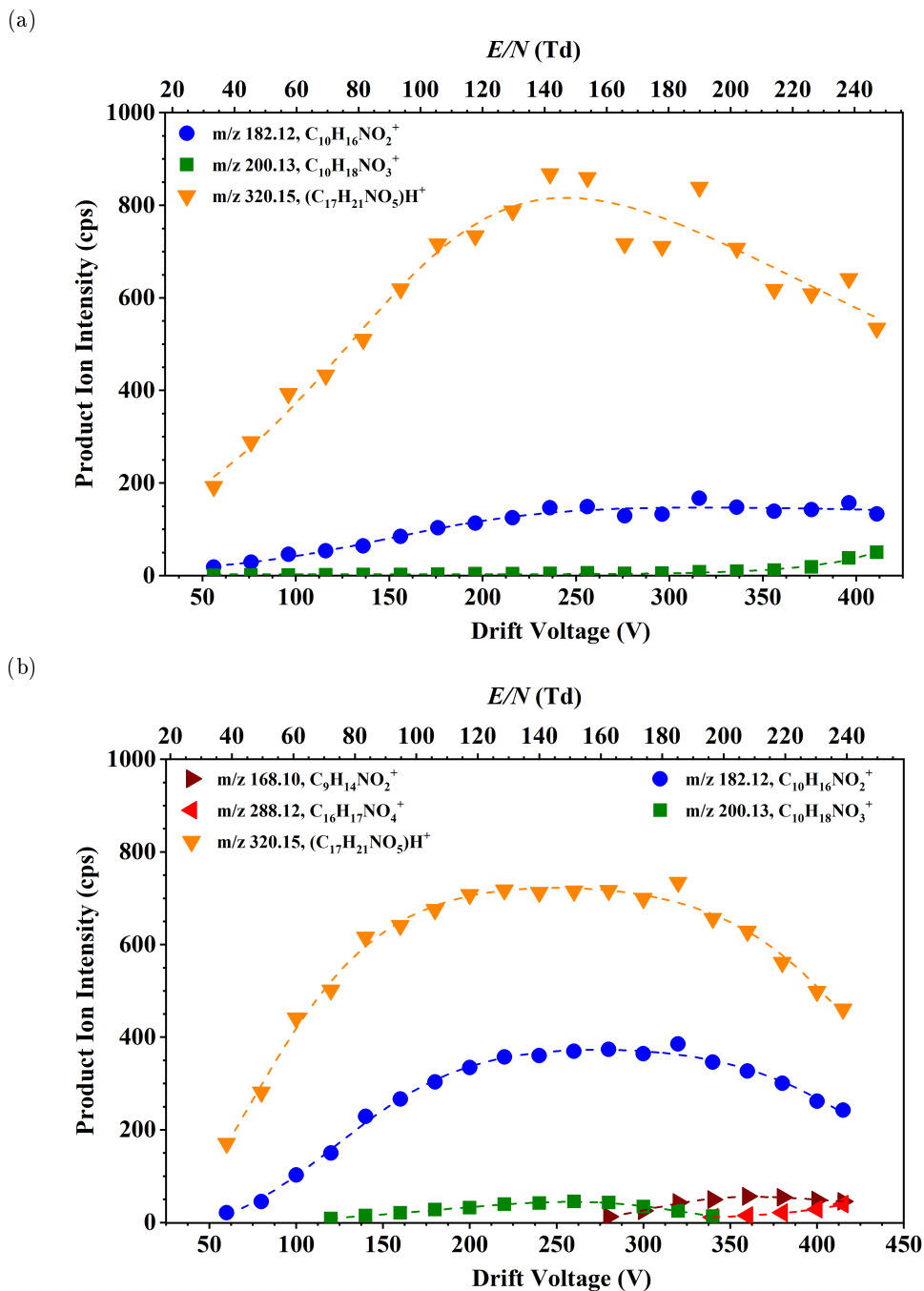


Figure 3.22: Product ion signal intensities in counts per second of the product ions resulting from reactions of the $H_3O^+ \cdot (H_2O)_n$ ($n = 0, 1, 2$) with o-hydroxycocaine as a function of the drift voltage and the reduced electric field in (a) normal and (b) humid conditions.

Chapter 4

Enhancement of Compound Selectivity Using a Radio Frequency Ion Funnel Proton Transfer Reaction Mass Spectrometer: Improved Specificity for Explosive Compounds

This chapter is a reformatted copy of my published article (reference [12]):

González-Méndez, R., Watts, P., Olivenza-León, D., Reich, D. F., Mullock, S. J., Corlett, C. A., Cairns, S., Hickey, P., Brookes, M. & Mayhew, C. A. Enhancement of Compound Selectivity Using a Radio Frequency Ion-Funnel Proton Transfer Reaction Mass Spectrometer: Improved Specificity for Explosive Compounds. *Analytical Chemistry* **88**, 10624–10630 (2016).

Declaration of contribution

My contribution to the article of which the present chapter is composed of was in the discussion and writing process of the manuscript.

4.1 Abstract

A key issue with any analytical system based on mass spectrometry with no initial separation of compounds is to have a high level of confidence in chemical assignment. This is particularly true for areas of security, such as airports, and recent terrorist attacks have highlighted the need for reliable analytical instrumentation. Proton transfer reaction mass spectrometry is a useful technology for these purposes because the chances of false positives are small owing to the use of a mass spectrometric analysis. However, the detection of an ion at a given m/z for an explosive does not guarantee that that explosive is present. There is still some ambiguity associated with any chemical assignment owing to the presence of isobaric compounds and, depending on mass resolution, ions with the same nominal m/z . In this article we describe how for the first time the use of a radio frequency ion-funnel (RFIF) in the reaction region (drift tube) of a proton transfer reaction – time-of-flight – mass spectrometer (PTR-ToF-MS) can be used to enhance specificity by manipulating the ion-molecule chemistry through collisional induced processes. Results for trinitrotoluene, dinitrotoluenes, and nitrotoluenes are presented to demonstrate the advantages of this new RFIF-PTR-ToF-MS for analytical chemical purposes.

Keywords: Ion-Funnel; PTR-MS; Explosives; proton transfer reactions; reduced electric field; collisional induced dissociation.

4.2 Introduction

Ion funnels (IF) have been used since the late 1990s in conjunction with several ionisation and mass spectrometric techniques with a key purpose of increasing ion transmission efficiency and hence instrumental sensitivity and dynamic range [59, 60]. Of relevance to our study, Schaffer et al. developed a radio-frequency (RF) IF for focusing and transmitting ions from relatively high pressure (> 1 Torr) ion sources to mass spectrometers [59]. Given that the typical operating pressure of a drift tube used in proton transfer reaction mass spectrometry (PTR- MS) is close to the optimum pressure for the operation of a RFIF, Kore Technology Ltd. designed and developed a RFIF to be incorporated into drift tubes in order to increase the instruments sensitivity [11]. This compact drift tube can simultaneously operate as an ion funnel and a reaction region with a controllable reaction time (dependent on the voltage supplied across the tube). The funnel design and the supplied RF and DC fields act in such a way to channel reagent and product

ions towards the exit orifice of the drift tube so that more ions leave the reaction region into the much lower pressure mass spectrometric region, thereby decreasing the loss of ions that occurs at the end of the drift tube. The proof-of principle study reported increases in sensitivity of this RFIF-PTR-ToF-MS system that were found to be dependent on the m/z of the product ions, but were typically between 1 and 2 orders of magnitude. For example enhancement factors of 45 and 200 were reported for protonated acetaldehyde and protonated acetone, respectively, at a reduced electric field of 120 Td (where this field refers to the DC voltage applied across the drift tube) [11].

Given that the RFIF forms part of the drift tube, we asked the question whether the high RF fields involved in the operation of an IF could be used to enhance collisions of the reagent and product ions with the buffer gas in the DT and hence change either the nature of the initial chemical ionisation process or induce collisional induced dissociation, respectively, occurring within the DT? We hypothesised that changes would result from raising the internal energy of the product ions and the energy of the reactions between reagent ions and neutral species through collisional processes as a result of the applied RF field. The real question is whether the RF collisional induced dissociation would lead to substantial fragmentation, or be more selective resulting in unique product ions that can be used to identify a chemical compound of interest with a higher specificity than that achievable just by using a standard drift tube at a given reduced electric field. Here we report details on a collaborative project involving KORE Technology Ltd. and the University of Birmingham which investigated the application of a RFIF drift tube of a PTR-ToF-MS for improved selectivity using several explosives as illustrative compounds, namely 2,4,6-trinitrotoluene (TNT), 2,4-, 2,6- and 3,4- dinitrotoluene (DNT) and 2-, 3- and 4-nitrotoluene (NT). We will show how the application of a RFIF leads to a higher confidence in compound identification. We thus demonstrate for the first time that the addition of a RFIF to a PTR-ToF-MS results in a more multi- dimensional analytical instrument that improves the selectivity that can be achieved by operating a drift tube of a PTR-MS in DC mode only.

4.3 Methodology

4.3.1 Experimental details

A KORE Technology Ltd. RFIF Series I PTR-ToF-MS was used. Details of KORE's PTR-ToF-MS system with no IF has been described in detail elsewhere [16, 61, 62], and hence only the salient points of this instrument are provided here. Using a needle valve, water vapour is introduced into a hollow cathode discharge where, after ionisation via electron impact and subsequent ion-molecule processes, the terminal reagent ion is H_3O^+ [6]. These ions are transferred from the ion source into the drift tube (the reaction region) of the PTR-ToF-MS, which is typically at a pressure of 1 mbar and temperature 100 °C, where they encounter the analyte. H_3O^+ ions react with the analyte M by donating their protons at the collisional rate, providing M has a proton affinity greater than that of water ($\text{PA}(\text{H}_2\text{O}) = 691 \text{ kJ mol}^{-1}$). This process can be non-dissociative (resulting in the protonated molecule MH^+) and/or dissociative. Dissociative proton transfer results in product ions which may be useful in the identification of a compound. Fragmentation may be spontaneous upon proton transfer or may require additional energy which is supplied through collisions with the buffer gas resulting during the migration of ions under the influence of the electric field, E. The ratio of E to the buffer gas number density, N, is an important parameter (known as reduced electric field) which determines the mean collisional energy of ions with the neutral buffer gas. Hence it is the parameter often referred to and changed for investigating product ion branching ratios [18, 26, 63–68].

The IF (schematically shown in Figure 2.4) consists of 29 stainless steel plates of 0.2 mm thickness, mounted on precision-machined ceramic rods at an even spacing of 3.2 mm per plate. Tabs on the electrodes permit a resistor chain on a ceramic strip to be connected in addition to two capacitor stacks which allow the RF to be applied to the second half of the reactor. The orifice diameters of the plates through the first half of the stack is 40 mm, as used in the standard drift tube reactor. In the second half of the drift tube the orifice diameter steadily decreases to 6 mm at the final plate before the exit orifice. Across the complete ion-funnel a DC voltage is applied driving ions axially. When just operating with this voltage we shall refer to the instrument as operating in DC-only mode. In addition to this, to the second part of the drift tube a RF field can be applied. The resonant frequency of the system is $\sim 760 \text{ kHz}$ and the amplitude selected for the majority of the studies (peak-to-peak) was 200 V, which is

superimposed on the dc voltage gradient across the drift tube.

The main purpose of the RF field is to focus ions radially by creating repulsive effective potentials at the edges of the electrodes. However, in addition to this intended purpose, the RF results in ions oscillating between electrodes as they drift down the reactor. This gives ions higher collisional energies than those in the first half of the drift tube. We shall refer to operating the instrument with the RF on as RF-mode. At the end of the drift tube is a 400 μm orifice, through which ions enter the ion transfer region for ToF-MS.

The use of specifying a reduced electric field, E/N , is an appropriate parameter to use in DC-only mode, because it is well defined. In RF-mode (ion funnel on) the presence of DC and RF electric fields complicates the situation, because the electric field strength varies with distance from the RF electrodes, so that specifying a reduced electric field is not appropriate. Barber *et al.* simply adopted an empirical effective reduced electric field by finding operating conditions for the ion-funnel drift tube that matched the performance of the same drift tube when operated under DC-only mode [11]. However, given that it is uncertain what the effective reduced electric field means, in this paper we refer to the DC voltage (V_{drift}) applied across the drift tube.

A thermal desorption unit (TDU) connected to the inlet of the drift tube was used to introduce the explosive samples, details of which have been given elsewhere [16]. The TDU, connecting lines and drift tube were operated at a temperature of 150°C. PTFE swabs (ThermoFisher Scientific) onto which known quantities of explosives were deposited were placed into the TDU. The swabs came prepared from the manufacturer mounted on rectangular cardboard for easy insertion into the TDU. Once a seal was created, a carrier gas (in this study laboratory air) is heated to the temperature of the TDU before it flows through a series of holes in a heated metal plate. This heated air then passes through the swab and into the inlet system driving any desorbed material through to the drift tube creating a temporal concentration “pulse” of typically between 10 – 20 seconds of an explosive in the drift tube [16]. Each swab provided one measurement, which was replicated three times and then the results were averaged and any background signals were subtracted.

Explosive standards were purchased from AccuStandard Inc., New Haven, CT. Typically these standards contained 0.1 mg of the explosive compound in 1 ml of solvent. For TNT, 2,4- and 2,6-DNT, and the NTs this involved an acetonitrile:methanol (1:1) mix. 3,4- DNT was just mixed with methanol. These samples were diluted in the appropriate solvent(s) (HPLC grade) to

provide the required quantity of an explosive. Typically 1 μ l of a solvent containing the required mass of an explosive was spotted onto a PTFE swab.

4.3.2 Electronic structure calculations

To aid in the interpretation of the experimental results a series of electronic structure calculations have been undertaken at 298 K. These involve density functional theory calculations using the GAUSSIAN09 PROGRAM with the GaussView 5 interface [40]. The B3LYP functional with the 6-31+G(d,p) basis set was used throughout. Although it is appreciated that the drift tube temperature and the effective ion temperature are greater than 298 K, with the effective ion temperature being uncertain, the thermochemical calculations simply provide us with an indicator as to whether a reaction pathway is energetically possible or not.

4.4 Results and discussion

4.4.1 Reagent ions

Before we begin discussing the results of the explosives, it is informative to present details on the reagent ion signal as a function of drift tube voltage, comparing intensities for DC-only mode (Figure 4.1(a)) and RF-mode (funnel-on) (Figure 4.1(b)) under identical operating conditions of hollow cathode and drift tube pressures and temperature. The observed decrease of H_3O^+ reagent ion signal with decreasing drift tube voltage is predominantly a result of the clustering with water molecules in the drift tube, which are not broken-up through collisions at lower drift tube voltages. The marked decrease in total reagent ion signal below about 50 Td is considered to be a result of the low SD potential, which scales with the DC drift tube potential. As the SD voltage decreases we can expect that fewer reagent ions reach the reactor entry.

Figure 4.1(a) shows that by 100 Td the H_3O^+ reagent ion signal has reduced significantly and that the protonated water clusters start to dominate at the lowest reduced electric field corresponding to a voltage drop across the drift tube of about 200 V under the operational temperature and pressure values used. (The actual percentage of protonated water clusters for fixed E/N is also strongly dependent on the humidity of the buffer gas in the drift tube, which is dependent on the amount of forward flow of H_2O from the ion source into the drift tube and the humidity of the laboratory air.) In RF-mode no protonated water clusters are observed,

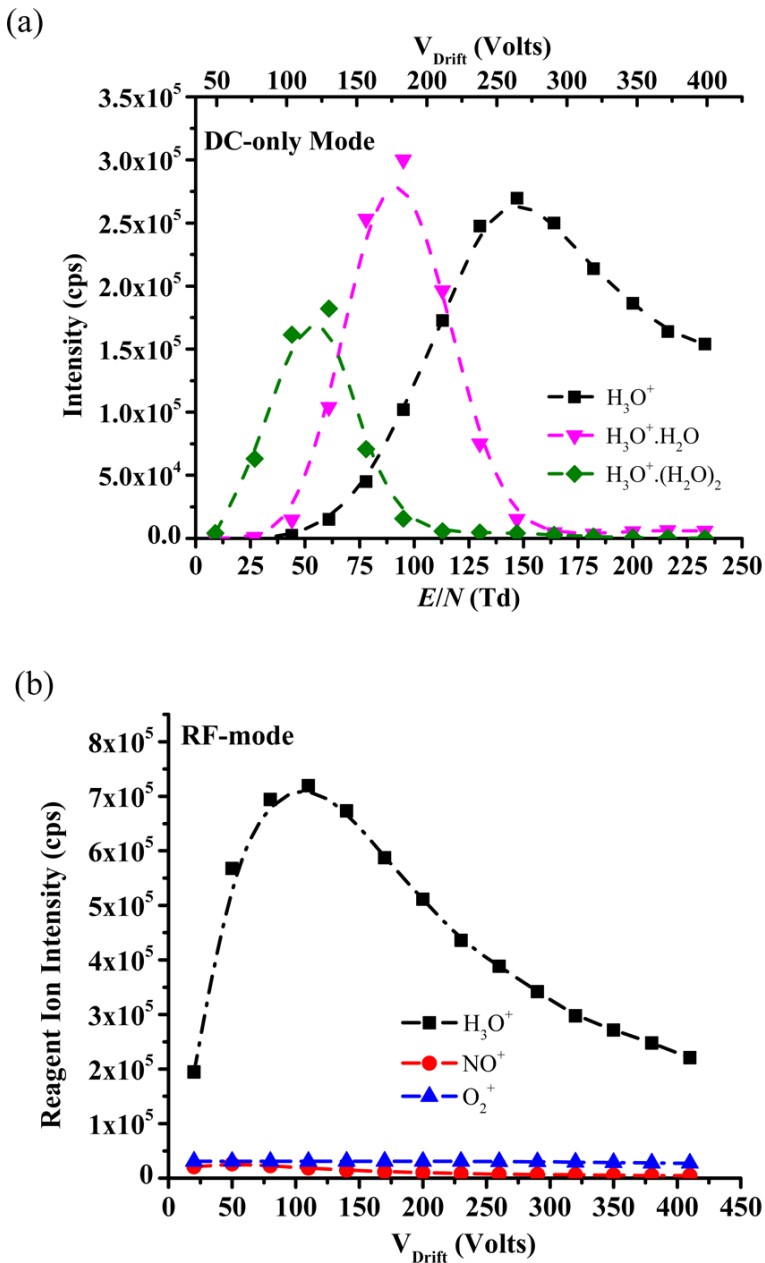


Figure 4.1: Ion intensities in counts per second (cps) of the water reagent ions present in the drift tube as a function of drift tube voltage (a) in DC-only mode and (b) in RF-mode (ion funnel on). For (b) the ion signals at m/z 30 (NO^+) and 32 (O_2^+) are presented because although low intensity they are still significant and are observed as a result of the improved ion transmission in RF-mode. In DC-mode the signal intensities of these ions are negligible and are therefore not presented.

because they are broken-up through collisions in the RFIF region of the drift tube. Furthermore, at about 120 V the H_3O^+ intensity is approximately at its maximum value. As the drift voltage decreases, the reagent ion signal decreases. However, even at a drift tube voltage of only 20 V (which in DC-only mode would correspond to a reduced electric field of only about 10 Td) there is still a significant reagent ion count. This enhancement of reagent ion signal at low drift tube voltages can only be a result of the trapping that the RF field provides thereby reducing the diffusional loss that occurs in DC-only mode under low drift tube voltages.

4.4.2 This is mine – Reagent ion in DC mode and RF mode

As stated before, proton donation to the targeted analyte comes from the collisions with the reagent ions, so it is crucial to monitor their signal to know the amount of available protons to be transferred to the analyte.

The signal of the hydronium and its clusters as a function of the drift tube voltage in both DC mode and RF mode is shown in figure..... These agree with the reagent ion signals previously observed [56]. The ^{18}O isotope peak is used to calculate the intensity of the reagent ions when their ^{16}O peak is saturated. The natural composition of oxygen is ^{16}O (99.76%), ^{17}O (0.03%) and ^{18}O (0.21%) [36].

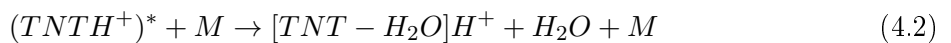
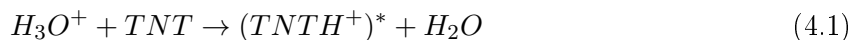
The reagent ions' dependence with the voltage in DC mode is very different to that in RF mode. In DC mode the clusters break apart as the drift voltage increases. On the other hand, the RF field in RF mode delivers an extra collisional energy that breaks the clusters apart independently of the drift voltage. Also, this RF field can create potential wells for the lighter masses generating a low-mass cut-off of the transmission [69]. It is also key to properly tune the capacitance from plate 29 to avoid “closing” the funnel.

The measured reagent ion signal depends on the clustering/declustering reactions and the transmission of the instrument. Furthermore, clustering depends on humidity, collisional energy (E/N) and drift time. The higher the pressure in the cathode, the more hydronium is produced but it also will tend to create hydrogen bonds with other ions. Moreover, the higher the collisional energy, the more collisions the clusters will undergo, making them dissociate eventually. And last, the longer the drift time (at a given collisional energy), the more time the ions have to break apart through collisions.

4.4.3 2,4,6-trinitrotoluene (TNT)

Using both PTR-ToF-MS and PTR-Quad-MS systems Sulzer et al. have previously shown that there is an unusual dependence of the intensity of protonated TNT on the reduced electric field in that there is an increase in the sensitivity of detection with increasing E/N [64, 70]. This increase continues until a maximum is reached at about 180 Td, after which the signal intensity shows the more usual behaviour of decreasing with increasing E/N . This is opposite to what is commonly found in PTR-MS studies, because with reduced reaction times, fragmentation to non-specific product ions, and reduction in ion transmission the protonated molecule intensity reduces with increasing E/N . The explanation of this unusual intensity dependence for TNTH^+ has been described in detail [64]. In brief, it is a result of a secondary reaction of $\text{TNTH}^+\cdot\text{H}_2\text{O}$ (which is readily formed at low E/N) with H_2O leading to a terminal ion which does not contain TNT, namely $\text{H}_3\text{O}^+\cdot\text{H}_2\text{O}$.

In DC-only mode and when a product ion signal is detected, for all E/N values investigated only one product ion is observed that contains the explosive, namely protonated TNT at m/z 228. However, in RF mode, another fragment ion is found at m/z 210, the intensity of which increases with decreasing drift tube voltage (i.e. decreasing E/N in DC mode) down to values under which the PTR-ToF-MS does not perform in DC mode owing to a lack of sufficient transmission of ions to the mass spectrometer (Figure 4.1(a)). Typical results obtained for TNT are shown in Figure 4.2. That the fragment ion m/z 210 intensity increases with decreasing drift tube voltage (Figure 4.2) is perhaps not what is expected given that decreasing DC voltage means lower collisional energies. However, that only applies in the first half of the drift tube. As the drift tube voltage is reduced more collisions in the RFIF region of the drift tube occur, which in turn enhances collisional induced dissociation. Following proton transfer the protonated molecule gains sufficient internal energy through collisions in the RFIF section of the drift tube to eliminate H_2O :



where M is a buffer gas molecule. Thus specificity can be increased by either switching off and on the RFIF at a specific drift tube voltage or by switching the drift tube voltage. Note that a

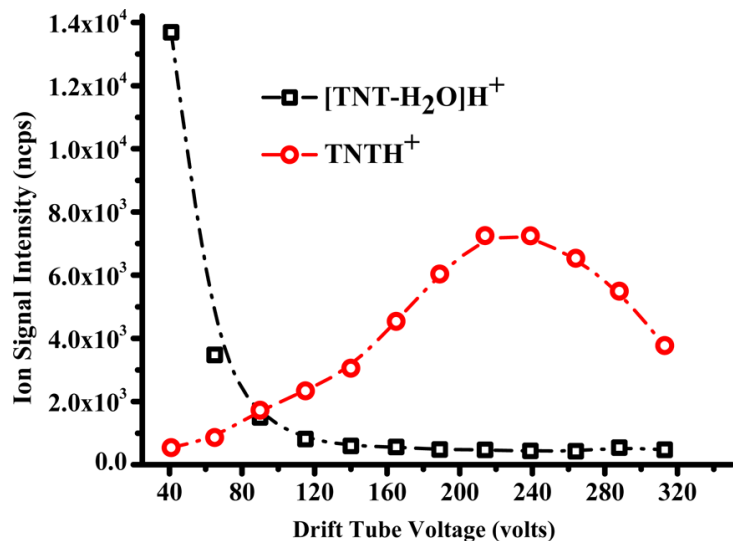


Figure 4.2: Product ion intensities as a function of drift tube voltage in RF mode. The data have been taken using 100 ng of TNT. The ion signals have been normalized to $10^6 \text{ H}_3\text{O}^+$ reagent ions and drift times. (The lines used in all graphs are just a guide to the eye.)

Table 4.1: Energetics for the proton transfer from H_3O^+ to TNT calculated using the B3LYP functional and the 6-31+G(d,p) basis set.

Products	ΔH_{298} (kJ/mol)	ΔG_{298} (kJ/mol)
TNTH ⁺ (2NO ₂ syn) + H ₂ O	-46	-47
TNTH ⁺ (2NO ₂ anti) + H ₂ O	-55	-55
TNTH ⁺ (4NO ₂) + H ₂ O	-68	-60
TS syn/anti + H ₂ O	-9	-5

minor percentage of the observed m/z 210 results from the reaction of the O_2^+ (always present in low concentrations in the drift tube as an impurity ion) with TNT via a dissociative charge transfer process leading to the loss of OH from TNT^+ [66].

That the reaction pathway leading to the elimination of H₂O is overall energetically favourable (Table 4.1) but is only observed in RF mode, is an indication that there must be an energy barrier for pathway (2). Evidence of this is provided from the results obtained when investigating the effects of changing the RF amplitude at fixed drift tube voltages and fixed frequency. Figure 4.3 provides a summary of these measurements, which shows that as the RF peak-to-peak voltage is decreased the intensity of the m/z 210 decreases for all drift tube voltages.

The initial step leading to m/z 228 is the transfer of a proton from H_3O^+ to TNT. Protonation of TNT can occur on the nitro groups at the 2 and 4 positions, both having similar proton

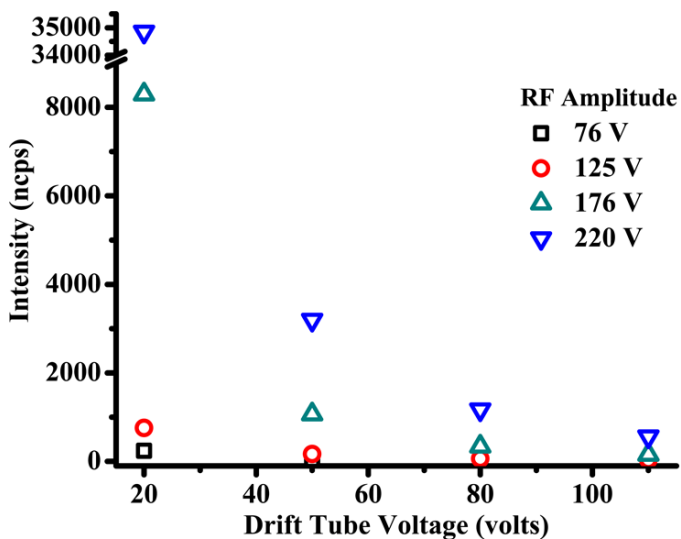


Figure 4.3: Intensities in ncps of the product ion [TNT - H₂O]H⁺ as a function of drift tube voltage and RF amplitude (volts) with the frequency kept at 760 kHz ($\pm 3\%$). slightly

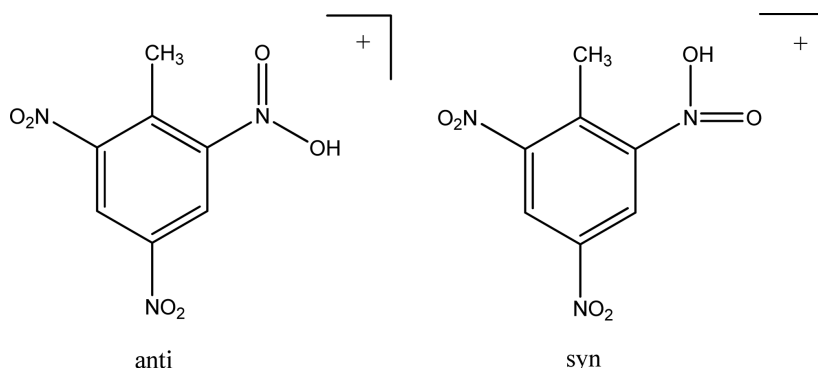
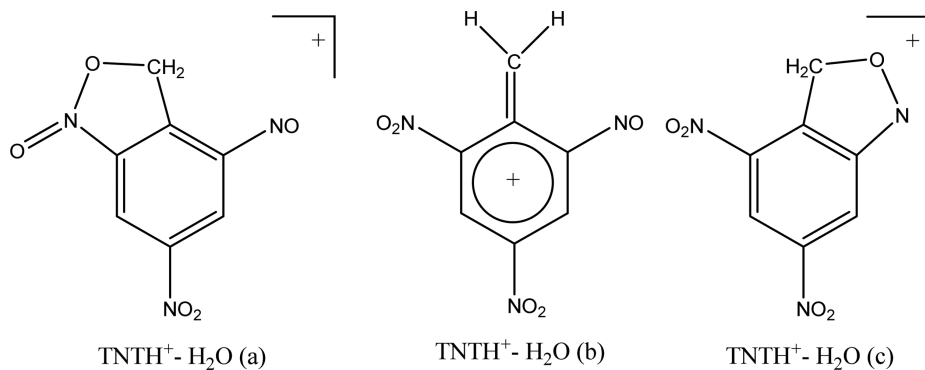


Figure 4.4: Two possible configurations resulting from protonation of TNT in the 2 position.

affinities, although as elimination of water from TNTH⁺ will presumably involve the methyl group only protonation of the nitro group in the 2- position is of relevance. However, protonation on the 4 nitro will occur (the PA and GB are slightly greater than the 2 nitro) and this will reduce the amount of TNTH⁺ available to lose water. Two configurations are possible for protonation in the 2 position as illustrated in Figure 4.4, with the anti being slightly more stable by ca. 8 kJ mol⁻¹. The transition state energetics for interconversion are $\Delta H_{298} +46$ kJ mol⁻¹ and $\Delta G_{298} +51$ kJ mol⁻¹ above the anti conformation, but whichever is formed there is sufficient energy in the initial protonation to allow rapid interconversion (Table 4.1).

There are three stable structures for the ion remaining after the elimination of water from TNTH⁺ (Figure 4.5). A fourth structure, similar to TNTH⁺ - H₂O (b) with the hydrogens of

Figure 4.5: Stable structures of the [TNT - H₂O]H⁺ ion.Table 4.2: Energetics for the elimination of water from TNT following proton transfer from H₃O⁺ for the three stable structures shown in Figure 4.5.

Products	ΔH_{298} (kJ/mol)	ΔG_{298} (kJ/mol)
TNTH ⁺ - H ₂ O (a) + 2H ₂ O	-104	-145
TNTH ⁺ - H ₂ O (b) + 2H ₂ O	+47	-7
TNTH ⁺ - H ₂ O (c) + 2H ₂ O	-128	-168

the methylene group orthogonal to the ring, proved to be unstable and rearranged to TNTH⁺ - H₂O (a). The energetics for the transformation of TNTH⁺ to TNTH⁺ - H₂O (a-c) + H₂O are given in Table 4.2.

Various attempts using the QST3 approach were made to find transition states for these possible reactions but all lead to TNTH⁺ - H₂O (c), though interestingly the transition state had a close resemblance to TNTH⁺ - H₂O (b). The transition state was characterised by one imaginary frequency and the internal reaction coordinate leading to TNTH⁺ - H₂O (c) in the forward direction and TNTH⁺ with the proton on the 2-nitro group in the syn conformation in the reverse direction. The activation energies relative to TNT + H₃O⁺ are $\Delta H_{298} +158$ kJ mol⁻¹ and $\Delta G_{298} +162$ kJ mol⁻¹.

The presumption that the elimination of water from protonated TNT can only occur when the methyl and nitro groups are adjacent to each other was readily tested by investigating isomers of DNT and NT. For those isomers that satisfy the condition of an adjacent nitro and methyl group, then [DNT-H₂O]H⁺ and [NT-H₂O]H⁺ fragment ions should be observed, otherwise not. Thus we predicted to observe elimination of water from the 2,6-DNT, 2,4-DNT and 2-NT but not from 3,4-DNT, 3-NT or 4-NT following proton transfer in RF mode.

4.4.4 Dinitrotoluenes

In both RF-mode and DC-only mode for 3,4-DNT the only primary product ion that is observed with any significant intensity for all drift tube voltages is the protonated molecule. That no m/z 165 is observed, which would correspond to the elimination of water from the protonated molecule, is in agreement with our prediction, because neither nitro group are adjacent to the methyl group. With decreasing drift tube voltage the protonated 3,4-DNT clusters with H_2O , leading to a reduction in the DNTH^+ signal. Whilst this is particularly significant in DC-only mode, with $\text{DNTH}^+ \cdot (\text{H}_2\text{O})_n$ ($n = 1, 2$ and 3) ions becoming the dominant product ions by about 100 Td, some water clustering is still observed in RF-mode. For example at a drift tube voltage of 20 V the percentage branching ratios are approximately 70%, 20% and 10% for DNTH^+ , $\text{DNTH}^+ \cdot \text{H}_2\text{O}$, and $\text{DNTH}^+ \cdot (\text{H}_2\text{O})_2$, respectively.

For the 2,4- and 2,6-DNT isomers, at low drift tube voltages in addition to an observed ion at m/z 201 corresponding to the $\text{DNTH}^+ \cdot \text{H}_2\text{O}$ in RF-mode a product ion is observed at m/z 165, which is $[\text{DNT}-\text{H}_2\text{O}]^+$. Figure 4.6 illustrates this for 2,6-DNT, which shows that the probability for the elimination of water increases with decreasing drift tube voltage (the results for 2,4-DNT in RF-mode are similar, although the production for $[\text{DNT}-\text{H}_2\text{O}]^+$ is less by about 10%). In DC-only mode, m/z 165 is also observed for 2,6-DNT, but its intensity only becomes significant when a high drift tube voltage is applied leading to reduced electric fields above about 180 Td, and even then the percentage ion product distribution is only approximately 10% (Figure 4.7). However, this can explain the slight increase in the production of m/z 165 in Figure 4.6 when the applied drift tube voltage is above about 275 V. With increasing drift tube voltage additional fragment ions are found at m/z 136 and 91, corresponding to an elimination of HONO and 2NO_2 , respectively, from the protonated molecule. These two ions are also found with significant intensities for 2,6-DNT when operating in DC-only mode when the reduced electric fields is greater than about 160 Td. That $\text{DNTH}^+ \cdot \text{H}_2\text{O}$ is observed in RF mode at low drift tube voltages, when no protonated water clusters are observed (Figure 4.1 (b)), requires some explanation. We propose that following a collision the energy involved is distributed in more degrees of freedom for $\text{DNTH}^+ \cdot \text{H}_2\text{O}$ than for $\text{H}_3\text{O}^+ \cdot (\text{H}_2\text{O})_n$ and hence it is less likely for energy to be concentrated into losing the water molecule.

Building on the comprehensive investigation of the TNT system we can go straight to the

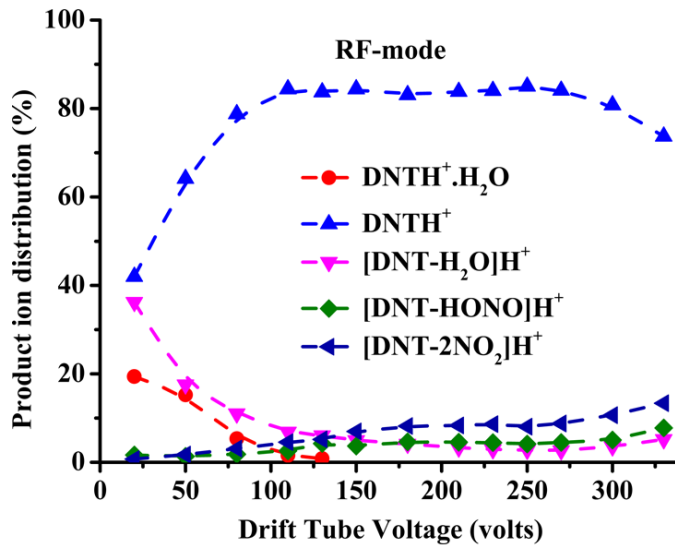


Figure 4.6: Percentage product ion distributions resulting from the reaction of H_3O^+ with 2,6-DNT in RF-mode including the secondary process resulting in the association of the protonated molecule with water as a function of supplied drift tube voltage.

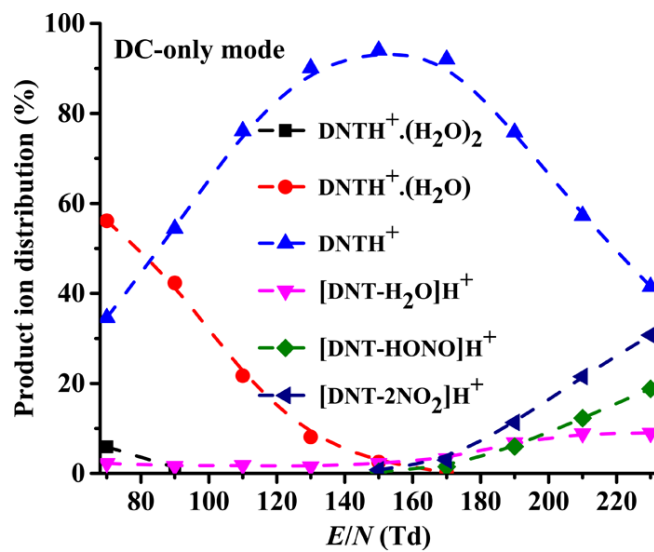


Figure 4.7: Percentage product ion distributions resulting from the reaction of H_3O^+ with 2,6-DNT in DC-only mode including the secondary process resulting in the association of the protonated molecule with water as a function reduced electric field.

Table 4.3: Energetics for the elimination of water from (a) 2,4-DNT and (b) 2,6-DNT following proton transfer from H_3O^+ .

Products	(a)	
	ΔH_{298} (kJ/mol)	ΔG_{298} (kJ/mol)
2,4-DNTH ⁺ (syn) + H ₂ O	-89	-87
2,4-DNTH ⁺ (anti) + H ₂ O	-96	-95
TS syn/anti + H ₂ O	-21	-16
TS for loss of H ₂ O + H ₂ O	+126	+130
2,4-DNT-H ₂ O (c) + 2H ₂ O	-146	-187

Products	(b)	
	ΔH_{298} (kJ/mol)	ΔG_{298} (kJ/mol)
2,6-DNTH ⁺ (syn) + H ₂ O	-87	-88
2,6-DNTH ⁺ (anti) + H ₂ O	-95	-95
TS syn/anti + H ₂ O	-42	-38
TS for loss of H ₂ O + H ₂ O	+117	+120
2,6-DNT-H ₂ O (c) + 2H ₂ O	-177	-217

salient structures and energetics for the loss of water from 2,4-DNT and 2,6-DNT following proton transfer from H_3O^+ . These calculations are given in Table 4.3 (a) and (b), respectively.

4.4.5 Nitrotoluenes

In order to further investigate the requirement of methyl and nitro functional groups to be adjacent in order to facilitate the elimination of water when using the RFIF, the three isomers of nitrotoluene have been investigated. We can expect in RF-mode that only 2-NT should have a reaction pathway which would lead to the elimination of water following proton transfer from H_3O^+ . For 3-NT and 4-NT no such elimination should occur. A review of the resulting mass spectra for all three isomers shows that that is the case. However, the nitrotoluenes are more complicated than TNT and the DNTs, because other product ions are observed even at the lowest drift tube voltage. The NT isomers show significant fragmentation following proton transfer. This is found to occur in not only RF-mode but also DC-only mode. In addition to the elimination of water, which is not the dominant product ion, channels corresponding to the elimination of C₂H₄, NO, CH₃NO, NO₂ and HONO are observed in both modes. This is illustrated in Figure 4.8 for 2-NT when operating (a) in RF- mode and (b) in DC-only mode. At low drift tube voltages NTH⁺.H₂O is observed (Figure 4.8(a)) in RF mode, presumably for reasons described above for DNT.

Table 4.4 presents the DFT energetics calculations for the elimination of water for 2-NT

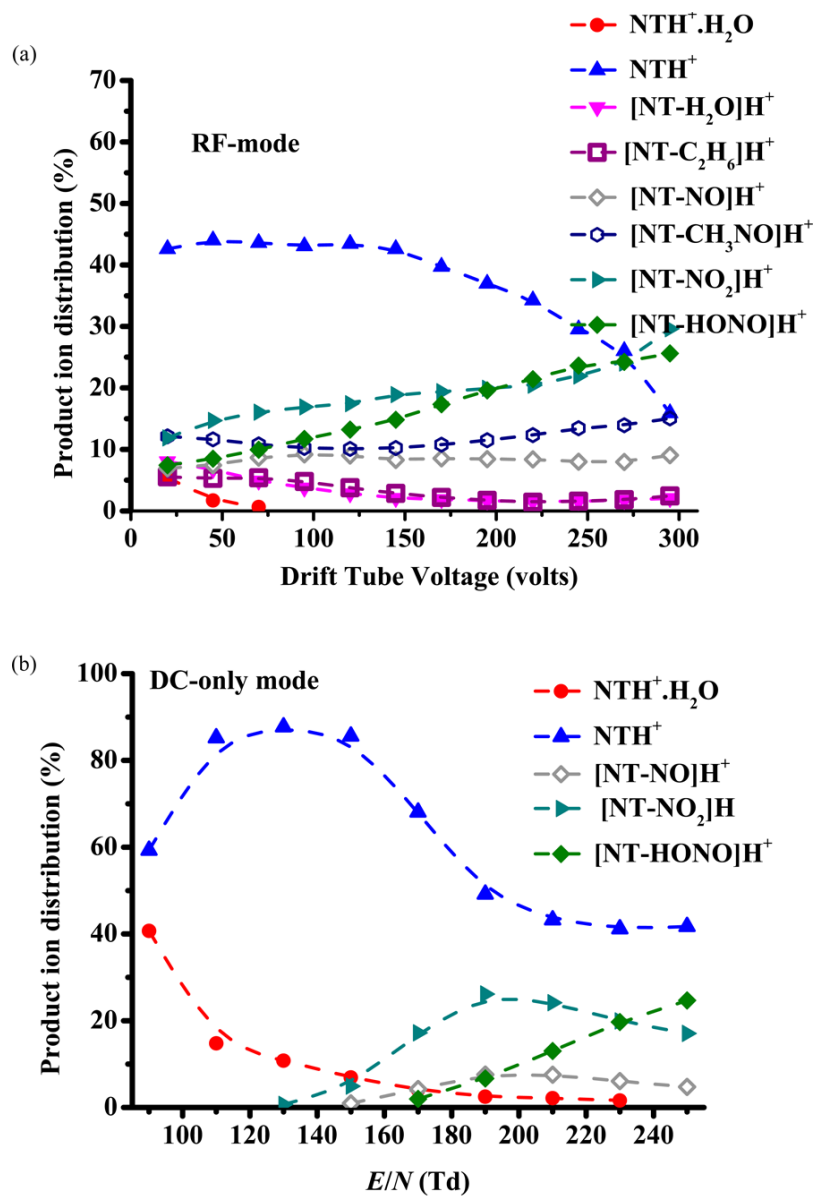


Figure 4.8: Percentage product ion distributions resulting from the reaction of H_3O^+ with 2-NT in (a) RF-mode and (b) DC-only mode as a function drift tube voltage. Included are the secondary ion-molecule processes resulting in the association of the protonated molecule with water.

Table 4.4: Energetics for the elimination of water from 2-NT following proton transfer from



Products	ΔH_{298} (kJ/mol)	ΔG_{298} (kJ/mol)
2-NTH ⁺ (syn) + H ₂ O	-132	-138
2-NTH ⁺ (anti) + H ₂ O	-105	-110
TS syn/anti + H ₂ O	-71	-76
TS for loss of H ₂ O + H ₂ O	+82	+78
2-NT-H ₂ O + 2H ₂ O	-93	-126

following proton transfer from H₃O⁺.

4.5 Conclusions

A PTR-ToF-MS equipped with a radio frequency ion funnel, originally designed to improve sensitivity, has been used in an unusual way to induce fragmentation of product ions through changes in collisional induced dissociation. We have illustrated how this can be used to improve compound specificity by monitoring the ion signal in RF-mode. We propose that the rapid switching between RF and DC modes would be the best method to enhance selectivity. We are currently developing the instrument to achieve this, and this will be the subject of another paper. The key point of this work is that in place of major and costly changes in instrumental design to improve chemical specificity, such as having a high mass resolution time-of-flight mass spectrometer or adding a pre-separation technique, which also makes the instrument unacceptable for use in security areas, a new analytical method has been described which at its heart manipulates the ion chemistry.

Chapter 5

Selective Reagent Ion Mass Spectrometric Investigations of the Nitroanilines

This chapter is a reformatted copy of my published article (reference [71]):

Olivenza-León, D., Mayhew, C. A. & González-Méndez, R. Selective Reagent Ion Mass Spectrometric Investigations of the Nitroanilines. *Journal of the American Society for Mass Spectrometry*, 1–8 (2019).

Declaration of contribution

My contribution to the article of which the present chapter is composed of was performing the experiments, analysing the results and writing the manuscript together with the coauthors. The DFT calculations used to aid in the interpretation of the data were made by Dr Peter Watts (Molecular Physics Research Group, University of Birmingham).

5.1 Abstract

This paper presents an investigation of proton and charge transfer reactions to 2-, 3- and 4-nitroaniline ($C_6H_6N_2O_2$) involving the reagent ions $H_3O^+.(H_2O)_n$ ($n = 0, 1$ and 2) and O_2^+ , respectively, as a function of reduced electric field (60-250 Td), using Selective Reagent Ion – Time-

of-Flight – Mass Spectrometry (SRI-ToF-MS). To aid in the interpretation of the $\text{H}_3\text{O}^+ \cdot (\text{H}_2\text{O})_n$ experimental data, the proton affinities and gas-phase basicities for the three nitroaniline isomers have been determined using density functional theory. These calculations show that proton transfer from both the H_3O^+ and $\text{H}_3\text{O}^+\cdot\text{H}_2\text{O}$ reagent ions to the nitroanilines will be exoergic and hence efficient, with the reactions proceeding at the collisional rate. For proton transfer from H_3O^+ to the NO_2 sites, the exoergicities are 171 kJ mol^{-1} (1.8 eV), 147 kJ mol^{-1} (1.5 eV), and 194 kJ mol^{-1} (2.0 eV) for 2-, 3- and 4-nitroaniline, respectively. Electron transfer from all three of the nitroanilines is also significantly exothermic by approximately 4 eV. Although a substantial transfer of energy occurs during the ion/molecule reactions, the processes are found to predominantly proceed via non-dissociative pathways over a large reduced electric field range. Only at relatively high reduced electric fields ($> 180 \text{ Td}$) is dissociative proton and charge transfer observed. Differences in fragment product ions and their intensities provides a means to distinguish the isomers, with proton transfer distinguishing 2-NA from 3- and 4-NA, and charge transfer distinguishing 4-NA from 2- and 3-NA, thereby providing a means to enhance selectivity using SRI-ToF-MS.

Keywords: Soft Chemical Ionisation-Mass Spectrometry; Proton Transfer Reaction Mass Spectrometry; Nitroanilines; Explosives; Charge transfer.

5.2 Introduction

Selective Reagent Ion Mass Spectrometry (SRI-MS) is a variation of the soft chemical ionisation technique PTR-MS that uses not only H_3O^+ but also other reagent ions, like O_2^+ and NO^+ , that undergo charge transfer with the analyte rather than proton transfer [6]. It has been proved an useful tool in several fields, like the environmental sciences, food sciences, atmospheric chemistry, health science and homeland security [19, 20, 26, 64, 65, 70, 72–76]. Like PTR-MS, SRI-MS is used to investigate ion/molecule reactions occurring inside a drift tube maintained at a known pressure, temperature, humidity and collisional energy. Then analyte molecules of interest are introduced through the inlet pipe (typically without pre-separation) into the drift tube, where they meet the reagent ions, and the proton or charge transfer reaction occurs. The switching between the different reagent ion species can be done quick enough ($\sim 100 \text{ ms}$), which makes SRI-MS a suitable tool for transient experiments.

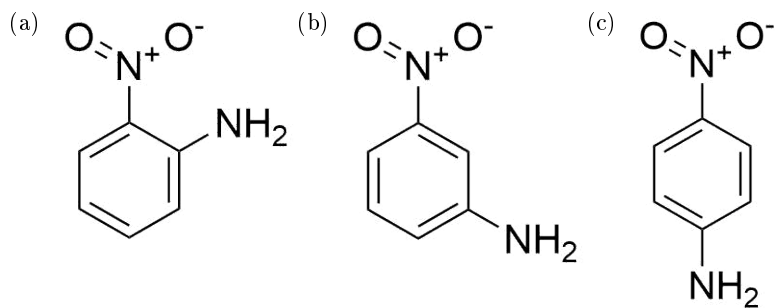


Figure 5.1: Structure of (a) 2-nitroaniline, (b) 3-nitroaniline and (c) 4-nitroaniline.

Over the last few years, many projects have been conducted to confirm the applicability of SRI-MS to Homeland Security [12, 13, 16, 64–67, 70, 77–81]. The main achieved goals are the development of instrumentation and the improvement of our understanding of the ion/molecule reactions happening in the drift tube. The former includes the use of different reagent ions [17], new sampling methods [16], implementation of radio frequency ion funnels [11, 12] and rapid electric field switching [13]. One of the drawbacks of SRI-MS is that it is not possible to directly distinguish between isomeric compounds, although there are exceptions [52]. Here we present a study of the reactions of three nitroaniline (NA) isomers with both O_2^+ and H_3O^+ as a function of the reduced electric field. The main goal is to determine if they can be distinguished without initial pre-separation by solely enhancing the ion/molecule reactions using different reagent ions.

The structures of 2-, 3- and 4-nitroaniline are shown in Figure 5.1. Nitroanilines ($\text{C}_6\text{H}_6\text{N}_2\text{O}_2$) are chemical compounds that are a derivative of aniline, a known reactant in the polymer industry, and are present in the fabrication of dyes, pesticides and pharmaceuticals products [82, 83]. Therefore, they are widespread in the environment. Also, their aromatic ring and nitro functional group makes them show explosive behaviour and hence this study represents a continuation of PTR-MS studies in the same topic [12, 13, 16, 64–67, 70, 78–81]. Furthermore, nitroanilines (specially the 4- isomer) are toxic compounds [84]. It is then key to have the analytical tools to rapidly and accurately detect and analyse them.

In the present study, the product ion distributions as a function of the reduced electric field obtained from the reactions of 2-, 3- and 4-nitroaniline with H_3O^+ and O_2^+ are presented, the role of the nitro group in these reactions is evaluated, and quantum chemical calculations are used to obtain the proton affinity and gas phase basicities, complementing the experimental work.

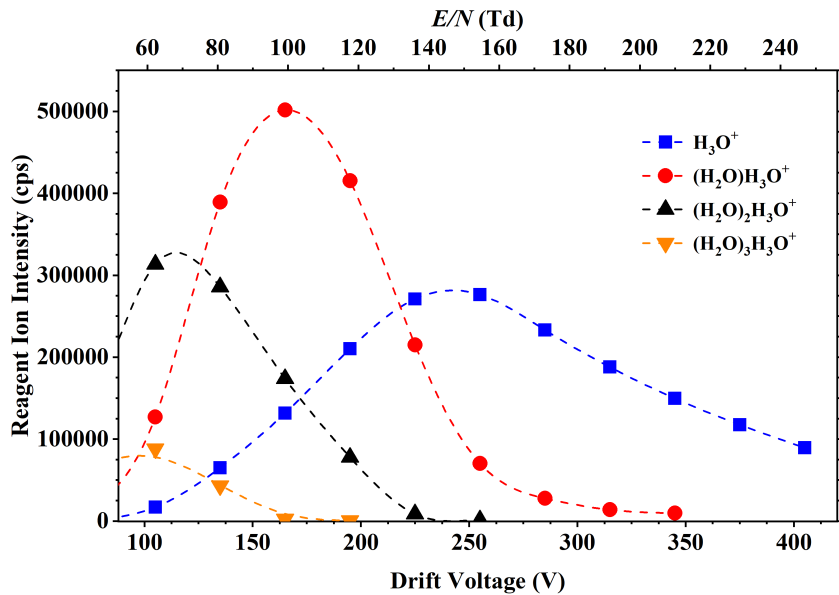


Figure 5.2: Ion intensities in counts per second of the water reagent ions ($H_3O^+ \cdot (H_2O)_n$, n = 0, 1, 2 and 3) recorded at the detector of the KORE SRI-ToF-MS as a function of reduced electric field (approximately 60–250 Td).

5.3 Experimental details

5.3.1 Selective Reagent Ion-Mass Spectrometry (SRI-MS)

The SRI-MS instrument used was a KORE Technology Ltd PTR-ToF-MS, and the different reagent ions were generated injecting different gases into its ion source. This device has been described in detail elsewhere [6, 12], so only a shallow overview will be given here.

5.3.1.1 Proton Transfer Reaction Mode

This mode has been described in chapter 2 and corresponds to the regular use of the instrument, where H_3O^+ (and the relevant water cluster ions) react with the analyte through the reactions described in Equation 1.1 and Equation 1.2. It is important to note, however, that, although proton transfer can be spontaneously dissociative, the energy available upon proton transfer from a protonated water cluster is much less than that compared to proton transfer from hydronium. Nevertheless, the reduced electric field in the reactor can trigger collisional induced dissociation when the proton transfer process has been non-dissociative, enhancing fragmentation of the protonated molecule.

The reagent ions for proton transfer mode were produced through the injection of water into the hollow cathode. These are then transferred into the drift tube. Figure 5.2 presents the reagent ion intensities (in counts per second) at the end of the drift tube as a function of the E/N and it shows that $\text{H}_3\text{O}^+(\text{H}_2\text{O})_n$ for $n = 0, 1$ and 2 are the most abundant water clusters, although the one with $n = 3$ is also noticeable at low E/N . Only at E/N values of 130 Td or more H_3O^+ becomes the dominant ion. Other impurity or contamination ions can sometimes be observed in the mass spectra, resulting from the back streaming of the analyte-containing buffer gas into the hollow cathode. The most usual impurity ions are NO^+ and O_2^+ , which, in this case, represented less than 0.5% of the total reagent ion signal for any reduced electric field. Also, the signal corresponding to hydronium and the water cluster ions is usually saturated and the intensity at the ^{18}O isotope was used in each case to calculate the signal of the relevant reagent ion.

5.3.1.2 Charge Transfer Reaction Mode

O_2^+ was generated injecting pure oxygen (99.998% purity, BOC Gases, Manchester, UK) into the hollow cathode. The O_2^+ ion signal as a function of the reduced electric field is displayed in Figure 5.3. Similarly to the reagent ion in the proton transfer mode, the O_2^+ signal is too large to be directly measured and the $^{18}\text{O}^{16}\text{O}^+$ isotope at m/z 34 can be used to calculate it. When O_2^+ encounters the analyte in the drift tube, charge transfer occurs if the analyte's ionisation energy (IE) is less than 12.07 eV. However, and contrary to what happens in proton transfer, even if the analyte has an ionisation energy of less than 12.07 eV, the reaction may not be occurring at the collisional rate [85]. Like in proton transfer, charge transfer can be either non-dissociative, yielding the M^+ ion, or dissociative, and fragmentation can be enhanced upon collisionally-induced processes. Regarding contamination and unwanted ions, hydronium can be formed in the ion source if there is residual water vapour but in these experiments it was only ca. 0.1% of the O_2^+ signal.

5.3.2 Chemicals

The samples in this investigation were acquired from Sigma Aldrich (Cheshire, UK). Each of the three nitroaniline isomers (yellow granulated solids, >98% purity) came in an individual container. Each of these substances were then used to create a solution of approximately 100

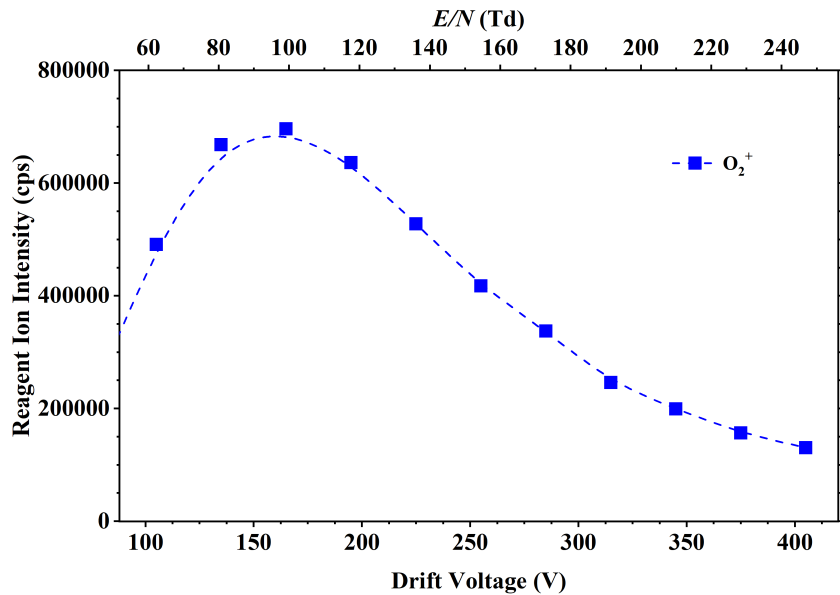


Figure 5.3: Ion intensities in counts per second of O_2^+ recorded at the detector of the KORE SRI-ToF-MS as a function of reduced electric field (approximately 60–250 Td).

$\mu\text{g}/\text{mL}$ of concentration in a mixture of methanol and acetonitrile (analytical grade). 1 μL of this diluted sample was placed on a swab, waiting one minute for the solvent to evaporate before inserting it into the TDU. The vapour pressure of 2-, 3- and 4- nitroaniline is 3.7×10^{-3} , 1.3×10^{-4} , and 4.3×10^{-6} mbar, respectively [86–88].

5.3.3 Operational procedures

The thermal desorption unit, described in subsection 2.3.1 and also elsewhere [16], was used in this study to get the nitroanilines solution into gas phase. Said TDU was connected to the inlet line through passivated Silconert® stainless steel and the carrier gas flowing through the TDU was oxygen-free nitrogen (99.998% purity, BOC Gases, Manchester, UK). Three measurements were acquired for each E/N value, which were then averaged and got the background subtracted. The reactor, inlet line and thermal desorption unit were kept at 150°C. The drift tube was at 1 mbar and the ion source at 1.4 mbar when generating both H_3O^+ and O_2^+ . The reduced electric field was manipulated only by adjusting the drift voltage in the reactor in the range from approximately 100 to 400 V, which corresponds to a E/N range from approximately 60 to 250 Td.

5.3.4 Density Functional Theory Calculations

The proton affinities and gas-phase basicities of the three nitroaniline isomers and the water monomer, dimer and trimer were computed through DFT calculations using Gaussian09W and GaussView05 for Windows by Dr Peter Watts [40]. The functional and the basis set used for this calculations were the B3LYP and 6-31+G(d,p), respectively, which have proved adequate in past studies [3, 89].

5.4 Results

In this section the experimental and DFT results are presented. The experimental work consists on the product ion distributions (PID) resulting from the reaction of each nitroaniline isomer with the proper reagent ion as a function of the reduced electric field (top x-axis) and the drift voltage (bottom x-axis). All the isotopologues were taken into account when calculating the product ion distributions, although only the lightest one is given. The uncertainty has been estimated to be around 10% for any of the percentages provided here.

5.4.1 DFT Results

The proton affinity and gas-phase basicity for the nitroaniline isomers and the water monomer, dimer and trimer are shown in Table 5.1, which also includes the ionisation energies of O₂ and the nitroanilines [90]. Furthermore, Table 5.1 also contains the calculations for the change in the enthalpy, ΔH_{298} , and Gibbs free energy, ΔG_{298} , for the addition of H₂O to the already protonated nitroaniline molecule. The calculated thermochemical data related to the proton transfer case (i.e. PA, GB, ΔH_{298} and ΔG_{298}) is given independently for the amino and nitro groups for comparison. These quantities were also calculated for the aniline and nitrobenzene molecules.

It is interesting to note that the PA and GB of the amine group in the aniline molecule are higher than those of the nitro group in nitrobenzene, but when both functional groups are present in the same molecule (i.e. for the three nitroaniline isomers), the values of PA and GB of the amine and nitro groups are reversed. This is caused by the NH₂ group donating electrons to the benzene ring and the NO₂ group pulling electrons from said ring. The calculated basicities show that all three nitroanilines can undergo proton transfer from H₃O⁺ and H₃O⁺·(H₂O), and that

Table 5.1: Proton affinities, gas phase basicities and ionisation energies for nitroaniline isomers. The PA and GB values have been calculated using the B3LYP functional and the 6-31+G(d,p) basis set at 298 K. ΔH_{298} and ΔG_{298} refer to the enthalpies and free energies for the addition of water to the protonated species. For convenience the ionisation energies of O₂ and the three nitroanilines are also provided.

Chemical	Site	PA*	GB*	ΔH_{298}^*	ΔG_{298}^*	IE†
Water		684	653			
Water dimer		842	777			
Water trimer		937	841			
O ₂					12.07 [91]	
2-NA	NH ₂	840	806	-69	-37	8.27
	NO ₂	858	824	-76	-43	
3-NA	NH ₂	824	796	-78	-43	8.31
	NO ₂	830	800	-84	-51	
4-NA	NH ₂	810	784	-78	-43	8.34
	NO ₂	879	847	-73	-39	
Aniline	NH ₂	874	846	-72	-40	
Nitrobenzene	NO ₂	806	775	-90	-55	

*Thermochemical data expressed in kJ/mol. †Ionisation energies (in eV) have been taken from NIST database [90].

4-nitroaniline can also do it from H₃O⁺.(H₂O)₂ to its nitro group. As proton transfer to both groups of the nitroanilines is exoergic, NA.H⁺ is thought to be a mixture of parent molecules protonated at the NH₂ and the NO₂ sites. However, as in 2-nitroaniline the two functional groups are very close, there the proton sits bonded to both functional groups.

5.4.2 Fragmentation patterns and branching ratios studies in proton transfer mode

5.4.2.1 2-nitroaniline

The product ion distributions for the reaction of 2-nitroaniline with H₃O⁺ and H₃O⁺.(H₂O) from 60 to 250 Td is shown in Figure 5.4. The most abundant ion from 60 to ca. 230 Td is the protonated parent molecule 2-NA.H⁺ at *m/z* 139.05. The ion coming from the association of the protonated parent with a water molecule (i.e. 2-NAH⁺.H₂O at *m/z* 157.06) is present at low *E/N*, and it decreases with the increasing *E/N*, with a maximum contribution to the total ion signal of ~15% at 60 Td. Additionally, further product ions are observed at high reduced electric

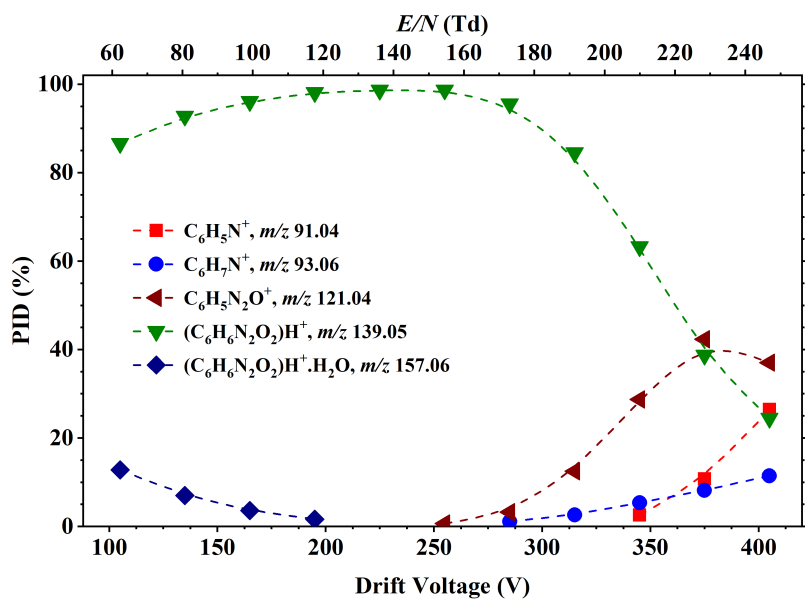


Figure 5.4: Percentage product ion distribution (PID in %) resulting from the reaction of 2-nitroaniline with $H_3O^+.(H_2O)_n$ ($n = 0$ and 1) as a function of the reduced electric field from 60 to 250 Td.

fields. $C_6H_5N_2O^+$ at m/z 121.04, which comes from the loss of water from the protonated parent, appears at 150 Td and becomes dominant at approximately 230 Td. Likewise, $C_6H_7N^+$ at m/z 93.06 and $C_6H_5N^+$ m/z 91.04 are also observed at high E/N . The former results from the loss of a nitro group from 2-NA. H^+ , while the latter comes from the loss of a hydrogen molecule after a loss of a nitro group from the protonated parent.

The mass spectra shown in Figure 5.5 are included as illustrative examples of the data acquired when performing these experiments. These two different data sets relate to measurements of 2-nitroaniline with different E/N values in the drift tube, while the rest of variables were kept constant. Comparable mass spectra were found with the rest of compounds in both proton transfer and charge transfer modes, but these are not included as those results are summarised in the PID plots, which include the product ions with a branching percentage higher than >1% for any E/N .

5.4.2.2 3-nitroaniline

The PID plot for the reaction of the 3- isomer with H_3O^+ and $H_3O^+.(H_2O)$ (Figure 5.6) shows that, like in the 2-NA case, the most abundant ion is the protonated parent, 3-NA. H^+ at m/z

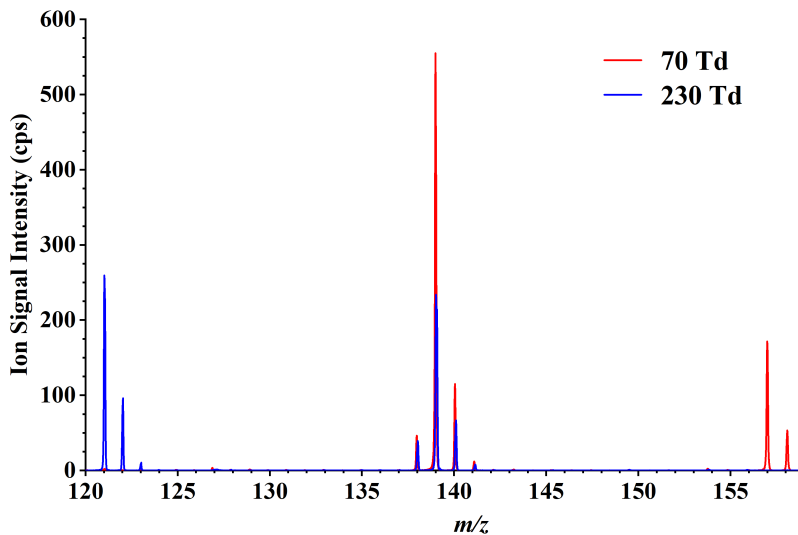


Figure 5.5: Overlaid mass spectra for 2-nitroaniline at 70 and 230 Td. This figure illustrates the clear difference in ion signal intensities for m/z 121.04, 139.05 and 157.06 upon the reduced electric field applied to the DT of the instrument.

139.05, over a large reduced electric field range. In addition to that, the three body association with water yielding $3\text{-NA}.\text{H}^+.\text{H}_2\text{O}$ is observed at low E/N , but in the case of 3-nitroaniline the presence of this ion is much higher than that in the 2-nitroaniline experiment, reaching roughly 50% at 60 Td and having the same intensity as the protonated parent signal.

On the other side, two other product ions are observed at high reduced electric field. $\text{C}_6\text{H}_7\text{N}^+$ at m/z 93.03 becomes the most abundant ion at around 230 Td. At the same, $\text{C}_6\text{H}_7\text{NO}^+$ at m/z 109.05, which was not found for 2-nitroaniline and comes from the loss of NO from the protonated parent, is observed for E/N values higher than 190 Td.

5.4.2.3 4-nitroaniline

The PID for the reaction of 4-nitroaniline with H_3O^+ , $\text{H}_3\text{O}^+.\text{(H}_2\text{O)}$ and potentially $\text{H}_3\text{O}^+.\text{(H}_2\text{O})_2$ is shown in Figure 5.7. The protonated parent ($4\text{-NA}.\text{H}^+$ at m/z 139.05) is the most abundant ion across the whole reduced electric field range (>80%). The clustering with water at low E/N has an intensity comparable to that in the 2-NA case (max 5-10% at 60 Td) and the only fragment ion ($\text{C}_6\text{H}_7\text{N}^+$ at m/z 93.06) is found at >160 Td.

A key result of these experiments is that protonated 3-nitroaniline shows more clustering

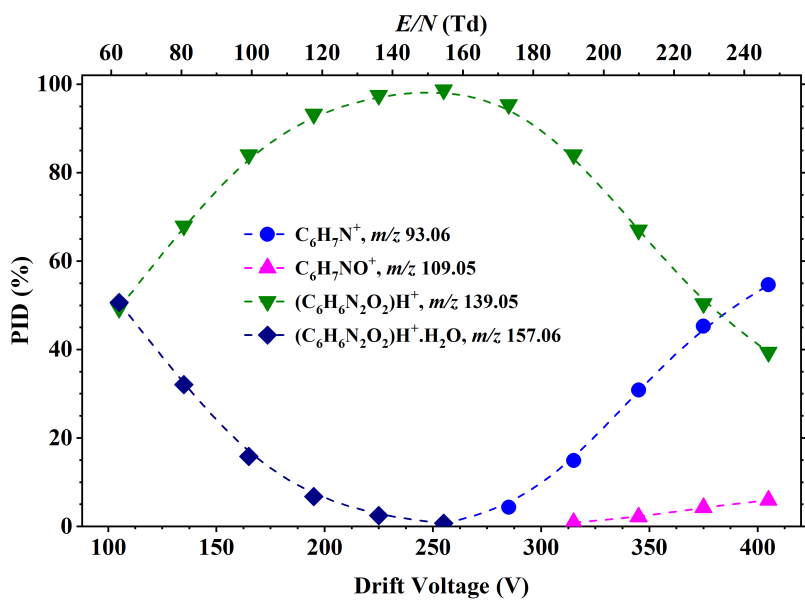


Figure 5.6: Percentage product ion distribution resulting from the reaction of 3-nitroaniline with $\text{H}_3\text{O}^+(\text{H}_2\text{O})_n$ ($n = 0$ and 1) as a function of the reduced electric field from 60 to 250 Td.

with water than the other two isomers but this can be explained in terms of the thermochemical data presented in Table 5.1. The calculated change in the Gibbs free energy, ΔG_{298} , for the clustering of 2-NA and 4-NA with water is 43 kJ mol^{-1} , while this is 51 kJ mol^{-1} for 3-NA. This 8 kJ mol^{-1} difference, translated into equilibrium constants at 298 K (i.e. $\exp(-\Delta G_{298}/RT)$), indicates that the solvation reaction is 25 times more effective for 3-NA. H^+ than for the other isomers. Furthermore, at the temperature of the drift tube (i.e. 150°C , 423 K) 8 kJ mol^{-1} represents a tenfold difference for the association of water with 3-NA. H^+ than for that with 2-NA. H^+ and 4-NA. H^+ .

In the 4-nitroaniline molecule, the nitro and amine functional groups are in opposite sites of the aromatic ring, which makes it difficult to create a transition state between said functional groups which would result in further product ions. The main consequence of this feature is that, as mentioned above, the protonated parent is the largely dominant ion, showing less fragmentation than the 2- and 3- isomers, which is in agreement with the chemical ionisation results for mononitroarenes with electron-releasing substituents [92].

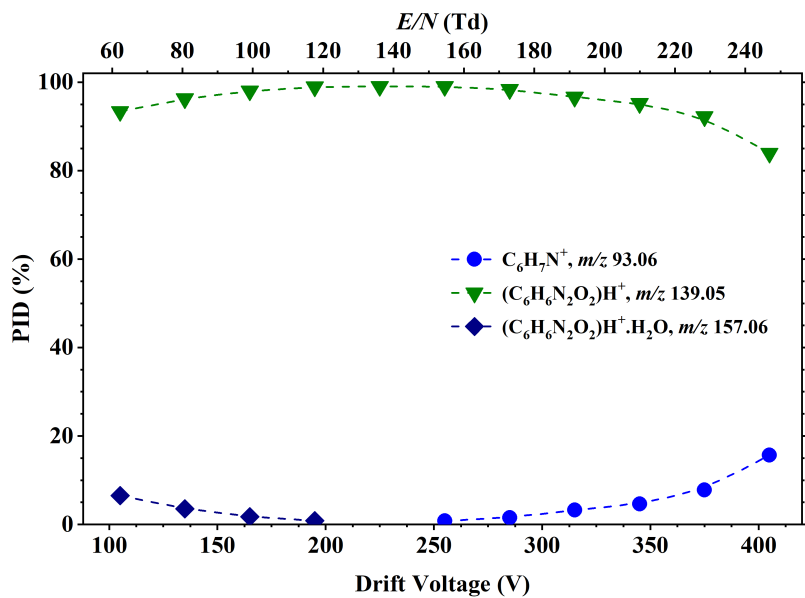


Figure 5.7: Percentage product ion distribution resulting from the reaction of 4-nitroaniline with $\text{H}_3\text{O}^+(\text{H}_2\text{O})_n$ ($n = 0, 1, 2$) as a function of the reduced electric field from 60 to 250 Td.

5.4.3 Fragmentation patterns and branching percentage studies in charge transfer mode

5.4.3.1 2-nitroaniline

The PID plot resulting from the reaction of 2-nitroaniline with O_2^+ as a function of the E/N is shown in Figure 5.8. The charge-transferred parent ion 2-NA^+ at m/z 138.04 is the most abundant ion below 230 Td. The branching percentage of this ion decreases with the E/N while other product ions arise, with $\text{C}_5\text{H}_6\text{N}^+$ at m/z 80.05 becoming dominant at 230 Td. The other observed fragment ions, in order of increasing m/z are C_5H_5^+ at m/z 65.04, the loss of the nitro group from 2-NA^+ (i.e. $\text{C}_6\text{H}_6\text{N}^+$) at m/z 92.05 and the loss of NO from 2-NA^+ (i.e. $\text{C}_6\text{H}_6\text{NO}^+$) at m/z 108.04. All these product ions have been reported by Beynon *et al.* for electron impact experiments [93].

5.4.3.2 3-nitroaniline

Figure 5.9 shows the PID plots for the reaction of 3-nitroaniline with O_2^+ as a function of the reduced electric field, which is quite similar to that of the 2- isomer in Figure 5.8. The observed product ions correspond to the same structures as indicated in the previous section, being in

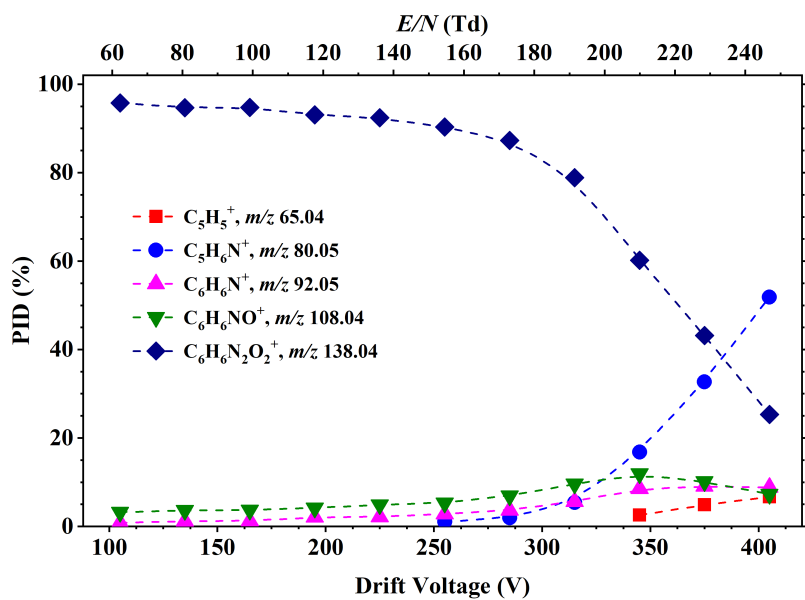


Figure 5.8: Percentage product ion distribution resulting from the reaction of 2-nitroaniline with O_2^+ as a function of the reduced electric field from 60 to 250 Td.

this case 3-NA $^+$ the parent ionised molecule. However, their branching percentages for a given E/N is slightly different. For the 3- isomer, the parent ion is the most abundant over the whole reduced electric field study except for values higher than 240 Td, where $\text{C}_5\text{H}_6\text{N}^+$ at m/z 80.05 becomes dominant. Also, $\text{C}_6\text{H}_6\text{N}^+$ at m/z 92.05 reaches a maximum product ion distribution of 15% for 3-NA, while only around 5% for 2-NA, and for C_5H_5^+ at m/z 65.04 it is 12% for 3-NA and around 6% for 2-NA.

5.4.3.3 4-nitroaniline

The PID plot in Figure 5.10 shows that the fragmentation for 4-NA is different to that for the 3- and 2- isomers showing only three product ions. As stated in the proton transfer mode case, this is an effect coming from the *para* arrangement of the functional groups in the ring. For the 4-nitroaniline isomer, the parent ion (4-NA $^+$ at m/z 138.04) is the most abundant from low reduced electric field up to around 190 Td, where $\text{C}_6\text{H}_6\text{NO}^+$ at m/z 108.04 becomes dominant. Furthermore, $\text{C}_5\text{H}_6\text{N}^+$ at m/z 80.05 appears at 190 Td and increases with the E/N , reaching a branching percentage of around 30% at 250 Td.

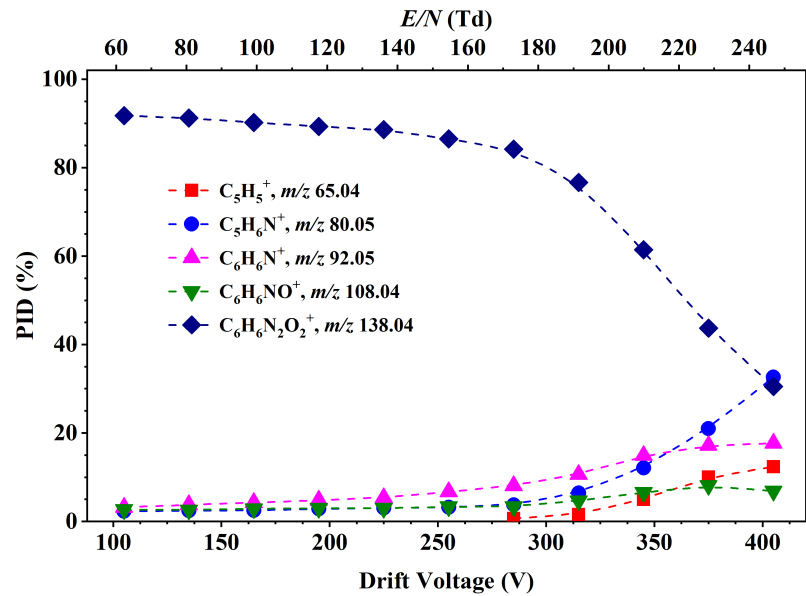


Figure 5.9: Percentage product ion distribution resulting from the reaction of 3-nitroaniline with O_2^+ as a function of the reduced electric field from 60 to 250 Td.

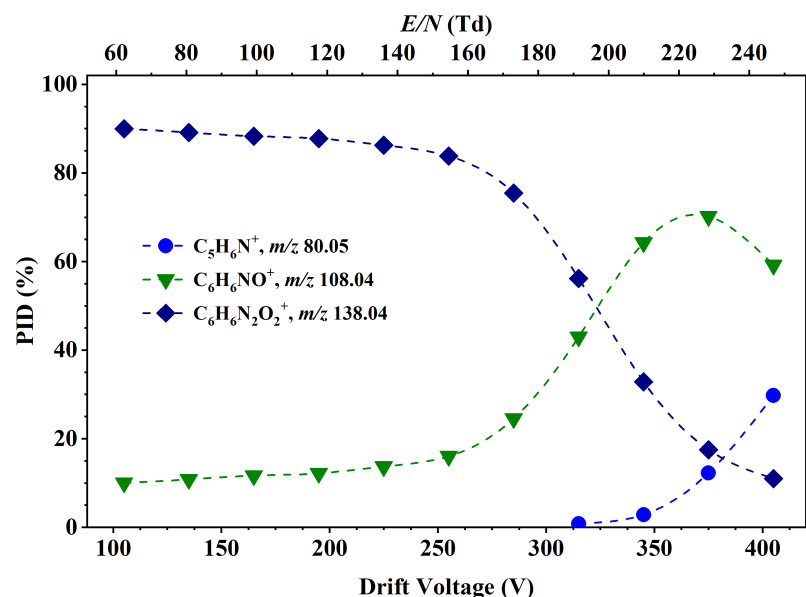


Figure 5.10: Percentage product ion distribution resulting from the reaction of 4-nitroaniline with O_2^+ as a function of the reduced electric field from 60 to 250 Td.

5.5 Conclusions

With this investigation we have shown how to separate nitroaniline isomers using the SRI-MS technique to enhance the ion/molecule reactions. This study contains the product ion distributions resulting from the reaction of the three isomers with H_3O^+ and O_2^+ as a function of the reduced electric field illustrated with quantum chemical results. We have proved that SRI-MS has good selectivity when detecting nitroanilines with H_3O^+ and O_2^+ as reagent ions.

In the proton transfer mode, the protonated parent at m/z 139.05 was the dominant ion over a wide E/N range for the three nitroanilines, while for the charge transfer mode the parent ion at m/z 138.04 was the most abundant for almost the whole E/N range. It is however the clustering with water in proton transfer mode and the presence of the product ion at m/z 108.04 in charge transfer mode what allows for isomer identification here. Whilst the product ion distributions of the reactions of 2- and 3-nitroaniline with O_2^+ are very similar, the 3- isomer shows higher clustering with water at low E/N in proton transfer mode, with the $3\text{-NA.H}^+\text{.H}_2\text{O}$ ion reaching ca. 50% at 60 Td (i.e. the lowest reduced electric field). Moreover, 4-nitroaniline shows less fragmentation than the 2- and 3- isomers in proton transfer mode but, in charge transfer mode, $\text{C}_6\text{H}_6\text{NO}^+$ at m/z 108.04 becomes the most abundant ion above approximately 190 Td. This ion enables the identification of the 4- isomer, as it never represents more than about 15% for 2- or 3-nitroaniline.

Chapter 6

Compendium of the Reactions of H₃O⁺ With Selected Ketones of Relevance to Breath Analysis Using Proton Transfer Reaction Mass Spectrometry

This chapter is a reformatted copy of my published article (reference [48]):

Malásková, M., Olivenza-León, D., Piel, F., Mochalski, P., Sulzer, P., Jürschik, S., Mayhew, C. & Maerk, T. Compendium of the reactions of H₃O⁺ with selected ketones of relevance to breath analysis using proton transfer reaction mass spectrometry. *Frontiers in Chemistry* **7**, 401 (2019).*

Declaration of contribution

My contribution to the article of which the present chapter is composed of was performing the experiments using a PTR-TOF 8000 at IONICON Analytik GmbH (Innsbruck, Austria) and analysing the data with Michaela Malásková and Felix Piel during several visits between 2016 and 2017. I also did the plots included and collaborated in writing the manuscript with the other coauthors.

*MM, DOL and FP are Early Stage Researchers who have contributed equally to the measurements, data analyses and contribution to the completion of this paper.

6.1 Abstract

Soft chemical ionization - mass spectrometric techniques, such as proton transfer reaction mass spectrometry (PTR-MS), are often used in breath analysis, being particularly powerful for real-time measurements. To ascertain the type and concentration of volatiles in exhaled breath clearly assignable product ions resulting from these volatiles need to be determined. This is difficult for compounds where isomers are common, and one important class of breath volatiles where this occurs are ketones. Here we present a series of extensive measurements on the reactions of H_3O^+ with a selection of ketones using PTR-MS. Of particular interest is to determine if ketone isomers can be distinguished without the need for pre-separation by manipulating the ion chemistry through changes in the reduced electric field. An additional issue for breath analysis is that the product ion distributions for these breath volatiles are usually determined from direct PTR-MS measurements of the compounds under the normal operating conditions of the instruments. Generally, no account is made for the effects on the ion-molecule reactions by the introduction of humid air samples or increased CO_2 concentrations into the drift tubes of these analytical devices resulting from breath. Therefore, another motivation of this study is to determine the effects, if any, on the product ion distributions under the humid conditions associated with breath sampling. However, the ultimate objective for this study is to provide a valuable database of use to other researchers in the field of breath analysis to aid in analysis and quantification of trace amounts of ketones in human breath. Here we present a comprehensive compendium of the product ion distributions as a function of the reduced electric field for the reactions of H_3O^+ . $(\text{H}_2\text{O})_n$ ($n = 0$ and 1) with nineteen ketones under normal and humid (100% relative humidity for 37°C) PTR-MS conditions. The ketones selected for inclusion in this compendium are (in order of increasing molecular weight): 2-butanone; 2-pentanone; 3-pentanone; 2-hexanone; 3-hexanone; 2-heptanone; 3-heptanone; 4-heptanone; 3-octanone; 2-nonalone; 3-nonalone; 2-decanone; 3-decanone; cyclohexanone; 3-methyl-2-butanone; 3-methyl-2-pentanone; 2-methyl-3-pentanone; 2-methyl-3-hexanone; and 2-methyl-3-heptanone.

Keywords: Ketones; Breath analysis; PTR-MS; Reduced electric field; FastGC.

6.2 Introduction

Although high resolution PTR-MS instruments can readily separate many isobaric compounds, the main strategy being used nowadays to deal with these mixtures is the manipulation of the ion-molecule chemistry, which can be done by changing: (i) the reagent ion species or distribution, or (ii) the reduced electric field (i.e. E/N) in the drift tube. The former approach was applied to investigations of explosives by Sulzer *et al.* and Agarwal *et al.* [66, 67], while Lanza *et al.* and Acton *et al.* did it for psychoactive substances [26, 68]. On the other hand, changing the reduced electric field to manipulate the collisional processes has been applied to homeland security: detection of chemical warfare agents [94], explosives [64, 66, 70], and rape drugs [18], and to the environmental sciences: identification of monoterpenes [95]. Moreover, the implementation of the radio frequency ion-funnel drift tube [12] and the computer-controlled fast switching drift tube [13] mentioned already in the chapter 2 of the present thesis are technical advances that were developed to enhance compound selectivity through changes in the reduced electric field. However, separating isomeric compounds presents a bigger challenge than isobaric ones, and in general their differentiation cannot be done without a pre-separation stage. Examples of isomeric distinction without pre-separation are the study from Lanza *et al.*, which differentiated between two isomeric drugs (4-methylethcathinone and N-ethylbuphedrone) using O_2^+ and NO^+ as reagent ions while reactions with H_3O^+ were not successful [52], and the study presented in chapter 5 of the present thesis, where 2-, 3- and 4-nitroaniline isomers can be separated because they yield different product ion distributions as a function of the reduced electric field for their reactions with H_3O^+ and O_2^+ [71]. But these are exceptions rather than the general case.

One of the best ways to investigate ketones isomers in PTR-MS is by coupling a pre-separation stage to the inlet of the instrument. The best choice for this is to use a fastGC device, as it gives a better compromise than standard GC systems to maintain the real-time advantages of PTR-MS. FastGC systems allow quick analysis (1-2 minutes) while still separating compounds in a fairly good way and thus enhancing specificity of PTR-MS [49, 50, 96]. In the present study we present a wide database resulting from the investigations of the reaction of a number of ketones with H_3O^+ as a function of the reduced electric field using the fastGC PTR-MS technique, where the fastGC made the product ion identification easier, helping to discard products coming from impurities or potential contamination in the samples.

Ketones can be detected in breath, blood and urine [97]. Their importance resides in the roles they play in metabolic processes in the human body and the possibility of them being detected through breath analysis for non-invasive monitoring and assessment of health processes and concerns. The main ketone found in the human body is acetone, which is linked to fat metabolism as other ketones but it is not included in the present study as it has been widely investigated in the past [96]. We have focused however in bigger molecular-weight ketones, including linear, cyclic and branched ones, which are found in smaller quantities, and are not present in many PTR-MS studies, while still being of relevance.

One of the differences between the standard working conditions in PTR-MS and the human breath is the humidity. Dry air or N₂ are typically used as carrier gas in PTR-MS, and this is not comparable to the amount of moisture present in the human breath. The implications of this humidity issue in the reaction processes happening in PTR-MS have been mentioned in the literature [98–100], and this should be accordingly accounted for. A 100% relative humidity at 34°C, like that in breath samples, can influence the reactions in the drift tube in different ways. First of all, there is less energy available when the analyte reacts with a water cluster ion (i.e. (H₂O)_nH₃O⁺ for n>0) instead of with H₃O⁺ as the proton affinity of the water clusters is higher than that of water (see Table 1.2). Also, higher humidity translates in a higher presence of water cluster ions for a given reduced electric field in the clustering-declustering processes compared to those in drier conditions, and this is particularly remarkable at low E/N (i.e. less than 120 Td). For instance, for a molecule with a proton affinity between that of water and the first water cluster, this means that sensitivity can be compromised for that particular compound, yielding a misleading amount in its detected concentration. Moreover, even when the protonation is energetically allowed, other secondary ion processes can occur, like clustering of the product ions with water molecules, which can also produce confusing results. As the consequences of humid operating conditions are not often considered in the literature because the experiments are carried out in “normal” conditions, one of our goals is to study the role of humidity in ketones product ions.

There are several studies available on the literature about how humidity affects the detection of different families of compounds. The most remarkable one is that from Warneke *et al.* where, at a constant E/N, they demonstrate that benzene and toluene do not reach with H₃O⁺·(H₂O)_n clusters as the product ion yield decreases with increasing humidity [98]. A work-

around for this was proposed by de Gouw *et al.*, who defined a humidity factor that compensates for the unreactive behaviour of a particular compound with $\text{H}_3\text{O}^+ \cdot (\text{H}_2\text{O})$ taking into account the $\text{H}_3\text{O}^+ \cdot (\text{H}_2\text{O})/\text{H}_3\text{O}^+$ ratio [14]. Moreover, de Gouw *et al.* calculated said factors and successfully corrected the product ion signal for the humidity effects for methanol, acetonitrile, acetaldehyde, acetone, benzene and toluene [101]. Demarcke *et al.* studied the influence of the humidity in PTR-MS from the reactions of H_3O^+ with α -cedrene and longifolene (i.e. two sesquiterpenes), although in this case there was no significant variation in the product ion signal [102]. Furthermore, Trefz *et al.* found considerable differences between the dry and humid cases when studying more than 20 volatile organic compounds, including aldehydes, ketones, aromatic compounds and hydrocarbons at a fixed E/N [73], while Kari *et al.* reported no meaningful change in the product ion signal for investigations of α -pinene, δ -limonene, and longifolene with different humidity levels [103]. It is possible to conclude then, taking into account the information available in the literature, the effects of humidity strongly vary from a compound to another.

In the present study we discuss the reactions of H_3O^+ and water cluster ions with several ketones for a broad reduced electric field range in both “normal” and “humid” operating conditions. This different operating conditions have been proved to yield different product ion distributions, which implies that humidity should be taken into account when breath analysis is being performed with a PTR-MS instrument to avoid misleading ion signal yields.

6.3 Materials and Methods

6.3.1 Sample preparation

Two different procedures were followed to prepare the samples. The measurements in normal conditions were done by first purging the headspace of the ketone-storing glass vial with dry N_2 (Alphagaz 1, Air Liquide GmbH., Austria) to remove the air and the possibly contaminated headspace, and replace it with N_2 to minimise the presence of O_2 and water vapour. The N_2 had been purified to 6.0 prior the purging process using a P300-1 Filter (VICI AG, Switzerland). Some parafilm was then used to cover the vial and some headspace was taken from the vial by injecting a glass syringe through the parafilm. Then, this headspace (containing both the ketone and N_2) was introduced into a 3-litre PTFE bag that had been previously been filled with dry 6.0 N_2 and that was connected to the inlet line of the PTR-MS instrument. Different headspace

volumes, from 5 μL to 10 mL, were used for different ketones owing to their different volatilities. On the other hand, a LCU was employed to generate the humid samples. As explained in subsection 2.3.3, this device can create a defined gaseous stream of a compound using liquid samples. In the present study, the liquid samples consisted of 1-10 μL of liquid ketone sample diluted in 100 mL of water in a 16 mL glass vials kept at 30°C. This mixture was injected into the LCU at a rate of 35 $\mu\text{L}/\text{min}$ while diluted in a carrier gas flow (N_2) of 950 mL/min to yield a 5% absolute humidity. This was then injected into the fastGC through the inlet of the PTR-MS instrument. A concentration of the ketones of approximately 100 ppbv was generated and introduced in the PTR-MS instrument in both dry and humid measurements.

An automated routine was used to perform the experiments shown in this study. This routine started with a 5-minute background study, which for the dry case consisted on measuring the N_2 -filled bag with no ketone traces, while for the humid case it was measuring a vial containing only purified water. Then the ketone sample was connected and a 2-minute stabilisation period followed. Then a fastGC study at 180 Td for 2 minutes 40 seconds was performed to aid in the product ions identification. The final part was a E/N study from 100 to 220 Td in steps of 10 Td at a speed of 1 minute/step, in both directions (i.e. from 100 to 220 Td and back), lasting 26 minutes in total. The whole study was repeated two times for each ketone for both humid and dry conditions.

6.3.2 FastGC PTR-ToF-MS

A wide description of PTR-ToF-MS operating techniques was given in chapter 2 besides being also available in the literature [6], and therefore only a short description stating the differences with the typical setup is needed here. For this piece of research, a PTR-TOF 8000 with a fastGC add-on (IONICON Analytik GmbH, Austria) was used [104, 105]. The basic working of this apparatus is similar to any PTR-MS instrument. In essence, $\text{H}_3\text{O}^+ \cdot (\text{H}_2\text{O})_n$ ($n = 0, 1, 2, \dots$) are created in the ion source through electron ionisation of water and ion-molecule reactions, and are transported to the drift tube, where they are dragged downstream by the electric field. Figure 6.1 shows the dependence of the water cluster ions signal as a function of the reduced electric field for the normal and humid case. It is important to note that these are the reagent ion intensities measured at the end of the drift tube and that the analyte molecules may have encountered a different distribution of reagent ions upstream. In other words, the analyte would encounter at

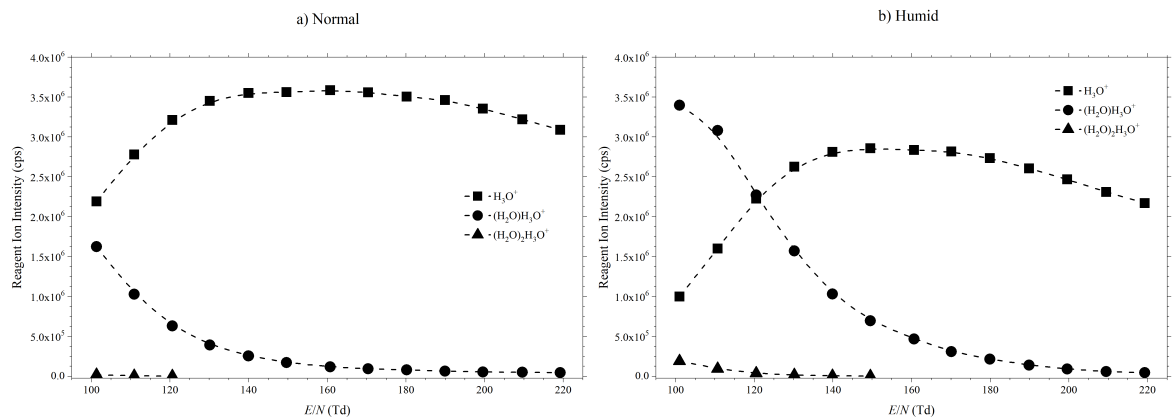


Figure 6.1: Reagent ion intensities in counts per second (cps) as a function of the reduced electric field for (a) normal (dry buffer gas) and (b) humid (5% absolute humidity buffer gas) conditions.

the beginning of the drift tube more water cluster ions that broke up through collisions with the buffer gas in the reactor region and that at the end of the drift tube have already dissociated to hydronium and (directly undetectable) neutral water molecules.

If the analyte, which is fed through the inlet pipe into the drift tube, has a proton affinity higher than that of water ($\text{PA}(\text{H}_2\text{O}) = 691 \text{ kJ mol}^{-1}$), it undergoes proton transfer from hydronium (or from the relevant protonated water cluster if the analyte's proton affinity is higher than that of the proper water cluster). The protonation process can be either dissociative or non-dissociative, and it is important to note that protonated molecule fragmentation can be a barrierless and spontaneous process or may be caused by the reagent ion collision with the analyte and/or charged analyte with the buffer gas.

The drift tube of the PTR-TOF 8000 was kept at 2.3 mbar and 100°C, being this also the temperature of the inlet line. These values were the same for all the measurements, giving a constant N , and thus the reduced electric field was solely manipulated by changing the drift voltage in the range from 410 V to 890 V, which corresponds to a E/N range from 100 to 220 Td. To aid in the product ion identification a fastGC was used, which is a modified version of that from Romano *et al.* and Ruzsanyi *et al.* [49, 50]. Details of this device were already given earlier in this thesis (see subsection 2.3.2) and are also available in the literature [48].

It is worth clarifying the choice of terms for the operating conditions regarding the humidity in the drift tube. Even when the carrier gas is dry N_2 , some water vapour can diffuse from the

ion source into the reactor. Thus, referring to this as “dry” is not totally correct and we will refer to it as the “normal” operating condition. On the other hand, when the carrier gas is not under dry conditions because it has been moisturised in the LCU we will refer to this as “humid” conditions.

6.3.3 Chemicals

The chemicals used in this study, their purities and their respective providers are: 2-butanone (99.5%, Honeywell), 2-pentanone (98%, Sigma-Aldrich), 3-pentanone (99%, Sigma-Aldrich), 2-hexanone (98%, Sigma-Aldrich), 3-hexanone (98%, Sigma-Aldrich), 2-heptanone (98.5%, Honeywell), 3-heptanone (analytical standard, Sigma-Aldrich), 4-heptanone (98%, Sigma-Aldrich), 3-octanone (99%, Acros Organics) 2-nonenone (99%, Sigma-Aldrich), 3-nonenone (99%, Sigma-Aldrich), 2-decanone (98%, Sigma-Aldrich), 3-decanone (97%, SAFC), cyclohexanone (99.8%, Sigma-Aldrich), 3-methyl-2-pentanone (99%, Sigma-Aldrich), 2-methyl-3-pentanone (97%, Sigma-Aldrich), 2-methyl-3-hexanone (98%, Sigma-Aldrich), 2-methyl-3-heptanone (99%, Sigma-Aldrich) and 3-methyl-2-butanone (98.5%, Honeywell). No further purification process was applied to these substances.

6.3.4 Data analysis

The analysis of the data for this study was done with the “PTR-MS Viewer” (IONICON Analytik GmbH, Austria) software (Figure 6.2), which was used to extract the data from the experiment files. The multi-peak feature of this software was also useful to separate some isobaric ions, like for example C_3H_3^+ and the ^{18}O isotopes of $(\text{H}_2\text{O})\text{H}_3\text{O}^+$ (i.e. $(\text{H}_2\ ^{18}\text{O})\text{H}_3\text{O}^+ + (\text{H}_2\text{O})\text{H}_3\ ^{18}\text{O}^+$), which are both found at m/z 39. For easier comparison with other instruments, the raw data was not corrected for transmission effects, although it was normalised to 10^6 reagent ion counts and the background signals were subtracted. Only the ion signal from H_3O^+ was used to normalise that from 2-butanone (827 kJ mol^{-1}), 2-pentanone (833 kJ mol^{-1}), 3-pentanone (837 kJ mol^{-1}), and 3-methyl-2-butanone (836 kJ mol^{-1}) because their proton affinity is higher than that of $(\text{H}_2\text{O})_2$ (808 kJ mol^{-1}). For the rest of the ketones, the sum of the counts from H_3O^+ and $(\text{H}_2\text{O})\text{H}_3\text{O}^+$ was used to normalise the ion yield.

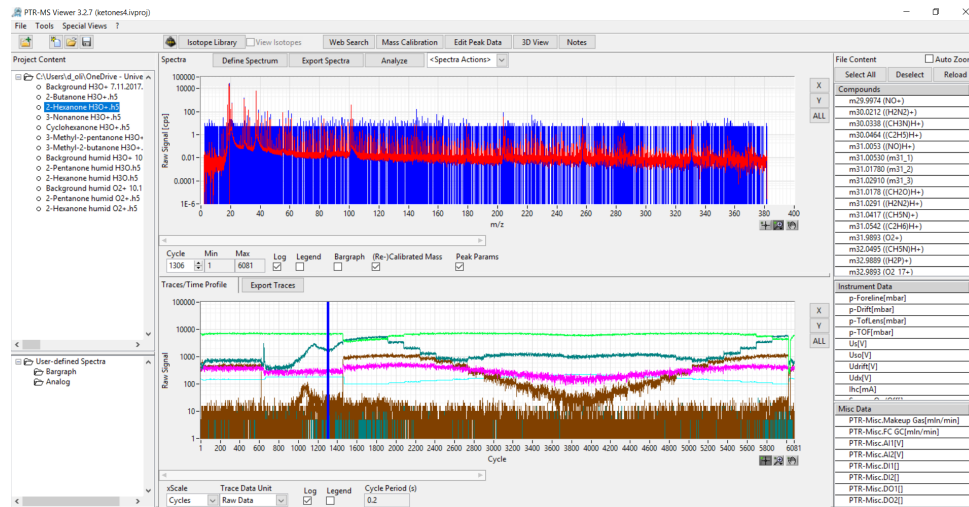


Figure 6.2: Screenshot of the user interface of the PTR-MS Viewer software used for the data analysis in this study.

6.4 Results and Discussion

The product ion distributions for all the compounds studied in this investigation are shown in Table 6.1 at 100, 140 and 180 Td for both normal and humid conditions. These numbers provide a fast picture of the observed product ions for each ketone and show promptly the impacts, if any, of humidity on the distribution of product ions. The ketones presented in Table 6.1 (in increasing molecular weight) are thirteen linear, one cyclic and five branched ones. Moreover, Figure 6.3 graphically presents the product ion distributions as a function of the reduced electric field. The product ions considered in this study are those that represent at least 3% of the total product ion signal at any given E/N . Furthermore, the ^{13}C peak intensities and the exact m/z were used to tentatively assign the product ions to the provided chemical compositions in both Table 6.1 and Figure 6.3.

Table 6.1: Product ions identified and their associated product ion branching ratios (percentages) measured at reduced electric fields of 100, 140, and 180 Td resulting from the reactions of H_3O^+ with several ketones.

Ketone Molecular Formula Nominal MW	Product Ion <i>m/z</i>	Product Ion Formula	Product Ion Branching Percentages					
			Normal <i>E/N</i> (Td)			Humid <i>E/N</i> (Td)		
			100	140	180	100	140	180
Linear ketones								
2-butanone $\text{C}_4\text{H}_8\text{O}$ 72	73.07 55.05 39.02	$\text{C}_4\text{H}_8\text{OH}^+$ C_4H_7^+ C_3H_3^+	100 0 0	99 1 0	87 10 3	100 0 0	100 0 0	88 10 2
2-pentanone $\text{C}_5\text{H}_{10}\text{O}$ 86	87.08 45.03 39.02	$\text{C}_5\text{H}_{10}\text{OH}^+$ $\text{C}_2\text{H}_5\text{O}^+$ C_3H_3^+	99 1 0	67 33 0	20 70 10	99 1 0	84 16 0	29 66 5
3-pentanone $\text{C}_5\text{H}_{10}\text{O}$ 86	87.08 69.07 45.03 41.04 39.02	$\text{C}_5\text{H}_{10}\text{OH}^+$ C_5H_9^+ $\text{C}_2\text{H}_5\text{O}^+$ C_3H_5^+ C_3H_3^+	98 1 1 0 0	72 4 20 3 1	23 2 55 5 15	99 1 0 0 0	91 4 4 1 0	43 4 39 5 9
2-hexanone $\text{C}_6\text{H}_{12}\text{O}$ 100	101.1 59.05 45.03 39.02	$\text{C}_6\text{H}_{12}\text{OH}^+$ $\text{C}_3\text{H}_7\text{O}^+$ $\text{C}_2\text{H}_5\text{O}^+$ C_3H_3^+	100 0 0 0	94 1 5 0	48 3 39 10	100 0 0 0	95 1 4 0	49 3 40 8
3-hexanone $\text{C}_6\text{H}_{12}\text{O}$ 100	101.1 83.09 59.05 55.05 45.03 41.04 39.02 31.02	$\text{C}_6\text{H}_{12}\text{OH}^+$ $\text{C}_6\text{H}_{11}^+$ $\text{C}_3\text{H}_7\text{O}^+$ C_4H_7^+ $\text{C}_2\text{H}_5\text{O}^+$ C_3H_5^+ C_3H_3^+ CH_3O^+	93 1 3 0 2 0 1 0	73 4 9 3 5 4 1 1	31 4 15 5 15 6 18 6	96 1 3 0 0 0 0 0	88 4 7 0 0 1 0 0	44 5 17 12 0 9 13 0
2-heptanone $\text{C}_7\text{H}_{14}\text{O}$	115.11 97.1	$\text{C}_7\text{H}_{14}\text{OH}^+$ $\text{C}_7\text{H}_{13}^+$	94 4	76 10	31 7	96 2	86 7	52 9

(Continued)

Ketone Molecular Formula Nominal MW	Product Ion <i>m/z</i> Formula	Product Ion Formula	Product Ion Branching Percentages					
			Normal <i>E/N</i> (Td)			Humid <i>E/N</i> (Td)		
			100	140	180	100	140	180
114	59.05	C ₃ H ₇ O ⁺	1	2	4	2	3	6
	55.05	C ₄ H ₇ ⁺	0	9	14	0	4	20
	45.03	C ₂ H ₅ O ⁺	1	3	15	0	0	0
	39.02	C ₃ H ₃ ⁺	0	0	29	0	0	13
3-heptanone C ₇ H ₁₄ O	115.11	C ₇ H ₁₄ OH ⁺	98	89	35	99	95	57
	97.1	C ₇ H ₁₃ ⁺	2	5	4	1	4	5
	114	C ₃ H ₇ O ⁺	0	0	0	0	1	7
	55.05	C ₄ H ₇ ⁺	0	4	8	0	0	12
	41.04	C ₃ H ₅ ⁺	0	1	7	0	0	3
	39.02	C ₃ H ₃ ⁺	0	0	27	0	0	16
4-heptanone C ₇ H ₁₄ O	115.11	C ₇ H ₁₄ OH ⁺	98	90	52	99	95	70
	73.07	C ₄ H ₉ O ⁺	0	1	2	0	0	0
	114	C ₃ H ₇ O ⁺	1	2	6	1	1	4
	55.05	C ₄ H ₇ ⁺	0	6	15	0	4	16
	53.04	C ₄ H ₅ ⁺	0	0	5	0	0	3
	39.02	C ₃ H ₃ ⁺	1	1	20	0	0	7
3-octanone C ₈ H ₁₆ O	129.13	C ₈ H ₁₆ OH ⁺	99	96	46	100	98	73
	69.07	C ₅ H ₉ ⁺	0	3	5	0	1	6
	128	C ₃ H ₇ O ⁺	1	1	3	0	1	4
	41.04	C ₃ H ₅ ⁺	0	0	11	0	0	10
	39.02	C ₃ H ₃ ⁺	0	0	35	0	0	7
	143.14	C ₉ H ₁₈ OH ⁺	100	93	34	100	97	62
2-nonanone C ₉ H ₁₈ O	83.09	C ₆ H ₁₁ ⁺	0	0	0	0	1	4
	69.07	C ₅ H ₉ ⁺	0	4	4	0	2	6
	55.05	C ₄ H ₇ ⁺	0	1	4	0	0	7
	41.04	C ₃ H ₅ ⁺	0	1	10	0	0	10
	39.02	C ₃ H ₃ ⁺	0	1	48	0	0	11
	143.14	C ₉ H ₁₈ OH ⁺	100	87	48	100	100	79
3-nonanone C ₉ H ₁₈ O	55.05	C ₄ H ₇ ⁺	0	4	6	0	0	5
	41.04	C ₃ H ₅ ⁺	0	8	11	0	0	6

(Continued)

Ketone Molecular Formula Nominal MW	Product Ion <i>m/z</i> Formula	Product Ion Formula	Product Ion Branching Percentages					
			Normal <i>E/N</i> (Td)			Humid <i>E/N</i> (Td)		
			100	140	180	100	140	180
	39.02	C ₃ H ₃ ⁺	0	1	35	0	0	10
2-decanone	157.16	C ₁₀ H ₂₀ OH ⁺	100	94	48	100	99	81
C ₁₀ H ₂₀ O	83.09	C ₆ H ₁₁ ⁺	0	2	3	0	1	6
156	55.05	C ₄ H ₇ ⁺	0	3	13	0	0	13
	39.02	C ₃ H ₃ ⁺	0	1	36	0	0	0
3-decanone	157.16	C ₁₀ H ₂₀ OH ⁺	99	95	48	100	100	86
C ₁₀ H ₂₀ O	55.05	C ₄ H ₇ ⁺	1	4	10	0	0	7
156	39.02	C ₃ H ₃ ⁺	0	1	42	0	0	7
Cyclic ketone								
cyclohexanone	99.08	C ₆ H ₁₀ OH ⁺	99	88	30	99	93	40
C ₆ H ₁₀ O	81.07	C ₆ H ₉ ⁺	1	12	65	1	7	56
98	79.05	C ₆ H ₇ ⁺	0	0	5	0	0	3
	39.02	C ₃ H ₃ ⁺	0	0	0	0	0	1
Branched ketones								
3-methyl-2-butanone	87.08	C ₅ H ₁₀ OH ⁺	100	98	63	99	96	66
C ₅ H ₁₀ O	69.07	C ₅ H ₉ ⁺	0	2	5	1	3	7
86	45.03	C ₂ H ₅ O ⁺	0	0	8	0	0	8
	41.04	C ₃ H ₅ ⁺	0	0	4	0	1	8
	39.02	C ₃ H ₃ ⁺	0	0	20	0	0	11
3-methyl-2-pentanone	101.1	C ₆ H ₁₂ OH ⁺	100	70	23	100	73	22
C ₆ H ₁₂ O	59.05	C ₃ H ₇ O ⁺	0	11	28	0	7	26
100	57.07	C ₄ H ₉ ⁺	0	4	3	0	5	4
	45.03	C ₂ H ₅ O ⁺	0	15	39	0	15	40
	39.02	C ₃ H ₃ ⁺	0	0	7	0	0	8
2-methyl-3-pentanone	101.1	C ₆ H ₁₂ OH ⁺	98	61	17	95	74	24
C ₆ H ₁₂ O	59.05	C ₃ H ₇ O ⁺	1	15	29	3	9	29
100	57.07	C ₄ H ₉ ⁺	0	4	2	0	3	3
	45.03	C ₂ H ₅ O ⁺	1	20	41	2	13	40
	39.02	C ₃ H ₃ ⁺	0	0	11	0	1	4
2-methyl-3-hexanone	115.11	C ₇ H ₁₄ OH ⁺	95	66	24	96	72	24
C ₇ H ₁₄ O	97.1	C ₇ H ₁₃ ⁺	5	14	8	4	10	7

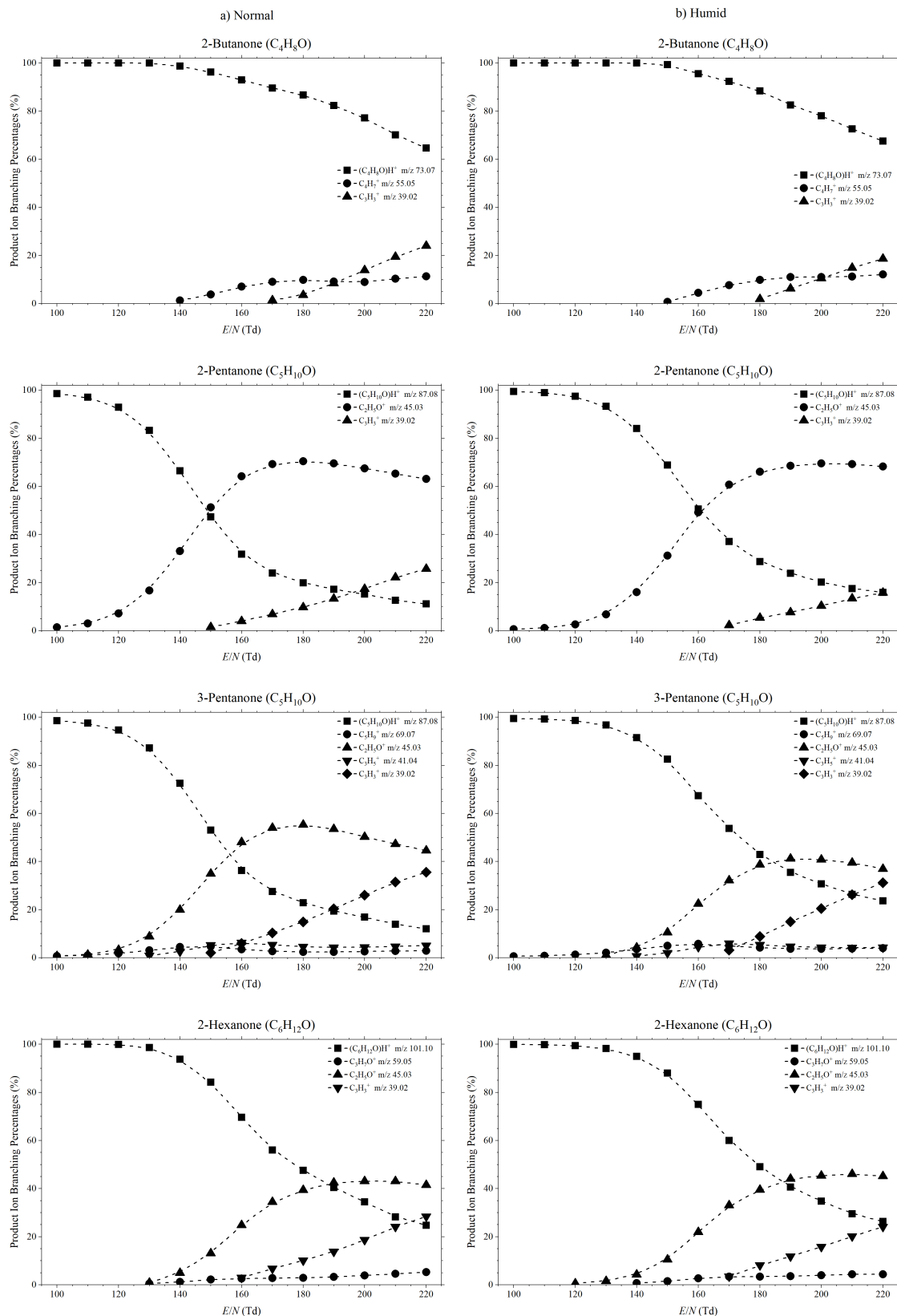
(Continued)

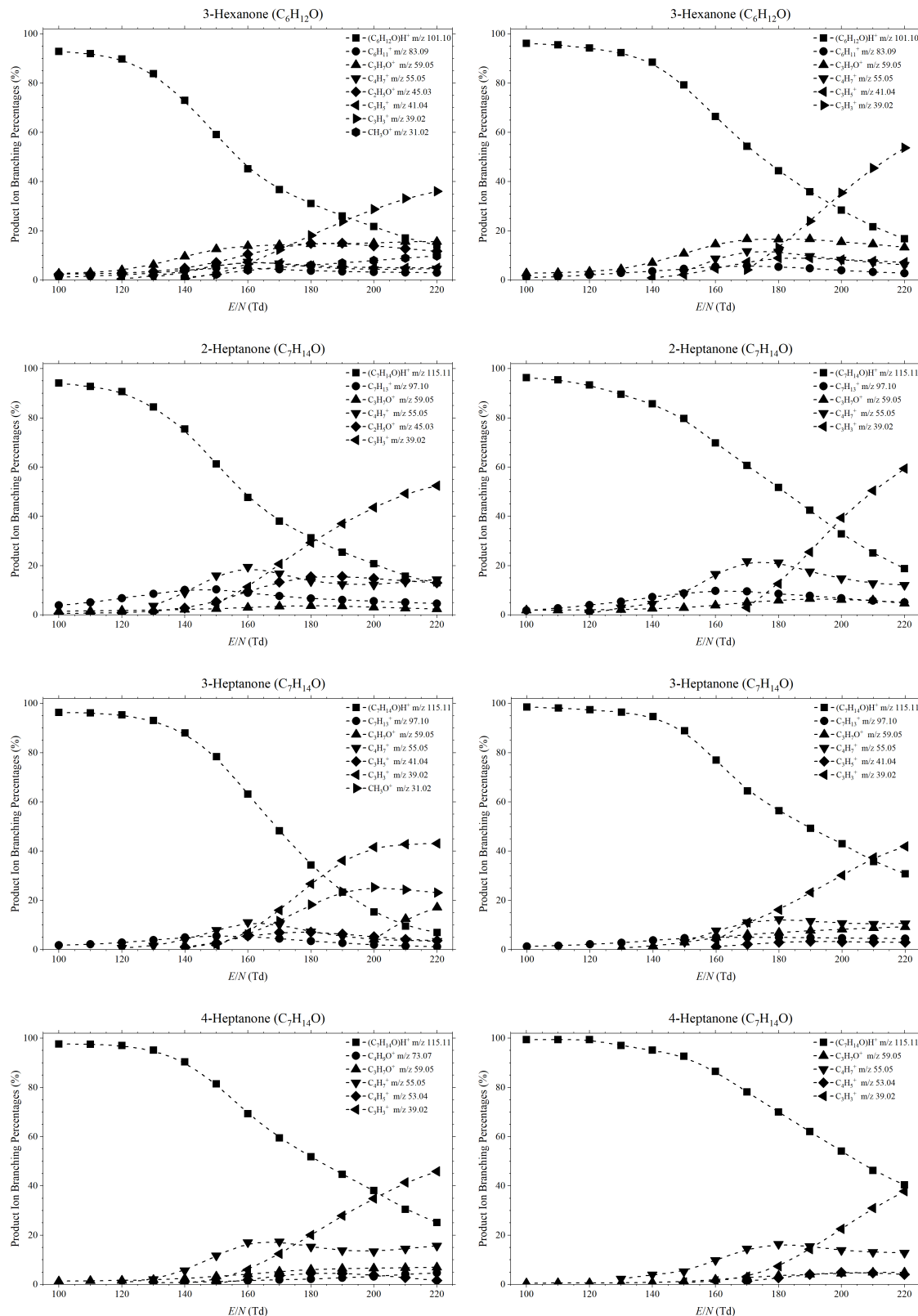
Ketone Molecular Formula Nominal MW	Product Ion <i>m/z</i> Formula	Product Ion Formula	Product Ion Branching Percentages					
			Normal <i>E/N</i> (Td)			Humid <i>E/N</i> (Td)		
			100	140	180	100	140	180
114 2-methyl-3-heptanone C ₈ H ₁₆ O	59.05	C ₃ H ₇ O ⁺	0	8	17	0	4	17
	55.05	C ₄ H ₇ ⁺	0	4	5	0	2	7
	45.03	C ₂ H ₅ O ⁺	0	5	17	0	11	27
	41.04	C ₃ H ₅ ⁺	0	3	7	0	1	6
	39.02	C ₃ H ₃ ⁺	0	0	22	0	0	12
128 129.13 111.12 69.07 59.05 45.03 43.05 41.04 39.02	129.13	C ₈ H ₁₆ OH ⁺	96	76	26	97	81	28
	111.12	C ₈ H ₁₅ ⁺	3	5	3	2	5	3
	69.07	C ₅ H ₉ ⁺	0	8	5	0	4	5
	59.05	C ₃ H ₇ O ⁺	0	0	0	0	3	14
	45.03	C ₂ H ₅ O ⁺	0	2	8	0	3	10
	43.05	C ₃ H ₇ ⁺	1	2	2	1	2	3
	41.04	C ₃ H ₅ ⁺	0	6	15	0	2	15
	39.02	C ₃ H ₃ ⁺	0	1	41	0	0	22

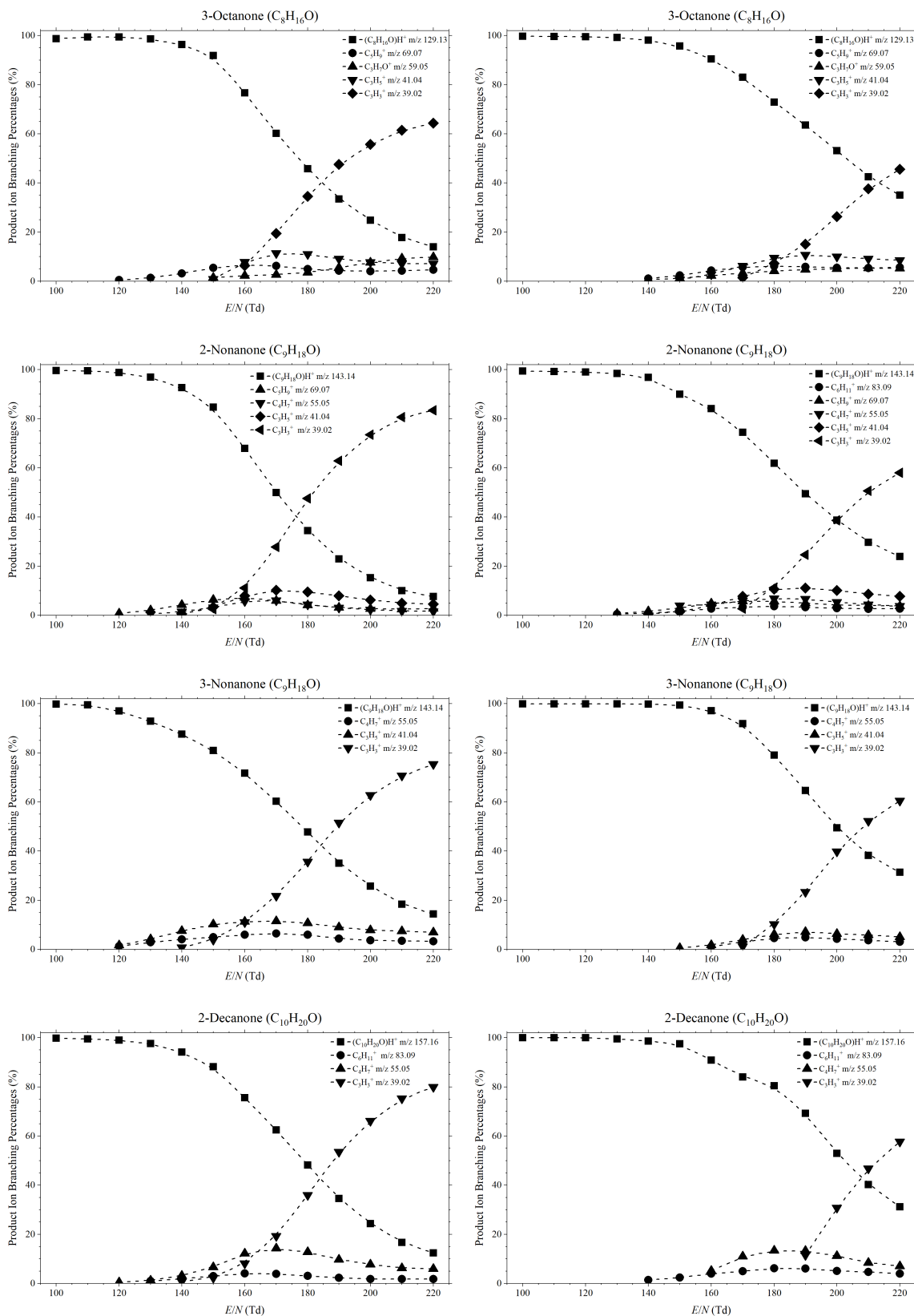
The protonated parent molecule is the dominant ion for all ketones at low *E/N* values (<140 Td). This is in agreement with some studies present in the literature, like the one from Buhr *et al.*, where they demonstrated that, independently of the chain length, the main reaction channel between ketones and hydronium at approximately 140 Td is non-dissociative proton transfer. SIFT-MS [107–109] and SIFDT-MS [110] investigations also agree with the observation of the protonated parent being dominant at low collisional energies.

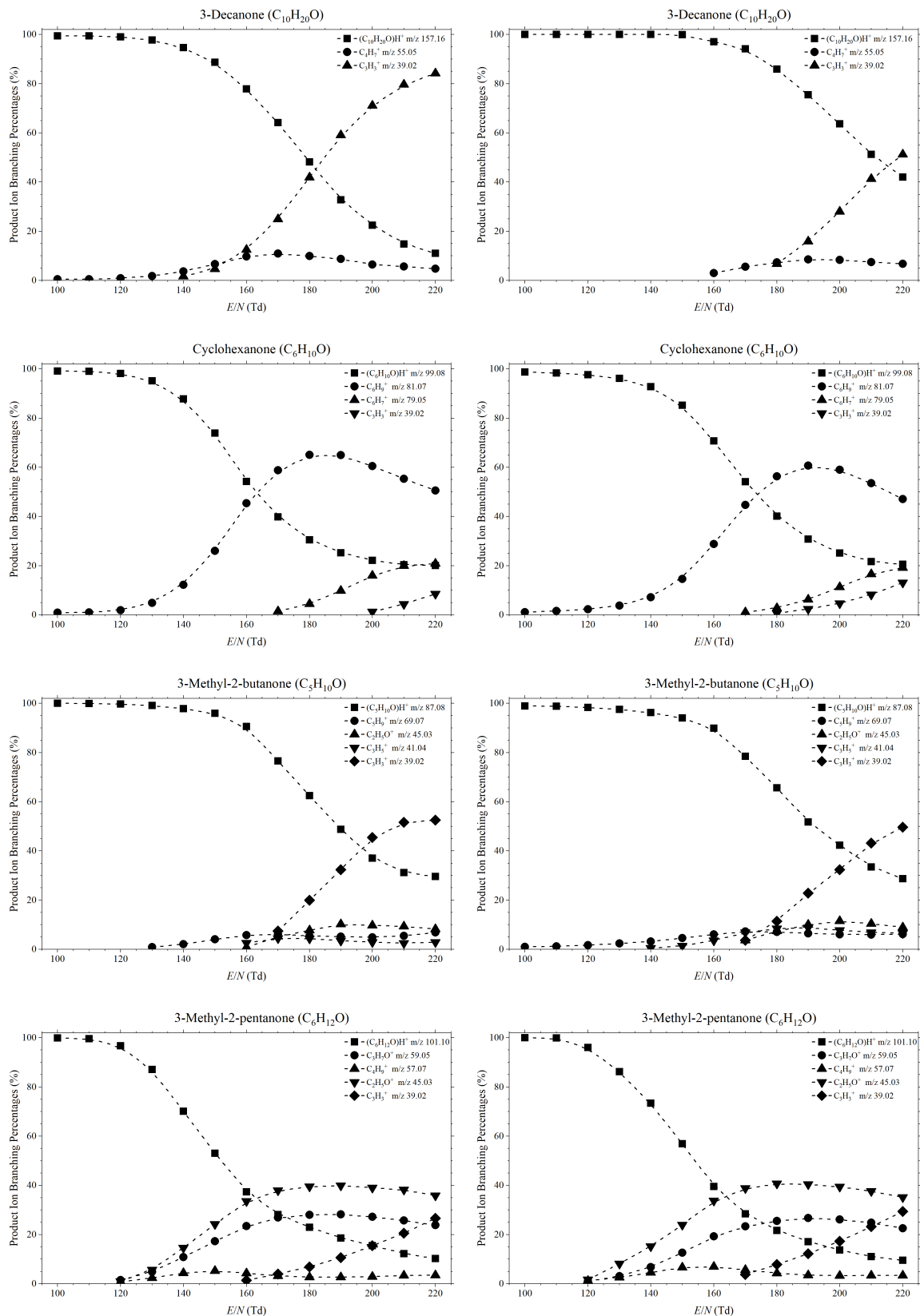
On the other hand, other product ions rather than the protonated parent molecule are observed for high *E/N* values (>140 Td). This does not agree with Buhr *et al.* for 2-butanone, 2-hexanone, 2-heptanone, 3-heptanone, 4-heptanone, 3-octanone, 2-nonenone and 2-decanone as they reported the protonated parent ion as the only product ion. However, Buhr *et al.* did observe for 2-pentanone, although at a lower percentage compared to our study, a product ion at *m/z* 45 tentatively assigned to protonated acetaldehyde (C₂H₅O⁺), but these discrepancies could be explained in terms of the different equipment used in each case.

Further discrepancies are observed when comparing our product ion distributions with those from Pan *et al.*, who investigated 2-butanone, 2-pentanone, 2-hexanone, 2-heptanone and cyclohexanone with a dipolar PTR-Quad-MS over a range of low *E/N* values (50–110 Td) [111].

Figure 6.3: *Continued*

Figure 6.3: *Continued*

Figure 6.3: *Continued*

Figure 6.3: *Continued*

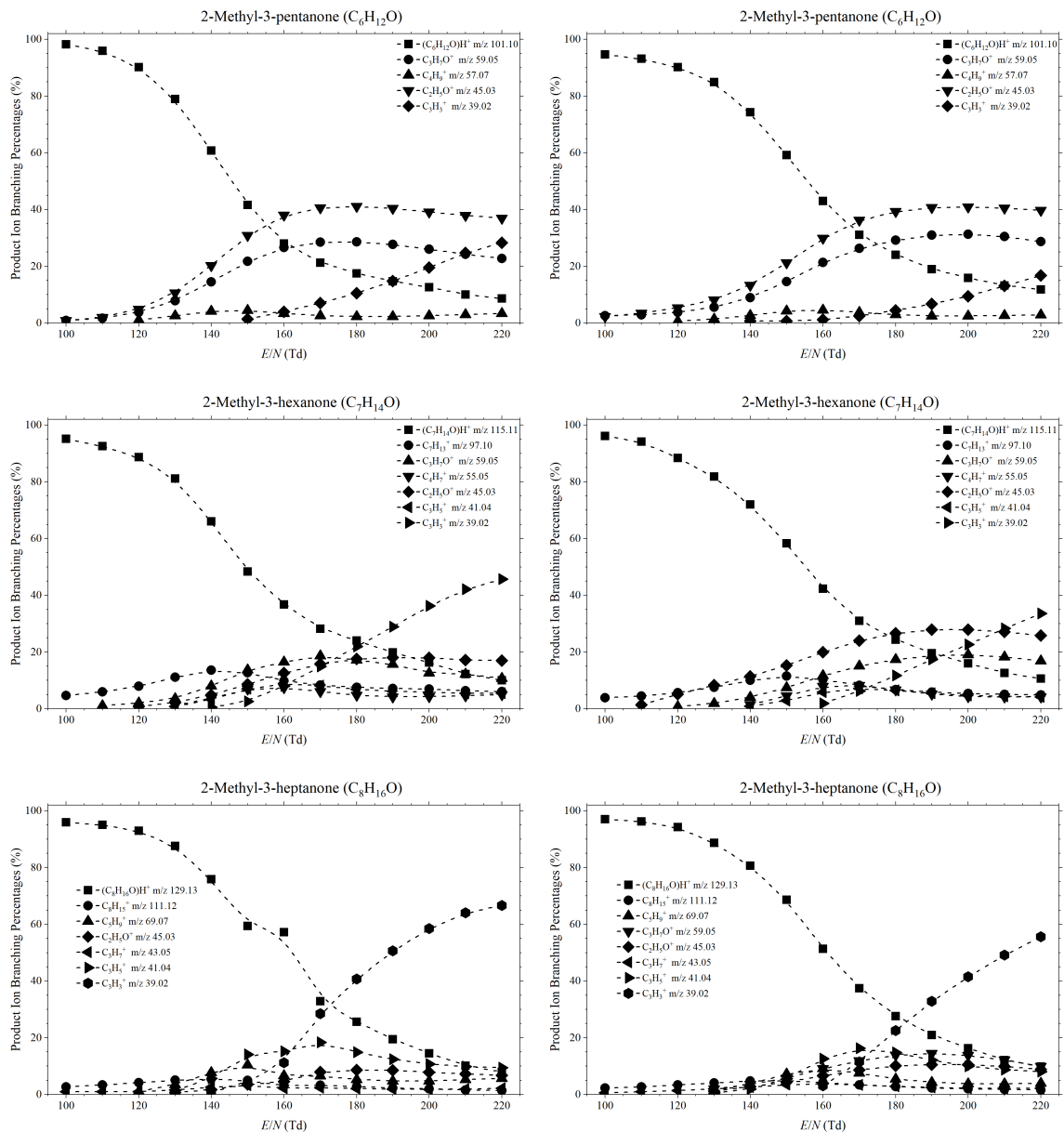


Figure 6.3: Product ion distributions (branching percentages) as a function of E/N resulting from reaction with H_3O^+ (and potentially $H_3O^+\cdot H_2O$ as stated above) under (a) normal and (b) high humidity drift tube conditions with several ketones.

Pan *et al.* observed an unexpected amount of hydrocarbon ions ($C_nH_m^+$) at those collisional energies, which are also found in our investigations but only at high E/N values. This is another proof showing that the findings of various PTR-MS instruments need to be compared carefully.

In the present study, in general the protonated parent ion dominates (>80% branching percentage) up to ca. 130 Td, although 2-7 further product ions have been observed for each ketone. However, their contribution to the total ion signal was only noticeable at high E/N values in most cases. For example, of $C_3H_3^+$ and $C_3H_5^+$ only appear at reduced electric values of approximately 150 Td or higher. The analytes showing the highest number of fragmentation channels were 3-hexanone (7 channels), 3-heptanone (6 channels), 2-methyl-3-hexanone (6 channels) and 2-methyl-3-heptanone (7 channels). Higher molecular weight ketones were found to be more stable and show less fragmentation channels.

Additionally, the loss of H_2O was also observed for some of the analysed ketones, yielding hydrocarbons with a $C_nH_{2n-1}^+$ composition, but these represent a low percentage of the total product ion signal and also they rapidly break up at high E/N . Furthermore, it has been observed for C5 and C6 ketones that the fragmentation path resulting in $C_2H_5O^+$ very common.

The main observed result of the higher humidity conditions is that it lessens the fragmentation of the ketones, with the product ion distributions at a given E/N in normal conditions being comparable to those at a reduced electric field approximately 20 Td higher in humid conditions. This behaviour is more noticeable at mid reduced electric field values (ca. 150 Td) because of the higher presence of protonated water clusters compared to normal conditions and the emerging fragment ions at higher collisional energies. At low E/N the higher humidity makes no difference in this ketone study because the main observed product ion is the protonated parent. Also, the three body association of the protonated parent with water was not observed in any case. On the other side, at high E/N the protonated water clusters are broken up through collisions with the buffer gas, which reduces this humidity effect. This can be illustrated monitoring the protonated parent molecules from 2-pentanone and 3-nonenone, which, at 150 Td and normal and dry conditions, represent 47% and 69%, and 48% and 79%, respectively.

Figure 6.4 presents one of the acquired mass spectra for illustrative purposes, corresponding in this case to 3-hexanone at 180 Td. This figure shows all the detected product ions, although some of them (i.e. $C_4H_5^+$ and $C_4H_9^+$) are not included in Figure 6.3 or Table 6.1 because they represent less than 3% of the total product ion signal.

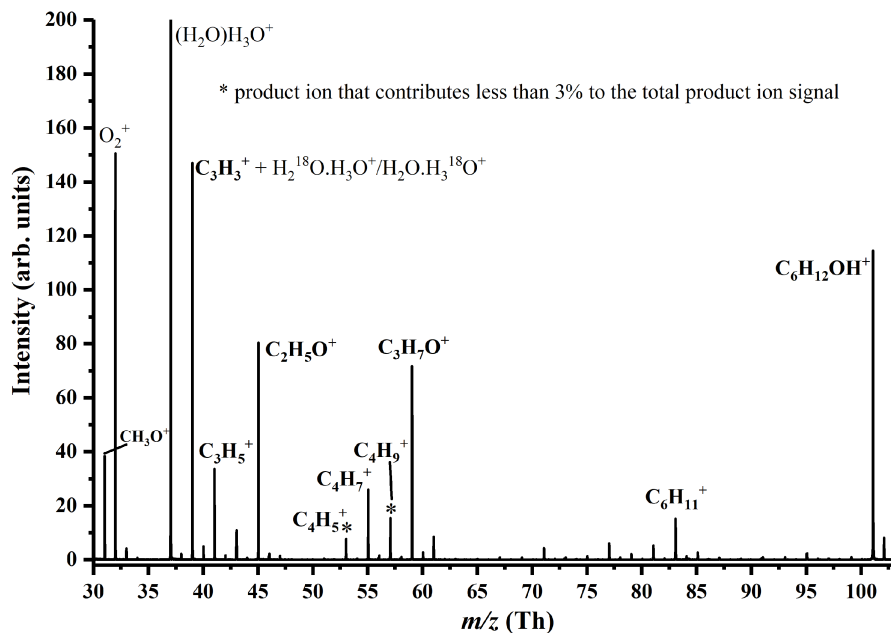


Figure 6.4: Mass spectrum for 3-hexanone recorded at 180 Td. Product ions coming from the compound are identified. The product ions C_4H_5^+ and C_4H_9^+ each contribute $<3\%$ to the total product ion percentage even at the highest reduced electric field investigated.

6.5 Conclusions

The research exposed in this chapter offers a broad database for PTR-MS users of the product ions and their relative intensities as a function of the reduced electric for the reactions of H_3O^+ and $\text{H}_3\text{O}^+ \cdot (\text{H}_2\text{O})$ with a variety of ketones. Initially conceived thinking in the relevance of ketones in breath analysis, this study can however be relevant as well in the environmental sciences and atmospheric chemistry.

It is important to note that the product ion branching ratios presented here are associated to a certain PTR-MS under specific conditions (e.g. humidity in the drift tube), and that these may vary when using different instrumentation and configurations. Thus, these product ion branching ratios are only indicatives of the main ion-molecule reactions and fragmentation channels occurring in the drift tube. Also, no enhancement of selectivity was found for any of the ketones through manipulation of the collisional energy. This means that a pre-separation stage (i.e. a fastGC device) is required when analysing ketones mixtures containing isomeric compounds (e.g. breath samples) to distinguish between them.

A final remark is that aldehydes, which are isomers of ketones, should be accounted for when

working with breath samples, as they cannot be directly separated from ketones in PTR-MS. This needs further investigation, although one of the key differences between these two families of compounds is that aldehydes fragment remarkably more than ketones in PTR-MS, with the protonated parent ion usually representing less than 10% of the total product ion signal [106, 112]. Consequently, aldehydes will only represent a small portion of the parent ions corresponding to aldehydes and ketones observed in a breath sample at low and mid reduced electric fields.

Chapter 7

Studies pertaining to the monitoring of isoflurane and sevoflurane by proton transfer reaction mass spectrometry

[This chapter might be deleted if the thesis gets too long]

7.1 Introduction

7.2 Methodology

7.2.1 PTR-MS vs SIFT-MS vs SIFDT-MS

The home-built SIFDT-MS instrument at the Heyrovsky Institute of Physical Chemistry of the Academy of Sciences in Prague (Czech Republic) has been described in detail elsewhere [113].

The calculation of the rate constant comes from Su [114].

The data for α and μ_D can be found in [115].

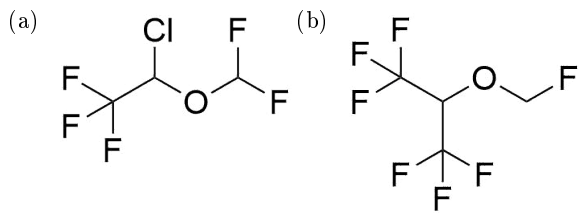


Figure 7.1: Structure of (a) isoflurane and (b) sevoflurane.

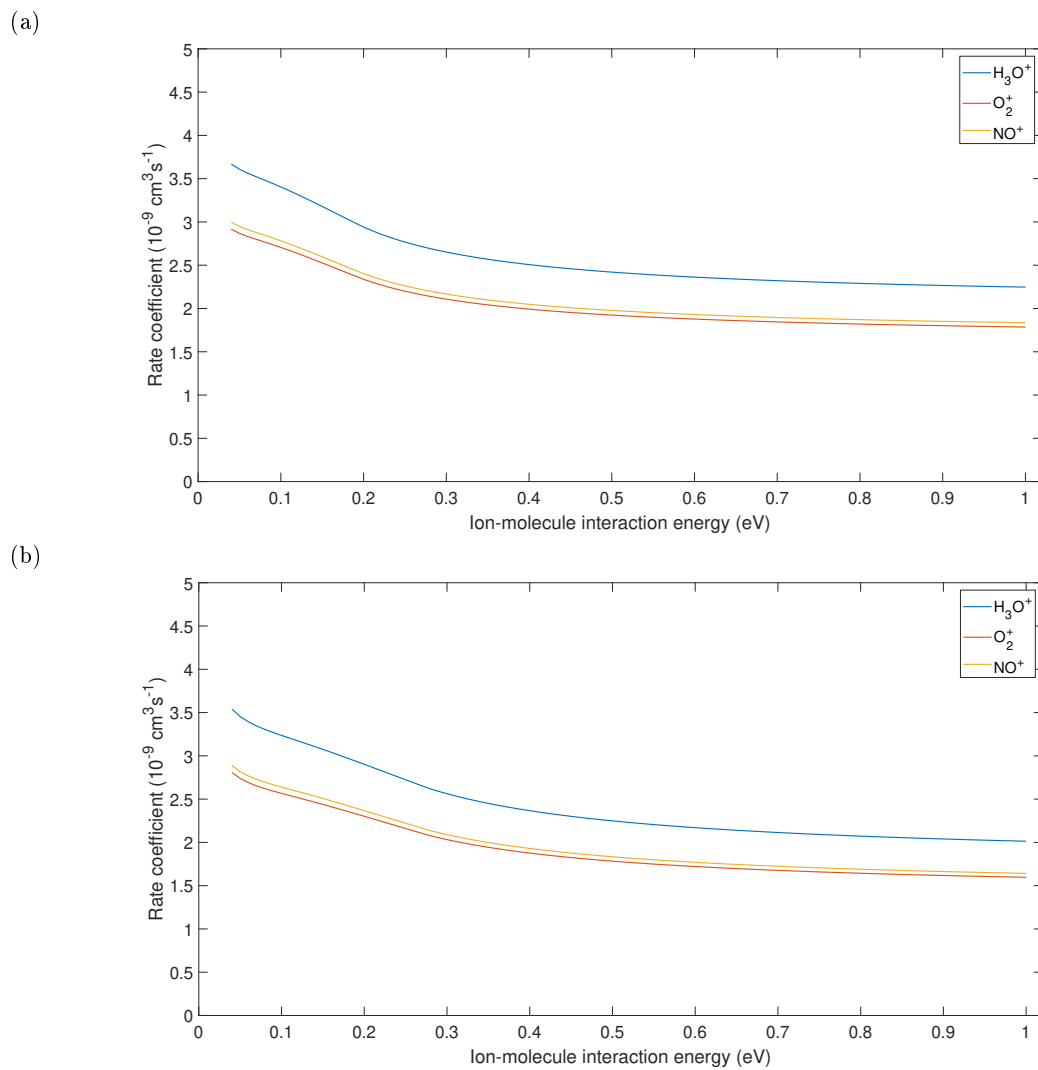


Figure 7.2: Collisional rate coefficients of (a) isoflurane and (b) sevoflurane with different reagent ions as a function of the interaction energy as predicted by the Su model [114]

7.2.2 Isoflurane and sevoflurane

7.2.2.1 Rate constants

7.3 Concerns at the moment

There are some concerns regarding isoflurane:

- It is very sensitive to humidity. In the past, people thought that the discrepancies in the PTRMS results from isoflurane measurements were due to the difference geometries of the instruments from different manufacturers, which raised doubts about the standardisation of PTRMS.
- There is an ion reported at m/z 163 by [108]. The energy required for its fragmentation is too high, around 1.8 eV.
- Furthermore, the ion assigned to m/z 147 does not have proper isotopic distribution (note that the scale is logarithmic and m/z 149 is not 1/3 of m/z 147)

7.4 Results and discussion

7.4.1 PTR-MS

7.4.1.1 Isoflurane reaction with H_3O^+

7.4.1.2 Isoflurane reaction with O_2^+

7.4.1.3 Sevoflurane reaction with H_3O^+

7.5 Conclusions and further remarks

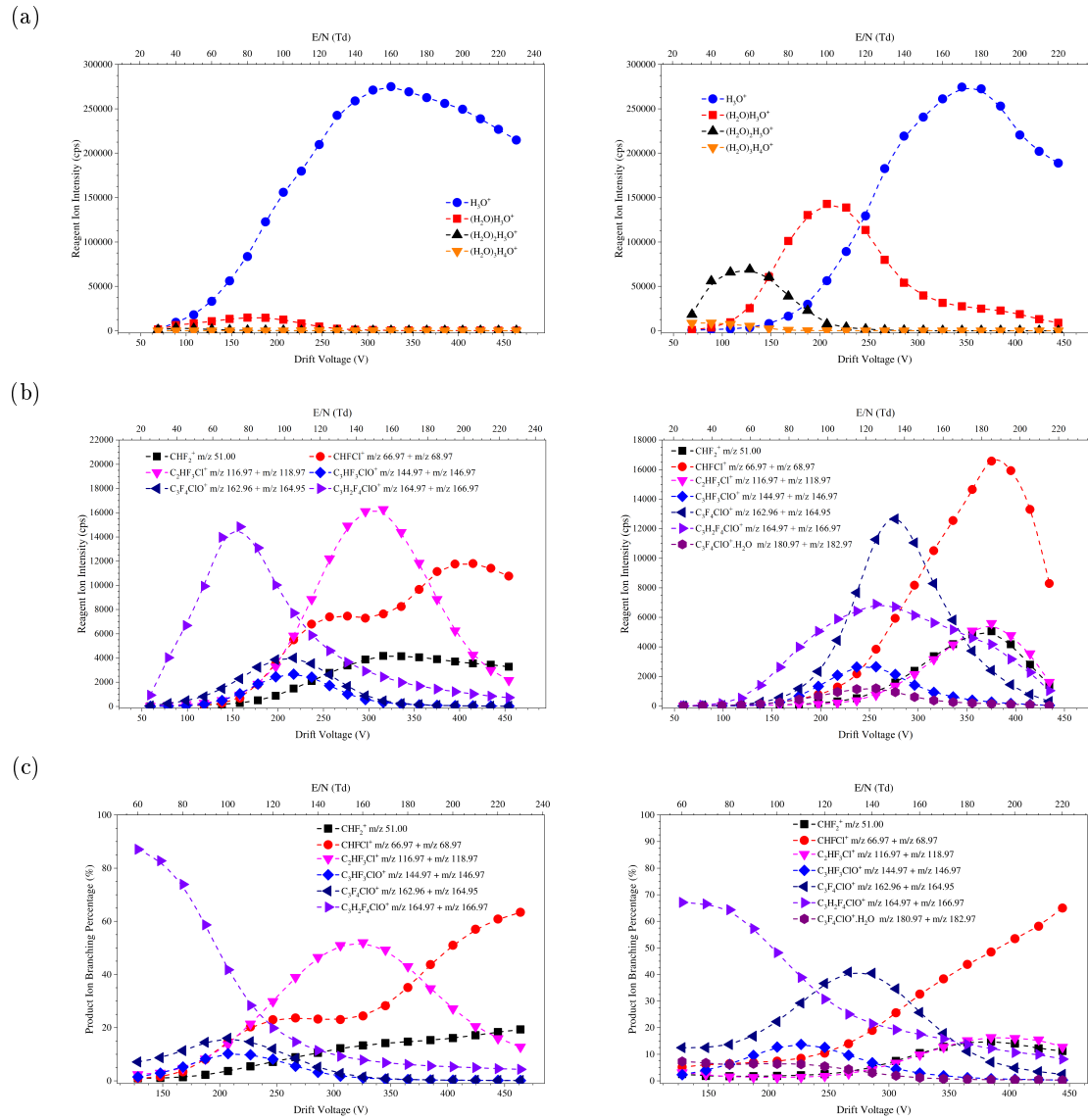


Figure 7.3: Reagent ions intensity (a) and ISOF product ions intensity (b) and distribution plots (c) in dry (left) and humid (right) conditions, H_3O^+ .

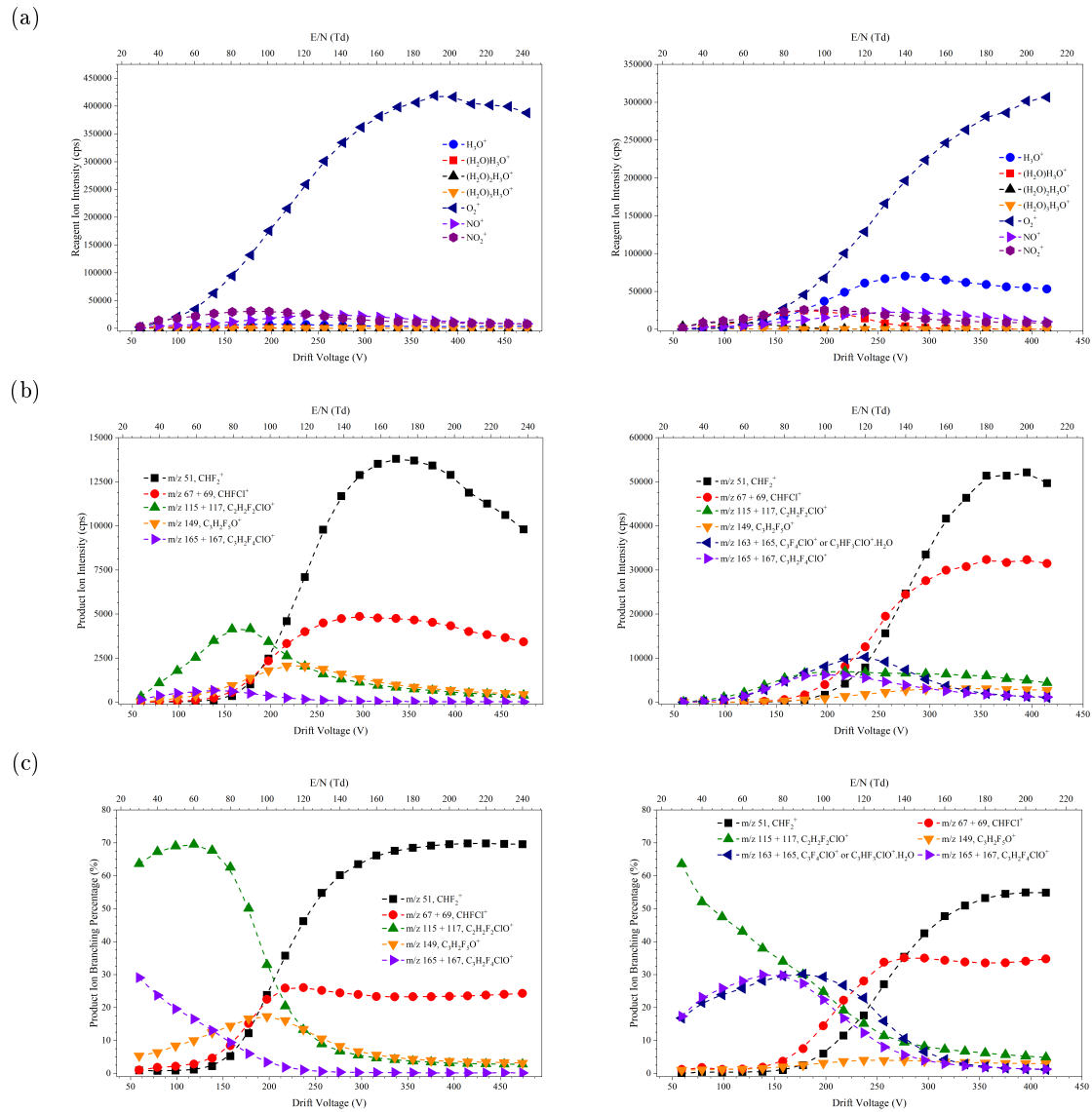


Figure 7.4: Reagent ions intensity (a) and ISOF product ions intensity (b) and distribution plots (c) in dry (left) and humid (right) conditions, O_2^+ .

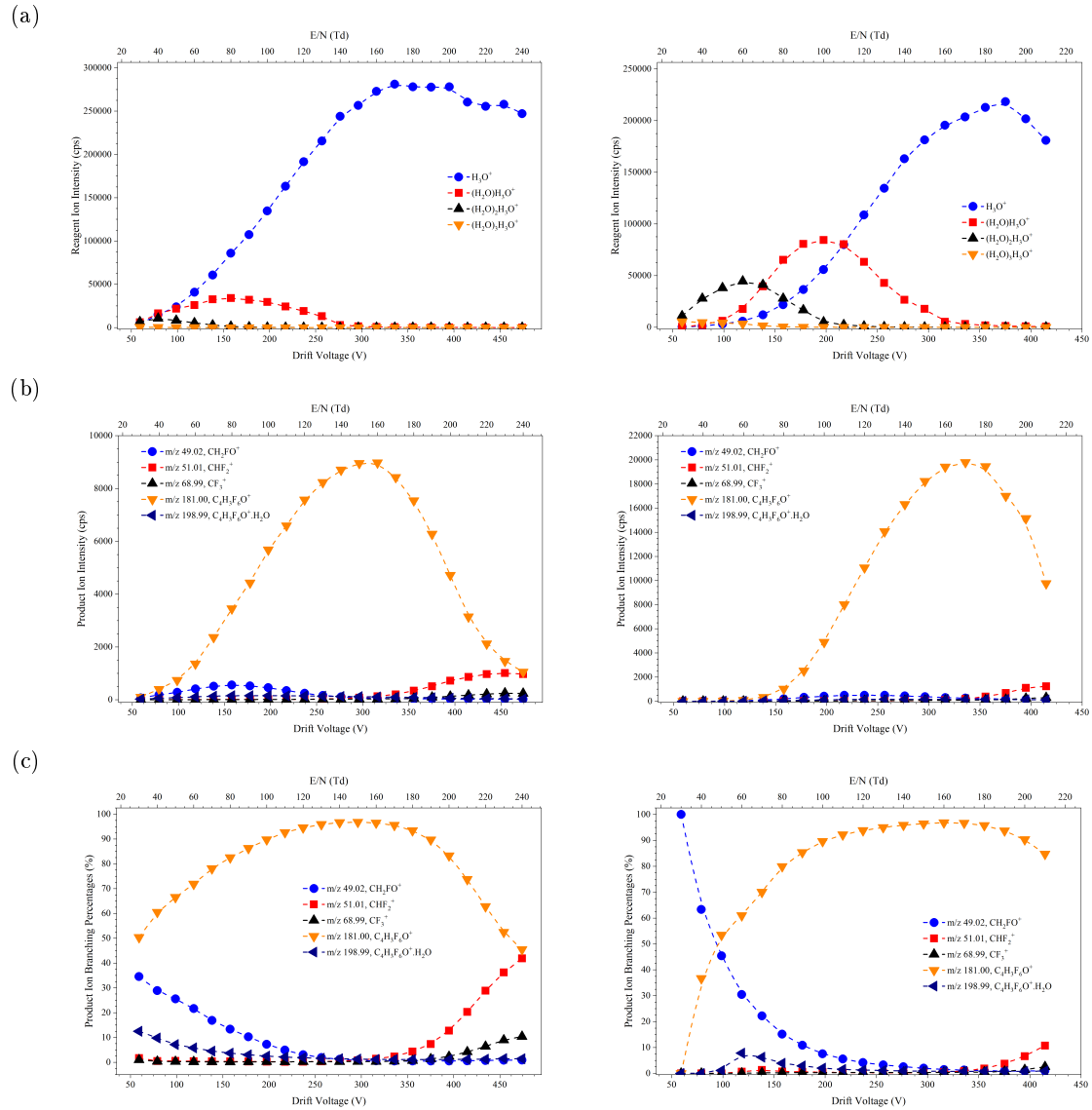


Figure 7.5: Reagent ions intensity (a) and SEVO product ions intensity (b) and distribution plots (c) in dry (left) and humid (right) conditions, H_3O^+ .

References

1. Hunter, E. P. L. & Lias, S. G. Evaluated Gas Phase Basicities and Proton Affinities of Molecules: An Update. *Journal of Physical and Chemical Reference Data* **27**, 413–656 (1998).
2. Schiff, H. I. & Bohme, D. K. Flowing afterglow studies at York University. *International Journal of Mass Spectrometry and Ion Physics* **16**, 167–189 (1975).
3. González-Méndez, R., Watts, P., Howse, D., Procino, I., McIntyre, H. & Mayhew, C. Ion Mobility Studies on the Negative Ion-Molecule Chemistry of Isoflurane and Enflurane. *Journal of the American Society for Mass Spectrometry* **28**, 939–946 (2017).
4. Michalcuk, B., Moravsky, L., Papp, P., Mach, P., Sabo, M. & Matejcik, S. Isomer and Conformer Selective Atmospheric Pressure Chemical Ionisation of dimethyl phthalate. *Physical Chemistry Chemical Physics* **21**, 13679–13685 (2019).
5. Borsdorf, H. & Eiceman, G. A. Ion mobility spectrometry: principles and applications. *Applied Spectroscopy Reviews* **41**, 323–375 (2006).
6. Ellis, A. M. & Mayhew, C. A. *Proton Transfer Reaction Mass Spectrometry: Principles and Applications* (John Wiley & Sons, 2013).
7. Smith, D. & Španěl, P. Selected ion flow tube mass spectrometry (SIFT-MS) for on-line trace gas analysis. *Mass spectrometry reviews* **24**, 661–700 (2005).
8. Turner, C., Španěl, P. & Smith, D. A longitudinal study of ammonia, acetone and propanol in the exhaled breath of 30 subjects using selected ion flow tube mass spectrometry, SIFT-MS. *Physiological Measurement* **27**, 321 (2006).

9. Lindinger, W., Hansel, A. & Jordan, A. On-line monitoring of volatile organic compounds at pptv levels by means of proton-transfer-reaction mass spectrometry (PTR-MS). Medical applications, food control and environmental research. *International Journal of Mass Spectrometry and Ion Processes* **173**, 191–241 (1998).
10. IONICON Analytik GmbH. *Sensitivity and LoD* <http://www.ionicon.com/information/technology/sensitivity-and-lod> (2018).
11. Barber, S., Blake, R. S., White, I. R., Monks, P. S., Reich, F., Mullock, S. & Ellis, A. M. Increased sensitivity in proton transfer reaction mass spectrometry by incorporation of a radio frequency ion funnel. *Analytical chemistry* **84**, 5387–5391 (2012).
12. González-Méndez, R., Watts, P., Olivenza-León, D., Reich, D. F., Mullock, S. J., Corlett, C. A., Cairns, S., Hickey, P., Brookes, M. & Mayhew, C. A. Enhancement of Compound Selectivity Using a Radio Frequency Ion-Funnel Proton Transfer Reaction Mass Spectrometer: Improved Specificity for Explosive Compounds. *Analytical Chemistry* **88**, 10624–10630 (2016).
13. González-Méndez, R., Watts, P., Reich, D. F., Mullock, S. J., Cairns, S., Hickey, P., Brookes, M. & Mayhew, C. A. Use of Rapid Reduced Electric Field Switching to Enhance Compound Specificity for Proton Transfer Reaction-Mass Spectrometry. *Analytical Chemistry* **90**, 5664–5670 (2018).
14. De Gouw, J. A., Goldan, P. D., Warneke, C., Kuster, W. C., Roberts, J. M., Marchewka, M., Bertman, S. B., Pszenny, A. A. P. & Keene, W. C. Validation of proton transfer reaction-mass spectrometry (PTR-MS) measurements of gas-phase organic compounds in the atmosphere during the New England Air Quality Study (NEAQS) in 2002. *Journal of Geophysical Research: Atmospheres* **108** (2003).
15. Rogers, T., Grimsrud, E., Herndon, S., Jayne, J., Kolb, C., Allwine, E., Westberg, H., Lamb, B., Zavala, M., Molina, L., Molina, M. & Knighton, W. On-road measurements of volatile organic compounds in the Mexico City metropolitan area using proton transfer reaction mass spectrometry. *International Journal of Mass Spectrometry* **252**, 26–37 (2006).

16. González-Méndez, R., Reich, D. F., Mullock, S. J., Corlett, C. A. & Mayhew, C. A. Development and use of a thermal desorption unit and proton transfer reaction mass spectrometry for trace explosive detection: Determination of the instrumental limits of detection and an investigation of memory effects. *International Journal of Mass Spectrometry* **385**, 13–18 (2015).
17. Sulzer, P., Agarwal, B., Jürschik, S., Lanza, M., Jordan, A., Hartungen, E., Hanel, G., Mark, L., Mark, T. D., González-Méndez, R., Watts, P. & Mayhew, C. A. Applications of switching reagent ions in proton transfer reaction mass spectrometric instruments for the improved selectivity of explosive compounds. *International Journal of Mass Spectrometry* **354**, 123–128 (2013).
18. Jürschik, S., Agarwal, B., Kassebacher, T., Sulzer, P., Mayhew, C. A. & Märk, T. D. Rapid and facile detection of four date rape drugs in different beverages utilizing proton transfer reaction mass spectrometry (PTR-MS). *Journal of Mass Spectrometry* **47**, 1092–1097 (2012).
19. Agarwal, B., Petersson, F., Jürschik, S., Sulzer, P., Jordan, A., Märk, T. D., Watts, P. & Mayhew, C. A. Use of proton transfer reaction time-of-flight mass spectrometry for the analytical detection of illicit and controlled prescription drugs at room temperature via direct headspace sampling. *Analytical and Bioanalytical Chemistry* **400**, 2631–2639 (2011).
20. Fernández del Río, R., O'Hara, M., Holt, A., Pemberton, P., Shah, T., Whitehouse, T. & Mayhew, C. Volatile Biomarkers in Breath Associated With Liver Cirrhosis – Comparisons of Pre- and Post-liver Transplant Breath Samples. *EBioMedicine* **2**, 1243–1250 (2015).
21. Karl, T., Prazeller, P., Mayr, D., Jordan, A., Rieder, J., Fall, R. & Lindinger, W. Human breath isoprene and its relation to blood cholesterol levels: new measurements and modeling. *Journal of Applied Physiology* **91**, 762–770 (2001).
22. Amann, A., Mochalski, P., Ruzsanyi, V., Broza, Y. Y. & Haick, H. Assessment of the exhalation kinetics of volatile cancer biomarkers based on their physicochemical properties. *Journal of Breath Research* **8**, 016003 (2014).
23. Boscaini, E., van Ruth, S., Biasioli, F., Gasperi, F. & Märk, T. D. Gas Chromatography-Olfactometry (GC-O) and Proton Transfer Reaction-Mass Spectrometry (PTR-MS) Ana-

- lysis of the Flavor Profile of Grana Padano, Parmigiano Reggiano, and Grana Trentino Cheeses. *Journal of Agricultural and Food Chemistry* **51**, 1782–1790 (2003).
24. Aprea, E., Biasioli, F., Carlin, S., Endrizzi, I. & Gasperi, F. Investigation of Volatile Compounds in Two Raspberry Cultivars by Two Headspace Techniques: Solid-Phase Microextraction/Gas Chromatography-Mass Spectrometry (SPME/GC-MS) and Proton-Transfer Reaction-Mass Spectrometry (PTR-MS). *Journal of Agricultural and Food Chemistry* **57**, 4011–4018 (2009).
25. Fabris, A., Biasioli, F., Granitto, P. M., Aprea, E., Cappellin, L., Schuhfried, E., Soukoulis, C., Märk, T. D., Gasperi, F. & Endrizzi, I. PTR-TOF-MS and data-mining methods for rapid characterisation of agro-industrial samples: influence of milk storage conditions on the volatile compounds profile of Trentingrana cheese. *Journal of Mass Spectrometry* **45**, 1065–1074.
26. Lanza, M., Acton, W. J., Sulzer, P., Breiev, K., Jürschik, S., Jordan, A., Hartungen, E., Hanel, G., Märk, L., Märk, T. D. *et al.* Selective reagent ionisation-time of flight-mass spectrometry: a rapid technology for the novel analysis of blends of new psychoactive substances. *Journal of Mass Spectrometry* **50**, 427–431 (2015).
27. Ikezoe, Y., Matsuoka, S., Takebe, M. & Viggiano, A. Gas Phase Ion - Molecule Reaction Rate Constants Through 1986. *Maruzen Company Ltd, Tokyo* (1987).
28. Wannier, G. H. Motion of gaseous ions in a strong electric field. *Physical Review* **83**, 281–289 (1951).
29. Wannier, G. H. Motion of gaseous ions in a strong electric field. II. *Physical Review* **87**, 795–798 (1952).
30. McFarland, M., Albritton, D., Fehsenfeld, F., Ferguson, E. & Schmeltekopf, A. Flow-drift technique for ion mobility and ion-molecule reaction rate constant measurements. II. Positive ion reactions of N⁺, O⁺, and H₂⁺ with O₂ and O⁺ with N₂ from thermal to 2 eV. *The Journal of chemical physics* **59**, 6620–6628 (1973).
31. Spesyvyyi, A. & Španěl, P. Determination of residence times of ions in a resistive glass selected ion flow-drift tube using the Hadamard transformation. *Rapid Communications in Mass Spectrometry* **29**, 1563–1570.

32. Hirschfelder, J. O., Curtiss, C. F., Bird, R. B. & Mayer, M. G. *Molecular theory of gases and liquids* (Wiley New York, 1954).
33. Ismail, A. F., Khulbe, K. C. & Matsuura, T. Gas separation membranes. *Switzerland: Springer*, 14 (2015).
34. IONICON Analytik GmbH. *SION BOOSTER – IONICON ion funnel technology* <https://www.ionicon.com/information/technology/ion-booster> (2019).
35. Krechmer, J., Lopez-Hilfiker, F., Koss, A., Hutterli, M., Stoermer, C., Deming, B., Kimmel, J., Warneke, C., Holzinger, R., Jayne, J. *et al.* Evaluation of a new reagent-ion source and focusing ion–molecule reactor for use in proton-transfer-reaction mass spectrometry. *Analytical chemistry* **90**, 12011–12018 (2018).
36. NIST. *Atomic weights and isotopic compositions for oxygen* https://physics.nist.gov/cgi-bin/Compositions/stand_alone.pl?ele=O&isotype=some (2019).
37. NIST. *Atomic weights and isotopic compositions for carbon* https://physics.nist.gov/cgi-bin/Compositions/stand_alone.pl?ele=C&isotype=some (2019).
38. NIST. *Atomic weights and isotopic compositions for chlorine* https://physics.nist.gov/cgi-bin/Compositions/stand_alone.pl?ele=Cl&isotype=some (2019).
39. NIST. *Atomic weights and isotopic compositions for bromine* https://physics.nist.gov/cgi-bin/Compositions/stand_alone.pl?ele=Br&isotype=some (2019).
40. Frisch, M. J., Trucks, G., Schlegel, H., Scuseria, G., Robb, M., Cheeseman, J., Scalmani, G., Barone, V., Mennucci, B., Petersson, G. *et al.* Gaussian 09, Revision D. 01, Gaussian. Inc.: Wallingford, CT (2009).
41. Müller, M., Eichler, P., D'Anna, B., Tan, W. & Wisthaler, A. Direct sampling and analysis of atmospheric particulate organic matter by proton-transfer-reaction mass spectrometry. *Analytical chemistry* **89**, 10889–10897 (2017).
42. KORE Technology Ltd. *PREFICS - Pre concentrator with Fast Integrated Chromatographic Separation* <https://www.kore.co.uk/prefics.htm> (2019).
43. Conrad, F. J. *Hand held explosives detection system*. US Patent 5 138 889. Aug. 1992.
44. Carroll, A. L., Miskolczy, G., Fraim, F. W., Achter, E. K. & Lieb, D. P. *Hand-held sample gun for vapor collection*. US Patent 5 123 274. June 1992.

45. Jjunju, F. P., Maher, S., Li, A., Syed, S. U., Smith, B., Heeren, R. M., Taylor, S. & Cooks, R. G. Hand-held portable desorption atmospheric pressure chemical ionization ion source for in situ analysis of nitroaromatic explosives. *Analytical chemistry* **87**, 10047–10055 (2015).
46. Staymates, M. E., MacCrehan, W. A., Staymates, J. L., Kunz, R. R., Mendum, T., Ong, T.-H., Geurtzen, G., Gillen, G. J. & Craven, B. A. Biomimetic sniffing improves the detection performance of a 3D printed nose of a dog and a commercial trace vapor detector. *Scientific Reports* **6**, 36876 (2016).
47. Blenkhorn, D. J. *Novel approaches to the measurement of complex atmospheric VOC mixtures using proton transfer reaction mass spectrometry*. PhD thesis (University of Birmingham, 2019).
48. Malásková, M., Olivenza-León, D., Piel, F., Mochalski, P., Sulzer, P., Jürschik, S., Mayhew, C. & Maerk, T. Compendium of the reactions of H₃O⁺ with selected ketones of relevance to breath analysis using proton transfer reaction mass spectrometry. *Frontiers in Chemistry* **7**, 401 (2019).
49. Ruzsanyi, V., Fischer, L., Herbig, J., Ager, C. & Amann, A. Multi-capillary-column proton-transfer-reaction time-of-flight mass spectrometry. *Journal of Chromatography A* **1316**, 112–118 (2013).
50. Romano, A., Fischer, L., Herbig, J., Campbell-Sills, H., Coulon, J., Lucas, P., Cappellin, L. & Biasioli, F. Wine analysis by FastGC proton-transfer reaction-time-of-flight-mass spectrometry. *International Journal of Mass Spectrometry* **369**, 81–86 (2014).
51. Fischer, L., Klinger, A., Herbig, J., Winkler, K., Gutmann, R. & Hansel, A. *The LCU: Versatile Trace Gas Calibration. Proceedings of the 6th International Conference on Proton Transfer Reaction Mass Spectrometry and its Applications*. Obergurgl, Austria (eds Hansel, A. & Dunkl, J.) (Innsbruck University Press, Feb. 2013), 192–195.
52. Lanza, M., Acton, W. J., Jürschik, S., Sulzer, P., Breiev, K., Jordan, A., Hartungen, E., Hanel, G., Märk, L., Mayhew, C. A. *et al.* Distinguishing two isomeric mephedrone substitutes with selective reagent ionisation mass spectrometry (SRI-MS). *Journal of Mass Spectrometry* **48**, 1015–1018 (2013).

53. Mastroianni, N., López-García, E., Postigo, C., Barceló, D. & de Alda, M. L. Five-year monitoring of 19 illicit and legal substances of abuse at the inlet of a wastewater treatment plant in Barcelona (NE Spain) and estimation of drug consumption patterns and trends. *Science of The Total Environment* **609**, 916–926 (2017).
54. McCance-Katz, E. F., Price, L. H., McDougle, C. J., Kosten, T. R., Black, J. E. & Jatlow, P. I. Concurrent cocaine-ethanol ingestion in humans: pharmacology, physiology, behavior, and the role of cocaethylene. *Psychopharmacology* **111**, 39–46 (1993).
55. U.S. Environmental Protection Agency. *Chemistry Dashboard: Properties of cocaine*.
56. Price, P., Swofford, H. & Buttrill, S. New drift-tube source for use in chemical ionization mass spectrometry. *Analytical Chemistry* **49**, 1497–1500 (1977).
57. Wang, P. & Bartlett, M. G. Collision-induced dissociation mass spectra of cocaine, and its metabolites and pyrolysis products. *Journal of mass spectrometry* **33**, 961–967 (1998).
58. Clauwaert, K. M., Van Bocxlaer, J. F., Lambert, W. E., Van den Eeckhout, E. G., Lemiere, F., Esmans, E. L. & De Leenheer, A. P. Narrow-bore HPLC in combination with fluorescence and electrospray mass spectrometric detection for the analysis of cocaine and metabolites in human hair. *Analytical chemistry* **70**, 2336–2344 (1998).
59. Shaffer, S. A., Tang, K., Anderson, G. A., Prior, D. C., Udseth, H. R. & Smith, R. D. A novel ion funnel for focusing ions at elevated pressure using electrospray ionization mass spectrometry. *Rapid communications in mass spectrometry* **11**, 1813–1817 (1997).
60. Kelly, R. T., Tolmachev, A. V., Page, J. S., Tang, K. & Smith, R. D. The ion funnel: theory, implementations, and applications. *Mass spectrometry reviews* **29**, 294–312 (2010).
61. Blake, R. S., Whyte, C., Hughes, C. O., Ellis, A. M. & Monks, P. S. Demonstration of proton-transfer reaction time-of-flight mass spectrometry for real-time analysis of trace volatile organic compounds. *Analytical Chemistry* **76**, 3841–3845 (2004).
62. Ennis, C., Reynolds, J., Keely, B. & Carpenter, L. A hollow cathode proton transfer reaction time of flight mass spectrometer. *International Journal of Mass Spectrometry* **247**, 72–80 (2005).

63. Brown, P., Watts, P., Märk, T. & Mayhew, C. Proton transfer reaction mass spectrometry investigations on the effects of reduced electric field and reagent ion internal energy on product ion branching ratios for a series of saturated alcohols. *International Journal of Mass Spectrometry* **294**, 103–111 (2010).
64. Sulzer, P., Petersson, F., Agarwal, B., Becker, K. H., Jürschik, S., Märk, T. D., Perry, D., Watts, P. & Mayhew, C. A. Proton transfer reaction mass spectrometry and the unambiguous real-time detection of 2, 4, 6 trinitrotoluene. *Analytical chemistry* **84**, 4161–4166 (2012).
65. Kassebacher, T., Sulzer, P., Jürschik, S., Hartungen, E., Jordan, A., Edtbauer, A., Feil, S., Hanel, G., Jakusch, S., Märk, L. *et al.* Investigations of chemical warfare agents and toxic industrial compounds with proton-transfer-reaction mass spectrometry for a real-time threat monitoring scenario. *Rapid Communications in Mass Spectrometry* **27**, 325–332 (2013).
66. Sulzer, P., Agarwal, B., Jürschik, S., Lanza, M., Jordan, A., Hartungen, E., Hanel, G., Märk, L., Märk, T. D., González-Méndez, R. *et al.* Applications of switching reagent ions in proton transfer reaction mass spectrometric instruments for the improved selectivity of explosive compounds. *International Journal of Mass Spectrometry* **354**, 123–128 (2013).
67. Agarwal, B., González-Méndez, R., Lanza, M., Sulzer, P., Märk, T. D., Thomas, N. & Mayhew, C. A. Sensitivity and selectivity of switchable reagent ion soft chemical ionization mass spectrometry for the detection of picric acid. *The Journal of Physical Chemistry A* **118**, 8229–8236 (2014).
68. Acton, W. J., Lanza, M., Agarwal, B., Jürschik, S., Sulzer, P., Breiev, K., Jordan, A., Hartungen, E., Hanel, G., Märk, L. *et al.* Headspace analysis of new psychoactive substances using a Selective Reagent Ionisation-Time of Flight-Mass Spectrometer. *International journal of mass spectrometry* **360**, 28–38 (2014).
69. Lynn, E. C., Chung, M.-C. & Han, C.-C. Characterizing the transmission properties of an ion funnel. *Rapid Communications in Mass Spectrometry* **14**, 2129–2134 (2000).
70. Mayhew, C., Sulzer, P., Petersson, F., Haidacher, S., Jordan, A., Märk, L., Watts, P. & Märk, T. Applications of proton transfer reaction time-of-flight mass spectrometry for the

- sensitive and rapid real-time detection of solid high explosives. *International Journal of Mass Spectrometry* **289**, 58–63 (2010).
71. Olivenza-León, D., Mayhew, C. A. & González-Méndez, R. Selective Reagent Ion Mass Spectrometric Investigations of the Nitroanilines. *Journal of the American Society for Mass Spectrometry*, 1–8 (2019).
72. Biasioli, F., Yeretzian, C., Märk, T. D., Dewulf, J. & Van Langenhove, H. Direct-injection mass spectrometry adds the time dimension to (B) VOC analysis. *TrAC Trends in Analytical Chemistry* **30**, 1003–1017 (2011).
73. Trefz, P., Schubert, J. K. & Miekisch, W. Effects of humidity, CO₂ and O₂ on real-time quantitation of breath biomarkers by means of PTR-ToF-MS. *Journal of breath research* **12**, 026016 (2018).
74. Herbig, J. & Beauchamp, J. Towards standardization in the analysis of breath gas volatiles. *Journal of breath research* **8**, 037101 (2014).
75. Ruzsányi, V., Kalapos, M. P., Schmidl, C., Karall, D., Scholl-Bürgi, S. & Baumann, M. Breath profiles of children on ketogenic therapy. *Journal of breath research* **12**, 036021 (2018).
76. Critchley, A., Elliott, T., Harrison, G., Mayhew, C., Thompson, J. & Worthington, T. The proton transfer reaction mass spectrometer and its use in medical science: applications to drug assays and the monitoring of bacteria. *International Journal of Mass Spectrometry* **239**, 235–241 (2004).
77. Shen, C., Li, J., Han, H., Wang, H., Jiang, H. & Chu, Y. Triacetone triperoxide detection using low reduced-field proton transfer reaction mass spectrometer. *International Journal of Mass Spectrometry* **285**, 100–103 (2009).
78. Jürschik, S., Sulzer, P., Petersson, F., Mayhew, C., Jordan, A., Agarwal, B., Haidacher, S., Seehauser, H., Becker, K. & Märk, T. Proton transfer reaction mass spectrometry for the sensitive and rapid real-time detection of solid high explosives in air and water. *Analytical and bioanalytical chemistry* **398**, 2813–2820 (2010).

79. González-Méndez, R. *Development and applications of proton transfer reaction-mass spectrometry for homeland security: trace detection of explosives* PhD thesis (University of Birmingham, 2017).
80. Petersson, F., Sulzer, P., Mayhew, C. A., Watts, P., Jordan, A., Märk, L. & Märk, T. D. Real-time trace detection and identification of chemical warfare agent simulants using recent advances in proton transfer reaction time-of-flight mass spectrometry. *Rapid Communications in Mass Spectrometry* **23**, 3875–3880 (2009).
81. González-Méndez, R. & Mayhew, C. A. Applications of direct injection soft chemical ionisation-mass spectrometry for the detection of pre-blast smokeless powder organic additives. *Journal of the American Society for Mass Spectrometry* **30**, 615–624 (2019).
82. S., C. S. *Ullmann's Encyclopedia of Industrial Chemistry* **4**, 31–34 (MCB UP Ltd, Jan. 1988).
83. Yuan, H., Li, D., Liu, Y., Xu, X. & Xiong, C. Nitrogen-doped carbon dots from plant cytoplasm as selective and sensitive fluorescent probes for detecting p-nitroaniline in both aqueous and soil systems. *Analyst* **140**, 1428–1431 (2015).
84. Lu, X., Yang, Y., Zeng, Y., Li, L. & Wu, X. Rapid and reliable determination of p-nitroaniline in wastewater by molecularly imprinted fluorescent polymeric ionic liquid microspheres. *Biosensors and Bioelectronics* **99**, 47–55 (2018).
85. Jarvis, G., Kennedy, R., Mayhew, C. & Tuckett, R. Charge transfer from neutral perfluorocarbons to various cations: long-range versus short-range reaction mechanisms. *International Journal of Mass Spectrometry* **202**, 323–343 (2000).
86. U.S. Environmental Protection Agency. *Chemistry Dashboard: Properties of 2-nitroaniline*. <https://comptox.epa.gov/dashboard/dsstoxdb/results?search=DTXSID1025726#properties> (2019).
87. U.S. Environmental Protection Agency. *Chemistry Dashboard: Properties of 3-nitroaniline*. <https://comptox.epa.gov/dashboard/dsstoxdb/results?search=DTXSID8020961#properties> (2019).

88. U.S. Environmental Protection Agency. *Chemistry Dashboard: Properties of 4-nitroaniline.* <https://comptox.epa.gov/dashboard/dsstoxdb/results?search=DTXSID8020961#properties> (2019).
89. González-Méndez, R., Watts, P., Howse, D. C., Procino, I., McIntyre, H. & Mayhew, C. A. Ion mobility studies on the negative ion-molecule chemistry of pentachloroethane. *International Journal of Mass Spectrometry* **417**, 16–21 (2017).
90. Linstrom, P. & Mallard, W. *NIST chemistry webbook. NIST standard reference database 69.* National Institute of Standards and Technology 2015.
91. Tonkyn, R. G., Winniczek, J. W. & White, M. G. Rotationally resolved photoionization of O₂⁺ near threshold. *Chemical physics letters* **164**, 137–142 (1989).
92. Harrison, A. G. & Kallury, R. K. M. R. Chemical ionization mass spectra of mononitroarenes. *Organic Mass Spectrometry* **15**, 284–288 (1980).
93. Beynon, J., Lester, G. & Williams, A. Some specific molecular rearrangements in the mass spectra of organic compounds. *The Journal of Physical Chemistry* **63**, 1861–1868 (1959).
94. Petersson, F., Sulzer, P., Mayhew, C. A., Watts, P., Jordan, A., Märk, L. & Märk, T. D. Real-time trace detection and identification of chemical warfare agent simulants using recent advances in proton transfer reaction time-of-flight mass spectrometry. *Rapid Communications in Mass Spectrometry: An International Journal Devoted to the Rapid Dissemination of Up-to-the-Minute Research in Mass Spectrometry* **23**, 3875–3880 (2009).
95. Materić, D., Lanza, M., Sulzer, P., Herbig, J., Bruhn, D., Gauci, V., Mason, N. & Turner, C. Selective reagent ion-time of flight-mass spectrometry study of six common monoterpenes. *International Journal of Mass Spectrometry* **421**, 40–50 (2017).
96. Anderson, J. C. Measuring breath acetone for monitoring fat loss. *Obesity* **23**, 2327–2334 (2015).
97. De Lacy Costello, B., Amann, A., Al-Kateb, H., Flynn, C., Filipiak, W., Khalid, T., Osborne, D. & Ratcliffe, N. M. A review of the volatiles from the healthy human body. *Journal of breath research* **8**, 014001 (2014).

98. Warneke, C., Van der Veen, C., Luxembourg, S., De Gouw, J. & Kok, A. Measurements of benzene and toluene in ambient air using proton-transfer-reaction mass spectrometry: calibration, humidity dependence, and field intercomparison. *International Journal of Mass Spectrometry* **207**, 167–182 (2001).
99. Tani, A., Hayward, S. & Hewitt, C. Measurement of monoterpenes and related compounds by proton transfer reaction-mass spectrometry (PTR-MS). *International Journal of Mass Spectrometry* **223**, 561–578 (2003).
100. Tani, A., Hayward, S., Hansel, A. & Hewitt, C. N. Effect of water vapour pressure on monoterpene measurements using proton transfer reaction-mass spectrometry (PTR-MS). *International Journal of Mass Spectrometry* **239**, 161–169 (2004).
101. De Gouw, J. & Warneke, C. Measurements of volatile organic compounds in the earth's atmosphere using proton-transfer-reaction mass spectrometry. *Mass spectrometry reviews* **26**, 223–257 (2007).
102. Demarcke, M., Amelynck, C., Schoon, N., Dhooghe, F., Van Langenhove, H. & Dewulf, J. Laboratory studies in support of the detection of sesquiterpenes by proton-transfer-reaction-mass-spectrometry. *International Journal of Mass Spectrometry* **279**, 156–162 (2009).
103. Kari, E., Miettinen, P., Yli-Pirilä, P., Virtanen, A. & Faiola, C. L. PTR-ToF-MS product ion distributions and humidity-dependence of biogenic volatile organic compounds. *International Journal of Mass Spectrometry* **430**, 87–97 (2018).
104. Graus, M., Müller, M. & Hansel, A. High Resolution PTR-TOF: Quantification and Formula Confirmation of VOC in Real Time. *Journal of the American Society for Mass Spectrometry* **21**, 1037–1044 (2010).
105. Jordan, A., Haidacher, S., Hanel, G., Hartungen, E., Herbig, J., Märk, L., Schottkowsky, R., Seehauser, H., Sulzer, P. & Märk, T. An online ultra-high sensitivity Proton-transfer-reaction mass-spectrometer combined with switchable reagent ion capability (PTR+ SRI-MS). *International Journal of Mass Spectrometry* **286**, 32–38 (2009).
106. Buhr, K., van Ruth, S. & Delahunty, C. Analysis of volatile flavour compounds by Proton Transfer Reaction-Mass Spectrometry: fragmentation patterns and discrimination between

- isobaric and isomeric compounds. *International Journal of Mass Spectrometry* **221**, 1–7 (2002).
107. Španěl, P., Ji, Y. & Smith, D. SIFT studies of the reactions of H_3O^+ , NO^+ and O_2^+ with a series of aldehydes and ketones. *International journal of mass spectrometry and ion processes* **165**, 25–37 (1997).
108. Smith, D., Wang, T. & Španěl, P. Analysis of ketones by selected ion flow tube mass spectrometry. *Rapid communications in mass spectrometry* **17**, 2655–2660 (2003).
109. Smith, D., Španěl, P. & Dryahina, K. H_3O^+ , NO^+ and O_2^+ reactions with saturated and unsaturated monoketones and diones; focus on hydration of product ions. *International Journal of Mass Spectrometry* **435**, 173–180 (2019).
110. Spesvyi, A., Smith, D. & Španěl, P. Ion chemistry at elevated ion–molecule interaction energies in a selected ion flow-drift tube: reactions of H_3O^+ , NO^+ and O_2^+ with saturated aliphatic ketones. *Physical Chemistry Chemical Physics* **19**, 31714–31723 (2017).
111. Pan, Y., Zhang, Q., Zhou, W., Zou, X., Wang, H., Huang, C., Shen, C. & Chu, Y. Detection of ketones by a novel technology: dipolar proton transfer reaction mass spectrometry (DP-PTR-MS). *Journal of The American Society for Mass Spectrometry* **28**, 873–879 (2017).
112. Schwarz, K., Filipiak, W. & Amann, A. Determining concentration patterns of volatile compounds in exhaled breath by PTR-MS. *Journal of Breath Research* **3**, 027002 (2009).
113. Spesvyi, A., Smith, D. & Španěl, P. Selected Ion Flow-Drift Tube Mass Spectrometry: Quantification of Volatile Compounds in Air and Breath. *Analytical Chemistry* **87**, 12151–12160 (2015).
114. Su, T. Parametrization of kinetic energy dependences of ion–polar molecule collision rate constants by trajectory calculations. *The Journal of chemical physics* **100**, 4703–4703 (1994).
115. Lide, D. R. *et al.* *CRC handbook of chemistry and physics* (CRC Boca Raton, 2012).

Appendices

Appendix A

Articles in peer-reviewed journals

Published articles

The published articles are attached in the following pages.

1. González-Méndez, R., Watts, P., Olivenza-León, D., Reich, D. F., Mullock, S. J., Corlett, C. A., Cairns, S., Hickey, P., Brookes, M. & Mayhew, C. A. Enhancement of Compound Selectivity Using a Radio Frequency Ion-Funnel Proton Transfer Reaction Mass Spectrometer: Improved Specificity for Explosive Compounds. *Analytical Chemistry* **88**, 10624–10630 (2016).
2. Malásková, M., Olivenza-León, D., Piel, F., Mochalski, P., Sulzer, P., Jürschik, S., Mayhew, C. & Maerk, T. Compendium of the reactions of H_3O^+ with selected ketones of relevance to breath analysis using proton transfer reaction mass spectrometry. *Frontiers in Chemistry* **7**, 401 (2019).
3. Olivenza-León, D., Mayhew, C. A. & González-Méndez, R. Selective Reagent Ion Mass Spectrometric Investigations of the Nitroanilines. *Journal of the American Society for Mass Spectrometry*, 1–8 (2019).

In preparation

Enhancement of Compound Selectivity Using a Radio Frequency Ion-Funnel Proton Transfer Reaction Mass Spectrometer: Improved Specificity for Explosive Compounds

Ramón González-Méndez,^{*,†} Peter Watts,[†] David Olivenza-León,[†] D. Fraser Reich,[‡] Stephen J. Mullock,[‡] Clive A. Corlett,[‡] Stuart Cairns,[§] Peter Hickey,[§] Matthew Brookes,[⊥] and Chris A. Mayhew^{†,||}

[†]Molecular Physics Group, School of Physics and Astronomy, University of Birmingham, Edgbaston, Birmingham B15 2TT, U.K.

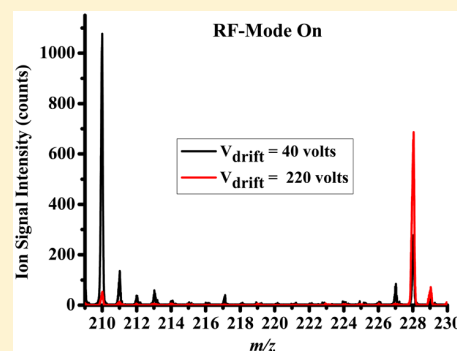
[‡]Kore Technology Ltd, Cambridgeshire Business Park, Ely, Cambridgeshire CB7 4EA, U.K.

[§]Defence Science and Technology Laboratory, Fort Halstead, Sevenoaks, Kent TN14 7BP, U.K.

[⊥]Defence Science and Technology Laboratory, Porton Down, Salisbury, Wilshire SP4 0JQ, U.K.

^{||}Institut für Atemgasanalytik, Leopold-Franzens-Universität Innsbruck, Innsbruck 6020, Austria

ABSTRACT: A key issue with any analytical system based on mass spectrometry with no initial separation of compounds is to have a high level of confidence in chemical assignment. This is particularly true for areas of security, such as airports, and recent terrorist attacks have highlighted the need for reliable analytical instrumentation. Proton transfer reaction mass spectrometry is a useful technology for these purposes because the chances of false positives are small owing to the use of a mass spectrometric analysis. However, the detection of an ion at a given m/z for an explosive does not guarantee that that explosive is present. There is still some ambiguity associated with any chemical assignment owing to the presence of isobaric compounds and, depending on mass resolution, ions with the same nominal m/z . In this article we describe how for the first time the use of a radio frequency ion-funnel (RFIF) in the reaction region (drift tube) of a proton transfer reaction–time-of-flight–mass spectrometer (PTR-ToF-MS) can be used to enhance specificity by manipulating the ion–molecule chemistry through collisional induced processes. Results for trinitrotoluene, dinitrotoluenes, and nitrotoluenes are presented to demonstrate the advantages of this new RFIF-PTR-ToF-MS for analytical chemical purposes.



Ion funnels (IF) have been used since the late 1990s in conjunction with several ionization and mass spectrometric techniques with a key purpose of increasing ion transmission efficiency and hence instrumental sensitivity and dynamic range.^{1,2} Of relevance to our study, Schaffer et al. developed a radio frequency (RF) IF for focusing and transmitting ions from relatively high pressure (>1 Torr) ion sources to mass spectrometers.¹ Given that the typical operating pressure of a drift tube used in proton transfer reaction mass spectrometry (PTR-MS) is close to the optimum pressure for the operation of a RFIF, Kore Technology Ltd. designed and developed a RFIF to be incorporated into drift tubes in order to increase the instruments sensitivity.³ This compact drift tube can simultaneously operate as an ion funnel and a reaction region with a controllable reaction time (dependent on the voltage supplied across the tube). The funnel design and the supplied RF and DC fields act in such a way to channel reagent and product ions toward the exit orifice of the drift tube so that more ions leave the reaction region into the much lower pressure mass spectrometric region, thereby decreasing the loss of ions that occurs at the end of the drift tube. The proof-of-principle study reported increases in sensitivity of this RFIF-PTR-ToF-MS system that were found to be dependent on the m/z of the

product ions, but were typically between 1 and 2 orders of magnitude. For example enhancement factors of 45 and 200 were reported for protonated acetaldehyde and protonated acetone, respectively, at a reduced electric field of 120 Td (where this field refers to the DC voltage applied across the drift tube).³

Given that the RFIF forms part of the drift tube, we asked the question whether the high RF fields involved in the operation of an IF could be used to enhance collisions of the reagent and product ions with the buffer gas in the DT and hence change either the nature of the initial chemical ionization process or induce collisional induced dissociation, respectively, occurring within the DT? We hypothesized that changes would result from raising the internal energy of the product ions and the energy of the reactions between reagent ions and neutral species through collisional processes as a result of the applied RF field. The real question is whether the RF collisional induced dissociation would lead to substantial fragmentation, or be more selective resulting in unique product ions that can be

Received: August 2, 2016

Accepted: October 7, 2016

Published: October 7, 2016

used to identify a chemical compound of interest with a higher specificity than that achievable just by using a standard drift tube at a given reduced electric field. Here we report details on a collaborative project involving KORE Technology Ltd. and the University of Birmingham which investigated the application of a RFIF drift tube of a PTR-ToF-MS for improved selectivity using several explosives as illustrative compounds, namely 2,4,6-trinitrotoluene (TNT), 2,4-, 2,6-, and 3,4-dinitrotoluene (DNT) and 2-, 3-, and 4-nitrotoluene (NT). We will show how the application of a RFIF leads to a higher confidence in compound identification. We thus demonstrate for the first time that the addition of a RFIF to a PTR-ToF-MS results in a more multidimensional analytical instrument that improves the selectivity that can be achieved by operating a drift tube of a PTR-MS in DC mode only.

METHODS

Experimental Details. A KORE Technology Ltd. RFIF Series I PTR-ToF-MS was used. Details of KORE's PTR-ToF-MS system with no IF has been described in detail elsewhere,^{4–6} and hence only the salient points of this instrument are provided here. Using a needle valve, water vapor is introduced into a hollow cathode discharge where, after ionization via electron impact and subsequent ion–molecule processes, the terminal reagent ion is H_3O^+ .⁷ These ions are transferred from the ion source into the drift tube (the reaction region) of the PTR-ToF-MS, which is typically at a pressure of 1 mbar and temperature 100 °C, where they encounter the analyte. H_3O^+ ions react with the analyte M by donating their protons at the collisional rate, providing M has a proton affinity greater than that of water ($\text{PA}(\text{H}_2\text{O}) = 691 \text{ kJ mol}^{-1}$). This process can be non-dissociative (resulting in the protonated molecule MH^+) and/or dissociative. Dissociative proton transfer results in product ions which may be useful in the identification of a compound. Fragmentation may be spontaneous upon proton transfer or may require additional energy which is supplied through collisions with the buffer gas resulting during the migration of ions under the influence of the electric field, E. The ratio of E to the buffer gas number density, N, is an important parameter (known as reduced electric field) which determines the mean collisional energy of ions with the neutral buffer gas. Hence it is the parameter often referred to and changed for investigating product ion branching ratios.^{8–15}

The IF (schematically shown in Figure 1) consists of 29 stainless steel plates of 0.2 mm thickness, mounted on precision-machined ceramic rods at an even spacing of 3.2 mm per plate. Tabs on the electrodes permit a resistor chain on a ceramic strip to be connected in addition to two capacitor stacks which allow the RF to be applied to the second half of the reactor. The orifice diameters of the plates through the first half of the stack is 40 mm, as used in the standard drift tube reactor. In the second half of the drift tube the orifice diameter steadily decreases to 6 mm at the final plate before the exit orifice. Across the complete ion-funnel a DC voltage is applied driving ions axially. When just operating with this voltage we shall refer to the instrument as operating in DC-only mode. In addition to this, to the second part of the drift tube a RF field can be applied. The resonant frequency of the system is ~760 kHz and the amplitude selected for the majority of the studies (peak-to-peak) was 200 V, which is superimposed on the dc voltage gradient across the drift tube.

The main purpose of the RF field is to focus ions radially by creating repulsive effective potentials at the edges of the

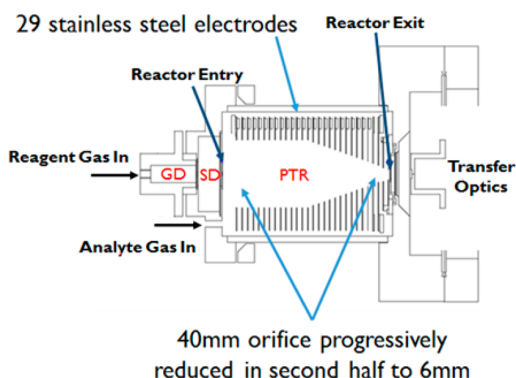


Figure 1. Schematic representation of the KORE Technology Ltd. radio frequency ion funnel drift tube (proton transfer reaction (PTR) region) used in this investigation. Also shown is the ion source region (glow discharge GD), and a source drift (SD) region which is used to extract ions from the GD, aid in breaking-up protonated water clusters and to enhance production of H_3O^+ via additional ion–molecule reactions involving ions that can react with water. After exiting the drift tube the transfer optics guide the ions into the ToF-MS region.

electrodes. However, in addition to this intended purpose, the RF results in ions oscillating between electrodes as they drift down the reactor. This gives ions higher collisional energies than those in the first half of the drift tube. We shall refer to operating the instrument with the RF on as RF-mode. At the end of the drift tube is a 400 μm orifice, through which ions enter the ion transfer region for ToF-MS.

The use of specifying a reduced electric field, E/N , is an appropriate parameter to use in DC-only mode, because it is well-defined. In RF-mode (ion funnel on) the presence of DC and RF electric fields complicates the situation, because the electric field strength varies with distance from the RF electrodes, so that specifying a reduced electric field is not appropriate. Barber et al.³ simply adopted an empirical effective reduced electric field by finding operating conditions for the ion-funnel drift tube that matched the performance of the same drift tube when operated under DC-only mode. However, given that it is uncertain what the effective reduced electric field means, in this article we refer to the DC voltage (V_{drift}) applied across the drift tube.

A thermal desorption unit (TDU) connected to the inlet of the drift tube was used to introduce the explosive samples, details of which have been given elsewhere.⁶ The TDU, connecting lines, and drift tube were operated at a temperature of 150 °C. PTFE swabs (ThermoFisher Scientific) onto which known quantities of explosives were deposited were placed into the TDU. The swabs came prepared from the manufacturer mounted on rectangular cardboard for easy insertion into the TDU. Once a seal was created, a carrier gas (in this study laboratory air) is heated to the temperature of the TDU before it flows through a series of holes in a heated metal plate. This heated air then passes through the swab and into the inlet system driving any desorbed material through to the drift tube creating a temporal concentration “pulse” of typically between 10–20 s of an explosive in the drift tube.⁶ Each swab provided one measurement, which was replicated three times and then the results were averaged and any background signals were subtracted.

Explosive standards were purchased from AccuStandard Inc., New Haven, CT. Typically these standards contained 0.1 mg of the explosive compound in 1 mL of solvent. For TNT, 2,4- and

2,6-DNT, and the NTs this involved an acetonitrile:methanol (1:1) mix. 3,4-DNT was just mixed with methanol. These samples were diluted in the appropriate solvent(s) (HPLC grade) to provide the required quantity of an explosive. Typically 1 μ L of a solvent containing the required mass of an explosive was spotted onto a PTFE swab.

Electronic Structure Calculations. To aid in the interpretation of the experimental results a series of electronic structure calculations have been undertaken at 298 K. These involve density functional theory calculations using the GAUSSIAN09 PROGRAM with the GaussView 5 interface.¹⁶ The B3LYP functional with the 6-31+G(d,p) basis set was used throughout. Although it is appreciated that the drift tube temperature and the effective ion temperature are greater than 298 K, with the effective ion temperature being uncertain, the thermochemical calculations simply provide us with an indicator as to whether a reaction pathway is energetically possible or not.

RESULTS AND DISCUSSION

Reagent Ions. Before we begin discussing the results of the explosives, it is informative to present details on the reagent ion signal as a function of drift tube voltage, comparing intensities for DC-only mode (Figure 2a) and RF-mode (funnel-on) (Figure 2b) under identical operating conditions of hollow cathode and drift tube pressures and temperature. The observed decrease of H_3O^+ reagent ion signal with decreasing drift tube voltage is predominantly a result of the clustering with water molecules in the drift tube, which are not broken-up through collisions at lower drift tube voltages. The marked decrease in total reagent ion signal below about 50 Td is considered to be a result of the low SD potential, which scales with the DC drift tube potential. As the SD voltage decreases we can expect that fewer reagent ions reach the reactor entry.

Figure 2a shows that by 100 Td the H_3O^+ reagent ion signal has reduced significantly and that the protonated water clusters start to dominate at the lowest reduced electric field corresponding to a voltage drop across the drift tube of about 200 V under the operational temperature and pressure values used. (The actual percentage of protonated water clusters for fixed E/N is also strongly dependent on the humidity of the buffer gas in the drift tube, which is dependent on the amount of forward flow of H_2O from the ion source into the drift tube and the humidity of the laboratory air.) In RF-mode no protonated water clusters are observed, because they are broken-up through collisions in the RFIF region of the drift tube. Furthermore, at about 120 V the H_3O^+ intensity is approximately at its maximum value. As the drift voltage decreases, the reagent ion signal decreases. However, even at a drift tube voltage of only 20 V (which in DC-only mode would correspond to a reduced electric field of only about 10 Td) there is still a significant reagent ion count. This enhancement of reagent ion signal at low drift tube voltages can only be a result of the trapping that the RF field provides thereby reducing the diffusional loss that occurs in DC-only mode under low drift tube voltages.

2,4,6-Trinitrotoluene (TNT). Using both PTR-ToF-MS and PTR-Quad-MS systems Sulzer et al. have previously shown that there is an unusual dependence of the intensity of protonated TNT on the reduced electric field in that there is an increase in the sensitivity of detection with increasing E/N .^{9,17} This increase continues until a maximum is reached at about 180 Td, after which the signal intensity shows the more usual

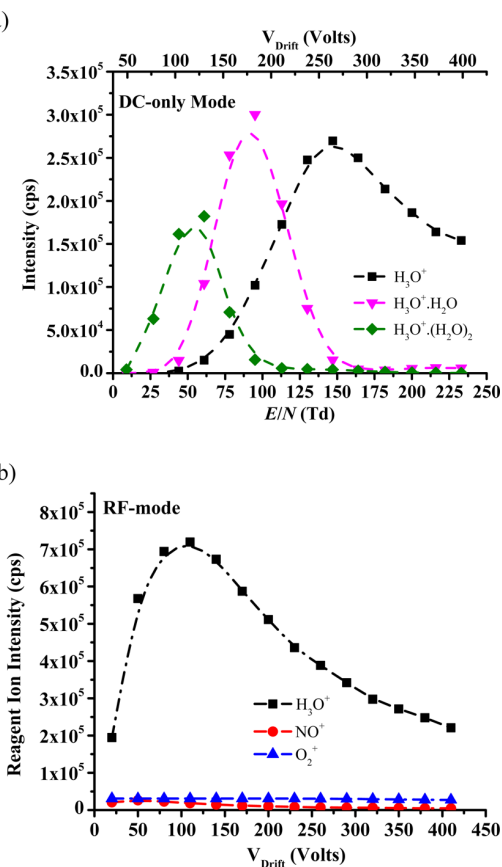


Figure 2. Ion intensities in counts per second (cps) of the water reagent ions present in the drift tube as a function of drift tube voltage (a) in DC-only mode and (b) in RF-mode (ion funnel on). For (b) the ion signals at m/z 30 (NO^+) and 32 (O_2^+) are presented because although low intensity they are still significant and are observed as a result of the improved ion transmission in RF-mode. In DC-mode the signal intensities of these ions are negligible and are therefore not presented.

behavior of decreasing with increasing E/N . This is opposite to what is commonly found in PTR-MS studies, because with reduced reaction times, fragmentation to non-specific product ions, and reduction in ion transmission the protonated molecule intensity reduces with increasing E/N . The explanation of this unusual intensity dependence for TNTH⁺ has been described in detail.⁹ In brief, it is a result of a secondary reaction of TNTH⁺· H_2O (which is readily formed at low E/N) with H_2O leading to a terminal ion which does not contain TNT, namely $\text{H}_3\text{O}^+\cdot\text{H}_2\text{O}$.

In DC-only mode and when a product ion signal is detected, for all E/N values investigated only one product ion is observed that contains the explosive, namely protonated TNT at m/z 228. However, in RF mode, another fragment ion is found at m/z 210, the intensity of which increases with decreasing drift tube voltage (i.e., decreasing E/N in DC mode) down to values under which the PTR-ToF-MS does not perform in DC mode owing to a lack of sufficient transmission of ions to the mass spectrometer (Figure 2a). Typical results obtained for TNT are shown in Figure 3. That the fragment ion m/z 210 intensity increases with decreasing drift tube voltage (Figure 3) is perhaps not what is expected given that decreasing DC voltage means lower collisional energies. However, that only applies in

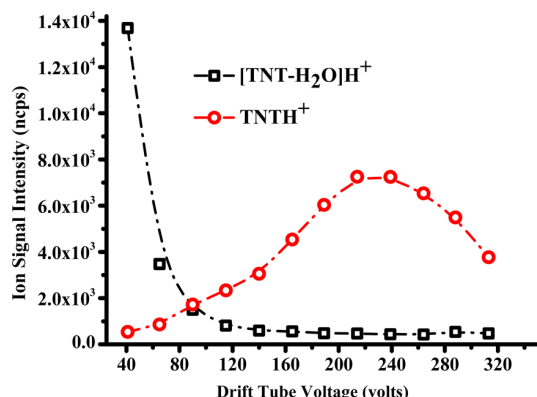
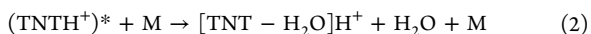
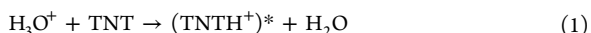


Figure 3. Product ion intensities as a function of drift tube voltage in RF mode. The data have been taken using 100 ng of TNT. The ion signals have been normalized to $10^6 \text{ H}_3\text{O}^+$ reagent ions and drift times. (The lines used in all graphs are just a guide to the eye.)

the first half of the drift tube. As the drift tube voltage is reduced more collisions in the RFIF region of the drift tube occur, which in turn enhances collisional induced dissociation.

Following proton transfer the protonated molecule gains sufficient internal energy through collisions in the RFIF section of the drift tube to eliminate H_2O :



where M is a buffer gas molecule. Thus, specificity can be increased by either switching off and on the RFIF at a specific drift tube voltage or by switching the drift tube voltage. Note that a minor percentage of the observed m/z 210 results from the reaction of the O_2^+ (always present in low concentrations in the drift tube as an impurity ion) with TNT via a dissociative charge transfer process leading to the loss of OH from TNTH^+ .¹²

That the reaction pathway leading to the elimination of H_2O is overall energetically favorable (Table 1) but is only observed

Table 1. Energetics for the Proton Transfer from H_3O^+ to TNT Calculated Using the B3LYP Functional and the 6-31+G(d,p) Basis Set

products	$\Delta H_{298} \text{ kJ mol}^{-1}$	$\Delta G_{298} \text{ kJ mol}^{-1}$
TNTH ⁺ (2NO ₂ syn) + H ₂ O	-46	-47
TNTH ⁺ (2NO ₂ anti) + H ₂ O	-55	-55
TNTH ⁺ (4NO ₂) + H ₂ O	-68	-60
TS syn/anti + H ₂ O	-9	-5

in RF mode, is an indication that there must be an energy barrier for pathway (2). Evidence of this is provided from the results obtained when investigating the effects of changing the RF amplitude at fixed drift tube voltages and fixed frequency. Figure 4 provides a summary of these measurements, which shows that as the RF peak-to-peak voltage is decreased the intensity of the m/z 210 decreases for all drift tube voltages.

The initial step leading to m/z 228 is the transfer of a proton from H_3O^+ to TNT. Protonation of TNT can occur on the nitro groups at the 2 and 4 positions, both having similar proton affinities, although as elimination of water from TNTH^+ will presumably involve the methyl group only protonation of the nitro group in the 2 position is of relevance. However, protonation on the 4 nitro will occur (the PA and GB are

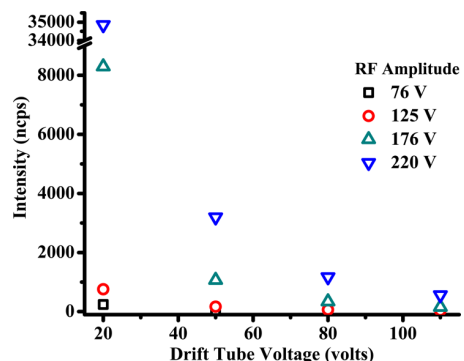


Figure 4. Intensities in ncps of the product ion $[\text{TNT}-\text{H}_2\text{O}]\text{H}^+$ as a function of drift tube voltage and RF amplitude (volts) with the frequency kept at 760 kHz ($\pm 3\%$).

slightly greater than the 2 nitro) and this will reduce the amount of TNTH^+ available to lose water. Two configurations are possible for protonation in the 2 position as illustrated in Figure 5, with the anti being slightly more stable by ca. 8 kJ

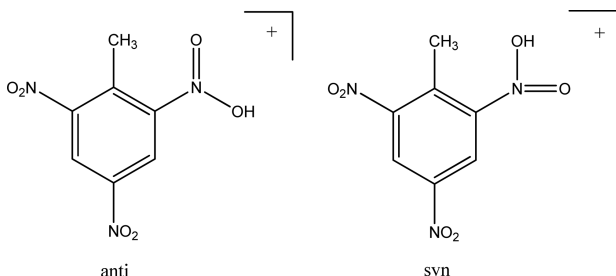


Figure 5. Two possible configurations resulting from protonation of TNT in the 2 position.

mol^{-1} . The transition state energetics for interconversion are $\Delta H_{298}^\ddagger + 46 \text{ kJ mol}^{-1}$ and $\Delta G_{298}^\ddagger + 51 \text{ kJ mol}^{-1}$ above the anti conformation, but whichever is formed there is sufficient energy in the initial protonation to allow rapid interconversion (Table 1).

There are three stable structures for the ion remaining after the elimination of water from TNTH^+ (Figure 6). A fourth structure, similar to $\text{TNTH}^+-\text{H}_2\text{O}$ (b) with the hydrogens of the methylene group orthogonal to the ring, proved to be unstable and rearranged to $\text{TNTH}^+-\text{H}_2\text{O}$ (a). The energetics for the transformation of TNTH^+ to $\text{TNTH}^+-\text{H}_2\text{O}$ (a–c) + H_2O are given in Table 2.

Various attempts using the QST3 approach were made to find transition states for these possible reactions but all lead to $\text{TNTH}^+-\text{H}_2\text{O}$ (c), though interestingly the transition state had a close resemblance to $\text{TNTH}^+-\text{H}_2\text{O}$ (b). The transition state was characterized by one imaginary frequency and the internal reaction coordinate leading to $\text{TNTH}^+-\text{H}_2\text{O}$ (c) in the forward direction and TNTH^+ with the proton on the 2-nitro group in the syn conformation in the reverse direction. The activation energies relative to $\text{TNT} + \text{H}_3\text{O}^+$ are $\Delta H_{298}^\ddagger + 158 \text{ kJ mol}^{-1}$ and $\Delta G_{298}^\ddagger + 162 \text{ kJ mol}^{-1}$.

The presumption that the elimination of water from protonated TNT can only occur when the methyl and nitro groups are adjacent to each other was readily tested by investigating isomers of DNT and NT. For those isomers that satisfy the condition of an adjacent nitro and methyl group,

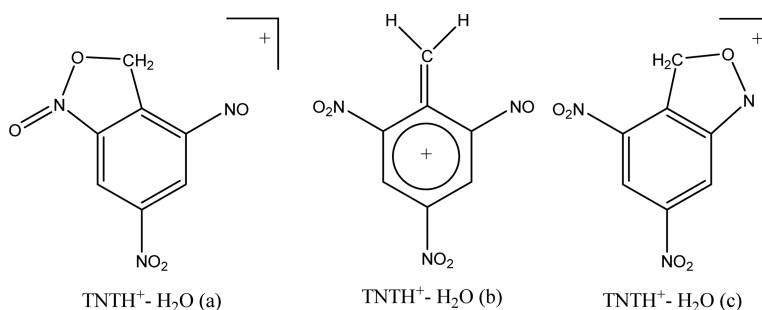


Figure 6. Stable structures of the $[\text{TNT}-\text{H}_2\text{O}]\text{H}^+$ ion.

Table 2. Energetics for the Elimination of Water from TNT Following Proton Transfer from H_3O^+ for the Three Stable Structures Shown in Figure 6

products	ΔH_{298} kJ mol ⁻¹	ΔG_{298} kJ mol ⁻¹
TNTH ⁺ - H ₂ O (a) + 2H ₂ O	-104	-145
TNTH ⁺ - H ₂ O (b) + 2H ₂ O	+47	-7
TNTH ⁺ - H ₂ O (c) + 2H ₂ O	-128	-168

then $[\text{DNT}-\text{H}_2\text{O}]\text{H}^+$ and $[\text{NT}-\text{H}_2\text{O}]\text{H}^+$ fragment ions should be observed, otherwise not. Thus, we predicted to observe elimination of water from the 2,6-DNT, 2,4-DNT, and 2-NT but not from 3,4-DNT, 3-NT, or 4-NT following proton transfer in RF mode.

Dinitrotoluenes. In both RF-mode and DC-only mode for 3,4-DNT the only primary product ion that is observed with any significant intensity for all drift tube voltages is the protonated molecule. That no m/z 165 is observed, which would correspond to the elimination of water from the protonated molecule, is in agreement with our prediction, because neither nitro group are adjacent to the methyl group. With decreasing drift tube voltage the protonated 3,4-DNT clusters with H₂O, leading to a reduction in the DNTH⁺ signal. While this is particularly significant in DC-only mode, with DNTH⁺·(H₂O)_n ($n = 1, 2$ and 3) ions becoming the dominant product ions by about 100 Td, some water clustering is still observed in RF-mode. For example at a drift tube voltage of 20 V the percentage branching ratios are approximately 70, 20, and 10% for DNTH⁺, DNTH⁺·H₂O, and DNTH⁺·(H₂O)₂, respectively.

For the 2,4- and 2,6-DNT isomers, at low drift tube voltages in addition to an observed ion at m/z 201 corresponding to the DNTH⁺·H₂O in RF-mode a product ion is observed at m/z 165, which is $[\text{DNT}-\text{H}_2\text{O}]\text{H}^+$. Figure 7 illustrates this for 2,6-DNT, which shows that the probability for the elimination of water increases with decreasing drift tube voltage (the results for 2,4-DNT in RF-mode are similar, although the production for $[\text{DNT}-\text{H}_2\text{O}]\text{H}^+$ is less by about 10%). In DC-only mode, m/z 165 is also observed for 2,6-DNT, but its intensity only becomes significant when a high drift tube voltage is applied leading to reduced electric fields above about 180 Td, and even then the percentage ion product distribution is only approximately 10% (Figure 8). However, this can explain the slight increase in the production of m/z 165 in Figure 7 when the applied drift tube voltage is above about 275 V. With increasing drift tube voltage additional fragment ions are found at m/z 136 and 91, corresponding to an elimination of HONO and 2NO₂, respectively, from the protonated molecule. These two ions are also found with significant intensities for 2,6-DNT when operating in DC-only mode when the reduced electric

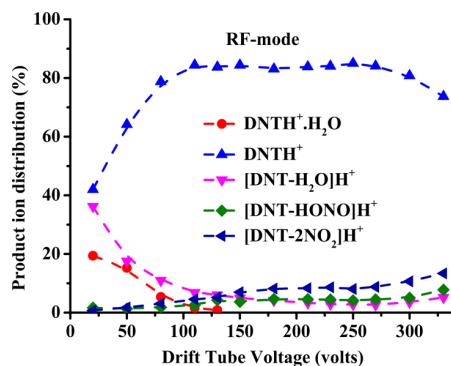


Figure 7. Percentage product ion distributions resulting from the reaction of H_3O^+ with 2,6-DNT in RF-mode including the secondary process resulting in the association of the protonated molecule with water as a function of supplied drift tube voltage.

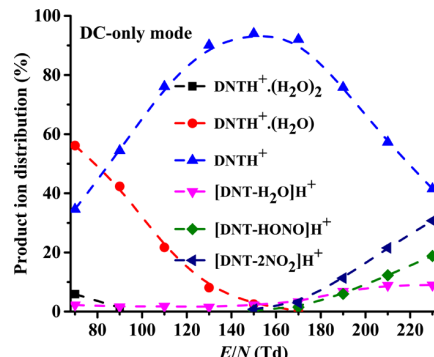


Figure 8. Percentage product ion distributions resulting from the reaction of H_3O^+ with 2,6-DNT in DC-only mode including the secondary process resulting in the association of the protonated molecule with water as a function reduced electric field.

fields is greater than about 160 Td. That DNTH⁺·H₂O is observed in RF-mode at low drift tube voltages, when no protonated water clusters are observed (Figure 2b), requires some explanation. We propose that following a collision the energy involved is distributed in more degrees of freedom for DNTH⁺·H₂O than for $\text{H}_3\text{O}^+ \cdot (\text{H}_2\text{O})_n$ and hence it is less likely for energy to be concentrated into losing the water molecule.

Building on the comprehensive investigation of the TNT system we can go straight to the salient structures and energetics for the loss of water from 2,4-DNT and 2,6-DNT following proton transfer from H_3O^+ . These calculations are given in Table 3a and b, respectively.

Table 3. Energetics for the Elimination of Water from (a) 2,4-DNT and (b) 2,6-DNT Following Proton Transfer from H_3O^+

products	ΔH_{298} kJ mol ⁻¹	ΔG_{298} kJ mol ⁻¹
2,4-DNTH ⁺ (syn) + H_2O	-89	-87
2,4-DNTH ⁺ (anti) + H_2O	-96	-95
TS syn/anti + H_2O	-21	-16
TS for loss of H_2O + H_2O	+126	+130
2,4-DNT- $\text{H}_2\text{O}(\text{c})$ + 2 H_2O	-146	-187
(b)		
products	ΔH_{298} kJ mol ⁻¹	ΔG_{298} kJ mol ⁻¹
2,6-DNTH ⁺ (syn) + H_2O	-87	-88
2,6-DNTH ⁺ (anti) + H_2O	-95	-95
TS syn/anti + H_2O	-42	-38
TS for loss of H_2O + H_2O	+117	+120
2,6-DNT- $\text{H}_2\text{O}(\text{c})$ + 2 H_2O	-177	-217

Nitrotoluenes. In order to further investigate the requirement of methyl and nitro functional groups to be adjacent in order to facilitate the elimination of water when using the RFIF, the three isomers of nitrotoluene have been investigated. We can expect in RF-mode that only 2-NT should have a reaction pathway which would lead to the elimination of water following proton transfer from H_3O^+ . For 3-NT and 4-NT no such elimination should occur. A review of the resulting mass spectra for all three isomers shows that is the case. However, the nitrotoluenes are more complicated than TNT and the DNTs, because other product ions are observed even at the lowest drift tube voltage. The NT isomers show significant fragmentation following proton transfer. This is found to occur in not only RF-mode but also DC-only mode. In addition to the elimination of water, which is not the dominant product ion, channels corresponding to the elimination of C_2H_6 , NO, CH_3NO , NO_2 , and HONO are observed in both modes. This is illustrated in Figure 9 for 2-NT when operating (a) in RF-mode and (b) in DC-only mode. At low drift tube voltages $\text{NTH}^+\cdot\text{H}_2\text{O}$ is observed (Figure 4a) in RF mode, presumably for reasons described above for DNT.

Table 4 presents the DFT energetics calculations for the elimination of water for 2-NT following proton transfer from H_3O^+ .

CONCLUSIONS

A PTR-ToF-MS equipped with a radio frequency ion funnel, originally designed to improve sensitivity, has been used in an unusual way to induce fragmentation of product ions through changes in collisional induced dissociation. We have illustrated how this can be used to improve compound specificity by monitoring the ion signal in RF-mode. We propose that the rapid switching between RF and DC modes would be the best method to enhance selectivity. We are currently developing the instrument to achieve this, and this will be the subject of another article. The key point of this work is that in place of major and costly changes in instrumental design to improve chemical specificity, such as having a high mass resolution time-of-flight mass spectrometer or adding a pre-separation technique, which also makes the instrument unacceptable for use in security areas, a new analytical method has been described which at its heart manipulates the ion chemistry.

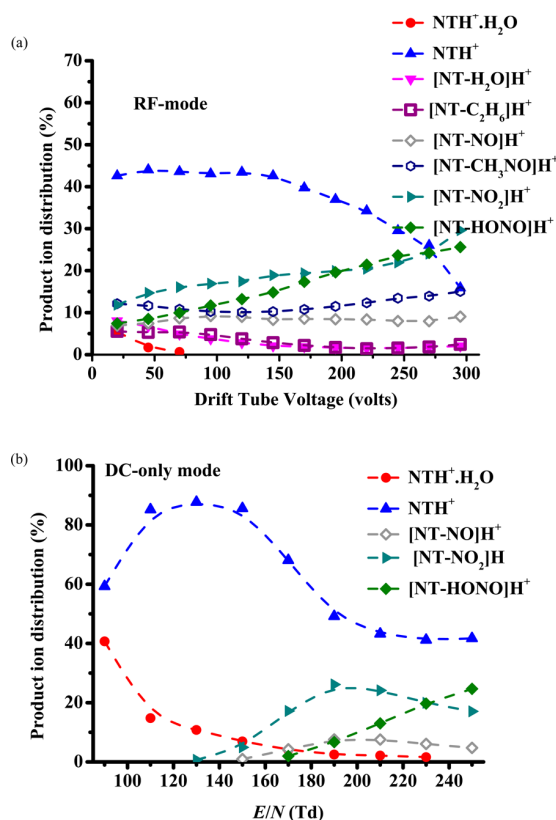


Figure 9. Percentage product ion distributions resulting from the reaction of H_3O^+ with 2-NT in (a) RF-mode and (b) DC-only mode as a function drift tube voltage. Included are the secondary ion-molecule processes resulting in the association of the protonated molecule with water.

Table 4. Energetics for the Elimination of Water from 2-NT Following Proton Transfer from H_3O^+

products	ΔH_{298} kJ mol ⁻¹	ΔG_{298} kJ mol ⁻¹
2-NT H_2O (syn) + H_2O	-132	-138
2-NT H_2O (anti) + H_2O	-105	-110
TS syn/anti + H_2O	-71	-76
TS for loss of H_2O + H_2O	+82	+78
2-NT- H_2O + 2 H_2O	-93	-126

AUTHOR INFORMATION

Corresponding Author

*Tel.: +44 121 414 4668; E-mail: R.GonzalezMendez@bham.ac.uk.

Notes

The authors declare no competing financial interest.

ACKNOWLEDGMENTS

We thank the Defence Science and Technology Laboratory for funding R.G.M. This project was in part supported by the PIMMS and IMPACT ITNs which are in turn supported by the European Commission's seventh Framework Programme under Grant Agreement Numbers 287382 and 674911, respectively.

REFERENCES

- Schaffer, S. A.; Tang, K.; Anderson, G. A.; Prior, D. C.; Udseth, H. R.; Smith, R. D. *Rapid Commun. Mass Spectrom.* **1997**, *11*, 1813.

- (2) Kelly, R. T.; Tolmachev, A. V.; Page, J. S.; Tang, K.; Smith, R. D.; et al. *Mass Spectrom. Rev.* **2010**, *29* (2), 294.
- (3) Barber, S.; et al. *Anal. Chem.* **2012**, *84* (12), 5387.
- (4) Blake, R. S.; Whyte, C.; Hughes, C. O.; Ellis, A. M.; Monks, P. S. *Anal. Chem.* **2004**, *76*, 3841.
- (5) Ennis, C. J.; Reynolds, J. C.; Keely, B. J.; Carpenter, L. J. *Int. J. Mass Spectrom.* **2005**, *247* (1–3), 72.
- (6) González-Méndez, R.; Reich, D. F.; Mullock, S. J.; Corlett, C. A.; Mayhew, C. A. *Int. J. Mass Spectrom.* **2015**, *385*, 13.
- (7) Ellis, A.M.; Mayhew, C.A. *Proton Transfer Reaction Mass Spectrometry: Principles and Applications*, First ed., John Wiley and Sons, 2014.
- (8) Brown, P.; Watts, P.; Märk, T. D.; Mayhew, C. A. *Int. J. Mass Spectrom.* **2010**, *294*, 103.
- (9) Sulzer, P.; Petersson, F.; Agarwal, B.; Becker, K. H.; Jürschik, S.; Märk, T. D.; Perry, D.; Watts, P.; Mayhew, C. A. *Anal. Chem.* **2012**, *84*, 4161.
- (10) Jürschik, S.; Agarwal, B.; Kassebacher, T.; Sulzer, P.; Mayhew, C. A.; Märk, T. D. *J. Mass Spectrom.* **2012**, *47*, 1092.
- (11) Kassebacher, T.; Sulzer, P.; Jürschik, S.; Hartungen, E.; Jordan, A.; Edtbauer, A.; Feil, S.; Hanel, G.; Jaksch, S.; Märk, L.; Mayhew, C. A.; Märk, T. D. *Rapid Commun. Mass Spectrom.* **2013**, *27*, 325.
- (12) Sulzer, P.; Agarwal, B.; Jürschik, S.; Lanza, M.; Jordan, A.; Hartungen, E.; Hanel, G.; Märk, L.; Märk, T. D.; González-Méndez, R.; Watts, P.; Mayhew, C. A. *Int. J. Mass Spectrom.* **2013**, *354*, 123.
- (13) Agarwal, B.; González-Méndez, R.; Lanza, M.; Sulzer, P.; Märk, T. D.; Thomas, N.; Mayhew, C. A. *J. Phys. Chem. A* **2014**, *118*, 8229.
- (14) Acton, W. J.; Lanza, M.; Agarwal, B.; Jurschik, S.; Sulzer, P.; Breiev, K.; Jordan, A.; Hartungen, E.; Hanel, G.; Märk, L.; Mayhew, C. A.; Märk, T. D. *Int. J. Mass Spectrom.* **2014**, *360*, 28.
- (15) Lanza, M.; Acton, W. J.; Sulzer, P.; Breiev, K.; Jürschik, S.; Jordan, A.; Hartungen, E.; Hanel, G.; Märk, L.; Märk, T. D.; Mayhew, C. A. *J. Mass Spectrom.* **2015**, *50*, 427.
- (16) DFT calculations were performed using the Gaussian 03 program with the GaussView interface. Frisch, M. J.; Trucks, G. W.; Schlegel, H. B.; Scuseria, G. E.; Robb, M. A.; Cheeseman, J. R.; Scalmani, G.; Barone, V.; Mennucci, B.; Petersson, G. A.; Nakatsuji, H.; Caricato, M.; Li, X.; Hratchian, H. P.; Izmaylov, A. F.; Bloino, J.; Zheng, G.; Sonnenberg, J. L.; Hada, M.; Ehara, M.; Toyota, K.; Fukuda, R.; Hasegawa, J.; Ishida, M.; Nakajima, T.; Honda, Y.; Kitao, O.; Nakai, H.; Vreven, T.; Montgomery, J. A., Jr.; Peralta, J. E.; Ogliaro, F.; Bearpark, M.; Heyd, J. J.; Brothers, E.; Kudin, K. N.; Staroverov, V. N.; Kobayashi, R.; Normand, J.; Raghavachari, K.; Rendell, A.; Burant, J. C.; Iyengar, S. S.; Tomasi, J.; Cossi, M.; Rega, N.; Millam, J. M.; Klene, M.; Knox, J. E.; Cross, J. B.; Bakken, V.; Adamo, C.; Jaramillo, J.; Gomperts, R.; Stratmann, R. E.; Yazev, O.; Austin, A. J.; Cammi, R.; Pomelli, C.; Ochterski, J. W.; Martin, R. L.; Morokuma, K.; Zakrzewski, V. G.; Voth, G. A.; Salvador, P.; Dannenberg, J. J.; Dapprich, S.; Daniels, A. D.; Farkas, O.; Foresman, J. B.; Ortiz, J. V.; Cioslowski, J.; Fox, D. J. *Gaussian 09*, Revision A.02; Gaussian, Inc.: Wallingford CT, 2009.
- (17) Mayhew, C. A.; Sulzer, P.; Petersson, F.; Haidacher, S.; Jordan, A.; Märk, L.; Watts, P.; Märk, T. D. *Int. J. Mass Spectrom.* **2010**, *289*, 58.



Compendium of the Reactions of H₃O⁺ With Selected Ketones of Relevance to Breath Analysis Using Proton Transfer Reaction Mass Spectrometry

Michaela Malásková ^{1†}, David Olivenza-León ^{2†}, Felix Piel ^{3,4†}, Paweł Mochalski ^{1,5*}, Philipp Sulzer ³, Simone Jürschik ³, Chris A. Mayhew ^{1,2} and Tilmann D. Märk ^{3,4}

OPEN ACCESS

Edited by:

Amala Dass,

University of Mississippi, United States

Reviewed by:

Michael H. Nantz,

University of Louisville, United States

Renato Zenobi,

ETH Zürich, Switzerland

***Correspondence:**

Paweł Mochalski

pawel.mochalski@uibk.ac.at

[†]Early Stage Researchers who have contributed equally to the measurements, data analyses and contribution to the completion of this paper

Specialty section:

This article was submitted to

Analytical Chemistry,

a section of the journal

Frontiers in Chemistry

Received: 08 March 2019

Accepted: 17 May 2019

Published: 13 June 2019

Citation:

Malásková M, Olivenza-León D, Piel F, Mochalski P, Sulzer P, Jürschik S, Mayhew CA and Märk TD (2019) Compendium of the Reactions of H₃O⁺ With Selected Ketones of Relevance to Breath Analysis Using Proton Transfer Reaction Mass Spectrometry. *Front. Chem.* 7:401. doi: 10.3389/fchem.2019.00401

¹ Institute for Breath Research, Fakultät für Chemie und Pharmazie, Leopold-Franzens-Universität Innsbruck, Dornbirn, Austria, ² Molecular Physics Group, School of Physics and Astronomy, University of Birmingham, Birmingham, United Kingdom, ³IONICON Analytik Gesellschaft m.b.H., Innsbruck, Austria, ⁴ Institut für Ionenphysik und Angewandte Physik, Universität Innsbruck, Innsbruck, Austria, ⁵ Institute of Chemistry, Faculty of Mathematics and Natural Sciences, Jan Kochanowski University, Kielce, Poland

Soft chemical ionization mass spectrometric techniques, such as proton transfer reaction mass spectrometry (PTR-MS), are often used in breath analysis, being particularly powerful for real-time measurements. To ascertain the type and concentration of volatiles in exhaled breath clearly assignable product ions resulting from these volatiles need to be determined. This is difficult for compounds where isomers are common, and one important class of breath volatiles where this occurs are ketones. Here we present a series of extensive measurements on the reactions of H₃O⁺ with a selection of ketones using PTR-MS. Of particular interest is to determine if ketone isomers can be distinguished without the need for pre-separation by manipulating the ion chemistry through changes in the reduced electric field. An additional issue for breath analysis is that the product ion distributions for these breath volatiles are usually determined from direct PTR-MS measurements of the compounds under the normal operating conditions of the instruments. Generally, no account is made for the effects on the ion-molecule reactions by the introduction of humid air samples or increased CO₂ concentrations into the drift tubes of these analytical devices resulting from breath. Therefore, another motivation of this study is to determine the effects, if any, on the product ion distributions under the humid conditions associated with breath sampling. However, the ultimate objective for this study is to provide a valuable database of use to other researchers in the field of breath analysis to aid in analysis and quantification of trace amounts of ketones in human breath. Here we present a comprehensive compendium of the product ion distributions as a function of the reduced electric field for the reactions of H₃O⁺. (H₂O)_n (*n* = 0 and 1) with nineteen ketones under normal and humid (100% relative humidity for 37 °C) PTR-MS conditions. The ketones selected for inclusion in this compendium are (in order of increasing molecular weight): 2-butanone; 2-pentanone; 3-pentanone; 2-hexanone; 3-hexanone;

2-heptanone; 3-heptanone; 4-heptanone; 3-octanone; 2-nonanone; 3-nonanone; 2-decanone; 3-decanone; cyclohexanone; 3-methyl-2-butanone; 3-methyl-2-pentanone; 2-methyl-3-pentanone; 2-methyl-3-hexanone; and 2-methyl-3-heptanone.

Keywords: ketones, breath analysis, PTR-MS, reduced electric field, fastGC

INTRODUCTION

Depending on the actual mass resolution, current proton transfer reaction mass spectrometers (PTR-MS) are easily capable of separating many protonated isobaric compounds through a peak fitting procedure providing their mass separation is at least 0.01 Da. The selectivity of PTR-MS can be further improved by the manipulation of the ion-molecule chemistry that occurs between a reagent ion and a given isobar in the drift tube to produce different product ions. This can be achieved by (i) changing the reagent ion, examples for which have been presented in the literature for explosives (Sulzer et al., 2013; Agarwal et al., 2014), or psychoactive substances (Acton et al., 2014; Lanza et al., 2015), and/or (ii) the collisional processes in the drift tube through changing the reduced electric field. Changes in the reduced electric field (the ratio of the electric field strength, E , to the gas number density, N , in the drift tube) to alter the product ion distributions have been demonstrated in the areas of homeland security, e.g., detection of chemical warfare agents (Petersson et al., 2009), explosives (Mayhew et al., 2010; Sulzer et al., 2012, 2013), and rape drugs (Jürschik et al., 2012), and in environmental science, e.g., the identification of monoterpenes (Materić et al., 2017).

This application of changing collisional processes through changes in the reduced electric field to enhance compound selectivity has led to the development of a computer-controlled fast switching drift tube voltage (González-Méndez et al., 2018) and the adaptation of a radio frequency ion-funnel drift tube (González-Méndez et al., 2016).

Although today there are several ways to enhance the selectivity of PTR-MS for isobaric compounds, distinguishing isomeric compounds is still more of an issue. With no pre-separation of isomeric compounds, rarely can isomers be easily identified using PTR-MS through differences in product ion distributions, even if the ion-molecule chemistry occurring in the drift tube of PTR-MS is manipulated in a structured way. One study has demonstrated how reactions of O_2^+ and NO^+ can be used to distinguish two isomeric mephedrone substitutes (4-methylcathinone and N-ethylbuphedrone) whereas reactions with H_3O^+ could not (Lanza et al., 2013). However, such examples in ion-isomer chemistry are usually the exception rather than the rule.

Isomers of ketones are so far difficult to identify unambiguously with a PTR-MS instrument. Pre-separation offered by standard gas chromatography (GC) techniques can be used, but they take away the main advantage of PTR-MS, namely its real-time analytical capabilities. The recent development of fast gas chromatography (fastGC) coupled to PTR-MS provides a compromise between real-time measurements, ensuring reasonably fast analysis (within approximately 90 s), whilst still taking advantage of limited pre-separation of compounds to

improve the analytical specificity of PTR-MS (Ruzsanyi et al., 2013; Romano et al., 2014; Anderson, 2015).

In this paper we have used the fastGC PTR-MS technique in order to accurately determine the product ion distributions for a large selection of ketones as a function of reduced electric field so that we can unambiguously determine their product ions, without any concerns from impurities in the samples. Ketones have been selected for this study, because they form a common class of compounds found in breath, blood and urine (de Lacy Costello et al., 2014), and their detection holds many possibilities for non-invasive diagnostic and monitoring procedures in health services. One example is the diagnosis of ketosis, resulting from the elevation of ketone bodies in the blood. Detecting changes in ketone concentrations could thus be used to diagnose diabetic ketosis. A key ketone found in high concentrations in breath is acetone, the production of which (as for most ketones) is linked to fat metabolism, and hence its detection in breath could provide a window to predict fat loss (Anderson, 2015). Given the importance of acetone in the breath, it has been investigated numerous times with PTR-MS, and hence acetone does not form part of this current study. Less attention has been given to other ketones in PTR-MS studies. Hence this investigation has focused its attention on other important breath ketones, although generally found in much lower concentrations in the breath than for acetone. This has produced a wealth of new data, providing a useful database of the product ion distributions resulting from the reactions of H_3O^+ and H_3O^+ (H_2O) with ketones using PTR-MS.

Awareness of possible changes in the reaction processes occurring in the drift tube of a PTR-MS instrument resulting from changes in humidity have been known for some time (Warneke et al., 2001; Tani et al., 2003, 2004). Breath samples are humid, and thus product ion distributions determined under the “normal” operating conditions of PTR-MS (e.g., using purified air or nitrogen as the buffer gas in the drift tube) may not be a true reflection of those associated with a humid gas sample in the drift tube. This is because it can be expected that a higher humidity associated with breath samples (100% relative humidity at 32–34°C) will affect the product ion distributions through changes in the energy associated with the collisional processes. Furthermore, if protonated water clusters can react with a breath volatile via proton transfer, far less energy will be available in the reaction than for that associated with H_3O^+ , and with higher humidity comes a greater production of protonated water clusters for a given reduced electric field. This effect will generally be more important at low reduced electric field values (i.e., $< \sim 120$ Td, $1 \text{ Td} = 10^{-17} \text{ V cm}^2$) when collisions will lead to less break-up of the protonated water clusters to H_3O^+ and neutral water(s). Moreover, if the protonated water clusters cannot react with a volatile, then a reduction in the sensitivity of detection of that compound results. Finally, differences in product ion

distributions will arise if secondary processes occur, such as when primary product ions react with water.

A review of the literature shows that PTR-MS product ion distributions of compounds of interest to breath research are generally determined under the “normal” operating conditions, i.e., where the humidity in the drift tube is determined by the diffusion of water from the discharge region into the drift tube, which will be less than that associated with a breath sample. An objective of this work is to improve our knowledge on the effects of humidity on product ion distributions.

The first studies associated with investigating the effects of humidity on reaction processes in PTR-MS focused on sensitivity issues. For example, Warneke et al. (2001) showed how the sensitivity for the detection of benzene and toluene at fixed reduced electric fields decreased with increasing humidity, owing to unreactive $\text{H}_3\text{O}^+ \cdot (\text{H}_2\text{O})_n$ clusters. Hence, de Gouw et al. (2003) suggested employing a humidity factor to determine the concentrations of a compound if it reacts with protonated water clusters, a factor which takes into account the efficiencies of the proton transfer reaction and the transmission of $\text{H}_3\text{O}^+ \cdot (\text{H}_2\text{O})_n$ relative to that of H_3O^+ . These factors were determined and used to correct for the influences of humidity on the detection sensitivity for methanol, acetonitrile, acetaldehyde, acetone, benzene and toluene by de Gouw and Warneke (2007). A PTR-MS investigation of the effects of humidity on the product ion distributions resulting from the reactions of H_3O^+ with two sesquiterpenes (α -cedrene and longifolene) was undertaken by Demarcke et al. (2009). In that study, no substantial influence of the humidity in the drift tube on the product ion yields was observed. More recently, the effects of humidity on product ion distributions have been investigated for α -pinene, δ -limonene, and longifolene by Kari et al. (2018) at two different E/N values (80 Td and 130 Td) (Kari et al., 2018), and for more than 20 volatile organic compounds (VOCs), including aldehydes, ketones, aromatic compounds and hydrocarbons by Trefz et al. (2018) at one fixed E/N (139 Td) (Trefz et al., 2018). In the former study, no significant changes in the product ion distributions were observed. However, Trefz et al. reported large differences in VOC intensities between “dry” and “humid” samples. Thus, the effect of humidity appears to depend very much on the volatile chemical compound.

In this paper we present details on the reactions of H_3O^+ and associated water clusters with a selected number of ketones over a large reduced electric field range of 100–220 Td, and compare product ions obtained under “normal” and “humid” operating conditions of the drift tube. This work demonstrates that changes in product ion distributions do occur for fixed E/N for different humidities, and hence it clearly demonstrates that humidity effects should be considered when relying on product ion distributions for undertaking breath research with a PTR-MS.

MATERIALS AND METHODS

Sample Preparation

Samples were prepared in two different ways depending on the humidity of the measurement.

For measurements under normal conditions, an open glass vial containing a ketone was purged with high purity N_2 (Alphagaz 1, Air Liquide GmbH, Austria), which had been previously passed through a P300-1 Filter (VICI AG, Switzerland) for purification (6.0). The vial was then covered with parafilm. Using a glass syringe a quantity of headspace was taken from the vial through the parafilm. This headspace containing the ketone and N_2 was then injected into a PTFE bag filled with 3L of dry 6.0 N_2 , which was already connected to the inlet of the PTR-ToF-MS instrument. This injected volume into the bag varied from 5 μL to 10 mL, depending on the volatility of the ketone.

Humid samples were prepared using a Liquid Calibration Unit (LCU, IONICON Analytik GmbH, Austria). The LCU generates defined gaseous concentrations from aqueous solutions of volatile and semi-volatile organics. A description of the LCU has already been provided in detail by Fischer et al. (2013). Briefly, a homebuilt liquid flow controller injects a defined flow into a nebuliser (X175, Burgener Research Inc., United Kingdom). Vaporization of the aqueous solution produces micro droplets, which are evaporated in a heating chamber maintained at 100°C. The heating chamber is being constantly flushed by a buffer gas, e.g., zero air or N_2 , diluting the organic sample and thus generating a continuous stream of a defined trace gas mixture.

For this study, to generate the humid samples, 16 mL glass vials, kept at a constant temperature of 30°C, were filled with a trace quantity of a ketone [1–10 μL (depending on the volatility of the ketone)] diluted in 100 mL of purified water. A sample flow of this ketone/water mixture at 35 $\mu\text{L}/\text{min}$ was diluted in a N_2 flow of 950 mL/min to achieve a 5% absolute humidity. The combined flow was then directly connected to the fastGC inlet system of the PTR-ToF-MS instrument.

For both the dry and humid measurements, the dilution of the samples were prepared to yield a concentration of the ketone in the drift tube to be approximately 100 ppbv.

The experiments presented here were done through an automated measurement procedure. This consisted of background measurements for 5 min. For the dry mixtures, this involved the PTFE bag filled only with purified N_2 . For the humid standards this step involved a vial containing only purified water. Next, the prepared samples were directed to the drift tube for a 2-min stabilization period, which was next followed by 2 min and 40 s of fastGC measurement at an E/N of 180 Td to help identify the product ions produced in the drift tube for a given ketone and a 26-min E/N set of measurements over the range 100–220 Td in steps of 10 Td (1 min each), in both directions, to provide two data sets.

FastGC PTR-ToF-MS

Details of PTR-ToF-MS and methods of operation have been reviewed extensively in the literature (Ellis and Mayhew, 2014), and therefore only brief details are required here. For this study, measurements were taken using a PTR-TOF 8000 with a fastGC add-on (IONICON Analytik GmbH, Austria) (Jordan et al., 2009; Graus et al., 2010). Briefly, water vapor is introduced into a hollow cathode discharge to generate $\text{H}_3\text{O}^+ \cdot (\text{H}_2\text{O})_n$ ($n = 0, 1, 2, \dots$), initially through electron ionization of water and subsequent ion-molecule reactions with water. These reagent ions are then

TABLE 1 | Product ions identified and their associated product ion branching ratios (percentages) measured at reduced electric fields of 100, 140, and 180 Td resulting from the reactions of H_3O^+ with several ketones.

Ketone Molecular formula Nominal MW	Product ion <i>m/z</i> (Th)	Product ion formula	Product ion branching percentages					
			Normal <i>E/N</i> (Td)			Humid <i>E/N</i> (Td)		
			100	140	180	100	140	180
2-butanone $\text{C}_4\text{H}_8\text{O}$ 72	73.07 55.05 39.02	$\text{C}_4\text{H}_8\text{OH}^+$ C_4H_7^+ C_3H_3^+	100 0 0	99 1 0	87 10 3	100 0 0	100 0 0	88 10 2
2-pentanone $\text{C}_5\text{H}_{10}\text{O}$ 86	87.08 45.03 39.02	$\text{C}_5\text{H}_{10}\text{OH}^+$ $\text{C}_2\text{H}_5\text{O}^+$ C_3H_3^+	99 1 0	67 33 0	20 70 10	99 1 0	84 16 0	29 66 5
3-pentanone $\text{C}_5\text{H}_{10}\text{O}$ 86	87.08 69.07 45.03 41.04 39.02	$\text{C}_5\text{H}_{10}\text{OH}^+$ C_5H_9^+ $\text{C}_2\text{H}_5\text{O}^+$ C_3H_5^+ C_3H_3^+	98 1 1 0 0	72 4 20 3 1	23 2 55 5 15	99 1 0 0 0	91 4 4 1 0	43 4 39 5 9
2-hexanone $\text{C}_6\text{H}_{12}\text{O}$ 100	101.10 59.05 45.03 39.02	$\text{C}_6\text{H}_{12}\text{OH}^+$ $\text{C}_3\text{H}_7\text{O}^+$ $\text{C}_2\text{H}_5\text{O}^+$ C_3H_3^+	100 0 0 0	94 1 5 0	48 3 39 10	100 0 0 0	95 1 4 0	49 3 40 8
3-hexanone $\text{C}_6\text{H}_{12}\text{O}$ 100	101.10 83.09 59.05 55.05 45.03 41.04 39.02 31.02	$\text{C}_6\text{H}_{12}\text{OH}^+$ $\text{C}_6\text{H}_{11}^+$ $\text{C}_3\text{H}_7\text{O}^+$ C_4H_7^+ $\text{C}_2\text{H}_5\text{O}^+$ C_3H_5^+ C_3H_3^+ CH_3O^+	93 1 3 0 2 0 1 0	73 4 9 3 5 4 1 1	31 4 15 5 15 6 18 6	96 1 3 0 0 0 0 0	88 4 7 0 0 1 0 0	44 5 17 12 0 9 13 0
2-heptanone $\text{C}_7\text{H}_{14}\text{O}$ 114	115.11 97.10 59.05 55.05 45.03 39.02	$\text{C}_7\text{H}_{14}\text{OH}^+$ $\text{C}_7\text{H}_{13}^+$ $\text{C}_3\text{H}_7\text{O}^+$ C_4H_7^+ $\text{C}_2\text{H}_5\text{O}^+$ C_3H_3^+	94 4 1 0 1 0	76 10 2 9 3 0	31 7 4 14 15 29	96 2 2 0 0 0	86 7 3 4 0 0	52 9 6 20 0 13
3-heptanone $\text{C}_7\text{H}_{14}\text{O}$ 114	115.11 97.10 59.05 55.05 41.04 39.02 31.02	$\text{C}_7\text{H}_{14}\text{OH}^+$ $\text{C}_7\text{H}_{13}^+$ $\text{C}_3\text{H}_7\text{O}^+$ C_4H_7^+ C_3H_5^+ C_3H_3^+ CH_3O^+	98 2 0 0 0 0 0	89 5 0 4 1 0 1	35 4 0 8 7 27 19	99 1 0 0 0 0 0	95 4 1 0 0 0 0	57 5 7 12 3 16 0
4-heptanone $\text{C}_7\text{H}_{14}\text{O}$ 114	115.11 73.07 59.05 55.05 53.04 39.02	$\text{C}_7\text{H}_{14}\text{OH}^+$ $\text{C}_4\text{H}_9\text{O}^+$ $\text{C}_3\text{H}_7\text{O}^+$ C_4H_7^+ C_4H_5^+ C_3H_3^+	98 0 1 0 0 1	90 1 2 6 0 1	52 2 6 15 5 20	99 0 1 0 0 0	95 0 1 4 0 0	70 0 4 16 3 7
3-octanone $\text{C}_8\text{H}_{16}\text{O}$ 128	129.13 69.07 59.05 41.04 39.02	$\text{C}_8\text{H}_{16}\text{OH}^+$ C_5H_9^+ $\text{C}_3\text{H}_7\text{O}^+$ C_3H_5^+ C_3H_3^+	99 0 1 0 0	96 3 1 0 0	46 5 3 11 35	100 0 0 0 0	98 1 1 0 0	73 6 4 10 7
2-nonanone $\text{C}_9\text{H}_{18}\text{O}$	143.14 83.09	$\text{C}_9\text{H}_{18}\text{OH}^+$ $\text{C}_6\text{H}_{11}^+$	100 0	93 0	34 0	100 0	97 1	62 4

(Continued)

TABLE 1 | Continued

Ketone Molecular formula Nominal MW	Product ion <i>m/z</i> (Th)	Product ion formula	Product ion branching percentages					
			Normal E/N (Td)			Humid E/N (Td)		
			100	140	180	100	140	180
142	69.07	C_5H_9^+	0	4	4	0	2	6
	55.05	C_4H_7^+	0	1	4	0	0	7
	41.04	C_3H_5^+	0	1	10	0	0	10
	39.02	C_3H_3^+	0	1	48	0	0	11
3-nonanone $\text{C}_9\text{H}_{18}\text{O}$	143.14	$\text{C}_9\text{H}_{18}\text{OH}^+$	100	87	48	100	100	79
142	41.04	C_3H_5^+	0	8	11	0	0	6
	39.02	C_3H_3^+	0	1	35	0	0	10
2-decanone $\text{C}_{10}\text{H}_{20}\text{O}$	157.16	$\text{C}_{10}\text{H}_{20}\text{OH}^+$	100	94	48	100	99	81
156	83.09	$\text{C}_6\text{H}_{11}^+$	0	2	3	0	1	6
	55.05	C_4H_7^+	0	3	13	0	0	13
	39.02	C_3H_3^+	0	1	36	0	0	0
3-decanone $\text{C}_{10}\text{H}_{20}\text{O}$	157.16	$\text{C}_{10}\text{H}_{20}\text{OH}^+$	99	95	48	100	100	86
156	55.05	C_4H_7^+	1	4	10	0	0	7
	39.02	C_3H_3^+	0	1	42	0	0	7
cyclohexanone $\text{C}_6\text{H}_{10}\text{O}$	99.08	$\text{C}_6\text{H}_{10}\text{OH}^+$	99	88	30	99	93	40
98	81.07	C_6H_9^+	1	12	65	1	7	56
	79.05	C_6H_7^+	0	0	5	0	0	3
	39.02	C_3H_3^+	0	0	0	0	0	1
3-methyl-2-butanone $\text{C}_5\text{H}_{10}\text{O}$	87.08	$\text{C}_5\text{H}_{10}\text{OH}^+$	100	98	63	99	96	66
86	69.07	C_5H_9^+	0	2	5	1	3	7
	45.03	$\text{C}_2\text{H}_5\text{O}^+$	0	0	8	0	0	8
	41.04	C_3H_5^+	0	0	4	0	1	8
	39.02	C_3H_3^+	0	0	20	0	0	11
3-methyl-2-pentanone $\text{C}_6\text{H}_{12}\text{O}$	101.10	$\text{C}_6\text{H}_{12}\text{OH}^+$	100	70	23	100	73	22
100	59.05	$\text{C}_3\text{H}_7\text{O}^+$	0	11	28	0	7	26
	57.07	C_4H_9^+	0	4	3	0	5	4
	45.03	$\text{C}_2\text{H}_5\text{O}^+$	0	15	39	0	15	40
	39.02	C_3H_3^+	0	0	7	0	0	8
2-methyl-3-pentanone $\text{C}_6\text{H}_{12}\text{O}$	101.10	$\text{C}_6\text{H}_{12}\text{OH}^+$	98	61	17	95	74	24
100	59.05	$\text{C}_3\text{H}_7\text{O}^+$	1	15	29	3	9	29
	57.07	C_4H_9^+	0	4	2	0	3	3
	45.03	$\text{C}_2\text{H}_5\text{O}^+$	1	20	41	2	13	40
	39.02	C_3H_3^+	0	0	11	0	1	4
2-methyl-3-hexanone $\text{C}_7\text{H}_{14}\text{O}$	115.11	$\text{C}_7\text{H}_{14}\text{OH}^+$	95	66	24	96	72	24
114	97.10	$\text{C}_7\text{H}_{13}^+$	5	14	8	4	10	7
	59.05	$\text{C}_3\text{H}_7\text{O}^+$	0	8	17	0	4	17
	55.05	C_4H_7^+	0	4	5	0	2	7
	45.03	$\text{C}_2\text{H}_5\text{O}^+$	0	5	17	0	11	27
	41.04	C_3H_5^+	0	3	7	0	1	6
	39.02	C_3H_3^+	0	0	22	0	0	12
2-methyl-3-heptanone $\text{C}_8\text{H}_{16}\text{O}$	129.13	$\text{C}_8\text{H}_{16}\text{OH}^+$	96	76	26	97	81	28
128	111.12	$\text{C}_8\text{H}_{15}^+$	3	5	3	2	5	3
	69.07	C_5H_9^+	0	8	5	0	4	5
	59.05	$\text{C}_3\text{H}_7\text{O}^+$	0	0	0	0	3	14
	45.03	$\text{C}_2\text{H}_5\text{O}^+$	0	2	8	0	3	10
	43.05	C_3H_7^+	1	2	2	1	2	3
	41.04	C_3H_5^+	0	6	15	0	2	15
	39.02	C_3H_3^+	0	1	41	0	0	22

Values for the product ion branching percentages are given whilst operating the drift tube under "normal" conditions and under "humid" (breath humidity) conditions. Errors in the branching percentages are estimated to be <20%.

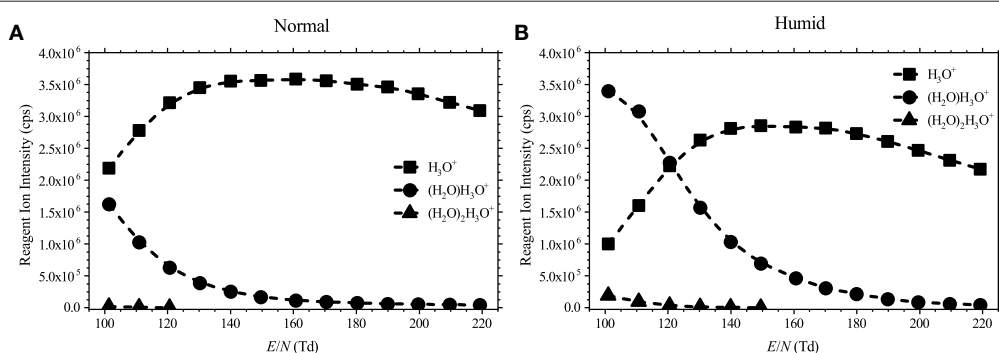


FIGURE 1 | Reagent ion intensities in counts per second (cps) as a function of the reduced electric field for (A) normal (dry buffer gas) and (B) humid (5% absolute humidity buffer gas) conditions.

transferred to the drift tube via a focusing lens. The distribution of the protonated water clusters in the reaction region depends on the E/N value and the humidity in the drift tube as shown in Figure 1.

These reagent ions are then transported down the drift tube under the influence of the uniform electric field. Analytes are injected into the drift tube through an inlet pipe. Proton transfer from hydronium to the analyte takes place within the drift tube if the proton affinity (PA) of the analyte is higher than that of water ($\text{PA}(\text{H}_2\text{O}) = 691 \text{ kJ mol}^{-1}$). Proton transfer can be non-dissociative and dissociative. However, it should be stressed that fragmentation of the protonated molecule can be a barrierless process and occur spontaneously, or it can be induced by the collision of the reagent ions with analyte and/or charged analyte with the buffer gas.

For all measurements the drift tube was kept at a pressure of 2.3 mbar, with both the inlet system and drift tube being maintained at 100°C. The collisional energies of the reagent and product ions were controlled by the value of the reduced electric field. For this study we kept the drift tube at constant pressure and temperature (and hence constant N), and changed the drift tube voltage to alter the value of E/N . The drift voltage could be changed from 410 V up to a maximum of 890 V. For the applied values of the drift tube pressure and temperature these values correspond to an E/N range from 100 to 220 Td.

Using a dry buffer gas in the drift tube of a PTR-MS instrument does not mean that it is operated under dry conditions, since some amounts of water vapor diffuse from the hollow cathode. This condition will be denoted as “normal” operating condition later in this paper. When a water saturated buffer gas was used, this is referred in the text as operating the drift tube under “humid” conditions.

FastGC was used to separate analytes of interest from possible contaminants in the produced standards. The fastGC add-on used in this study is a modification of the setup used by Romano et al. (2014) and Ruzsanyi et al. (2013). Therefore, only the modifications relevant for this study will be provided here. An MXT-1 column (10 m × 0.53 mm, film thickness 0.25 μm, dimethyl polysiloxane phase, Restek, USA) was used. The samples were injected into a 0.5 ml sample loop made of passivated stainless steel. A custom-made valve block consisting

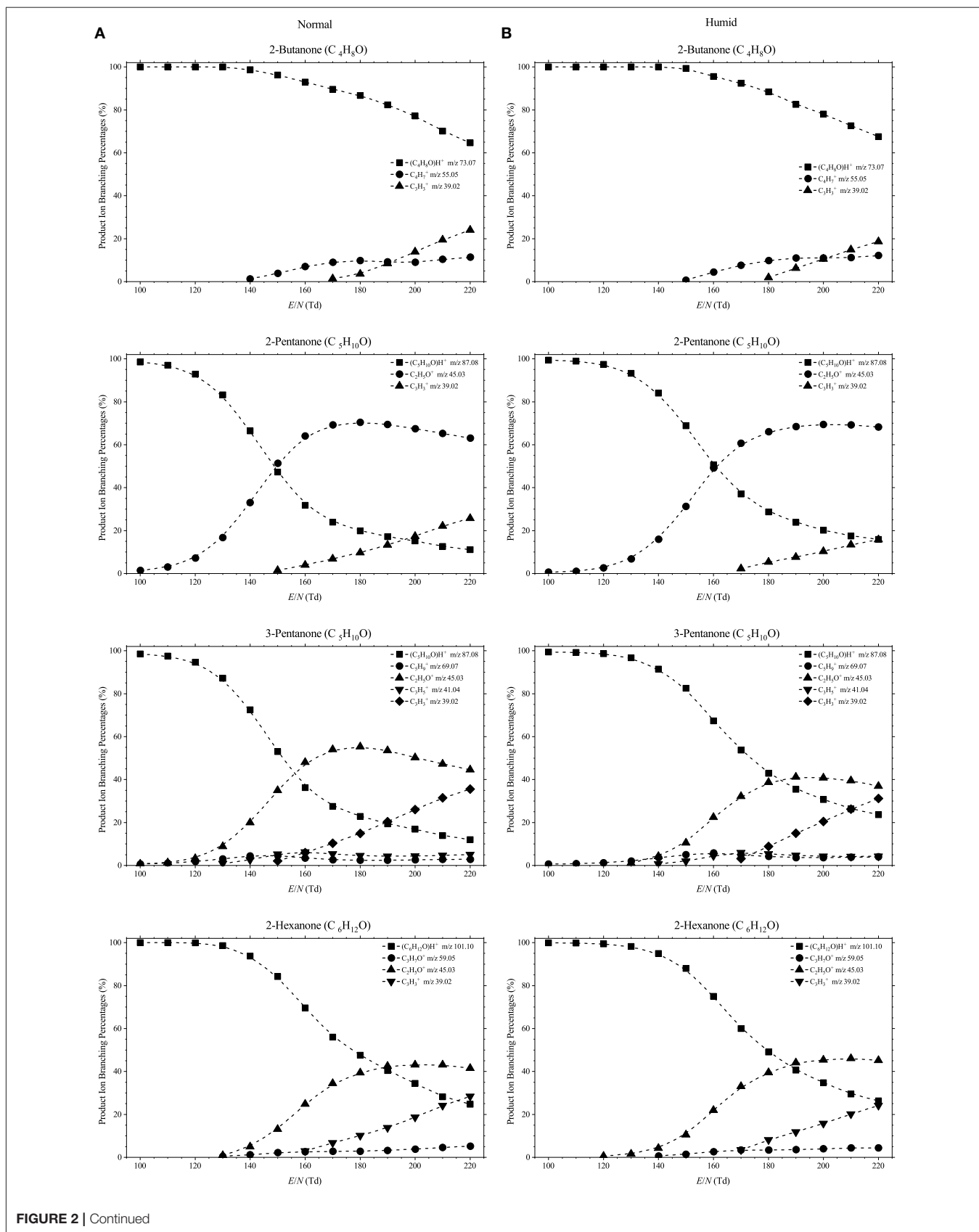
of four three-way valves and a needle valve has been replaced by a 10-port passivated valve (VICI AG, Switzerland) and a three-way gas valve made from polyether ether ketone (PEEK) was used. All parts of the inlet system are installed within the oven that houses the drift tube to prevent cold spots. This revised setup enabled constant filling of the sample loop and constant back-flushing of the capillary column with the carrier gas. 8 ml/min and 20 ml/min of 6.0 N₂ were used as carrier gas and make-up gas, respectively. A voltage ramp of 0.5 V/s from 10 V up to 80 V was applied raising the temperature of the capillary column from room value up to 240°C.

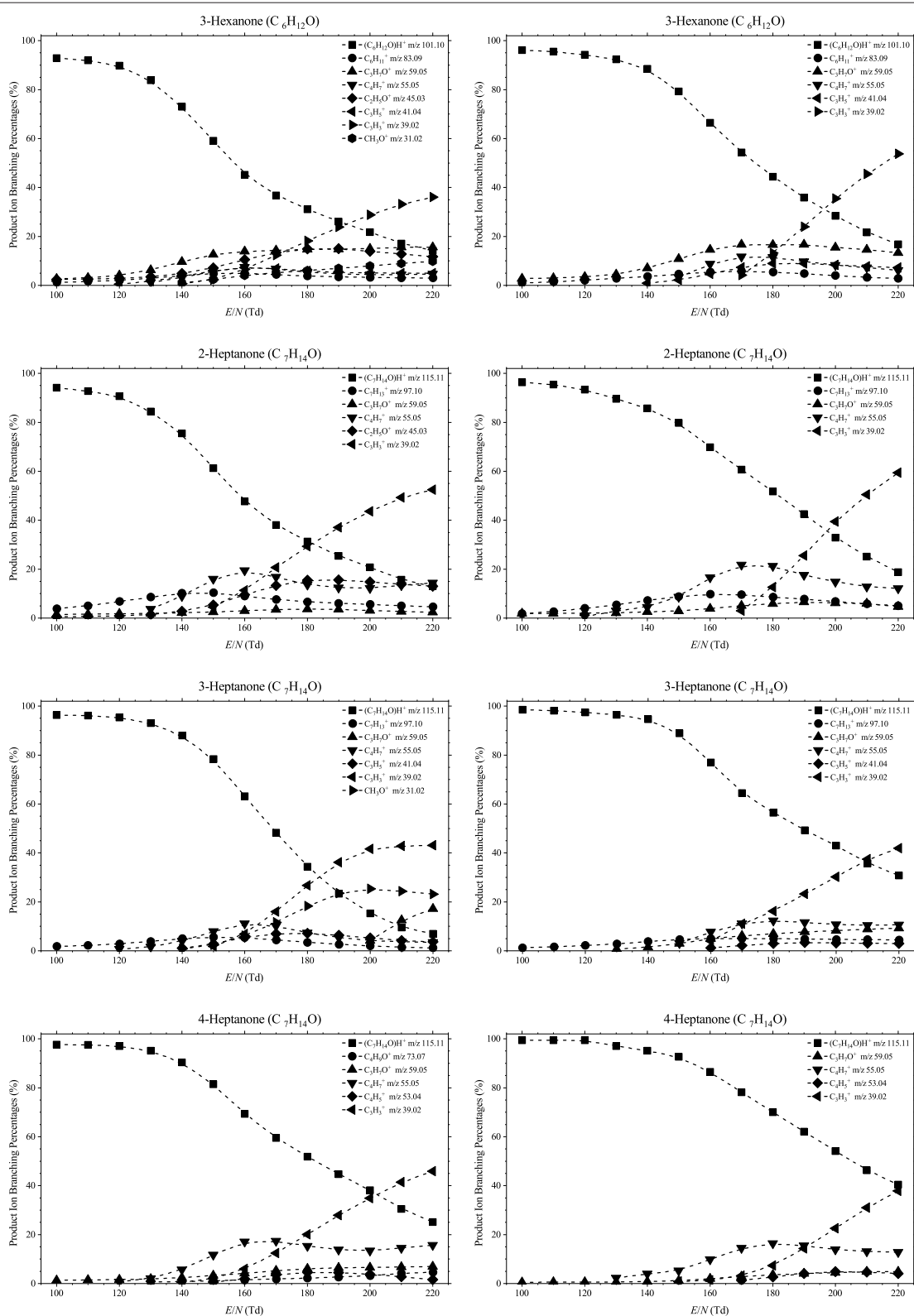
Chemicals

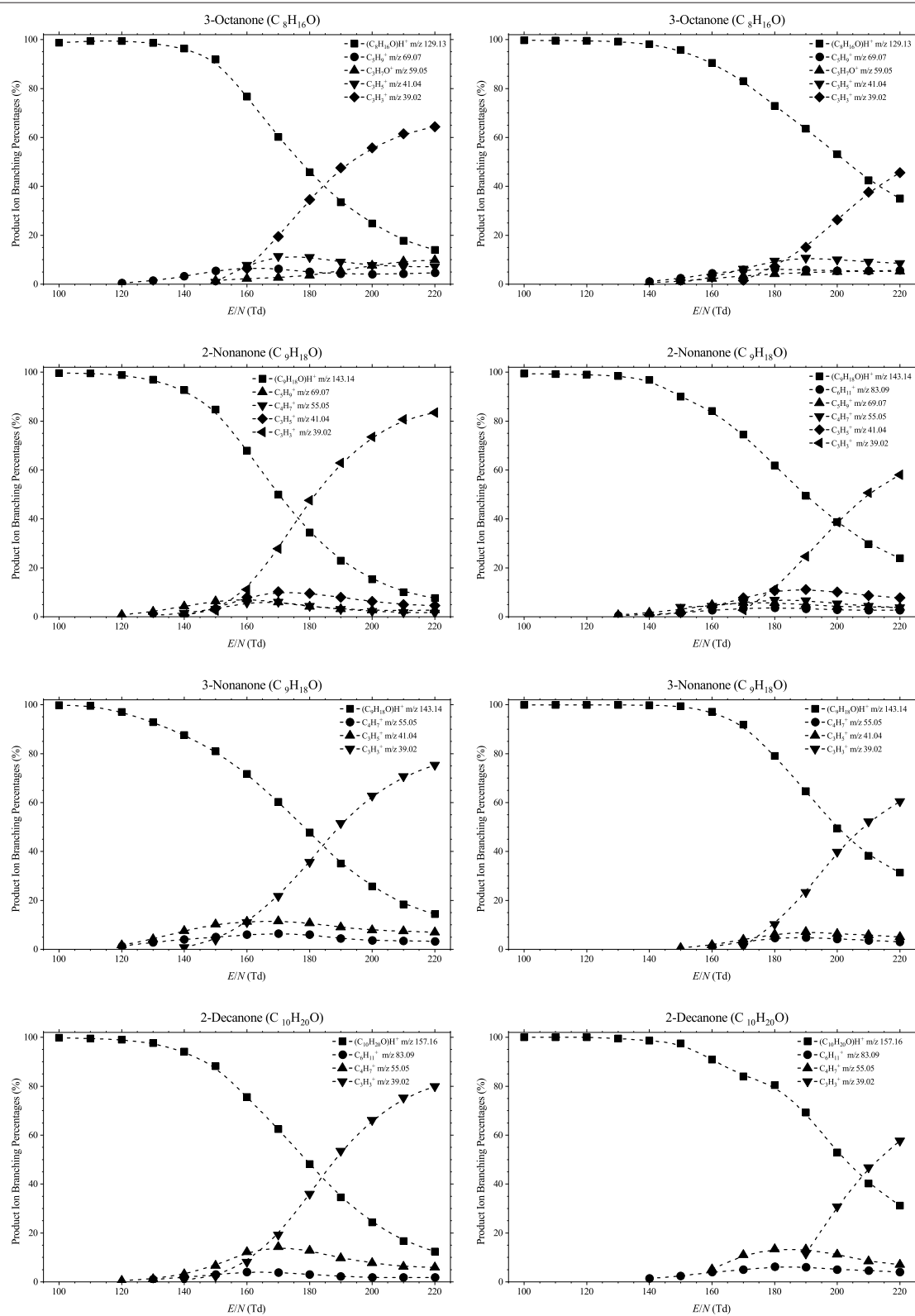
The following liquid substances were purchased from Sigma-Aldrich: 2-pentanone (98%), 3-pentanone (99%), 2-hexanone (98%), 3-hexanone (98%), 3-heptanone (analytical standard), 4-heptanone (98%), 2-nonenone (99%), 3-nonenone (99%), 2-decanone (98%), cyclohexanone (99.8%), 3-methyl-2-pentanone (99%), 2-methyl-3-pentanone (97%), 2-methyl-3-hexanone (98%), and 2-methyl-3-heptanone (99%). 2-butane (99.5%), 2-heptanone (98.5%), and 3-methyl-2-butane (98.5%) were purchased from Honeywell. 3-octanone (99%) and 3-decanone (97%) were purchased from Acros Organics and SAFC, respectively. These were used with no further purification.

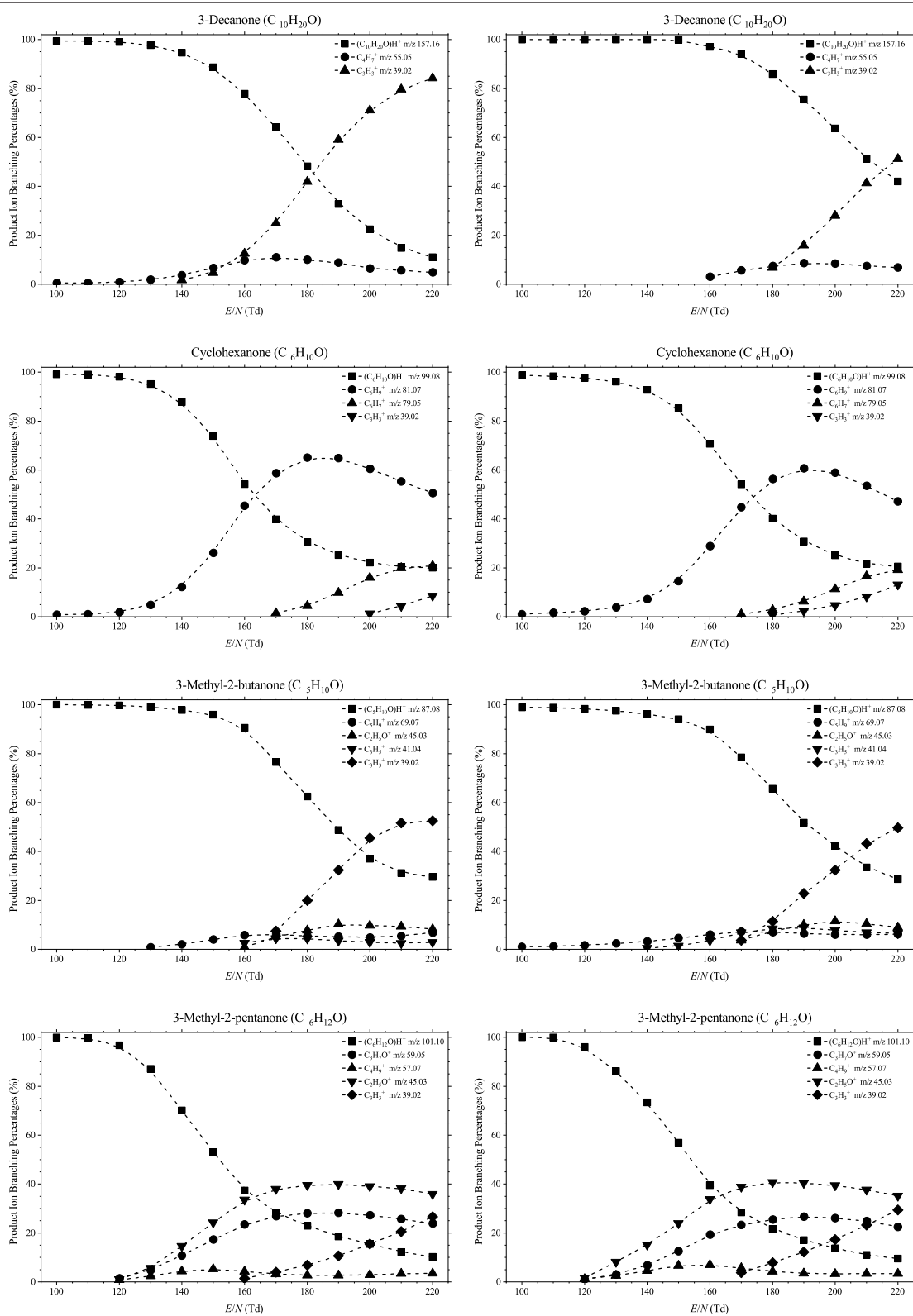
Data Analysis

The “PTR-MS Viewer” (IONICON Analytik GmbH, Austria) was used to identify peaks in the mass spectra and to extract peak data. Raw peak data, i.e., data not corrected for transmission factors, were normalized to 1 million reagent ions and had any backgrounds subtracted. By using the “raw” data, the product ion distributions we have determined here can be more easily compared with other measurements using different PTR-MS instruments. However, we emphasize that the product ion distributions that have been determined for the selection of ketones chosen for this study have to be taken with some caution if a PTR-TOF 8000 is not being used, and that researchers need to determine product ion distributions for their own instruments and conditions.

**FIGURE 2 |** Continued

**FIGURE 2 |** Continued

**FIGURE 2 |** Continued

**FIGURE 2 |** Continued

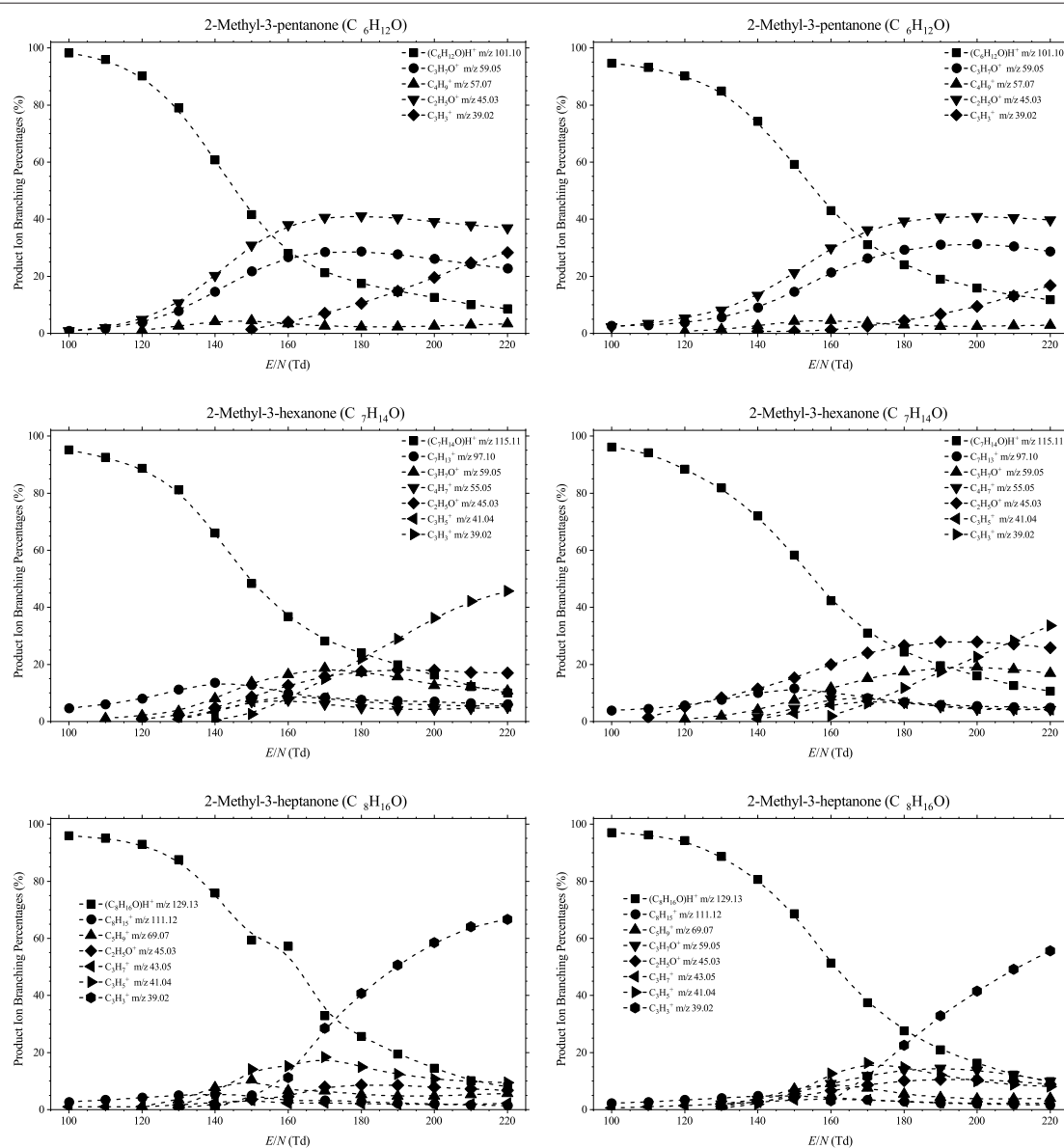


FIGURE 2 | Product ion distributions (branching percentages) as a function of E/N resulting from reaction with H_3O^+ (and potentially $\text{H}_3\text{O}^+\cdot\text{H}_2\text{O}$ as stated above) under **(A)** normal and **(B)** high humidity drift tube conditions with several ketones.

RESULTS AND DISCUSSION

Table 1 presents a summary of the product ion distributions (percentages) for all the ketones investigated in this study at three selected reduced electric fields, namely 100 Td, 140 Td, and 180 Td under normal and humid conditions. These values give a good representation of all product ions observed and quickly illustrate the effects of humidity on the product ion distributions, if any. The table starts with the thirteen linear chained ketones in order of molecular weight (MW), followed by the one cyclic ketone (cyclohexanone), and finishing with five non-linear ketones, also presented in order of increasing nominal MW, and, for low

E/N (see **Figure 1**), from reactions of $\text{H}_3\text{O}^+\cdot\text{H}_2\text{O}$ with those ketones whose proton affinities are greater than that associated with $(\text{H}_2\text{O})_2$ (808 kJ mol $^{-1}$), i.e., 2-butanone (827 kJ mol $^{-1}$), 2-pentanone (833 kJ mol $^{-1}$), 3-pentanone (837 kJ mol $^{-1}$), and 3-methyl-2-butanone (836 kJ mol $^{-1}$).

The dependence of the product ion branching percentages as a function of E/N are shown graphically in **Figure 2**. The chemical formulae of the product ions given in **Table 1** and **Figure 2** have been tentatively identified via the exact m/z (to 2 decimal places) and isotope (^{13}C) intensities. Only product ions who make a contribution to the branching percentage of at least 3% at any reduced electric field value are included in the table and figure.

Below approximately 140 Td, the protonated parent is the dominant product ion observed for all ketones. This is in reasonable agreement with other PTR-MS studies. For example, in the study by Buhr et al. (2002) at one reduced electric field of approximately 140 Td, the authors showed that proton transfer from H_3O^+ to ketones will predominantly be non-dissociative, regardless of chain length. This limited dissociation observed in PTR-MS for reduced electric fields below 140 Td also agrees with studies using the thermalized conditions in Selected Ion Flow Tube—Mass Spectrometry (SIFT-MS) (Spanel et al., 1997; Smith et al., 2003, 2019), and suprathermal Selected Ion Flow Drift Tube (SIFDT) investigations (Specyyvi et al., 2017).

Above 140 Td, fragmentation of the protonated parent is observed, a fact that was not reported by Buhr et al. for 2-butanone, 2-hexanone, 2-heptanone, 3-heptanone, 4-heptanone, 3-octanone, 2-nonanone, and 2-decanone, for which only the protonated parent is observed. Limited fragmentation is, however, reported by Buhr et al. at 140 Td for 2-pentanone, with a product ion being observed at m/z 45, which we also observe and assign it to be $\text{C}_2\text{H}_5\text{O}^+$ (protonated acetaldehyde) although it is found with a much higher relative intensity compared to the protonated parent in our study than found by Buhr et al. This difference in intensity is most probably associated with differences in the transmission of ions, because Buhr et al. used a quadrupole mass spectrometer.

In the present study, significant percentages of hydrocarbon ions, C_nH_m^+ , are seen. This agrees with another E/N study of the ketones, 2-butanone, 2-pentanone, 2-hexanone, 2-heptanone, and cyclohexanone by Pan et al. (2017), who used a dipolar proton transfer reaction (quadrupole) mass

spectrometer. Their study, which covered the reduced electric fields of approximately 50–110 Td, reported the m/z values of the product ions we have found, but observed substantially more fragmentation than we detected, even at their low E/N values. The amount of fragmentation reported at low E/N (as low as 50 Td) by Pan et al. is surprising, given that at these E/N values the reagent ion signal in our instruments would be protonated water clusters. This again illustrates that care must be taken when comparing results from different PTR-MS instruments.

In our study, typically 2–7 fragmentation channels have been observed. However, many of them were significant only at higher reduced electric field values. For instance, C_3H_3^+ and C_3H_5^+ ions occur only for E/N values higher than about 150 Td. Thus, for E/N values up to about 130 Td, the protonated molecules are dominant having well-above 80% branching percentages associated with that channel. Interestingly, the highest number of fragmentation channels was noted for 3-hexanone (7 channels) and C7 ketones; 2-heptanone (5 channels), 3-heptanone (6 channels), 4-heptanone (5 channels), and 2-methyl-3-hexanone (6 channels). As expected, heavier ketones are found to fragment considerably less.

For several ketones, the proton transfer process is followed by the elimination of an H_2O molecule leading to the observed hydrocarbon ions $\text{C}_n\text{H}_{2n-1}^+$. However, these channels have small associated branching percentages, and at higher values of the reduced electric field undergo further fragmentation.

The channel leading to the $\text{C}_2\text{H}_5\text{O}^+$ ion is very abundant in fragmentation patterns of C5 and C6 ketones. Interestingly, the mass spectra of C8 and C9 ketones do not have oxygen-containing fragmentation channels.

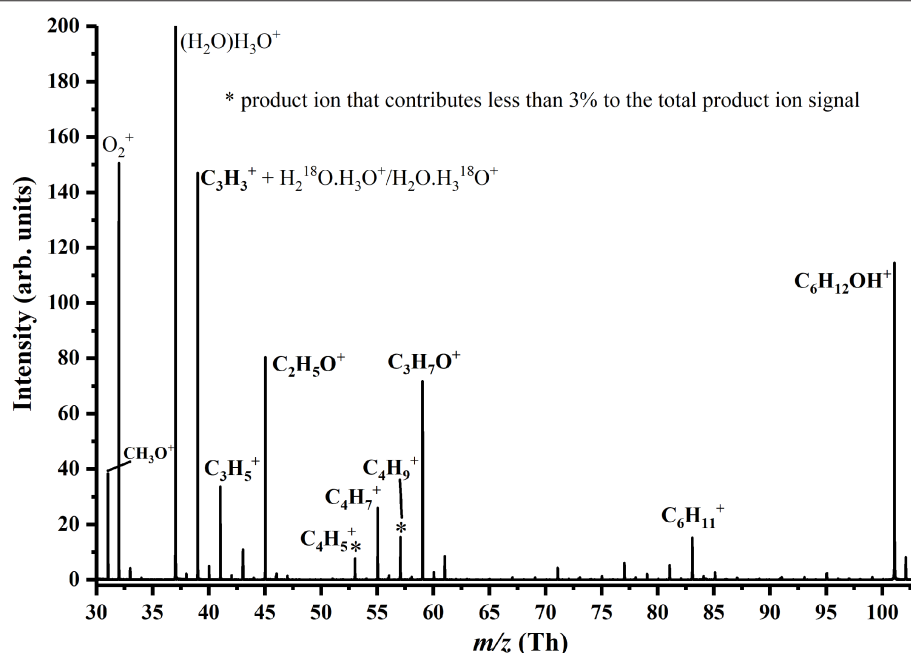


FIGURE 3 | Mass spectrum for 3-hexanone recorded at 180 Td. Product ions coming from the compound are identified. The product ions C_4H_5^+ and C_4H_9^+ each contribute <3% to the total product ion percentage even at the highest reduced electric field investigated.

High humidity reduces the fragmentation of ketones. Interestingly, this effect is most evident for the E/N values of 150–160 Td. For example, the abundance of the protonated parent ion of 2-pentanone under normal conditions for 150 Td is 47%; whereas, in humid air, it has a branching percentage of 69%. The analogous values for 3-nonenone are 48 and 79%, respectively. This interesting dependence can be attributed to the formation of considerable amounts of protonated water clusters, which can react with ketones of interest. Consequently, far less energy is available for fragmentation in such reactions than for those associated with H_3O^+ . At the higher E/N values formation of water clusters is suppressed and, thereby, the positive effect of humidity on having reduced fragmentation is weakened. The general effect of the higher humidity is to shift the product ion branching percentage curves by approximately 20 Td to higher E/N .

To illustrate the quality of the data, a mass spectrum recorded at 180 Td for 3-hexanone is provided in **Figure 3**. This highlights some product ions which are associated with the volatile, but are not included in the tabulation or **Figure 2**, because their contributions to the total relative abundance are <3% for any reduced electric field value.

CONCLUSIONS

This work provides a large body of data and an extensive library of product ion distributions as a function of reduced electric field for the reactions of $\text{H}_3\text{O}^+ \cdot (\text{H}_2\text{O})_n$ ($n = 0$ and 1) with a selection of ketones using the powerful analytical technique of PTR-ToF-MS. Although the study was originally conceived owing to the importance of ketones in the breath, and the need to determine what product ions should be monitored using PTR-MS, these results should be of interest to researchers working in other areas such as the environmental sciences and atmospheric chemistry.

A key outcome from this work is that product ion distributions at any specific reduced electric field can only be used to provide an indication of what ion-molecule channels are occurring. Detailed branching percentages are only specific to a given PTR-MS instrument and then under the specific operational conditions, not least the humidity present in the drift tube, as demonstrated in the results from this study.

Of the ketone isomers investigated in this study, it is apparent that it is not possible to provide any selectivity by manipulating

the ion chemistry through changes in the reduced electric field. For this to be accomplished, the use fast gas chromatography coupled to PTR-MS is needed when analyzing gas samples that contain a mixture of ketone isomers, as often occurs in breath samples.

In the context of the ketones analyses in real breath samples by PTR-MS, the functional isomers of species from this chemical family (such as e.g., aldehydes) also need to be considered and investigated as their protonated forms cannot be separated from the respective protonated ketones. The ketones' PTR-MS analyses in the presence of their functional isomers require further studies. However, it is worth mentioning here, that aldehydes undergo significant fragmentation in the PTR-MS instruments and the abundance of their protonated parent ions is usually very small (<10%) (Buhr et al., 2002; Schwartz et al., 2009). Consequently, the presence of aldehydes in the breath sample can only have minor influence on the parent ions of the respective ketones.

DATA AVAILABILITY

The raw data supporting the conclusions of this manuscript will be made available by the authors, without undue reservation, to any qualified researcher.

AUTHOR CONTRIBUTIONS

MM, DOL, and FP are Early Stage Researchers employed on the EU IMPACT ITN. They contributed equally to the experimental measurements, data analyses and contribution to the completion of this paper. PM proposed the study. PM, PS, SJ, CAM, and TDM contributed equally to the writing of the paper.

ACKNOWLEDGMENTS

We thank the Marie Skłodowska-Curie Actions Innovative Training Network: Ion-Molecule Processes for Analytical Chemistry Technologies (IMPACT) (www.impact-h2020itn.com) which has supported this research through the European Commission's HORIZON 2020 Programme under Grant Agreement Number 674911. The first three authors of this paper, MM, DOL, and FP are Early Stage Researchers in this IMPACT network.

REFERENCES

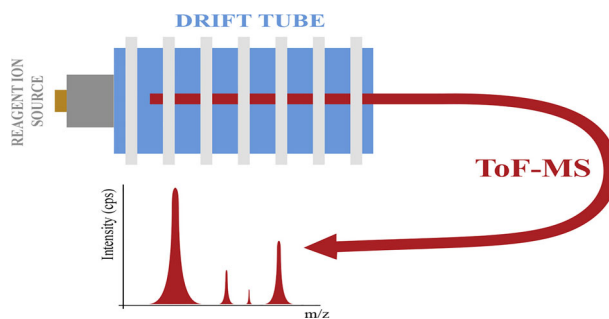
- Acton, J., Lanza, M., Agarwal, B., Jürschik, S., Sulzer, P., Breiev, K., et al. (2014). Headspace analysis of new psychoactive substances using a Selective Reagent Ionisation-Time of Flight-Mass Spectrometer. *Int. J. Mass Spectrom.* 360, 28–38. doi: 10.1016/j.ijms.2013.12.009
- Agarwal, B., González-Méndez, R., Lanza, M., Sulzer, P., Märk, T. D., Thomas, N., et al. (2014). Sensitivity and selectivity of switchable reagent ion soft chemical ionization mass spectrometry for the detection of picric acid. *J. Phys. Chem. A* 118, 8229–8236. doi: 10.1021/jp5010192
- Anderson, J. C. (2015). Measuring breath acetone for monitoring fat loss: review. *Obesity* 23, 2327–2334. doi: 10.1002/oby.21242
- Buhr, K., Van Ruth, S., and Delahunt, C. (2002). Analysis of volatile flavour compounds by Proton Transfer Reaction-Mass Spectrometry: fragmentation patterns and discrimination between isobaric and isomeric compounds. *Int. J. Mass Spectrometry* 221, 1–7. doi: 10.1016/S1387-3806(02)00896-5
- de Gouw, J. A., Goldan, P. D., Warneke, C., Kuster, W. C., Roberts, J. M., Marchewka, M., et al. (2003). Validation of proton transfer reaction-mass spectrometry (PTR-MS) measurements of gas-phase organic compounds in the atmosphere during the New England Air Quality Study (NEAQS) in 2002. *J. Geophys. Res.* 108:D4682. doi: 10.1029/2003JD003863
- de Gouw, J. A., and Warneke, C. (2007). Measurements of volatile organic compounds in the earth's atmosphere using proton-transfer-reaction mass spectrometry. *Mass Spectrom. Rev.* 26, 223–227. doi: 10.1002/mas.20119

- de Lacy Costello, B., Amann, A., Al-Kateb, H., Flynn, C., Filipiak, W., Khalid, T., et al. (2014). A review of the volatiles from the healthy human body. *J. Breath Res.* 8:014001. doi: 10.1088/1752-7155/8/1/014001
- Demarcke, M., Amelynck, C., Schoon, N., Dhooghe, F., Van Langenhove, H., and Dewulf, J. (2009). Laboratory studies in support of the detection of sesquiterpenes by proton-transfer-reaction-mass-spectrometry. *Int. J. Mass Spectrom.* 279, 156–162. doi: 10.1016/j.ijms.2008.10.023
- Ellis, A. M., and Mayhew, C. A. (2014). *Proton Transfer Reaction Mass Spectrometry: Principles and Applications*. Chichester: John Wiley & Sons.
- Fischer, L., Klinger, A., Herbig, J., Winkler, K., Gutmann, R., and Hansel, A. (2013). In: Proceedings of the 6th International Conference on Proton Transfer Reaction Mass Spectrometry and its Applications) 192–194.
- González-Méndez, R., Watts, P., Fraser Reich, D., Mullock, S. J., Cairns, S., Hickey, P., et al. (2018). Use of rapid reduced electric field switching to enhance compound specificity for proton transfer reaction-mass spectrometry. *Anal. Chem.* 90, 5664–5670. doi: 10.1021/acs.analchem.7b05211
- González-Méndez, R., Watts, P., Olivenza Leon, D., Reich, D. F., and Mullock, S. J., Corlett, et al. (2016). Enhancement of compound selectivity using a radio frequency ion-funnel proton transfer reaction mass spectrometer: improved specificity for explosive compounds. *Anal. Chem.* 88, 10624–10630. doi: 10.1021/acs.analchem.6b02982
- Graus, M., Müller, M., and Hansel, A. (2010). High resolution PTR-TOF: quantification and formula confirmation of VOC in real time. *J. Am. Soc. Mass Spectrom.* 21, 1037–1044. doi: 10.1016/j.jasms.2010.02.006
- Jordan, A., Haidacher, S., Hanel, G., Hartungen, E., Märk, L., Seehauser, H., et al. (2009). An online ultra-high sensitivity Proton-transfer-reaction-mass-spectrometer combined with switchable reagent ion capability (PTR + SRI – MS). *Int. J. Mass Spectrom.* 286, 32–38. doi: 10.1016/j.ijms.2009.06.006
- Jürschik, S., Agarwal, B., Kassebacher, T., Sulzer, P., Mayhew, C. A., and Märk, T. D. (2012). Rapid and facile detection of four “date rape drugs” in different beverages utilizing Proton-Transfer-Reaction Mass Spectrometry (PTR-MS). *J. Mass Spectrom.* 47, 1092–1097. doi: 10.1002/jms.2993
- Kari, E., Miettinen, P., Yli-Pirilä, P., Virtanen, A., and Faiol, C. L. (2018). PTR-ToF-MS product ion distributions and humidity-dependence of biogenic volatile organic compounds. *Int. J. Mass Spectrom.* 430, 87–97. doi: 10.1016/j.ijms.2018.05.003
- Lanza, M., Acton, W. J., Jürschik, S., Sulzer, P., Breiev, K., Jordan, A., et al. (2013). Distinguishing two isomeric mephedrone substitutes with selective reagent ionisation mass spectrometry (SRI-MS). *J. Mass Spectrom.* 48, 1015–1018. doi: 10.1002/jms.3253
- Lanza, M., Acton, W. J., Sulzer, P., Breiev, K., Jürschik, S., Jordan, A., et al. (2015). Selective reagent ionisation-time-of flight-mass spectrometry: a rapid technology for the novel analysis of blends of new psychoactive substances. *J. Mass Spectrom.* 50, 427–431. doi: 10.1002/jms.3514
- Materić, D., Lanza, M., Sulzer, P., Herbig, J., Bruhn, D., Gauci, V., et al. (2017). Selective reagent ion-time of flight-mass spectrometry study of six common monoterpenes. *Int. J. Mass Spectrom.* 421, 40–50. doi: 10.1016/j.ijms.2017.06.003
- Mayhew, C. A., Sulzer, P., Petersson, F., Haidacher, S., Jordan, A., Märk, L., et al. (2010). Applications of proton transfer reaction time-of-flight mass spectrometry for the sensitive and rapid real-time detection of solid high explosives. *Int. J. Mass Spectrom.* 289, 58–63. doi: 10.1016/j.ijms.2009.09.006
- Pan, Y., Zhang, Q., Zhou, W., Zou, X., Wang, H., Huang, C., et al. (2017). Detection of ketones by a novel technology: dipolar proton transfer reaction mass spectrometry (DP-PTR-MS). *J. Am. Soc. Mass Spectrom.* 28, 873–879. doi: 10.1007/s13361-017-1638-7
- Petersson, F., Sulzer, P., Mayhew, C. A., Watts, P., Jordan, A., Märk, L., et al. (2009). Real-time trace detection and identification of chemical warfare agent simulants using recent advances in proton transfer reaction time-of-flight mass spectrometry. *Rapid Commun. Mass Spectrom.* 23, 3875–3880. doi: 10.1002/rcm.4334
- Romano, A., Fischer, L., Herbig, J., Campbell-Sills, H., Coulon, J., Lucas, P., et al. (2014). Wine analysis by FastGC proton-transfer reaction-time-of-flight mass spectrometry. *Int. J. Mass Spectrom.* 369, 81–86. doi: 10.1016/j.ijms.2014.06.006
- Ruzsanyi, V., Fischer, L., Herbig, J., Ager, C., and Amann, A. (2013). Multi-capillary-column proton-transfer-reaction time-of-flight mass spectrometry. *J. Chromatogr. A* 1316, 112–118. doi: 10.1016/j.chroma.2013.09.072
- Schwartz, K., Filipiak, W., and Amann, A. (2009). Determining concentration patterns of volatile compounds in exhaled breath by PTR-MS. *J. Breath Res.* 3:027002. doi: 10.1088/1752-7155/3/2/027002
- Smith, D., Spanel, P., and Dryahina, K. (2019). H₃O⁺, NO⁺ and O₂⁺ reactions with saturated and unsaturated monoketones and diones; focus on hydration of product ions. *Int. J. Mass Spectrom.* 435, 173–180. doi: 10.1016/j.ijms.2018.10.027
- Smith, D., Wang, T., and Spanel, P. (2003). Analysis of ketones by selected ion flow tube mass spectrometry. *Rapid Comm. Mass Spectrom.* 17, 2655–2660. doi: 10.1002/rclm.1244
- Spanel, P., Ji, Y., and Smith, D. (1997). SIFT studies of the reactions of H₃O⁺, NO⁺ and O₂⁺ with a series of aldehydes and ketones. *Int. J. Mass Spectrom.* 165/166, 25–37. doi: 10.1016/S0168-1176(97)00166-3
- Specywyi, A., Smith, D., and Spanel, P. (2017). Ion chemistry at elevated ion-molecule interaction energies in a selected ion flow-drift tube: reactions of H₃O⁺, NO⁺ and O₂⁺ with saturated aliphatic ketones. *Phys. Chem. Chem. Phys.* 19, 31714–31723. doi: 10.1039/C7CP05795D
- Sulzer, P., Agarwal, B., Jürschik, S., Lanza, M., and Jordan, A., Hartungen, et al. (2013). Applications of switching reagent ions in proton transfer reaction mass spectrometric instruments for the improved selectivity of explosive compounds. *Int. J. Mass Spectrom.* 354–355, 123–128. doi: 10.1016/j.ijms.2013.05.004
- Sulzer, P., Petersson, F., Agarwal, B., Becker, K. H., Jürschik, S., Märk, T. D., et al. (2012). Proton transfer reaction mass spectrometry and the unambiguous real-time detection of 2,4,6 TNT. *Anal. Chem.* 84, 4161–4166. doi: 10.1021/ac3004456
- Tani, A., Hayward, S., Hansel, A., Hewitt, C. N. (2004). Effect of water vapour pressure on monoterpene measurements using proton transfer reaction-mass spectrometry (PTR-MS). *Int. J. Mass Spectrom.* 239, 161–169. doi: 10.1016/j.ijms.2004.07.020
- Tani, A., Hayward, S., and Hewitt, C. N. (2003). Measurement of monoterpenes and related compounds by proton transfer reaction-mass spectrometry (PTR-MS). *Int. J. Mass Spectrom.* 223–224, 561–578. doi: 10.1016/S1387-3806(02)00880-1
- Trefz, P., Schubert, J. K., and Miekisch, W. (2018). Effects of humidity, CO₂ and O₂ on real-time quantitation of breath biomarkers by means of PTR-ToF-MS. *J. Breath Res.* 12:026016. doi: 10.1088/1752-7163/a9eea
- Warneke, C., Van Der Veen, C., Luxembourg, S., De Gouw, J. A., and Kok, A. (2001). Measurements of benzene and toluene in ambient air using proton-transfer-reaction mass spectrometry: calibration, humidity dependence, and field intercomparison. *Int. J. Mass Spectrom.* 207:167. doi: 10.1016/S1387-3806(01)00366-9
- Conflict of Interest Statement:** FP and TDM was employed by company IONICON Analytik Gesellschaft m.b.H.
- The remaining authors declare that the research was conducted in the absence of any commercial or financial relationships that could be construed as a potential conflict of interest.
- Copyright © 2019 Malásková, Olivenza-León, Piel, Mochalski, Sulzer, Jürschik, Mayhew and Märk. This is an open-access article distributed under the terms of the Creative Commons Attribution License (CC BY). The use, distribution or reproduction in other forums is permitted, provided the original author(s) and the copyright owner(s) are credited and that the original publication in this journal is cited, in accordance with accepted academic practice. No use, distribution or reproduction is permitted which does not comply with these terms.



RESEARCH ARTICLE

Selective Reagent Ion Mass Spectrometric Investigations of the Nitroanilines

David Olivenza-León,¹ Chris A. Mayhew,^{1,2} Ramón González-Méndez^{1,3} ¹Molecular Physics Group, School of Physics and Astronomy, University of Birmingham, Edgbaston, Birmingham, B15 2TT, UK²Institut für Atemgasanalytik, Leopold-Franzens-Universität Innsbruck, Rathausplatz 4, 6850, Dornbirn, Austria³Centre for Agroecology, Water and Resilience, Coventry University, Coventry, CV1 5FB, UK

Abstract. This paper presents an investigation of proton and charge transfer reactions to 2-, 3- and 4-nitroanilines ($C_6H_5N_2O_2$) involving the reagent ions $H_3O^+ \cdot (H_2O)_n$ ($n=0, 1$ and 2) and O_2^+ , respectively, as a function of reduced electric field (60–240 Td), using Selective Reagent Ion–Time-of-Flight–Mass Spectrometry (SRI–ToF–MS). To aid in the interpretation of the $H_3O^+ \cdot (H_2O)_n$ experimental data, the proton affinities and gas-phase basicities for the three nitroaniline isomers have

been determined using density functional theory. These calculations show that proton transfer from both the H_3O^+ and $H_3O^+ \cdot H_2O$ reagent ions to the nitroanilines will be exoergic and hence efficient, with the reactions proceeding at the collisional rate. For proton transfer from H_3O^+ to the NO_2 sites, the exergicities are 171 kJ mol^{-1} (1.8 eV), 147 kJ mol^{-1} (1.5 eV) and 194 kJ mol^{-1} (2.0 eV) for 2-, 3- and 4-nitroanilines, respectively. Electron transfer from all three of the nitroanilines is also significantly exothermic by approximately 4 eV. Although a substantial transfer of energy occurs during the ion/molecule reactions, the processes are found to predominantly proceed via non-dissociative pathways over a large reduced electric field range. Only at relatively high reduced electric fields (> 180 Td) is dissociative proton and charge transfer observed. Differences in fragment product ions and their intensities provide a means to distinguish the isomers, with proton transfer distinguishing 2-nitroaniline (2-NA) from 3- and 4-NA, and charge transfer distinguishing 4-NA from 2- and 3-NA, thereby providing a means to enhance selectivity using SRI–ToF–MS.

Keywords: Soft chemical i-mass spectrometry, Proton transfer reaction mass spectrometry, Nitroanilines, Explosives, Charge transfer

Received: 22 June 2019/Revised: 14 August 2019/Accepted: 15 August 2019

Introduction

Selective Reagent Ion–Mass Spectrometry (SRI–MS) is a commonly used soft chemical ionisation technique used in a broad range of analytical fields and applications [1, 2]. These include environmental analysis, food science, atmospheric chemistry, health science, homeland security and breath analysis [3–12]. Its analytical technique is based on ion/molecule reactions in a controlled environment, namely a drift tube maintained at a constant pressure, temperature, humidity and fixed electric field. Commonly used reagent ions are H_3O^+ and O_2^+ , which react with traces of neutral organic molecules, injected directly into the drift tube of the instrument, usually with no pre-separation step. This allows for real-time analysis with a time resolution of approx.

Research highlights

- First investigations on the use of selective reagent ion mass spectrometry for nitroaniline isomers involving proton transfer and charge transfer reactions as a function of reduced electric field
- DFT calculations of the proton affinities and gas-phase basicities of the nitroanilines
- Identification of individual isomers through the manipulation of the ion chemistry

Correspondence to: Ramón González-Méndez;
e-mail: R.GonzalezMendez@bham.ac.uk;
Ramon.Gonzalez-Mendez@coventry.ac.uk

100 ms. These attributes make SRI-MS an ideal technique for detecting compounds that are only transiently (seconds) present in the drift tube. When H_3O^+ is only used as the reagent ion, the technique is better known as Proton Transfer Reaction–Mass Spectrometry (PTR–MS) [1]. In this study, we investigated reactions involving both O_2^+ and H_3O^+ , and hence, the term SRI–MS is more appropriate for the work presented here.

During the last 10 years, a large amount of work exploring the capabilities of SRI–MS for Homeland Security has been undertaken [3–5, 13–22]. Two key objectives of this work are the following: (i) instrumental development for enhancing SRI–MS analytical performance (such as use of different reagent ions [16], new sample inlet methods [13], use of ion funnel for either enhanced sensitivity or selectivity [18, 23] and fast reduced electric field switching for enhanced selectivity [20]) and (ii) improving our knowledge of the underlying ion/molecule chemistry occurring within the reagent region of the analytical device.

A limitation with the selectivity of SRI–MS is associated with its capability to distinguish isomers. This is particularly true for proton transfer reactions, where often only the protonated parent¹ is observed, but not necessarily so for other reaction processes such as charge transfer [24]. Here we present a SRI–MS study of the isomers of nitroanilines (2-, 3- and 4-nitroaniline) to ascertain whether they can be distinguished through the manipulation of the ion/chemistry. Another motivation for this study is that nitroanilines exhibit certain explosive characteristics, owing to their structure (aromatic ring with nitro functional group substituents). Therefore, these compounds represent a natural continuation of our SRI–MS studies of explosive compounds [3–5, 13, 15–22].

An additional interest is that nitroanilines are a family of chemical compounds used in the manufacture of dyes, pharmaceuticals and pesticides [25], so it is important to characterise them from a quality control need as different isomers have different properties and reactivities. They also exhibit a high toxicity, particularly the [1, 4] isomer [26], so it is relevant to develop analytical methods for quick, selective and reliable identification for environmental purposes.

Nitroanilines ($\text{C}_6\text{H}_5\text{N}_2\text{O}_2$, m/z 138.04 Da (lightest isotopologue)) are a derivative of aniline, a commonly used precursor in the polymer industry, and hence is widespread in the environment [27]. Here we investigate whether the position of the nitro group plays a role in the ion/molecule processes. We present details on the product ion distributions resulting from the reactions of H_3O^+ and O_2^+ . To aid in the interpretation of the experimental measurements involving the reagent ions $\text{H}_3\text{O}^+\cdot(\text{H}_2\text{O})_n$ ($n = 0, 1$ and 2), quantum mechanical calculations have been undertaken to determine proton affinities and gas-phase basicities.

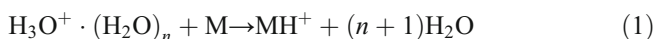
¹Although revised IUPAC recommendations for terminology in mass spectrometry (Pure Appl. Chem., 2013, Vol. 85, No. 7, pp. 1515–1609) suggest replacing the term “parent” with “precursor”, since for this work, ions are not mass selected, the term “precursor” is not appropriate. We note that “protonated parent” is commonly used within the PTR–MS community [1].

Experimental Details

SRI–MS

For this investigation, a Kore Technology Ltd. Series I Selective Reagent Ion–Time of Flight–Mass Spectrometer (SRI–ToF–MS) instrument was used, details of which been given elsewhere [1, 28], and therefore only brief and pertinent details will be presented in this paper.

Proton Transfer Reaction Mode This mode exploits the proton transfer reaction of H_3O^+ and, depending on the reduced electric field (the ratio of the electric field strength (E) to the gas number density (N) applied in the drift tube and the humidity, also protonated water clusters with molecules of interest M:



where $n = 0, 1$ and 2 are the most important for our operational conditions (see Figure 1) but also (in low concentrations and only at low E/N (less than approximately 100 Td (1 Td = 10^{-17} V cm²))) $n = 3$. Proton transfer can be either non-dissociative or spontaneously dissociative. Following non-dissociative proton transfer, collisional induced dissociation may occur, with the probability of this increasing with increasing reduced electric field.

To produce the reagent ions, a series of ion-molecule processes (including three-body association) take place in a hollow cathode glow discharge, initiated by an electric discharge in water vapour and associated drift tube buffer gas that has diffused back into the ionisation source. The reagent ions that are generated in the ion source region are transferred into the drift tube by an applied voltage gradient. The relative intensities of the water reagent ions in the drift tube of the KORE instrument used as a function of E/N are summarised in Figure 1, which illustrates that under our operating conditions,

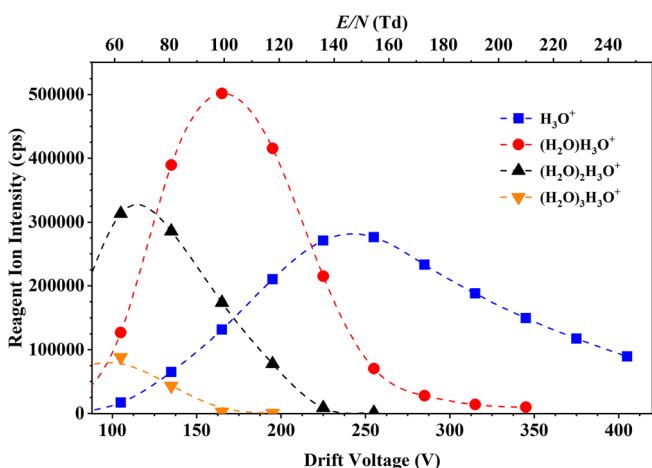


Figure 1. Ion intensities in counts per second (cps) of the water reagent ions $(\text{H}_3\text{O}^+\cdot(\text{H}_2\text{O})_n$, $n = 0, 1, 2$ and 3) recorded at the detector of the KORE SRI–ToF–MS as a function of reduced electric field (approximately 60–250 Td).

only at relatively high E/N values (greater than 140 Td) does H_3O^+ become the dominant reagent ion.

Although H_3O^+ (and associated protonated water clusters—depending on the value of the reduced electric field) dominates the reagent ion signal, other reagent ions are always present in the drift tube. These “impurity” reagent ions result from back diffusion of the buffer gas in the drift tube into the ion source. These reagent ions are those that cannot react with water, such as O_2^+ . However, these are at very low concentrations. Under our experimental conditions, the intensity of was O_2^+ was maintained below 0.5% of that of the H_3O^+ signal.

The signal intensity of $\text{H}_3^{16}\text{O}^+$ is generally too large to be measured directly. Therefore, the signal intensity for the spectral line peaking at m/z 21.02, corresponding to $\text{H}_3^{18}\text{O}^+$, was recorded. The m/z 19.02 intensity, corresponding to $\text{H}_3^{16}\text{O}^+$, was determined in the normal manner by multiplying the m/z 21.02 signal by 487. Similarly, the m/z 37.03 signal intensity, corresponding to $\text{H}_3^{16}\text{O}^+\cdot\text{H}_2^{16}\text{O}$, was not measured directly. Instead, the signal intensity at m/z 39.03 ($\text{H}_3^{18}\text{O}^+\cdot\text{H}_2^{16}\text{O}$ or $\text{H}_3^{16}\text{O}^+\cdot\text{H}_2^{18}\text{O}$) was recorded and multiplied by 243.

Charge Transfer Reaction Mode For the production of O_2^+ , pure oxygen (99.998% purity, BOC Gases, Manchester, UK) was flowed into the ion source. This leads to the formation of mainly O_2^+ reagent ions (> 95%). Figure 2 shows the O_2^+ ion signal intensity in counts per second (cps) as a function of E/N . Once injected into the drift tube, O_2^+ may react with the analyte M via charge transfer, provided that the ionisation energy (IE) of M is less than that of O_2 (IE (O_2) = 12.07 eV). Unlike proton transfer, an exothermic reaction is a necessary but not sufficient criterion for charge transfer to occur, and hence, the reaction rate coefficient may not necessarily be collisional [29]. However, if charge transfer does occur, it may also be either non-dissociative (resulting in the singly charged parent ion (M^+)) or dissociative. Fragmentation might be spontaneous upon charge transfer or require additional energy through collisions in the drift tube. H_3O^+ is also observed when operating the ion source

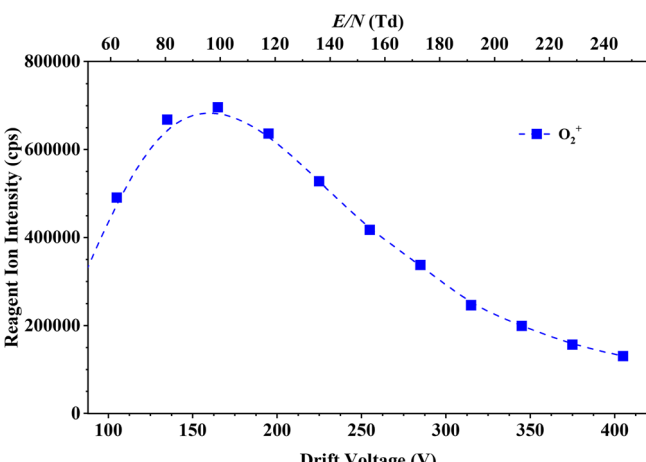


Figure 2. Ion intensities in counts per second (cps) of O_2^+ recorded at the detector of the KORE SRI-ToF-MS as a function of reduced electric field (approximately 60–250 Td)

in oxygen mode. This is due to residual water vapour in the system. However, this can be ignored owing to its signal intensity being approximately 0.1% of the O_2^+ signal for the experimental conditions used throughout our measurements.

Operational Procedures

Liquid samples were vapourised making use of a thermal desorption unit (TDU), connected to the inlet of the drift tube via passivated stainless steel (Silconert®). Details of the TDU have been given elsewhere [13]. The TDU, connecting lines and drift tube were operated at a temperature of 150 °C. For this study, oxygen-free nitrogen (99.998% purity, BOC Gases, Manchester, UK) was used as the carrier gas. PTFE swabs (Thermo Fisher Scientific, Cheshire, UK), onto which known quantities of the sample had been deposited, were manually placed into the TDU. Upon closure of the TDU unit, a high force annular “anvil” compressed the PTFE to plastically deform and convert it into a gas tight circular seal around the rim of the swab. At the same time, laboratory air heated to a specified temperature rapidly heats the PTFE and as it passes through carries any thermally desorbed material into the heated inlet line through to the drift (reaction) region. The temporal desorption profile is typically between 10 and 20 s [13]. For each measurement, one swab was used, which was replicated three times. The results were then averaged, and any background signals were subtracted.

The drift tube pressure was set at 1 mbar, and the glow discharge (for both water vapour and oxygen) was set at 1.4 mbar. The only variable was the operating drift tube voltage, which was adjusted over a range of approximately 100 to 400 V to provide an appropriate reduced electric field range of about 60–250 Td.

Chemicals

Individual nitroaniline (2-, 3- and 4-) isomers for this study were purchased from Sigma Aldrich (Cheshire, UK), all of which came with stated purities of at least 98%. At room temperature, nitroanilines are yellowish-orange granulated solids. For the measurements, granules were dissolved in a mixture of MeOH:AcN 1:1 (V/V) (analytical grade) to provide a concentration of approx. 100 µg/mL. A volume of 1 µL of this solution was deposited onto the swab and left the solvents to evaporate at room temperature for approximately 1 min before placing the swab into the TDU.

DFT Calculations

Density functional theory (DFT) calculations have been undertaken to determine the proton affinities and gas-phase basicities of the water monomer, dimer and trimer and the three nitroanilines. These calculations were conducted using Gaussian09W and GaussView05 for Windows [30]. The B3LYP functional with the 6-31+G(d,p) basis set was used throughout, a combination which has been found to be satisfactory based on our previous work [31, 32].

Results

For this section, only product ions with branching percentages greater than 1% for any given reduced electric field value are reported. The uncertainty in any branching percentage is approximately 10%. In all cases, only the mass to charge ratio of the lightest isotope is given. However, when calculating the product ion distributions, we considered all of the isotopologues. For the product ion distribution (PID) plots (branching percentages), the voltage applied to the drift tube is shown in the main x -axis, and the reduced electric field E/N achieved for that particular voltage is showed in the secondary x -axis.

DFT Calculations

Table 1 presents the calculated proton affinities (PA) and gas-phase basicities (GB) for the water monomer, the water dimer, the water trimer and the three nitroanilines. For the nitroaniline isomers, values are provided for the two possible protonation sites, namely on the amino and nitro groups. Aniline and nitrobenzene are also shown for comparison. Table 1 also provides for convenience the ionisation energies of oxygen and the nitroanilines [33].

The proton affinities of the water dimer and trimer are higher than that of the monomer, because of the added stability by sharing the proton with additional waters. The proton affinity of water clusters increases as the number of water molecules increases, but the incremental effect declines as the cluster grows as illustrated in the DFT calculations.

As shown in Table 1, whilst for simpler chemical structures as aniline and nitrobenzene, the aniline's NH_2 substituent is much more basic than the NO_2 of nitrobenzene, this is not the case in the nitroanilines where both groups are on the ring. The interaction of the nitro group (electron withdrawing effect from the aromatic ring) and the amine group (electron donating effect to the aromatic ring) reverse their basicities, in the order 4-nitroaniline (4-NA) > 2-NA > 3-NA. Based on this data, with the exception of the 2-NA where the groups are in close

proximity, it is likely that the $\text{NA}\cdot\text{H}^+$ for the 3 and 4 isomers is a mixture of species.

The DFT calculations show that proton transfer from $\text{H}_3\text{O}^+\cdot(\text{H}_2\text{O})_n$ ($n=0$ and 1) to both sites of all three of the nitroanilines is exoergic. $\text{H}_3\text{O}^+\cdot(\text{H}_2\text{O})_2$ can also proton transfer to the NO_2 site of 4-NA.

Fragmentation Patterns and Branching Ratios Studies for Reactions with H_3O^+

2-Nitroaniline Figure 3 shows the product ion distribution (PID) plot for 2-nitroaniline resulting reactions with $\text{H}_3\text{O}^+\cdot(\text{H}_2\text{O})_n$ ($n=0$ and 1) (see Figure 1) as a function of E/N over the range from 60 to 250 Td. The protonated parent, $[\text{2-NA}\cdot\text{H}]^+$, at m/z 139.05 is the most intense product ion until about 220 Td, after which fragment product ions dominate. Fragment product ions begin to appear at about 150 Td, starting with at m/z 121.04 (resulting from the loss of a water molecule from the protonated parent, $[\text{2-NA}\cdot\text{H}_2\text{O}]^+$), and which becomes dominant above about 220 Td. Other fragment product ions are observed with increasing E/N , namely m/z 93.06 (assigned to the loss of a nitro group from the protonated parent, leading to a $\text{C}_6\text{H}_7\text{N}^+$ ion) and m/z 91.04 (caused by the loss of a nitro group followed by the sequential loss of a hydrogen molecule, leading to a $\text{C}_6\text{H}_5\text{N}^+$ ion). At low reduced electric fields (less than about 120 Td), a product ion is observed at m/z 157.06, which is simply $2\text{-NAH}^+\cdot\text{H}_2\text{O}$, resulting from a third body association reaction of the protonated parent with water. Its intensity increases as the E/N decreases because of reduced collisional induced dissociation.

Figure 4 shows two overlaid mass spectra at two different E/N values for 2-nitroaniline, exemplifying the difference in performance for the instrument—similar plots (not shown) were found for the rest of the samples and for oxygen chemistry.

3-Nitroaniline Figure 5 shows the PID plot for 3-nitroaniline resulting from its reaction with $\text{H}_3\text{O}^+\cdot(\text{H}_2\text{O})_n$

Table 1. Proton Affinities (PA), Gas-Phase Basicities (GB) and Ionisation Energies (IE) for Nitroaniline (NA) Isomers. The PA and GB Values Have Been Calculated Using the B3LYP Functional and the 6-31+G(d,p) Basis Set at 298 K. ΔH_{298} and ΔG_{298} Refer to the Enthalpies and Free Energies for the Addition of Water to the Protonated Species. For Convenience, the Ionisation Energies of O_2 and the Three Nitroanilines Are Also Provided

Chemical	Site	PA ^a	GB ^a	$\Delta H_{298}^{\text{a}}$	$\Delta G_{298}^{\text{a}}$	IE (eV) ^b
Water		684	653			
Water dimer		842	777			
Water trimer		937	841			
O_2						12.07 [34]
						8.27
2-NA	NH_2	840	806	-69	-37	
	NO_2	858	824	-76	-43	
3-NA	NH_2	824	796	-78	-43	
	NO_2	830	800	-84	-51	8.31
4-NA	NH_2	810	784	-78	-43	
	NO_2	879	847	-73	-39	8.34
Aniline	NH_2	874	846	-72	-40	
Nitrobenzene	NO_2	806	775	-90	-55	

^aThermochemical data expressed in kilojoules per mole

^bIonisation energies (in eV) have been taken from NIST database [33]

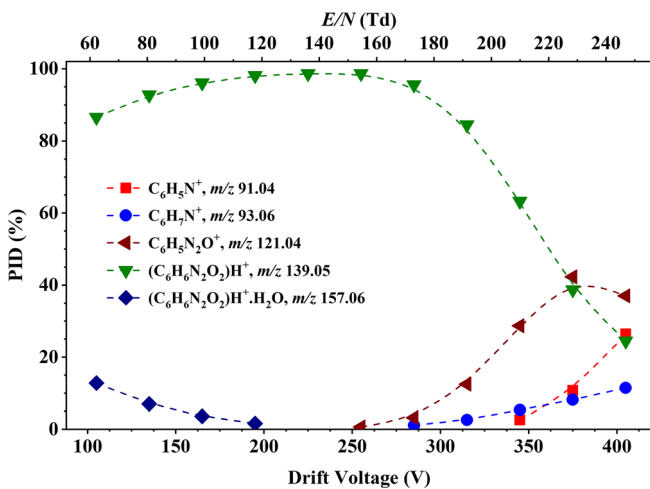


Figure 3. Percentage product ion distribution (PID in %) resulting from the reaction of 2-nitroaniline with $\text{H}_3\text{O}^+\cdot(\text{H}_2\text{O})_n$ ($n = 0$ and 1) as a function of the reduced electric field from 60 to 250 Td

($n = 0$ and 1) as a function of the reduced electric field E/N for the range from 20 to 250 Td. Similar to the results obtained for 2-NA, the protonated parent [$3\text{-NA}\cdot\text{H}]^+$ is the dominant product ion up to about 220 Td. However, unlike 2-NA, much more association of the protonated parent with water is observed at low reduced electric fields (< 140 Td), under identical operational (reduced electric field and humidity) conditions. At 60 Td, $3\text{-NAH}^+\cdot\text{H}_2\text{O}$ has approximately the same branching percentage as the protonated parent.

Above ca. 230 Td, the fragment product ion $\text{C}_6\text{H}_7\text{N}^+$ dominates. Another product ion, starting at an E/N value of approximately 190 Td, is observed at m/z 109.05. This is considered to result from the loss of NO from the protonated parent leading to $\text{C}_6\text{H}_7\text{NO}^+$ [35]. This product ion was not observed for 2-nitroaniline.

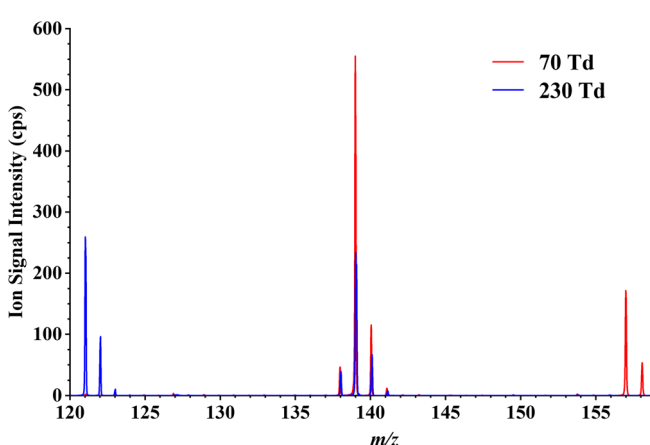


Figure 4. Overlaid mass spectra for 2-nitroaniline at 70 and 230 Td. This figure illustrates the clear difference in ion signal intensities for m/z 121.04, 139.05 and 157.06 upon the reduced electric field applied to the DT of the instrument

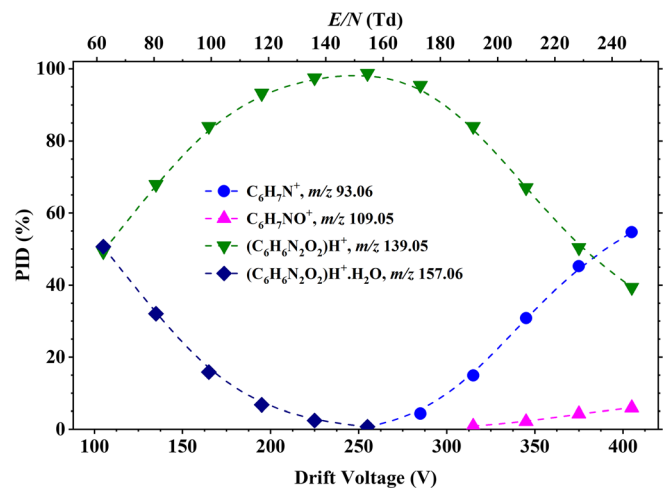


Figure 5. Percentage product ion distribution resulting from the reaction of 3-nitroaniline with $\text{H}_3\text{O}^+\cdot(\text{H}_2\text{O})_n$ ($n = 0$ and 1) as a function of the reduced electric field from 60 to 250 Td

4-Nitroaniline Figure 6 presents the PID for the reaction of 4-nitroaniline with $\text{H}_3\text{O}^+\cdot(\text{H}_2\text{O})_n$ ($n = 0$ and 1) as a function of the reduced electric field E/N for the range from 60 to 250 Td. For this isomer, the protonated parent, $[4\text{-NA}\cdot\text{H}]^+$, dominates throughout the whole E/N range. Little fragmentation occurs, with only one product ion being observed at m/z 93.06 (corresponding to the loss of a nitro group from the protonated parent molecule) above about 160 Td. Three-body association of the protonated parent with water is also observed at m/z 157.06, with a similar intensity to that found for 2-NA.

Thus, we find that protonated 3-NA solvates more readily than do protonated 2-NA and 4-NA, and this merits some discussion. Table 1 shows that the ΔG_{298} for the association of water to protonated 2 and 4-NA is 43 kJ mol^{-1} , whereas the ΔG_{298} for association of water to protonated 3-NA is 51 kJ mol^{-1} . Whilst 8 kJ mol^{-1} may not seem a great difference, when converted into equilibrium constants, at the operating

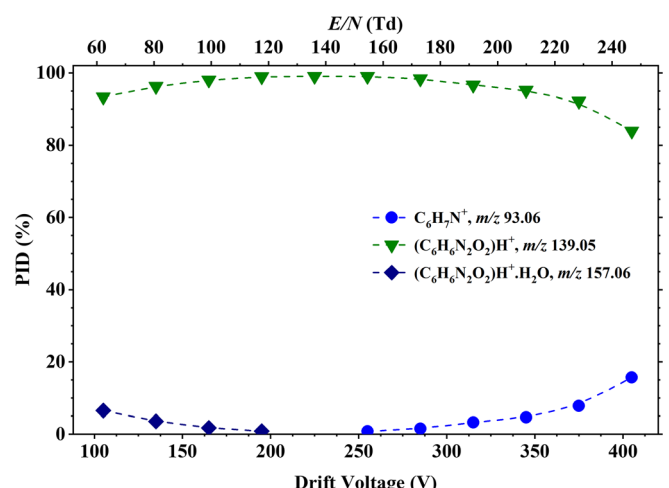


Figure 6. Percentage product ion distribution resulting from the reaction of 4-nitroaniline with $\text{H}_3\text{O}^+\cdot(\text{H}_2\text{O})_n$ ($n = 0, 1$ and 2) as a function of the reduced electric field from 60 to 250 Td

temperature of the drift tube (423 K), 3-NAH⁺ binds water approximately ten times better than 2-NAH⁺ and 4-NAH⁺.

In comparison to the product ion fragmentation patterns found for 2- and 3-NA, the 4-NA isomer is quite different. This is a direct effect of the *para* position for the functional groups in the aromatic ring. The amine and nitro substituents are far off from each other, and therefore, there is no option for an intermediate transition state where a ring is formed prior to leading to the final product ion. This is consistent with chemical ionisation work reported for the nitroarenes with electron-releasing substituents [36].

Fragmentation Patterns and Branching Percentage Studies for Reactions with O₂⁺

2-Nitroaniline Figure 7 presents a summary of the results for the reaction of O₂⁺ with 2-NA as a function of reduced electric field. The parent ion at *m/z* 138.04, [2-NA]⁺, resulting from non-dissociative charge transfer, dominates up to about 230 Td. Its abundance decreases as the reduced electric field increases, and at *E/N*, above ca. 230 Td, *m/z* 80.05 (assigned to the product ion C₅H₆N⁺) becomes dominant. Other product ions, resulting from dissociative charge transfer, are observed at *m/z* 65.04 (C₅H₅⁺), *m/z* 92.07 (C₆H₆N⁺) (loss of NO₂), *m/z* 108.04 (C₆H₆NO⁺) (loss of NO) and *m/z* 121.04 (C₆H₅N₂O⁺) (loss of OH). C₆H₅N₂O⁺ was not observed in any of the other isomers.

3-Nitroaniline For 3-NA, a very similar fragmentation product ion pattern found for that of 2-NA is observed, as shown in Figure 8. Products ions are observed at *m/z* 65.04 (C₅H₅⁺), 80.05 (C₅H₆N⁺), *m/z* 92.07 (C₆H₆N⁺), *m/z* 108.04 (C₆H₆NO⁺) and *m/z* 138.04, [3-NA]⁺, but with slight differences in their intensities at very high *E/N* values. For 3-NA, the parent ion at *m/z* 138.04, [3-NA]⁺ dominates for most of the reduced electric field investigated. But by about 240 *m/z*, 80.05 (C₅H₆N⁺)

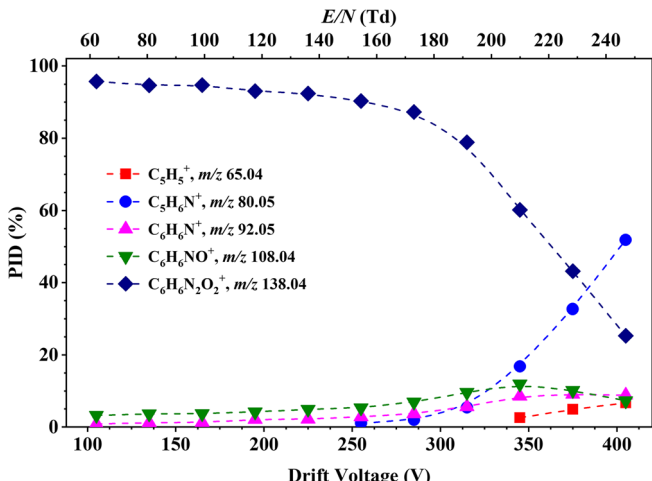


Figure 7. Percentage product ion distribution resulting from the reaction of 2-nitroaniline with O₂⁺ as a function of the reduced electric field from 60 to 250 Td

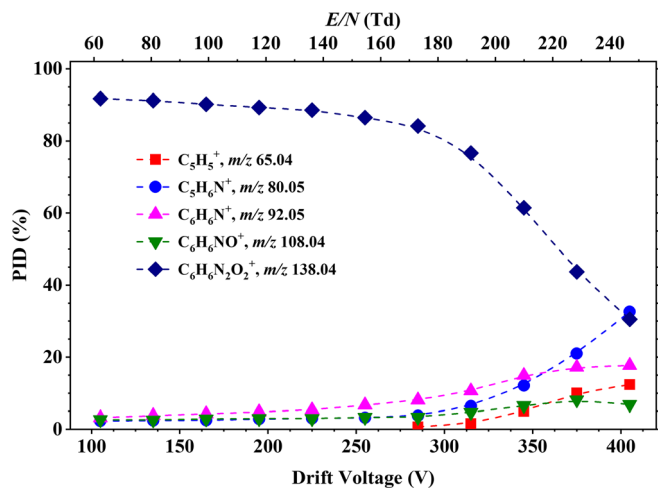


Figure 8. Percentage product ion distribution resulting from the reaction of 3-nitroaniline with O₂⁺ as a function of the reduced electric field in the range from 60 to 250 Td

becomes dominant. A clear difference is the intensity for the product ion at *m/z* 92.05 (C₆H₆N⁺), going up to ca. 15% (compared to only ca. 5% for 2-NA) and at *m/z* 65.04 (C₅H₅⁺) (ca. 12% for 3-NA compared to ca. 6% for 2-NA).

4-Nitroaniline The product ion fragmentation pattern for 4-NA, as shown in Figure 9, is very different from that observed for the other two isomers, with a simpler product ion distribution being observed, having only three product ions. This is a direct consequence of the *para* position for the substituents in the aromatic ring. The parent ion at *m/z* 138.04, [4-NA]⁺, dominates from 60 Td up to ca. 190 Td, after which the product ion at *m/z* 108.04 (C₆H₆NO⁺) becomes dominant. For *E/N* values above 190 Td, another fragment ion at *m/z* 80.05 (C₅H₆N⁺) becomes relevant, having a maximum intensity of ca. 30% at an *E/N* value of 250 Td.

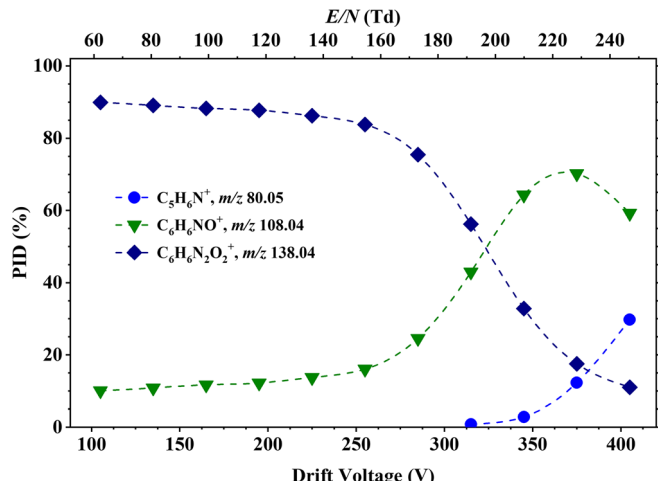


Figure 9. Percentage product ion distribution resulting from the reaction of 4-nitroaniline with O₂⁺ as a function of the reduced electric field in the range from 60 to 250 Td

Conclusions

This work reports the product ions from the reaction of 2-, 3- and 4-nitroaniline isomers with H_3O^+ and O_2^+ as a function of the reduced electric field in a SRI-ToF-MS. We have shown that selective reagent ion mass spectrometry, using either water or oxygen as reagent gases, can be used to detect nitroaniline isomers with good selectivity. The most abundant product ion for all the isomers for the reactions with H_3O^+ is the protonated parent at m/z 139.05 over an extended reduced electric field range. For the reactions with O_2^+ , non-dissociative charge transfer results in the parent ion at m/z 138.04 being the most abundant product ion. However, relative ion abundances are different for each reagent ion. 2- and 3-NA show very similar fragmentation patterns with O_2^+ , whilst with H_3O^+ , 2-NA shows smaller water clustering at low E/N and its fragment product ions become dominant at a lower E/N than found for 3-NA. 4-NA shows less fragmentation with H_3O^+ , and for the reaction with O_2^+ , a distinctive fragment ion is observed at m/z 108.04, which becomes dominant above about 190 Td. The presence or absence of this product ion at m/z 108.04 easily allows for reliable identification of the 4-NA isomer.

This study demonstrates how it is possible to distinguish isomers based on the manipulation of the ion/molecule chemistry and/or using different reagent ions that favour different ionisation mechanisms.

Acknowledgements

We thank the Marie Skłodowska-Curie Actions Innovative Training Network: Ion-Molecule Processes for Analytical Chemistry Technologies (IMPACT) (www.impact-h2020itn.com) which has supported this research through the European Commission's HORIZON 2020 Programme under Grant Agreement Number 674911. DOL is an Early Stage Researcher on IMPACT. We also thank Dr. Peter Watts (a member of the Molecular Physics Group, School of Physics and Astronomy, University of Birmingham, UK) for undertaking the DFT calculations presented in this paper. The authors also thank Mahroz Mirzahekmati for producing the graphical abstract.

Open Access

This article is distributed under the terms of the Creative Commons Attribution 4.0 International License (<http://creativecommons.org/licenses/by/4.0/>), which permits unrestricted use, distribution, and reproduction in any medium, provided you give appropriate credit to the original author(s) and the source, provide a link to the Creative Commons license, and indicate if changes were made.

References

- Ellis, A. M., Mayhew, C. A.: Proton Transfer Reaction Mass Spectrometry: Principles and Applications. 1st ed. Wiley, p 336 (2014)
- Biasioli, F., Yeretzian, C., Märk, T.D., Dewulf, J., Van Langenhove, H.: Direct-injection mass spectrometry adds the time dimension to (B) VOC analysis. *TrAC Trends Anal. Chem.* **30**(7), 1003–1017 (2011)
- Mayhew, C.A., Sulzer, P., Petersson, F., Haidacher, S., Jordan, A., Märk, L., Watts, P., Märk, T.D.: Applications of proton transfer reaction time-of-flight mass spectrometry for the sensitive and rapid real-time detection of solid high explosives. *Int. J. Mass Spectrom.* **289**(1), 58–63 (2010)
- Sulzer, P., Petersson, F., Agarwal, B., Becker, K.H., Jürschik, S., Märk, T.D., Perry, D., Watts, P., Mayhew, C.A.: Proton transfer reaction mass spectrometry and the unambiguous real-time detection of 2,4,6 trinitrotoluene. *Anal. Chem.* **84**(9), 4161–4166 (2012)
- Kassebacher, T., Sulzer, P., Jürschik, S., Hartungen, E., Jordan, A., Edtbauer, A., Feil, S., Hanel, G., Jakusch, S., Märk, L., Mayhew, C.A., Märk, T.D.: Investigations of chemical warfare agents and toxic industrial compounds with proton-transfer-reaction mass spectrometry for a real-time threat monitoring scenario. *Rapid Commun. Mass Spectrom.* **27**(2), 325–332 (2013)
- Fernández del Río, R., O'Hara, M.E., Holt, A., Pemberton, P., Shah, T., Whitehouse, T., Mayhew, C.A.: Volatile biomarkers in breath associated with liver cirrhosis — comparisons of pre- and post-liver transplant breath samples. *EBioMedicine*. **2**(9), 1243–1250 (2015)
- Trefz, P., Schubert, J.K., Miekisch, W.: Effects of humidity, CO₂ and O₂ on real-time quantitation of breath biomarkers by means of PTR-ToF-MS. *J. Breath. Res.* **12**(2), 026016 (2018)
- Herbig, J., Beauchamp, J.: Towards standardization in the analysis of breath gas volatiles. *J. Breath. Res.* **8**(3), 037101 (2014)
- Ruzsányi, V., Kalapos, M.P., Schmidl, C., Karall, D., Scholl-Bürgi, S., Baumann, M.: Breath profiles of children on ketogenic therapy. *J. Breath. Res.* **12**(3), 036021 (2018)
- Agarwal, B., Petersson, F., Jürschik, S., Sulzer, P., Jordan, A., Märk, T.D., Watts, P., Mayhew, C.A.: Use of proton transfer reaction time-of-flight mass spectrometry for the analytical detection of illicit and controlled prescription drugs at room temperature via direct headspace sampling. *Anal. Bioanal. Chem.* **400**(8), 2631–2639 (2011)
- Lanza, M., Acton, W.J., Sulzer, P., Breiev, K., Jürschik, S., Jordan, A., Hartungen, E., Hanel, G., Märk, L., Märk, T.D., Mayhew, C.A.: Selective reagent ionisation-time of flight-mass spectrometry: a rapid technology for the novel analysis of blends of new psychoactive substances. *J. Mass Spectrom.* **50**(2), 427–431 (2015)
- Critchley, A., Elliott, T., Harrison, G., Mayhew, C., Thompson, J., Worthington, T.: The proton transfer reaction mass spectrometer and its use in medical science: applications to drug assays and the monitoring of bacteria. *Int. J. Mass Spectrom.* **239**(2–3), 235–241 (2004)
- González-Méndez, R., Reich, D.F., Mullock, S.J., Corlett, C.A., Mayhew, C.A.: Development and use of a thermal desorption unit and proton transfer reaction mass spectrometry for trace explosive detection: determination of the instrumental limits of detection and an investigation of memory effects. *Int. J. Mass Spectrom.* **385**, 13–18 (2015)
- Shen, C., Li, J., Han, H., Wang, H., Jiang, H., Chu, Y.: Triacetone triperoxide detection using low reduced-field proton transfer reaction mass spectrometer. *Int. J. Mass Spectrom.* **285**(1–2), 100–103 (2009)
- Jürschik, S., Sulzer, P., Petersson, F., Mayhew, C.A., Jordan, A., Agarwal, B., Haidacher, S., Seehauser, H., Becker, K., Märk, T.D.: Proton transfer reaction mass spectrometry for the sensitive and rapid real-time detection of solid high explosives in air and water. *Anal. Bioanal. Chem.* **398**(7–8), 2813–2820 (2010)
- Sulzer, P., Agarwal, B., Jürschik, S., Lanza, M., Jordan, A., Hartungen, E., Hanel, G., Märk, L., Märk, T.D., González-Méndez, R., Watts, P., Mayhew, C.A.: Applications of switching reagent ions in proton transfer reaction mass spectrometric instruments for the improved selectivity of explosive compounds. *Int. J. Mass Spectrom.* **354–355**(0), 123–128 (2013)
- Agarwal, B., González-Méndez, R., Lanza, M., Sulzer, P., Märk, T.D., Thomas, N., Mayhew, C.A.: Sensitivity and selectivity of switchable reagent ion soft chemical ionization mass spectrometry for the detection of picric acid. *J. Phys. Chem. A.* **118**(37), 8229–8236 (2014)
- González-Méndez, R., Watts, P., Olivenza-León, D., Reich, D.F., Mullock, S.J., Corlett, C.A., Cairns, S., Hickey, P., Brookes, M., Mayhew, C.A.: Enhancement of compound selectivity using a radio frequency ion-funnel proton transfer reaction mass spectrometer: improved specificity for explosive compounds. *Anal. Chem.* **88**(21), 10624–10630 (2016)

19. González-Méndez, R.: Development and Applications of Proton Transfer Reaction-Mass Spectrometry for Homeland Security: Trace Detection of Explosives. PhD, University of Birmingham, (2017)
20. González-Méndez, R., Watts, P., Reich, D.F., Mullock, S.J., Cairns, S., Hickey, P., Brookes, M., Mayhew, C.A.: Use of rapid reduced electric field switching to enhance compound specificity for proton transfer reaction-mass spectrometry. *Anal. Chem.* **90**(9), 5664–5670 (2018)
21. Petersson, F., Sulzer, P., Mayhew, C.A., Watts, P., Jordan, A., Märk, L., Märk, T.D.: Real-time trace detection and identification of chemical warfare agent simulants using recent advances in proton transfer reaction time-of-flight mass spectrometry. *Rapid Commun. Mass Spectrom.* **23**(23), 3875–3880 (2009)
22. González-Méndez, R., Mayhew, C.A.: Applications of direct injection soft chemical ionisation-mass spectrometry for the detection of pre-blast smokeless powder organic additives. *J. Am. Soc. Mass Spectrom.* **30**(4), 615–624 (2019)
23. Barber, S., Blake, R.S., White, I.R., Monks, P.S., Reich, F., Mullock, S., Ellis, A.M.: Increased sensitivity in proton transfer reaction mass spectrometry by incorporation of a radio frequency ion funnel. *Anal. Chem.* **84**(12), 5387–5391 (2012)
24. Lanza, M., Acton, W.J., Jürschik, S., Sulzer, P., Breiev, K., Jordan, A., Hartungen, E., Hanel, G., Märk, L., Mayhew, C.A., Märk, T.D.: Distinguishing two isomeric mephedrone substitutes with selective reagent ionisation mass spectrometry (SRI-MS). *J. Mass Spectrom.* **48**(9), 1015–1018 (2013)
25. Yuan, H.; Li, D.; Liu, Y.; Xu, X.; Xiong, C.: Nitrogen-doped carbon dots from plant cytoplasm as selective and sensitive fluorescent probes for detecting p-nitroaniline in both aqueous and soil systems. *Analyst.* **140**(5), 1428–1431 (2015)
26. Lu, X., Yang, Y., Zeng, Y., Li, L., Wu, X.: Rapid and reliable determination of p-nitroaniline in wastewater by molecularly imprinted fluorescent polymeric ionic liquid microspheres. *Biosens. Bioelectron.* **99**, 47–55 (2018)
27. Booth, G.: Ullmann's encyclopedia of industrial chemistry. *Ref. Serv. Rev.* **16**(4), 31–34 (2007)
28. Blake, R.S., Monks, P.S., Ellis, A.M.: Proton-transfer reaction mass spectrometry. *Chem. Rev.* **109**(3), 861–896 (2009)
29. Jarvis, G., Kennedy, R., Mayhew, C., Tuckett, R.P.: Charge transfer from neutral perfluorocarbons to various cations: long-range versus short-range reaction mechanisms. *Int. J. Mass Spectrom.* **202**(1–3), 323–343 (2000)
30. Frisch, M.; Trucks, G.; Schlegel, H.; Scuseria, G.; Robb, M.; Cheeseman, J.; Scalmani, G.; Barone, V.; Mennucci, B.; Petersson, G.: Gaussian 09, revision A. 1. Gaussian Inc., Wallingford (2009)
31. González-Méndez, R., Watts, P., Howse, D.C., Procino, I., McIntyre, H., Mayhew, C.A.: Ion mobility studies on the negative ion-molecule chemistry of isoflurane and enflurane. *J. Am. Soc. Mass Spectrom.* **28**(5), 939–946 (2017)
32. González-Méndez, R., Watts, P., Howse, D.C., Procino, I., McIntyre, H., Mayhew, C.A.: Ion mobility studies on the negative ion-molecule chemistry of pentachloroethane. *Int. J. Mass Spectrom.* **417**, 16–21 (2017)
33. P.J. Linstrom, W. G. M., Eds., NIST Chemistry WebBook. (2015)
34. Tonkyn, R.G., Winniczek, J.W., White, M.G.: Rotationally resolved photoionization of O₂⁺ near threshold. *Chem. Phys. Lett.* **164**(2–3), 137–142 (1989)
35. Beynon, J., Lester, G., Williams, A.: Some specific molecular rearrangements in the mass spectra of organic compounds. *J. Phys. Chem.* **63**(11), 1861–1868 (1959)
36. Harrison, A.G., Kallury, R.K.M.R.: Chemical ionization mass spectra of mononitroarenes. *Org. Mass Spectrom.* **15**(6), 284–288 (1980)